IN SITU DETERMINATION OF DYNAMIC SOIL PROPERTIES UNDER AN EXCITED SURFACE FOUNDATION

A Dissertation

by

JAEHUN AHN

Submitted to the Office of Graduate Studies of
Texas A&M University
in partial fulfillment of the requirements for the degree of

DOCTOR OF PHILOSOPHY

August 2007

Major Subject: Civil Engineering

IN SITU DETERMINATION OF DYNAMIC SOIL PROPERTIES UNDER AN EXCITED SURFACE FOUNDATION

A Dissertation

by

JAEHUN AHN

Submitted to the Office of Graduate Studies of
Texas A&M University
in partial fulfillment of the requirements for the degree of

DOCTOR OF PHILOSOPHY

Approved by:

Chair of Committee,	Giovanna Biscontin
Committee Members,	Jose M. Roësset
	Luciana Barroso
	Deepa Kundur
Head of Department,	David Rosowsky

August 2007

Major Subject: Civil Engineering

ABSTRACT

In Situ Determination of Dynamic Soil Properties
Under an Excited Surface Foundation. (August 2007)
Jaehun Ahn, B.S., Korea University, Korea;
M.S., Korea University, Korea
Chair of Advisory Committee: Dr. Giovanna Biscontin

The dynamic properties of soil are normally inferred from laboratory tests on collected samples or from empirical relations. The soil properties measured in the field can be very different from those predicted from laboratory tests. It is very difficult to determine directly in the field the variation of the shear modulus and damping with the level of excitation (level of strains). This remains today a major gap in our knowledge and our ability to conduct reliable seismic analyses.

The main objective of this study is to assess the feasibility of determining reliably in situ the shear modulus and damping of the soil as functions of the level of strains, developing a method to compute these properties from the measured data and providing practical recommendations for the use of the procedure. To achieve this objective, extensive and comprehensive sets of experimental and analytical studies were conducted in parallel. Some numerical analyses were performed to provide a better understanding for performing in situ tests with the newly developed vibroseis loading systems. In addition, the dynamic response of a surface foundation in vertical vibration were studied. This dissertation mostly focuses on the numerical aspects of the problem while some experimental data are also studied and utilized.

Field tests were conducted to estimate shear moduli of silty sands at two sites, the Capital Aggregate Quarry and the Texas A&M University sites. Estimated nonlinear shear moduli presented very consistent trends regardless of the analysis methods and

test sites. They showed larger elastic threshold shear strains, 1.5×10^{-3} % for the Capital Aggregate Quarry site and 2×10^{-3} % for the Texas A&M University site, than the mean of shear modulus curve for cohesionless soils proposed by Seed and Idriss (1970). Estimated moduli closely followed the mean of Seed and Idriss (1970) at strains larger than 6×10^{-3} % for both sites. Internal damping ratio can also be estimated if additional data are gathered from in situ tests in the future.

To my parents, brother, and my wife

ACKNOWLEDGMENTS

I am deeply grateful to Dr. Giovanna Biscontin for her guidance and support during my graduate study at Texas A&M University. She provided the great opportunity and environment for the research work. I could develop myself and enjoy working on an interesting research topic under her support.

Dr. Jose M. Roësset's assistance and guidance, which have made this dissertation possible, is gratefully acknowledged. I enjoyed discovering what he has done in the past and developing new tools based on them. I have learned a lot but there is still more to learn from him.

I would also like to thank my other dissertation committee members, Dr. Luciana Barroso and Dr. Deepa Kundur, for reviewing the dissertation and their valuable contributions. They were really good mentors whenever I needed advice.

I would like to express my appreciation to other professors at Texas A&M University - Dr. Jean-Louis Briaud, Dr. James D. Murff, Dr. Charles Aubeny, and Dr. Tanner Blackburn - and at Korea University - Dr. In-Mo Lee and Dr. Woo-Jin Lee - for their excellent teaching and guidance during my graduate studies.

I would like to extend my appreciation to my coworkers, Dr. Kenneth H. Stokoe, II, Kwangsoo Park, and Dr. Won-Seok Seo for excellent experimental works and intuition on this research. I am grateful for their expertise on the field experiments.

I would also like to thank my family, friends, and my wife. I am indebted to them for their enduring support.

The support through the Network for Earthquake Engineering Simulations (NEES) by NSF is gratefully acknowledged.

TABLE OF CONTENTS

CHAPTER Page

CHAPTER Page

LIST OF TABLES

TABLE Page

LIST OF FIGURES

FIGURE Page

FIGURE Page

FIGURE Page

FIGURE Page

FIGURE Page

FIGURE Page

FIGURE Page

FIGURE Page

CHAPTER I

INTRODUCTION

The two main sources of uncertainty in geotechnical earthquake engineering are the characteristics of the earthquakes that can be expected at a given site and the soil properties in situ as a function of depth and level of strains. Much work has been done, and continues to be done, in improving our understanding of the characteristics (amplitudes and frequency content) of the expected seismic motions as a function of the type of earthquake, its magnitude, length of rupturing, distance from the hypocenter, topography of the region, geometry estimated, and soil properties at the site. The soil properties are normally inferred from laboratory tests on collected samples or from empirical relations. Over the last 30 years considerable progress has been achieved in the direct determination in the field, by non-destructive means, of the soil shear modulus at very low levels of strain. However, the values measured in the field can be very different from those predicted from laboratory tests. Very little has been done, on the other hand, to determine directly in the field values of material damping and the variation of the shear modulus and damping with the level of excitation (level of strains). This remains today a major gap in our knowledge and our ability to conduct reliable seismic analyses. Until recently this was a very difficult problem. Recently, under the Network for Earthquake Engineering Simulations (NEES) program, Dr. Stokoe at the University of Texas at Austin developed equipment that would allow the field measurement of soil modulus and damping as a function of strain γ. The objective of this study is to explore the feasibility of determining reliable in situ curves of shear modulus and damping as functions of strain, developing a procedure

---

The journal model is *ASCE Geotechnical and Geoenvironmental Engineering*.

to compute these properties from the measurements, comparing the results to the corresponding laboratory curves and concluding with recommendations for the use of this procedure in practice.

1.1. Background

The research conducted over the second half of last century helped to clarify our understanding of soil dynamics and geotechnical earthquake engineering in general, including both the effect of the local soil conditions on the characteristics of the expected ground motions (soil amplification) and the effects of soil structure interaction. It produced an important number of new formulations and computational tools, based on analytical or semi-analytical approaches (Roesset and Whitman, 1969; Seed and Idriss, 1969; Veletsos and Wei, 1971; Luco and Westmann, 1971; Veletsos and Verbic, 1974), finite elements (Waas, 1972; Kausel, 1974) or boundary elements (Dominguez, 1978; Wolf, 1985). All these formulations assume that the excitation and the soil properties are known. We must realize, however, that there are still many uncertainties associated with the use of these methods in actual practice, as well as limitations in our knowledge. The two main sources of uncertainties in practical situations result from the definition of the seismic excitation itself and from our lack of adequate knowledge and characterization of the soil properties at the site. For important structures it is common to perform detailed seismic risk analyses. This would normally require the use of more sophisticated analysis models; however the validity of doing it will depend on the quantity and quality of the available information. It does not make much sense to use very detailed and often expensive models if one lacks reliable data on the soil properties. The minimum information needed would be the values of the elastic moduli for very low levels of strain (in the linear range) and their variation

with depth, properties that can be determined in situ using seismic methods based on shear or surface waves (Kalinski, 1998). If one wanted to account properly for nonlinear effects it would be necessary to know in addition the nonlinear constitutive models for the materials present at the site for two and three dimensional states of strain. The variation of modulus and damping with level of strain (Seed and Idriss, 1970) has been normally determined from either laboratory tests or empirical relations. However, soil properties measured in situ can be very different from those determined in the laboratory, not only because of sample disturbance but also because of time effects (Anderson and Woods, 1975, 1976; Anderson and Stokoe, 1978). A number of studies have attempted to explain these differences and to provide correction factors to apply to the laboratory data (Lewis, 1990; Kim, 1991; Darendeli, 2001). The basic assumption has been that the relative variation of the shear modulus (dividing the modulus by its maximum value corresponding to very low levels of strain) and damping with strain level would be the same in the laboratory tests and in the field. More recent studies cast some doubt on the validity of this assumption but, until now, it has been impossible to measure in situ shear modulus and damping for different levels of excitation. The recent development of special equipment at the University of Texas at Austin, under the NEES program offers the opportunity to do so in a realistic manner, but work is needed on the interpretation of the data to obtain the desired properties. There is a scarcity of experimental data to help validate different approaches, formulations and models and one must guarantee that when experimental studies are conducted in the field all pertinent data are properly measured. Laboratory tests have the advantage that the excitation and the system parameters can be controlled and measured accurately. By the same token, their disadvantage is that this control can prevent the occurrence of an unexpected phenomenon that would, or could, in fact occur in the field. Field tests are much more important from this

point of view, particularly for geotechnical studies because of the importance of the radiation of waves into the far field. One must be careful however to ensure that the instrumentation is as complete as possible to avoid reaching the wrong conclusions.

While not much has been studied for the in situ determination of soil dynamic properties, there are few examples of notable achievements in development of in situ devices. Henke and Henke (1993) developed a torsional cylindrical impulse shear test. A cylinder probe is intruded into the soil and torsional impulses are generated at selected levels of excitation. Roblee and Riemer (1998) came up with an idea of the Downhole Freestanding Shear Device (DFSD), which is designed to create and subsequently test a freestanding soil column at the bottom of a borehole. Safaqah and Riemer (2006) applied the DFSD to estimate nonlinear moduli in situ. These devices are applicable to soil cylinders in situ but the size of test sample is limited. Larger scale in situ testing has been the subject of a number of studies by the University of Texas at Austin using vibroseis loading systems. Axtell et al. (2002) used a vibroseis loading system to generate harmonic excitation up to nonlinear level. The wave velocities were measured by geophones embedded in the soil deposit. Recently, the vibroseis trucks with triaxial loading system were developed through the Network for Earthquake Engineering Simulation program supported by National Science Foundation (Stokoe et al., 2006).

In this study, vibroseis trucks were used to determine in situ soil dynamic properties under a joint research project by Texas A&M University and the University of Texas at Austin.

1.2. Objectives and Organizations

The main objective of this study is to assess the feasibility of determining reliably in situ the shear modulus and damping of the soil as functions of the level of strains, developing a method to compute these properties from the measured data and providing practical recommendations for the use of the procedure. To achieve this objective, extensive and comprehensive sets of experimental and analytical studies have been conducted in parallel. Some numerical work was also been carried out in order to provide guidance in performing in situ tests using newly developed vibroseis loading systems. This dissertation focuses mostly on the numerical aspects of problem; however, some experimental data are also studied and utilized.

Chapter II deals with shear wave velocity in nonlinear medium. In experimental tests, an initial static load is vertically imposed before dynamic excitation, and shear stresses are induced in the soil deposit due to the static load. It is necessary to determine the effect of static shear stresses on the estimation of shear wave velocity from which shear modulus can be easily derived. True nonlinear dynamic analyses were performed using a simple one-dimensional discrete model with nonlinear material properties for this purpose. Short impacts and harmonic excitations were applied at the top of the discrete model and waveforms were recorded to calculate the shear wave velocities. The calculated wave velocities were compared with those of the baseline materials.

Chapter III discusses the type of wave velocities, either compression wave (P wave) or rod wave, generated and measured under a surface foundation during vertical harmonic excitations. Two analytical solutions (Kausel and Roesset, 1981; Kausel, 1981) and a finite element code (Kausel, 1974) were used for parametric studies. The phases of the displacements were recorded at different locations in the radial and

vertical directions to calculate the wave velocities from the phase differences for a certain range of forcing frequencies. The calculated wave velocities in either a linear or a nonlinear (equivalent-linear) material were compared to baseline wave velocities to see what wave velocity, either compression or rod wave, is close to the measured velocity.

Chapter IV deals with the nonlinear shear moduli from the in situ harmonic excitation tests. The nonlinear shear moduli could be estimated using the phase difference and inverse analyses with the horizontal and vertical excitation test data, respectively. In the proposed inversion procedure, the Levengerg-Marquardt method (Levenberg, 1944; Marquardt, 1963) was employed as a parameter adjustment algorithm, and a finite element method with consistent transmitting boundaries (Kausel, 1974) was used as a numerical model. The proposed method was validated through sets of parametric studies and then used to estimate nonlinear shear moduli for the soil in situ. The feasibility of estimating the internal damping ratios using the inversion procedure was also discussed.

Chapter V is devoted to the estimation of dynamic characteristics of the vertically excited surface foundation on a soil deposit. The approximated analytical solutions (Verbic, 1972) and a finite element code with transmitting boundary (Kausel, 1974) were used to obtain the frequency response functions of the system without and with horizontal layers in soil deposit, respectively. Analyses were performed also with the inputs from actual material properties in the field, and the results were compared to those of stepped sine excitation tests in situ.

Summary and conclusions are presented in Chapter VI with the suggestion for future work.

CHAPTER II

WAVE PROPAGATION IN NONLINEAR ONE-DIMENSIONAL SOIL MODEL

2.1. Introduction

Different types of seismic tests have been used to determine soil properties in situ. Some are performed without any additional static load imposed on the ground, such as the refraction and reflection seismic tests, the crosshole seismic test, the suspension logging test, the uphole and downhole seismic tests, the seismic cone penetration test, or the spectral analysis of surface waves (SASW). However, if an initial vertical load is applied on the ground before the excitation, as in the case of this research, the initial state of stresses under the loaded area will be affected. It is expected the change in stress states affects measured wave velocities. Therefore, it is necessary to observe the effect of the initial static load on the wave velocity measurements.

The main purpose of this chapter is to investigate how the initial state of stresses affects the estimated axial or shear modulus of a column or a shear beam using a one dimensional discrete model with nonlinear material properties and applying either a very short impulse or a harmonic load with variable amplitude.

The equations of motion of a continuous elastic shear beam under dynamic excitation are solved analytically first. The theoretical background for modeling of nonlinear shear beam and estimating the wave velocity are presented next. Finally, two sets of parametric studies are described following the comparison of the results of the numerical model to the closed form solution for verification purposes.

2.2. Closed Form Solution for Elastic Medium

The equation of motion was solved analytically for a linear elastic one dimensional continuous element to establish a baseline for comparison with the results of the numerical model which will be used for the nonlinear analyses. Two types of external loading, a triangular impulse and a sinusoidal excitation, were applied at the free end of a one dimensional system that could represent either a column under axial forces or a shear beam under a transverse load, and the problem was solved using modal superposition.

2.2.1. Impulse Excitation

A one dimensional model of a shear beam is shown in Figure 2.1 where x is the distance from the bottom and L is the length of the member. When an external shear force $P(t)$ is applied at the free end of beam $x = L$, the equation of motion at any location x and any time t in terms of the displacement $u(x,t)$ is

$$G_s A u''(x,t) = -P(t)\delta(x-L) + m\ddot{u}(x,t) \tag{2.1}$$

where G_s is the shear modulus of the material, A is the cross sectional area of the beam, $\delta(x)$ is the Dirac delta function, m is the mass per unit length ($= \rho A$), and ρ is the density of the material. The triangular impulse used in this study was defined as a function of time by

$$P(t) = 2P_{I0}\frac{t}{T_d} \qquad \text{for} \quad 0 < t \leq \frac{T_d}{2} \tag{2.2a}$$

$$P(t) = 2P_{I0}(1 - \frac{t}{T_d}) \qquad \text{for} \quad \frac{T_d}{2} < t \leq T_d \tag{2.2b}$$

and $P(t) = 0$ for $t > T_d$ where P_{I0} is the impulse amplitude, and T_d is the duration of the impulse. The shape of the impact is plotted in Figure 2.2.

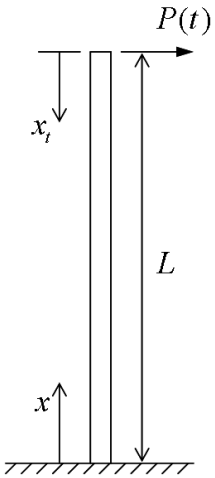

Figure 2.1 One dimensional shear beam

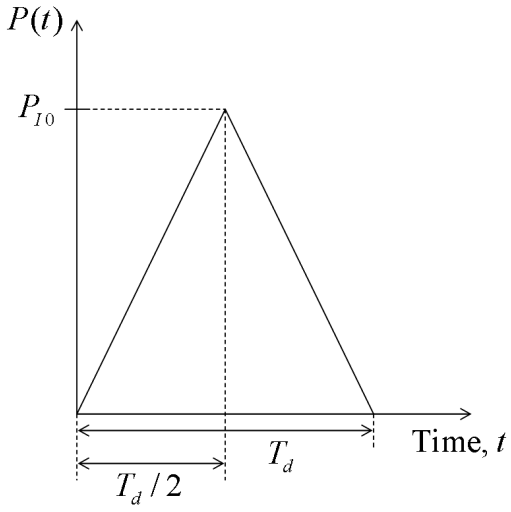

Figure 2.2 Triangular impact with amplitude P_{I0} and duration T_d

Equation (2.1) can be analyzed using modal superposition with the natural frequencies ω_i and the mode shapes ϕ_i of the i^{th} mode

$$\omega_i = \frac{(2i-1)\pi}{2}\sqrt{\frac{G_s A}{mL^2}} \tag{2.3}$$

$$\phi_i = \sin\frac{(2i-1)\pi x}{2L}. \tag{2.4}$$

Using modal analysis, the displacement $u(x,t)$ due to the triangular impact load can be expressed as

$$u(x,t) = \sum_{i=1}^{\infty} \frac{(-1)^{i-1}M}{\omega_i^2 T_d}[t - \frac{1}{\omega_i}\sin\omega_i t]\phi_i \qquad \text{for} \quad 0 < t \le \frac{T_d}{2} \tag{2.5a}$$

$$\begin{aligned} u(x,t) = &\sum_{i=1}^{\infty}[A_{1i}\sin\omega_i(t-\frac{T_d}{2}) + A_{2i}\cos\omega_i(t-\frac{T_d}{2}) - \\ &\frac{(-1)^{i-1}M}{\omega_i^2 T_d}(t-T_d)]\phi_i \qquad \text{for} \quad \frac{T_d}{2} < t \le T_d \end{aligned} \tag{2.5b}$$

$$u(x,t) = \sum_{i=1}^{\infty}[B_{1i}\sin\omega_i(t-T_d) + B_{2i}\cos\omega_i(t-T_d)]\phi_i \qquad \text{for} \quad t > T_d \tag{2.5c}$$

where

$$\begin{aligned} M &= \frac{4P_{I0}}{mL} \\ A_{1i} &= \frac{(-1)^{i-1}M}{\omega_i^3 T_d}(2 - \cos\omega_i\frac{T_d}{2}) \\ A_{2i} &= -\frac{(-1)^{i-1}M}{\omega_i^2 T_d}(\frac{1}{\omega_i}\sin\omega_i\frac{T_d}{2}) \\ B_{1i} &= A_{1i}\cos\omega_i\frac{T_d}{2} - A_{2i}\sin\omega_i\frac{T_d}{2} - \frac{(-1)^{i-1}M}{\omega_i^3 T_d} \\ B_{2i} &= A_{1i}\sin\omega_i\frac{T_d}{2} + A_{2i}\cos\omega_i\frac{T_d}{2}. \end{aligned}$$

The velocity $\dot{u}(x,t)$ is obtained by differentiating the displacement in Equation 2.5

leading to

$$\dot{u}(x,t) = \sum_{i=1}^{\infty} \frac{(-1)^{i-1} M}{\omega_i^2 T_d}[1 - \cos\omega_i t]\phi_i \qquad \text{for} \quad 0 < t \leq \frac{T_d}{2} \tag{2.6a}$$

$$\begin{aligned}\dot{u}(x,t) = \sum_{i=1}^{\infty} [&A_{1i}\omega_i \cos\omega_i(t - \frac{T_d}{2}) - \\ &A_{2i}\omega_i \sin\omega_i(t - \frac{T_d}{2}) - \frac{(-1)^{i-1} M}{\omega_i^2 T_d}]\phi_i \qquad \text{for} \quad \frac{T_d}{2} < t \leq T_d\end{aligned} \tag{2.6b}$$

$$\dot{u}(x,t) = \sum_{i=1}^{\infty} [B_{1i}\omega_i \cos\omega_i(t - T_d) - B_{2i}\omega_i \sin\omega_i(t - T_d)]\phi_i \qquad \text{for} \quad t > T_d. \tag{2.6c}$$

The plots of the displacement and the velocity time histories calculated using Equation 2.5 and 2.6 are presented in Figures 2.3(a) and 2.3(b), respectively. To calculate the responses, 5000 modes were superimposed.

2.2.2. Sinusoidal Excitation

We consider next the response of the shear beam to a sinusoidal load as illustrated in Figure 2.4.

$$P(t) = P_{S0} \sin\Omega t \quad \text{for} \quad 0 \leq t < \infty \tag{2.7}$$

where P_{S0} is the load amplitude, Ω the angular frequency of the load ($\Omega = 2\pi f = \frac{2\pi}{T_0}$), f the circular cyclic frequency, and T_0 the period.

The displacement $u(x,t)$ is then given by

$$u(x,t) = \sum_{i=1}^{\infty} \frac{2P_{S0}}{mL} \frac{(-1)^{i-1}}{\omega_i^2 - \Omega^2}(\sin\Omega t - \frac{\Omega}{\omega_i}\sin\omega_i t)\phi_i. \tag{2.8}$$

And the particle velocity $\dot{u}(x,t)$ is

$$\dot{u}(x,t) = \sum_{i=1}^{\infty} \frac{2P_{S0}}{mL} \frac{(-1)^{i-1}}{\omega_i^2 - \Omega^2}(\Omega\cos\Omega t - \Omega\cos\omega_i t)\phi_i. \tag{2.9}$$

The plot of the displacement and the velocity histories are presented in Figures

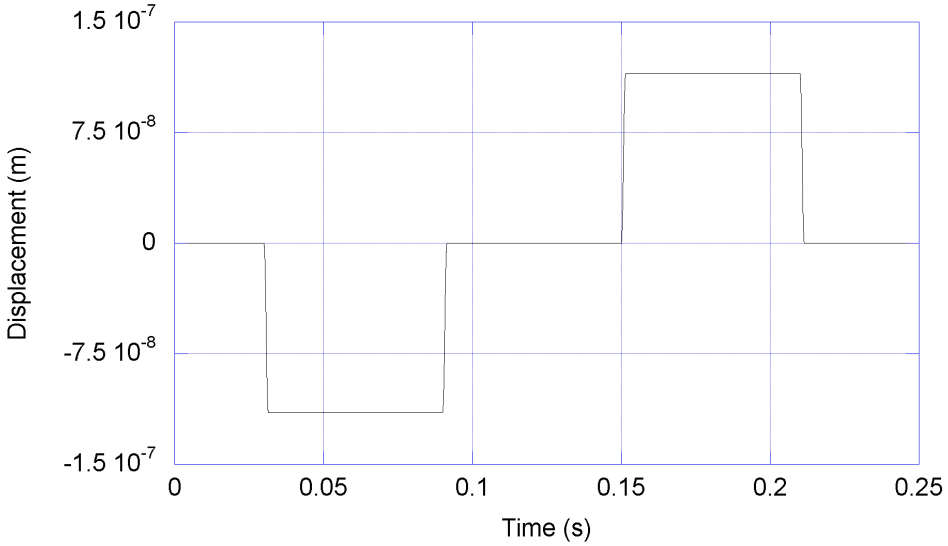

(a) Displacement history

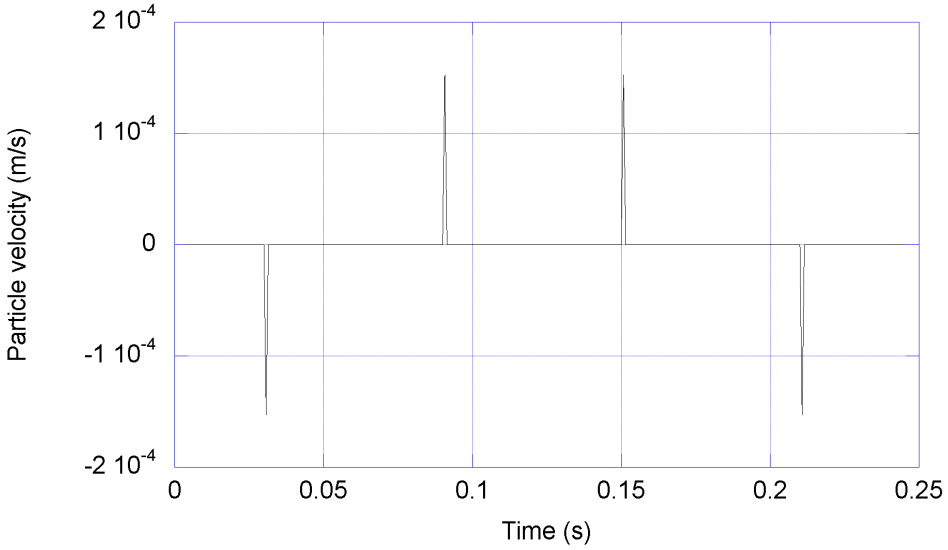

(b) Particle velocity history

Figure 2.3 Results of modal analysis at mid-length of shear beam with $T_d = 1.5\times10^{-5}$ s and $P_{I0} = 31.56$ N using closed form solution

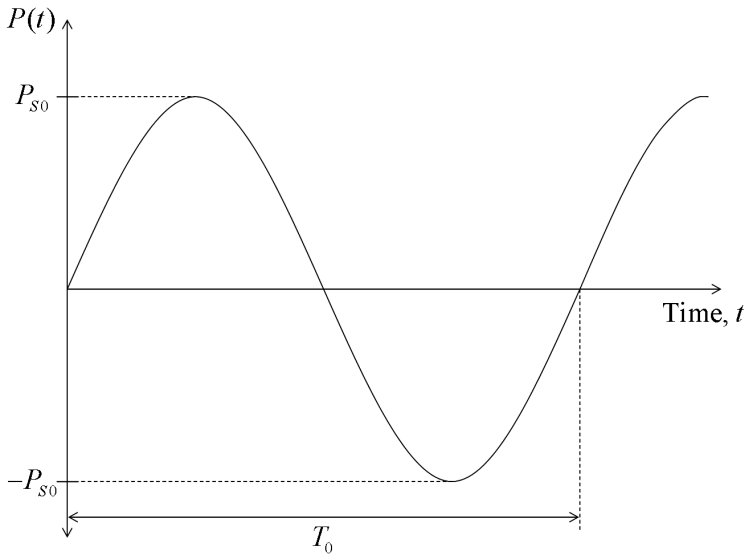

Figure 2.4 Sinusoidal load with amplitude P_{S0} and period T_0

2.5(a) and 2.5(b), respectively. Again, 5000 modes were superimposed to calculate responses.

2.3. Numerical Method

A discrete formulation was used to simulate the dynamic response of a soil beam, modeled as a shear beam under an impact or a harmonic excitation applied at the free end. The wave propagation velocity was estimated using cross-correlation of two signals (particle velocity time histories) at different points along the beam.

2.3.1. Analytical Model

The beam was represented by a series of lumped masses connected by shear springs. The schematic model of the beam is shown in Figure 2.6, P_{st} denotes an initial static load, $P(t)$ is the dynamic excitation, m_1 and m_2 are the lumped masses ($m_1 = m_2/2$), and k_{sh} denotes the nonlinear spring. Each of the nonlinear spring elements consist

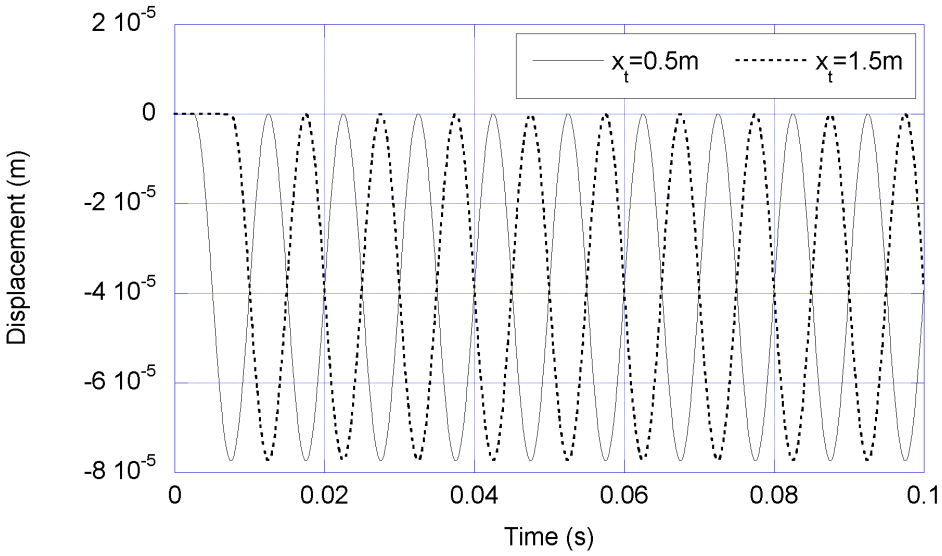

(a) Displacement history

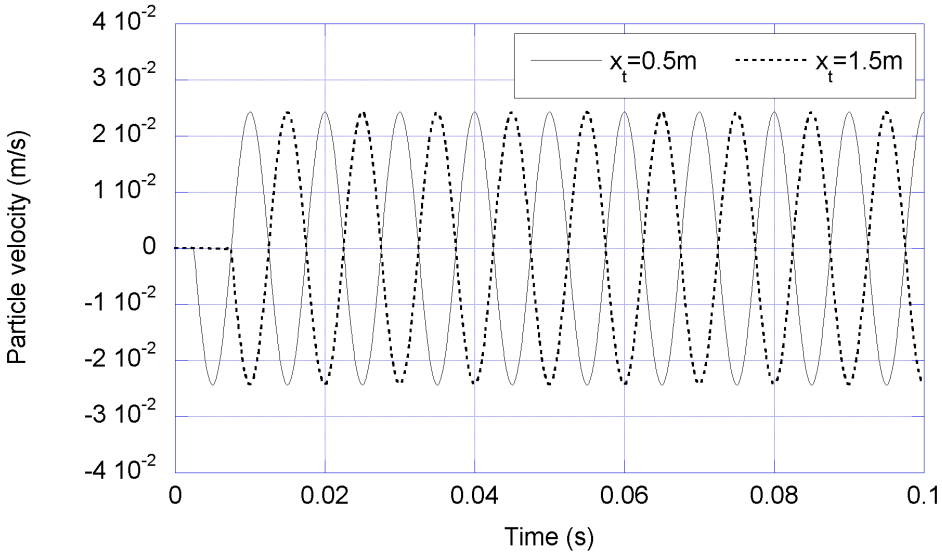

(b) Particle velocity history

Figure 2.5 Results of modal analysis at $x_t = 0.5$ m and $x_t = 1.5$ m with $f = 100$ Hz and $P_{S0} = 5000$ N using closed form solution

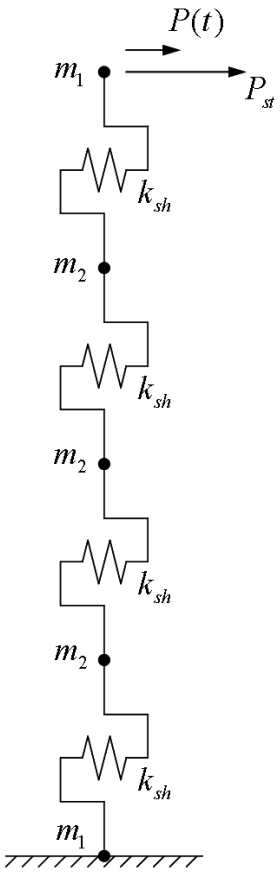

Figure 2.6 One dimensional discrete model in shear loading

of a set of elastic perfectly plastic springs acting in parallel. The bottom boundary is fixed, but the overall length L can be chosen large enough to avoid the effect of wave reflections at the bottom within the time interval of interest.

2.3.2. Nonlinear Material Model

It is possible to derive a shear stress-strain curve for the soil starting from a stiffness reduction curve relating the shear modulus to the shear strain. The nonlinear soil behavior of the stress-strain curve can be reproduced by a set of nonlinear, elastic perfectly plastic springs in parallel (Iwan, 1967). The i^{th} elastic perfectly plastic

spring is represented by the slope k_i and the yield stress τ_{yi} given by

$$k_i = \frac{\tau_i - \tau_{i-1}}{\gamma_i - \gamma_{i-1}} - \sum_{j=i+1}^{M_p} k_j \tag{2.10a}$$

$$\tau_{yi} = k_i \gamma_i \tag{2.10b}$$

where M_p is the total number of elastic perfectly plastic springs, and γ_i and τ_i are the shear strain and stress, respectively, in the stiffness reduction or the nonlinear stress-strain curve ($\gamma_0 = \tau_0 = 0$). An example of this scheme is illustrated in Figure 2.7 with three elastic perfectly plastic springs. From Equation 2.10, each elastic perfectly plastic spring in Figure 2.6 becomes

$$k_3 = \frac{\tau_3 - \tau_2}{\gamma_3 - \gamma_2} \qquad \tau_{y3} = k_3 \gamma_3 \tag{2.11a}$$

$$k_2 = \frac{\tau_2 - \tau_1}{\gamma_2 - \gamma_1} - k_3 \qquad \tau_{y2} = k_2 \gamma_2 \tag{2.11b}$$

$$k_1 = \frac{\tau_1}{\gamma_1} - k_2 - k_3 \qquad \tau_{y1} = k_1 \gamma_1. \tag{2.11c}$$

The nonlinear material model used in this study follows Masing's rules. The internal damping ratio D becomes

$$D = \frac{A_L}{4\pi A_T} \tag{2.12}$$

where A_L denotes the area of the hysteresis loop, and A_T is the maximum strain energy stored in each cycle of motion as represented by the triangular area in Figure 2.8.

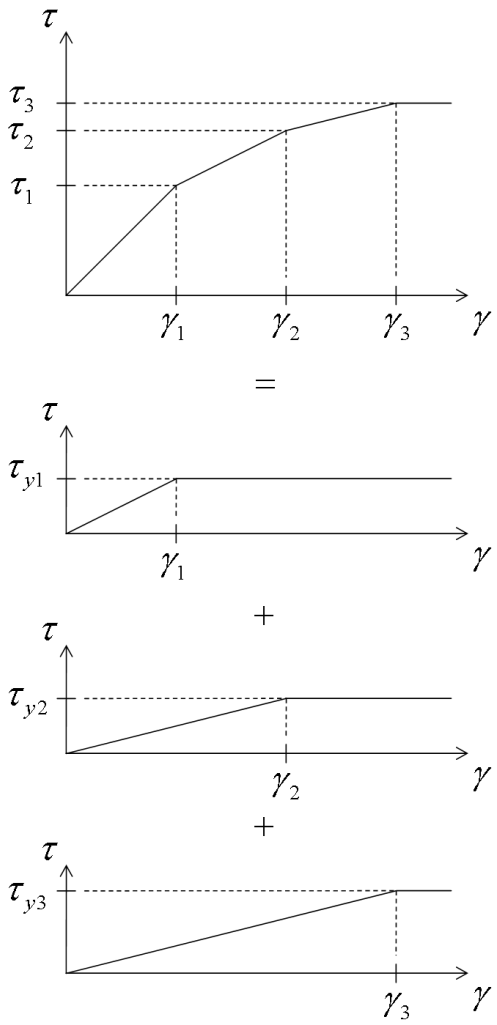

Figure 2.7 Illustration of equivalent nonlinear spring comprised of three elastic perfectly plastic springs

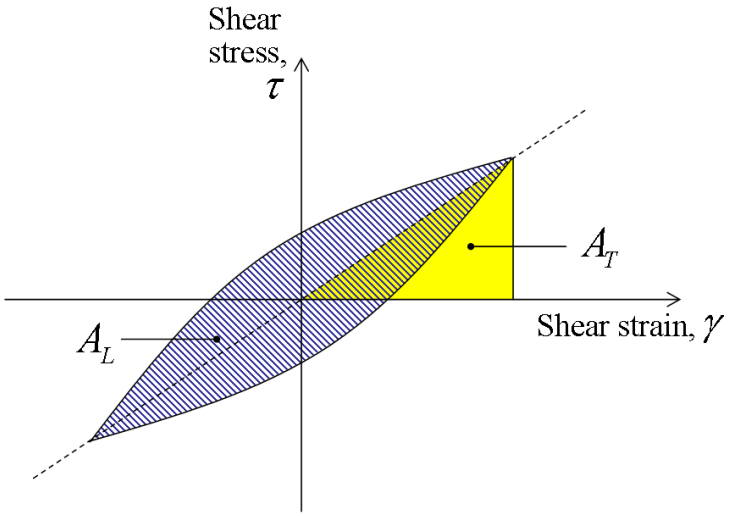

Figure 2.8 Stress-strain behavior with Masing's rule

2.3.3. Central Difference Formulation

The dynamic equilibrium equation for the i^{th} mass of the discrete system at a time step n can be expressed as

$$m_i \ddot{u}_{i,n} + F_{i-1,n} - F_{i,n} = P_{i,n} \tag{2.13}$$

where m_i is the i^{th} lumped mass, $\ddot{u}_{i,n}$ is the acceleration of the i^{th} mass, $F_{i-1,n}$ and $F_{i,n}$ are the forces applied by the nonlinear springs at each side of the mass, and $P_{i,n}$ is the external load on the i^{th} mass.

Using central differences, the velocity $\dot{u}_{i,n}$, and the acceleration $\ddot{u}_{i,n}$ can be expressed as

$$\dot{u}_{i,n} = \frac{1}{2\Delta t}(u_{i,n+1} - u_{i,n-1}) \tag{2.14a}$$

$$\ddot{u}_{i,n} = \frac{1}{\Delta t^2}(u_{i,n+1} - 2u_{i,n} + u_{i,n-1}) \tag{2.14b}$$

where Δt represents the length of a time step. When using a central difference scheme

the time step Δt must be smaller than a critical value Δt_{cr}:

$$\Delta t \leq \Delta t_{cr} = \frac{T_n}{\pi} \tag{2.15}$$

where T_n denotes the smallest natural period of the n degrees of freedom system.

By substituting Equation set 2.14 into Equation 2.13, we obtain

$$m_i \frac{1}{\Delta t^2}(u_{i,n+1} - 2u_{i,n} + u_{i,n-1}) + F_{i-1} - F_i = P_i. \tag{2.16}$$

Rearranging Equation 2.16 to calculate the $(n+1)^{th}$ step displacement $u_{i,n+1}$ yields

$$u_{i,n+1} = 2u_{i,n} - u_{i,n-1} + \frac{(P_{i,n} - F_{i-1,n} + F_{i,n})\Delta t^2}{m_i}. \tag{2.17}$$

Once the displacements at the $(n-1)^{th}$ and n^{th} time steps are known, the displacement at the $(n+1)^{th}$ time step can be calculated from this equation.

2.4. Wave Velocity Estimation

Two systematic ways of estimating the wave velocity, using phase difference or cross-correlation, are presented in this section. While an example of how to obtain the wave velocity using phase difference is presented, cross-correlation was used to calculate wave propagation velocities in most cases, as it gives a single representative value.

2.4.1. Wave Velocity from Phase Difference

The Discrete Fourier transform can be used to transfer a discrete signal from the time domain to the frequency domain (Roberts, 2004). In the frequency domain, the wave velocity can be calculated from the phase difference between two different points

using simple algebra. The discrete Fourier pairs used in this study are as following:

$$X[k] = \sum_{n=0}^{N_p-1} x[n] e^{-i\frac{2\pi kn}{N_p}} \Delta t \tag{2.18}$$

$$x[n] = \sum_{k=0}^{N_p-1} X[k] e^{i\frac{2\pi kn}{N_p}} \frac{1}{T_p} \tag{2.19}$$

where k is the frequency index, n is the time index, $X[k]$ is the Fourier transform of the original signal $x[n]$, N_p is the number of samples, Δt is the length of a time step, and $T_p = N_p \cdot \Delta t$.

Let $C_{v1}(\omega)$ and $C_{v2}(\omega)$ be the discrete Fourier transforms of two signals $c_{v1}(t)$ and $c_{v2}(t)$, respectively. Then, the phase difference can be obtained from

$$\phi = \tan^{-1} \frac{Im[C_{v1}(\omega)/C_{v2}(\omega)]}{Re[C_{v1}(\omega)/C_{v2}(\omega)]} \tag{2.20}$$

where $Im[\quad]$ and $Re[\quad]$ denote the imaginary and real parts of the complex number inside the bracket, respectively. When $c_{v1}(t)$ and $c_{v2}(t)$ represent the motion at two distinct points separated by a distance d, the wave velocity can be calculated from the phase difference as

$$c = d \cdot \omega / \phi \tag{2.21}$$

where ω is the angular frequency.

2.4.2. Wave Velocity from Cross-Correlation

Alternatively, the cross-correlation technique can also be used to estimate the time delay between two signals whose shapes are similar. If a discrete time signal $x[n]$ is separated from the other signal $y[n]$ as shown in Figure 2.9, the cross-correlation

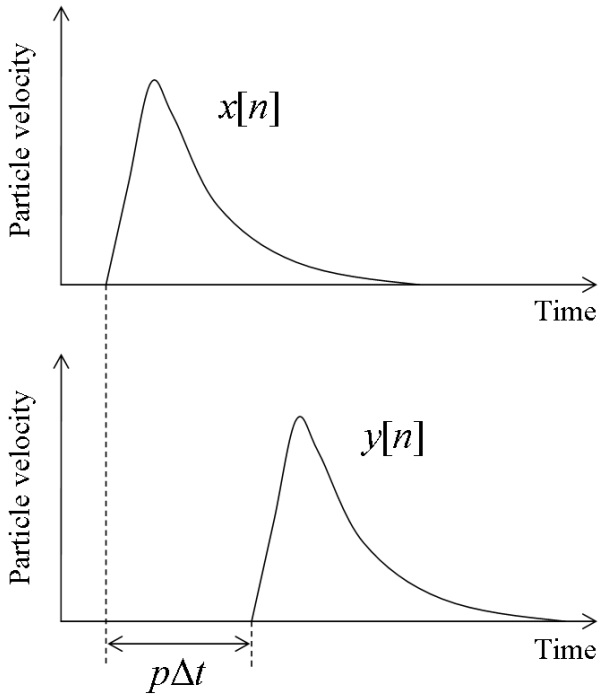

Figure 2.9 Two signals separated by a time delay $p\Delta t$

between the two signals can be obtained using the equation:

$$cc[p]^{<x,y>} = \sum_{n=-\infty}^{\infty} x[n]y[n+p] \tag{2.22}$$

where n, p are the time indices. The cross-correlation function is thus obtained from the multiplication of one signal $x[n]$ and the shifted signal $y[n+p]$ summed for all n for a given p. The maximum of the cross-correlation therefore occurs when the signals $x[n]$ and $y[n+p]$ overlap. The time index p when the maximum cross-correlation takes place can be used to estimate the time delay and the wave velocity of the traveling signal.

The convolution sum of the two signals in the time domain can be easily calculated by multiplying the Fourier transforms of the two signals in the frequency

domain. The expression of the cross-correlation function in the frequency domain is

$$CC[k]^{<x,y>} = Y[k]\overline{X}[k] \tag{2.23}$$

where $CC[k]^{<x,y>}$ represents the Fourier transform of the cross-correlation function $cc[n]^{<x,y>}$, $X[k]$ and $Y[k]$ are the Fourier transforms of the signals $x[n]$ and $y[n]$, respectively, and $\overline{X}[k]$ is the complex conjugate of $X[k]$. The calculated cross-correlation in the frequency domain $CC[k]^{<x,y>}$ needs to be transformed back to the time domain using the inverse Fourier transform to calculate the time delay $p\Delta t$.

2.5. Problem Definition

As described in the preceding sections, a one dimensional discrete model was used to simulate the dynamic response of a shear beam representing a soil beam under an impact or a sinusoidal load. The schematic of the one dimensional model was shown in Figure 2.6. The number of elements N_{elem} and the time step Δt were carefully chosen to accommodate high frequency dynamic loading, in order to avoid instability and to ensure accuracy, since the explicit finite difference scheme was used for the integration. The nonlinear equivalent springs comprised a number of individual elastic perfectly plastic springs to simulate the nonlinear material behavior. The properties of each elastic perfectly plastic spring were derived from the shear modulus reduction curve, as mentioned in the previous section. Also, the nonlinear springs follow Masing's behavior resulting in internal hysteretic damping under cyclic loading. The characteristics of the material will be described later in detail.

Two types of dynamic shear loading, a triangular impact and a sinusoidal load, were applied at the top of the soil beam after an initial shear static loading P_{st}. Several values of the static load - P_{st} = 0 N, 1000 N, 5000 N, 10000 N, and 20000 N for impact

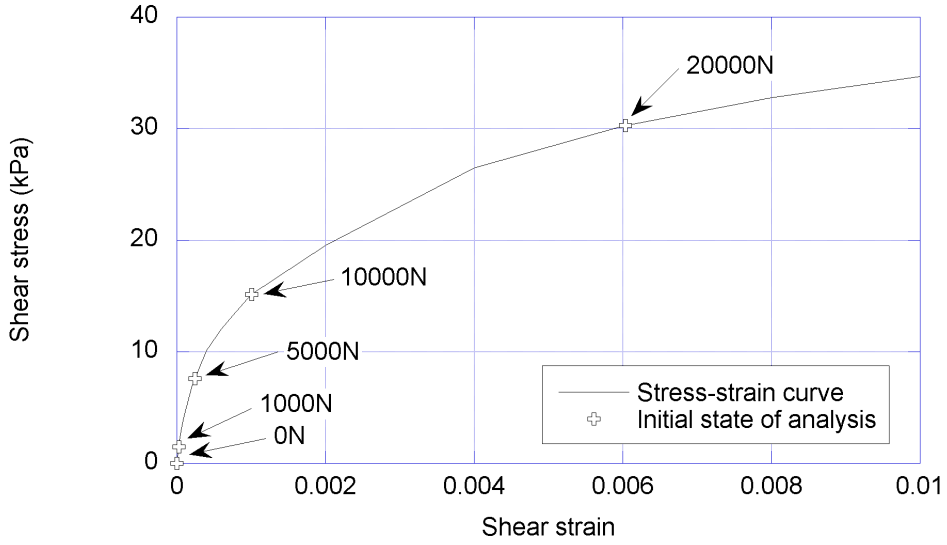

Figure 2.10 Initial shear loads and shear stresses used in the analysis

excitation and $P_{st} = 0$ N, 1000 N, and 10000 N for sinusoidal excitation - were used in this study to investigate the effect of the initial stress state on the computed wave propagation velocities along the soil beam. The static loads are marked on the stress strain curve in Figure 2.10. The the cross sectional area of the beam was selected as $A = 0.66$ m^2, which is the area the footing used in the experiments, that the ratio of the shear load to the corresponding shear stress is 0.66.

The shape of the triangular impact was again

$$P(t) = 2P_{I0}\frac{t}{T_d} \qquad \text{for} \quad 0 < t \leq \frac{T_d}{2}$$

$$P(t) = 2P_{I0}(1 - \frac{t}{T_d}) \qquad \text{for} \quad \frac{T_d}{2} < t \leq T_d$$

and $P(t) = 0$ for $t > T_d$ where P_{I0} is the impact amplitude, and T_d is the duration of impact. The sinusoidal loading used in the analysis was

$$P(t) = P_{S0} \sin \Omega t \quad \text{for} \quad 0 \leq t < \infty$$

where P_{S0} is the amplitude, and Ω the angular frequency.

The density and the maximum shear modulus of the soil were chosen as $\rho = 1560$ kg/m^3 and $G_{s,max} = 62400$ kN/m^2, respectively, which make the maximum shear wave velocity $c_{s,max} = \sqrt{\frac{G_{s,max}}{\rho}} = 200$ m/s. The stress-strain curve used in this study is shown in Figure 2.11.

2.6. Analysis Results: Impact Excitation

The response of the soil beam under a triangular impact, especially the wave propagation velocity, was obtained for various cases to understand the effects of variables such as the initial stress state, the load duration, the linear momentum of the loading, and the location at which the soil responses were obtained. In all the cases, the amplitude of the impact was selected small enough to keep the initial or the incremental shear modulus within the linear range.

2.6.1. Wave Propagation in Elastic Medium

The response of a 12 m elastic beam with a density $\rho = 1560$ kg/m^3 and a shear modulus $G_s = 62.4$ MPa was calculated first for an impact $P_{I0} = 31.56$ N applied at the free end. The number of segments used in the analysis was 4800, the time step $\Delta t = 1.25 \times 10^{-5}$ s, and the impact duration $T_d = 1.5 \times 10^{-3}$ s. The displacement and the particle velocity time histories recorded at the mid point of the beam $x_t = 6$ m are compared to the results of the close form solutions in Equation 2.5, where the coordinate x_t indicates the distance from the free end of the shear beam as shown in Figure 2.1. The displacement time histories using closed form solution and numerical solution are presented in Figure 2.12, and the particle velocity time histories in Figure 2.13.

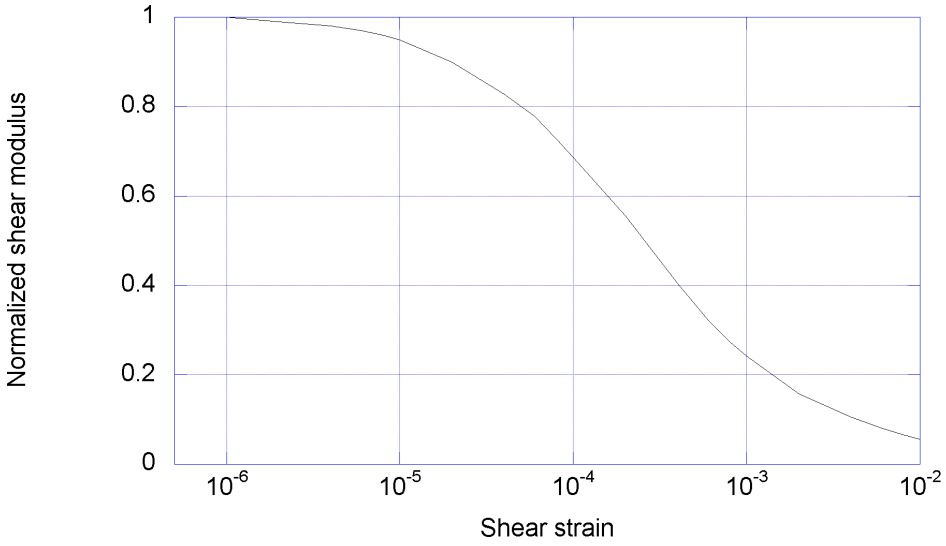

(a) Shear modulus reduction curve

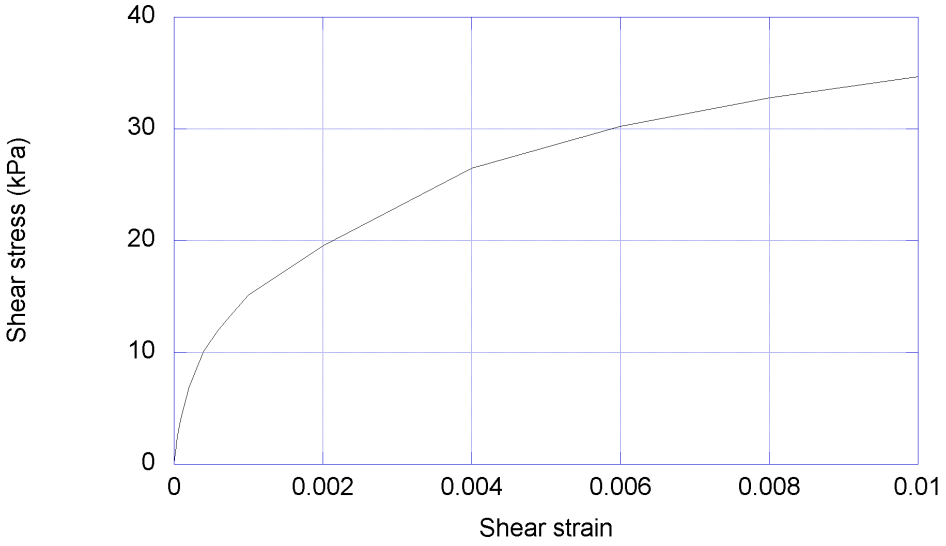

(b) Shear stress-strain curve

Figure 2.11 Material characteristics of the soil used in analyses

From the calculated response using both closed form and numerical analyses, the first wave arrival time at mid length is found to be the theoretical value, $t = 6/c_s = 0.03$ s ($c_s = \sqrt{G_s/\rho} = \sqrt{62.4 \times 10^6/1560} = 200$ m/s). Also the wave reflections at the rigid and the free ends are clearly noticeable. Using the particle velocity histories calculated at $x_t = 0.5$ m and 1.5 m, the cross-correlation was calculated. Figure 2.14(a) shows the original plot of the cross-correlation with respect to the time delay whereas Figure 2.14(b) shows the cross-correlation with respect to the wave velocity, which is the wave travel length divided by the time delay. The wave propagation velocity by the cross-correlation, c_{cc} in 2.14(b) matches the theoretical wave velocity, $c_s = 200$ m/s.

2.6.2. Effect of Initial Stress State

The wave propagation velocity for a nonlinear soil beam was estimated for several values of the initial stress. The impact amplitude $P_{I0} = 31.56$ N was used in this analysis. Five values of initial static shear load and the corresponding stresses are shown in Figure 2.10. A total of 4800 segments were used with a time step $\Delta t = 6.25 \times 10^{-6}$ s and a duration of the triangular impact $T_d = 1.5 \times 10^{-3}$ s. Two reference points were selected at $x_t = 0.5$ m and $x_t = 1.5$ m and the responses were cross-correlated to calculate the wave propagation velocities c_{cc}. Then, to observe the relation between estimated wave velocities and tangent shear moduli, calculated wave velocities c_{cc} were compared to the wave velocities c_{tan} resulting from the tangent shear modulus corresponding to the initial state of stress using the equation, $c_{tan} = \sqrt{G_{s,tan}/\rho}$ where $G_{s,tan}$ is the tangent modulus at the stress state due to the initial static loading. All the analyses were performed within the time range in which the wave reflection from the bottom would not affect the calculated values.

The analysis results are summarized in Figure 2.15 in terms of the cross-correlation

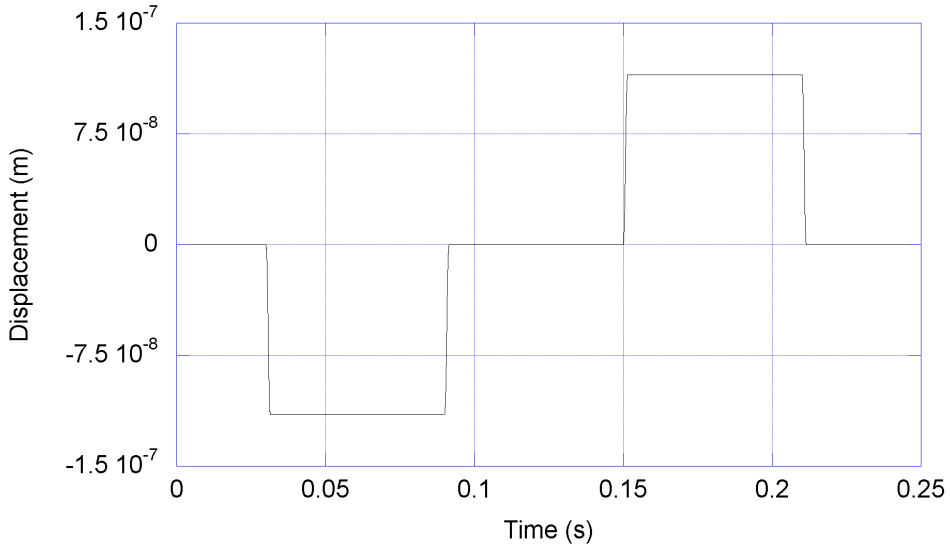

(a) Results from closed form solution with 5000 modes superimposed

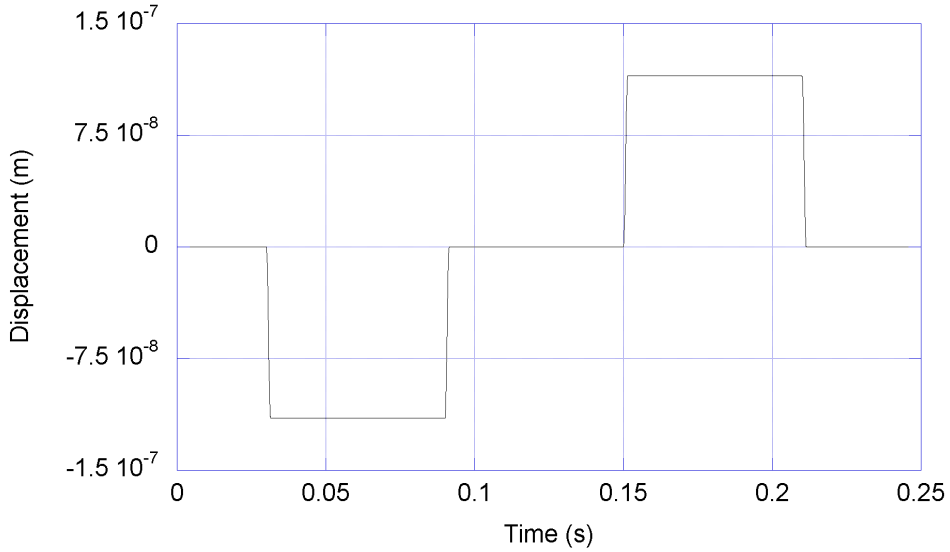

(b) Results from numerical analysis with $N_{elem} = 4800$ and $\Delta t = 1.25 \times 10^{-5}$ s

Figure 2.12 Displacement at mid length of beam with $T_d = 1.5 \times 10^{-5}$ s and $P_{S0} = 31.56$ N

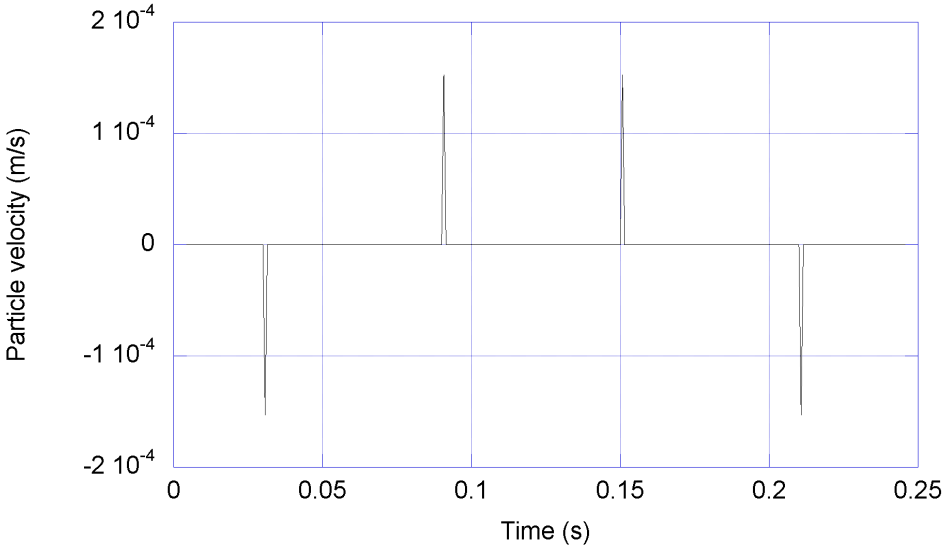

(a) Results from closed form solution with 5000 modes superimposed

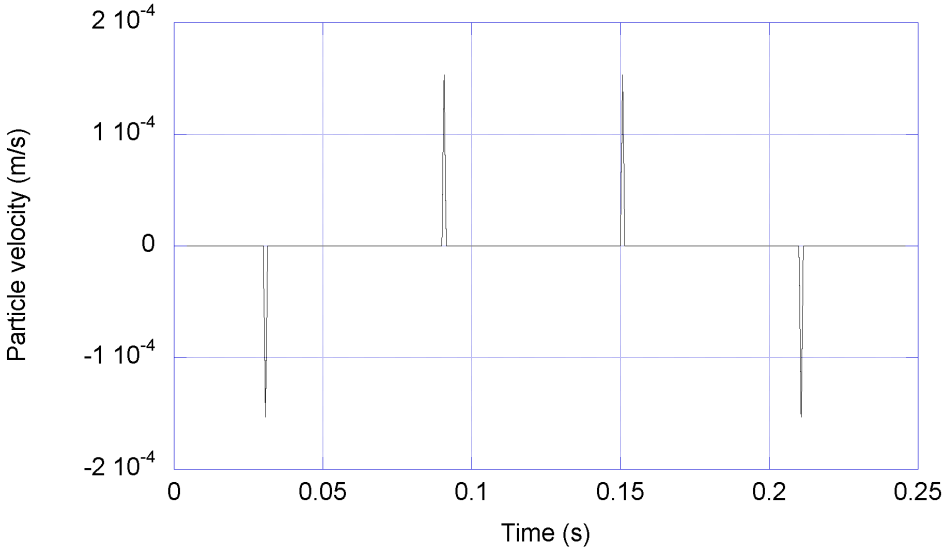

(b) Results from finite analysis with $N_{elem} = 4800$ and $\Delta t = 1.25 \times 10^{-5}$ s

Figure 2.13 Particle velocity at mid-length of beam with $T_d = 1.5 \times 10^{-5}$ s and $P_{S0} = 31.56$ N

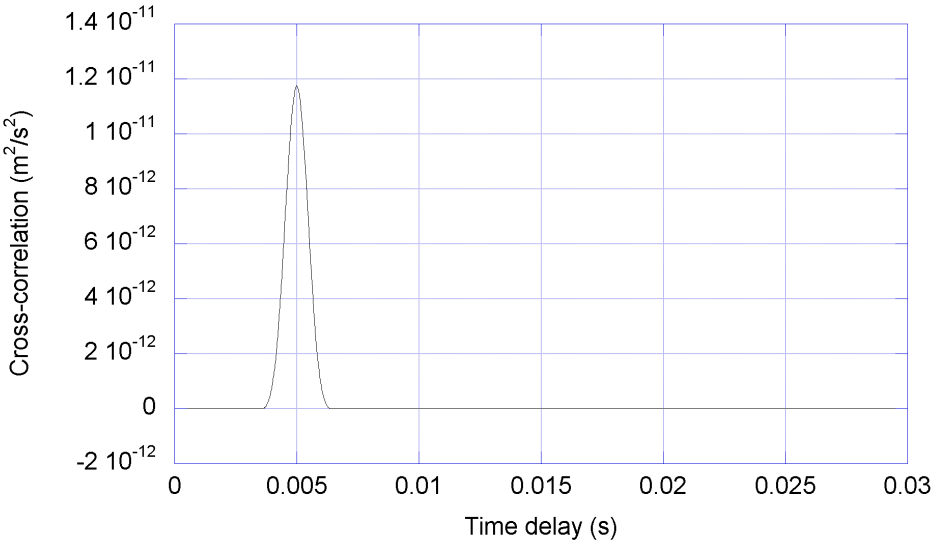

(a) Cross-correlation results in terms of time delay

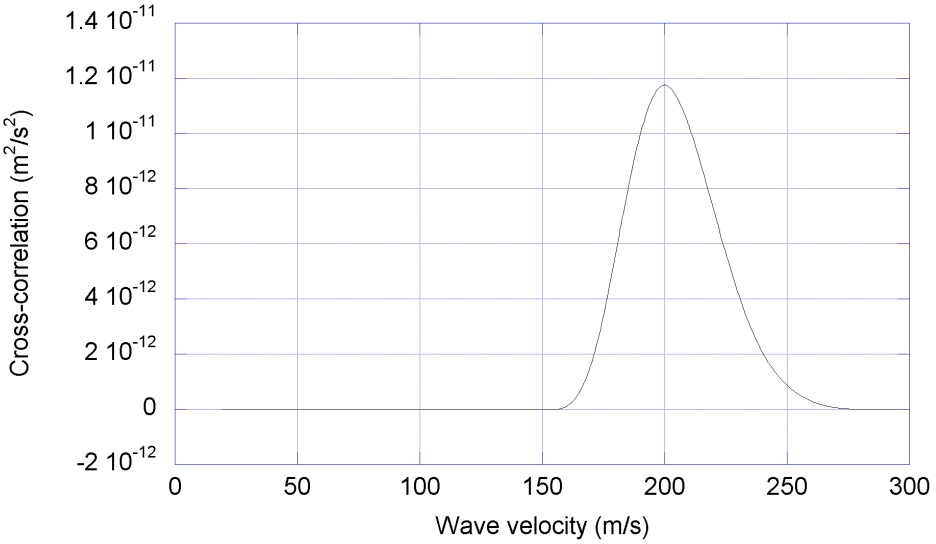

(b) Wave velocity from cross-correlation in terms of time delay

Figure 2.14 Cross-correlation of velocity histories at $x_t = 0.5$ m and 1.5 m in elastic medium

normalized by the maximum cross-correlation value. The wave propagation velocities c_{tan} corresponding to the tangent modulus are marked in the figure by solid triangular symbols. In Figure 2.15(b), the wave velocities c_{cc} from the cross-correlation closely match the wave velocities c_{tan} corresponding to the tangent modulus for values of P_{st} = 0 N, 5000 N, 10000 N, and 20000 N. However, for P_{st} = 1000 N, the cross-correlation result c_{cc} was slightly higher than the wave velocity c_{tan}. In an attempt to understand the reason for the discrepancy between c_{cc} and c_{tan} for P_{st} = 1000 N, the particle velocity histories for P_{st} = 1000 N and 10000 N are plotted in Figure 2.16 and compared. First, the wave velocities were calculated from the initial arrival time difference and the peak-to-peak time difference for P_{st} = 10000 N as shown in Figure 2.16(b). The wave velocities from the initial arrival time difference and peak-to-peak time difference were c_{ini} = 54.2 m/s and c_{peak} = 53.8 m/s, respectively, which compare quite well with the tangent wave velocity c_{tan} = 53.7 m/s and also with the cross-correlation result c_{cc} = 53.8 m/s. However, for P_{st} = 1000 N (Figure 2.16(a)), the wave velocity from the initial arrival time interval was c_{ini} = 174.8 m/s whereas the velocity from the peak-to-peak interval was c_{peak} = 185.6 m/s, while c_{tan} = 174.0 m/s and c_{cc} = 183.0 m/s. The cross-correlation prediction c_{cc} was close to the wave velocity c_{peak} from the peak-to-peak time difference whereas the c_{tan} was close to the value c_{ini} from the time of initial arrivals. This is because the shape of the particle velocity history, especially the sharply edged area, changed noticeably while traveling along the nonlinear soil beam in the case of P_{st} = 1000 N, which affects the calculation of the cross-correlation. Although the wave velocity c_{cc} predicted by the cross-correlation was higher than the wave velocity c_{tan} from the tangent modulus for this particular case, the difference is only about 5%.

The wave propagation velocities were calculated with the same particle velocity histories using phase difference to observe whether the two methods are consistent.

Figure 2.17 shows the estimated wave velocities for different levels of the initial shear load, corresponding to the results in Figure 2.15(b). When there is no initial shear load ($P_{st} = 0$ N), the modulus of the whole shear beam remains the same during the loading and unloading stages of the impulse excitation and the estimated wave velocity shows the theoretical value of 200 m/s over the entire frequency range examined. If initial shear loads are imposed, since the modulus is higher in the loading stage and lower in the unloading stage, the shapes of the computed time histories become irregular due to the material change during the excitation. In these cases, the distance between two locations where the waveforms are examined (the wave travel distance) should be sufficiently larger than the wave length for an accurate estimate of phase differences. The curves with initial shear loads (P_{st} = 1000 N, 5000 N, 10000 N, and 20000 N), show errors in the estimation of wave propagation velocities at small frequencies because the wave travel distances are not sufficiently larger than the wave lengths at those frequencies. If the initial shear load is larger, the wave travels slower and the wave length becomes shorter at a constant frequency. Therefore, the result with a larger static load are inconsistent only for a narrow range of frequency. Although the wave velocities using the phase difference fluctuate a little with the frequency, the results are very close to those using the cross-correlation, especially around the predominant frequency of the impulse applied (duration of 1.5×10^{-3} s resulting in predominant frequency of 667 Hz). For the remaining sections in this chapter, the cross-correlation function was used, as it was a simple and systematic way of estimating a single value of wave velocity.

2.6.3. Effect of Impact Duration

A duration of the impact $T_d = 1.5 \times 10^{-3}$ s was used for all analyses discussed so far. Half and twice of the original value, $T_d = 7.5 \times 10^{-4}$ s and 3.0×10^{-3} s, were considered

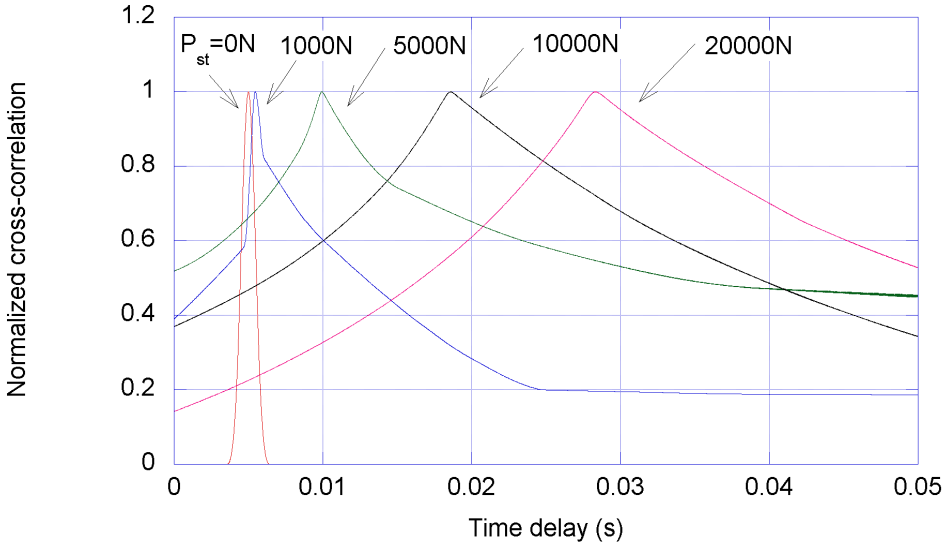

(a) Cross-correlation results in terms of time

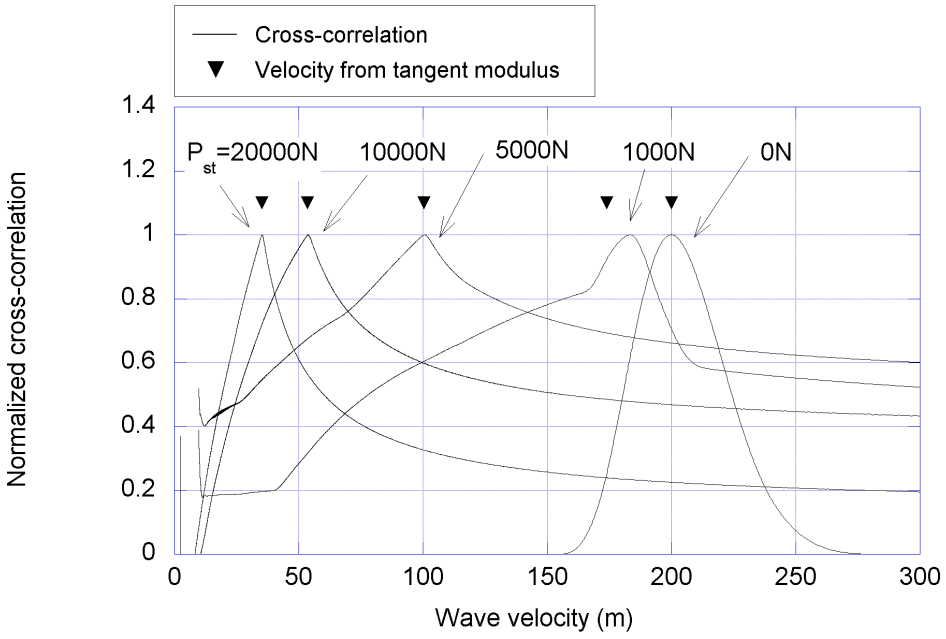

(b) Wave velocity from cross-correlation and tangent modulus

Figure 2.15 Wave velocity estimation in nonlinear soil for different initial stress with $T_d = 1.5 \times 10^{-3}$ s and $P_{I0} = 31.56$ N

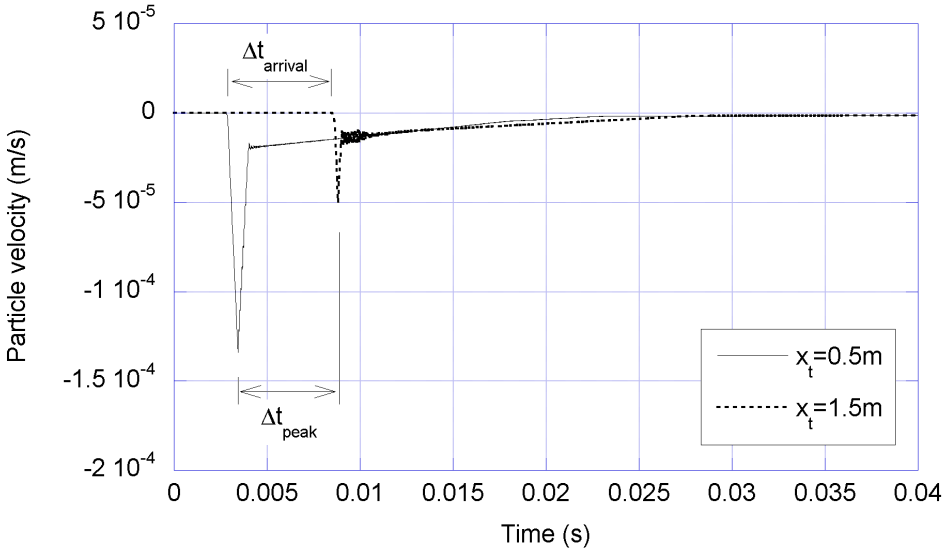

(a) Velocity history for $P_{st} = 1000$ N

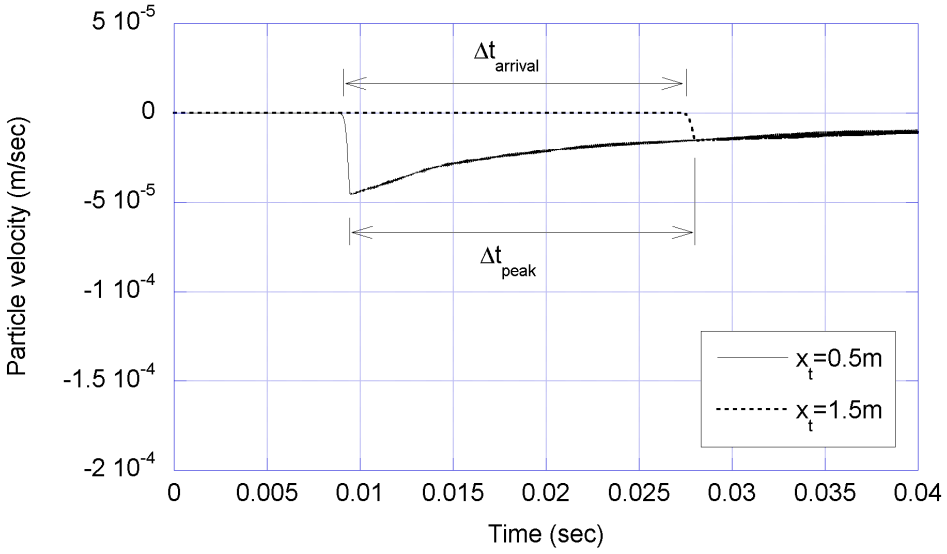

(b) Velocity history for $P_{st} = 10000$ N

Figure 2.16 Velocity history at $x_t = 0.5$ m and 1.5 m after triangular impact with $T_d = 1.5 \times 10^{-3}$ s and $P_{I0} = 31.56$ N

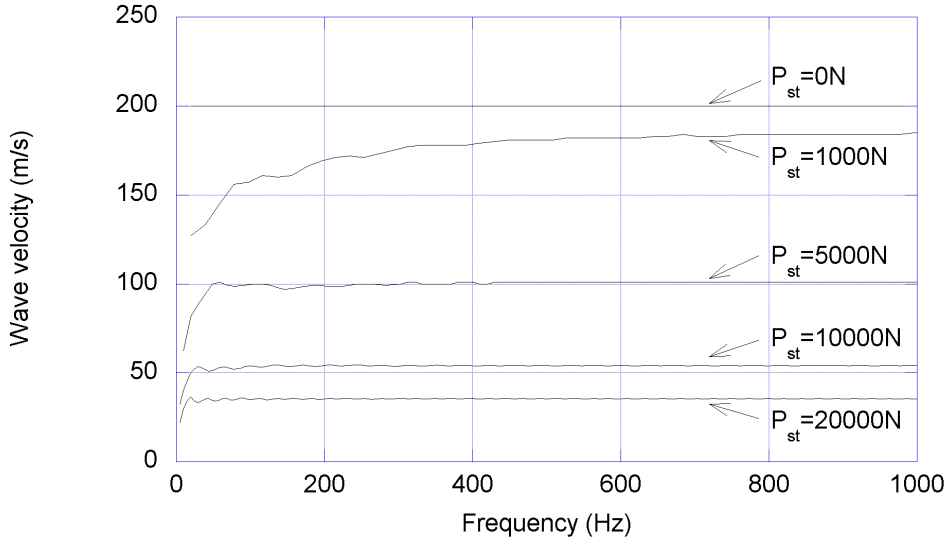

Figure 2.17 Wave velocity corresponding to frequency in nonlinear soil for different initial stress with $T_d = 1.5 \times 10^{-3}$ s and $P_{I0} = 31.56$ N

to study the effect of the impact duration on the wave velocity while keeping the linear momentum produced by the impact constant. The linear momentum, represented by the area of the force time history, is given by

$$\int_0^{T_d} P(t)dt = \frac{1}{2} P_{I0} T_d \tag{2.24}$$

where $P(t)$ is given in Equation 2.2. In order to keep the linear momentum constant, impact magnitudes of $P_{I0} = 63.12$ N and 15.78 N were used with $T_d = 7.5 \times 10^{-4}$ s and 3.0×10^{-3} s, respectively. The results of the analyses are shown in Figure 2.18 along with the previous case of $T_d = 1.5 \times 10^{-3}$ s. For $P_{st} = 10000$ N, the wave velocity c_{cc} from cross-correlation and the velocity c_{tan} from the tangent modulus coincide for all three values of T_d. However, for $P_{st} = 1000$ N, the only case when c_{cc} and c_{tan} coincide is the one with $T_d = 7.5 \times 10^{-4}$ s. The particle velocity histories for all cases are presented in Figure 2.19. For $T_d = 3.0 \times 10^{-3}$ s, the wave velocities were calculated again from the initial arrival time and from the peak-to-peak time differences to

explain the reason for the discrepancy between c_{cc} and c_{tan}. The wave velocities from the initial arrival time and the peak-to-peak time differences were $c_{ini} = 174.8$ m/s and $c_{peak} = 185.8$ m/s, respectively, while $c_{tan} = 174.0$ m/s, and $c_{cc} = 184.6$ m/s. The trend is the same previously observed for the case with $T_d = 1.5 \times 10^{-3}$ s with c_{ini} closer to c_{tan}, and c_{cc} to c_{peak}. As the impact duration increased, the cross-correlation predicted a wave velocity c_{cc} higher than the tangent wave velocity c_{tan}. However, the difference between the two was still about 5% of the cross-correlation result c_{cc}.

2.6.4. Effect of Linear Momentum of Impact

Two values of the impact durations, $T_d = 7.5 \times 10^{-4}$ s and 3.0×10^{-3} s, were used to estimate the effect of the linear momentum of the impact on the computed wave velocity, while keeping $P_{I0} = 31.56$ N constant. Thus, the linear momentum of the impact becomes half and double that of the original case with $T_d = 1.5 \times 10^{-3}$ s. In addition to the variation of the impact duration, two additional impact amplitudes $P_{I0} = 3.156$ N and 315.6 N were used while maintaining $T_d = 1.5 \times 10^{-3}$ s constant, making the linear momentum one tenth and ten times that of the original case when $P_{I0} = 31.56$ N. In all the cases, the amplitude of the impact did not make the initial shear modulus break away from the linear range. Both sets of analyses were performed for initial shear loads $P_{st} = 1000$ N and 10000 N. First, the analysis results with the impact durations $T_d = 7.5 \times 10^{-4}$ s and 3.0×10^{-3} s are presented in Figure 2.20 with previous results with $T_d = 1.5 \times 10^{-3}$ s. For $T_d = 7.5 \times 10^{-4}$ s, the cross-correlation results c_{cc} yield the same wave velocity as the tangent wave velocity c_{tan} for both $P_{st} = 1000$ N and 10000 N. For $T_d = 3.0 \times 10^{-3}$ s, however, the cross-correlation prediction c_{cc} is higher than the tangential wave velocity c_{tan} for $P_{st} = 1000$ N, which indicates the same trend as for the case with $T_d = 1.5 \times 10^{-3}$ s. As shown by the particle velocity time histories with $P_{st} = 1000$ N in Figure 2.21, the variable which

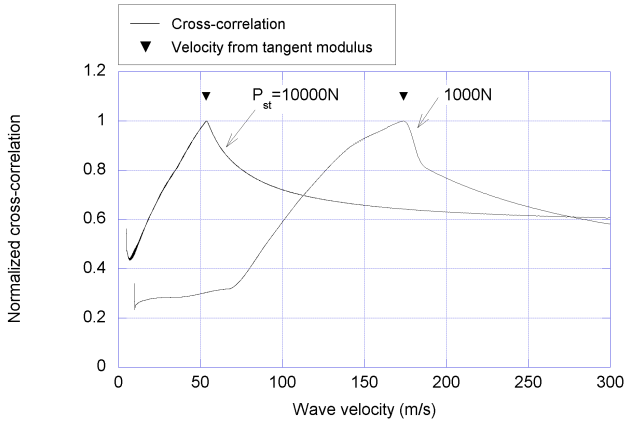

(a) Wave velocity with $T_d = 7.5 \times 10^{-4}$ s and $P_{I0} = 63.12$ N

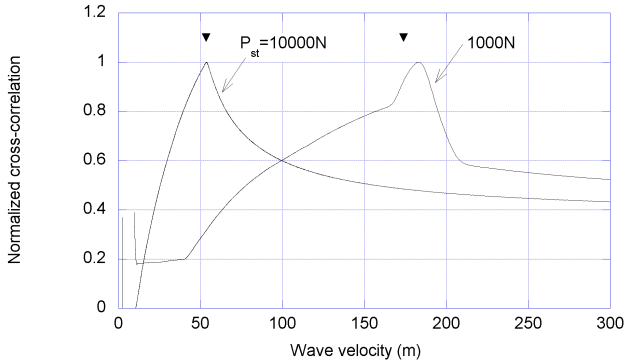

(b) Wave velocity for $T_d = 1.5 \times 10^{-3}$ s and $P_{I0} = 31.56$ N

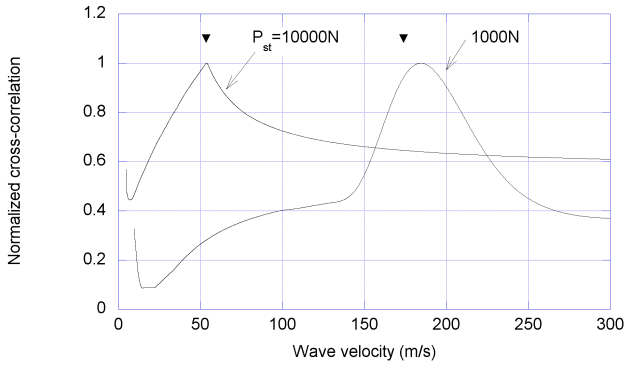

(c) Wave velocity for $T_d = 3.0 \times 10^{-3}$ s and $P_{I0} = 15.78$ N

Figure 2.18 Wave velocity from cross-correlation and tangent modulus with constant linear momentum of impact

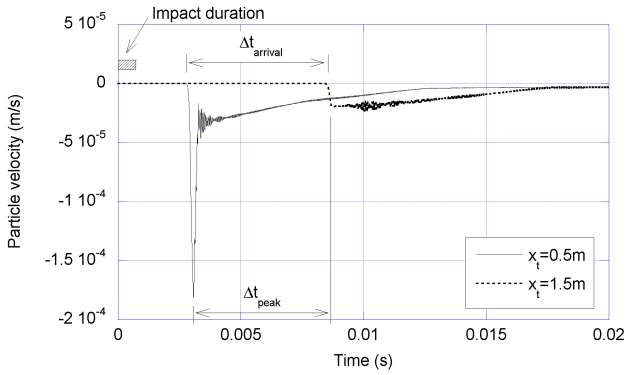

(a) Wave history with $T_d = 7.5 \times 10^{-4}$ s and $P_{I0} = 63.12$ N

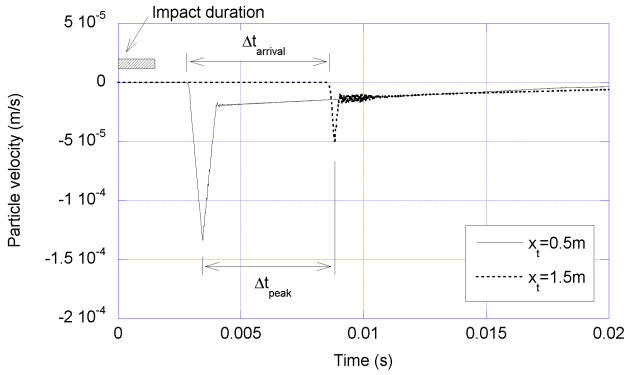

(b) Wave history with $T_d = 1.5 \times 10^{-3}$ s and $P_{I0} = 31.56$ N

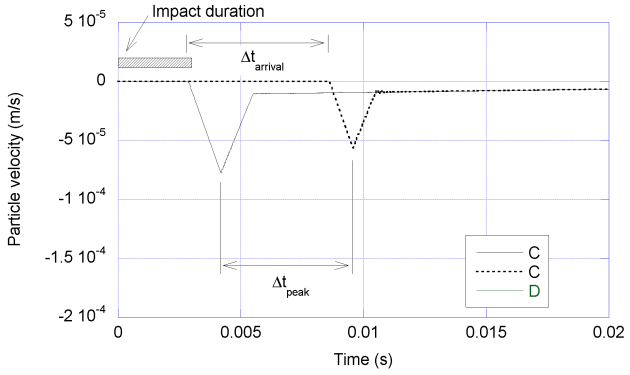

(c) Wave history with $T_d = 3.0 \times 10^{-3}$ s and $P_{I0} = 15.78$ N

Figure 2.19 Wave velocity with constant impact momentum and $P_{st} = 1000$ N

affects the estimation of the wave propagation velocity is the duration of the impact not the linear momentum. When the duration of the impact is the same, regardless of the amplitude of the impact, within the range of values studied here the estimates of the wave velocities are identical although the values may vary a little due to the estimation techniques (the cross-correlation function, the initial arrival time or the peak-to-peak time difference). This becomes clearer when Figure 2.21 is compared to Figure 2.19 and Figure 2.20 to Figure 2.18. The results of the analyses with $P_{st} = 3.156$ N and 315.6 N for $T_d = 1.5 \times 10^{-3}$ s are presented in Figure 2.22 with the case when $P_{st} = 31.56$ N. The cross-correlation results in the figure are all identical supporting the observation that the impact amplitude has no effect on the estimation of wave propagation velocity if the amplitude is small enough. On the other hand, the particle velocity time histories in Figure 2.23 when $P_{st} = 1000$ N show the effect of impact amplitude on the particle velocity. The impact amplitude is proportional to the magnitude of the particle velocity. The scale of the particle velocities in Figures 2.23(a) and 2.23(c) are one tenth and ten times that in Figure 2.23(b), respectively. Consequently, the linear momentum of the impact has an influence on the predicted wave velocity. This is because of the impact duration and not because of the impact amplitude. The difference in the cross-correlation result c_{cc} due to the impact duration is only about 5% of c_{cc} in the range of values considered.

2.6.5. Effect of Cross-Correlation Pairs

In the previous sections, the wave velocity c_{cc} was estimated from the cross-correlation of the velocity time histories at $x_t = 0.5$ m and 1.5 m. The results from different sets of cross-correlation locations were examined to investigate previously observed trends are consistent for different pairs of cross-correlation. The sets of cross-correlation pairs used in the analyses are presented in Table 2.1. The number of segments N_{elem}

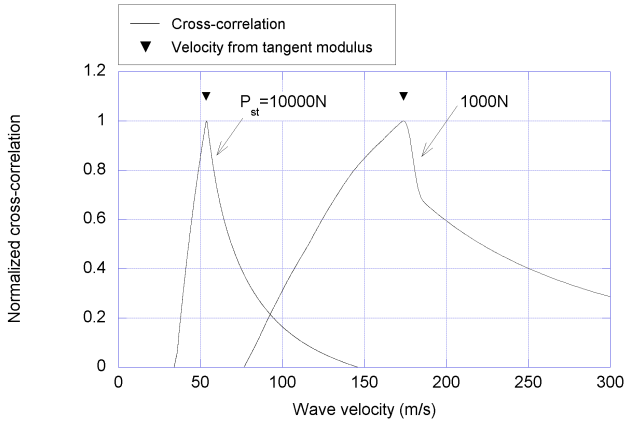

(a) Wave velocity with $T_d = 7.5 \times 10^{-4}$ s and $P_{I0} = 31.56$ N

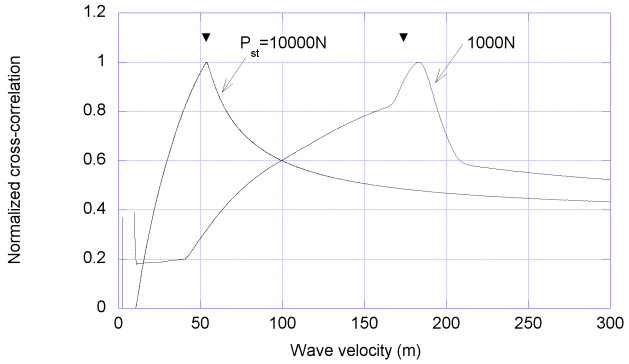

(b) Wave velocity for $T_d = 1.5 \times 10^{-3}$ s and $P_{I0} = 31.56$ N

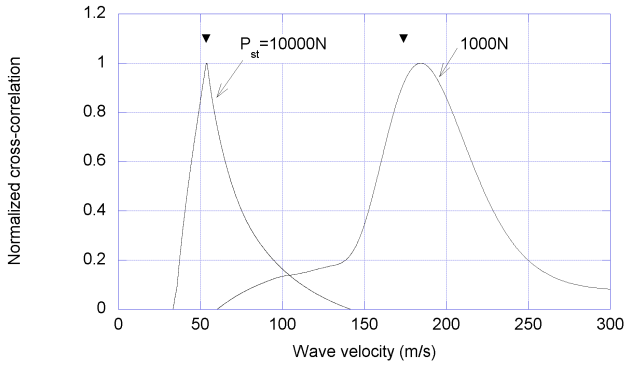

(c) Wave velocity with $T_d = 3.0 \times 10^{-3}$ s and $P_{I0} = 31.56$ N

Figure 2.20 Wave velocity from cross-correlation and tangent modulus with different linear momentum of impacts

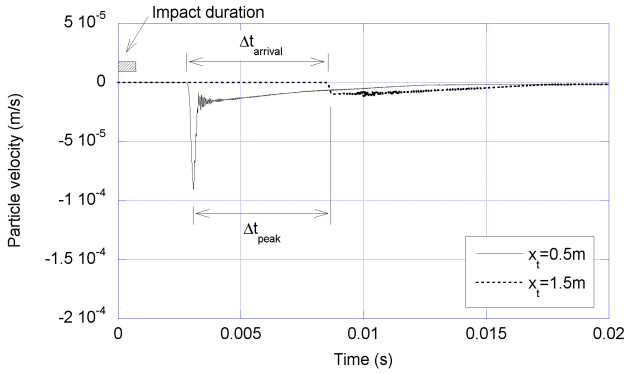

(a) Wave history with $T_d = 7.5 \times 10^{-4}$ s and $P_{I0} = 31.56$ N

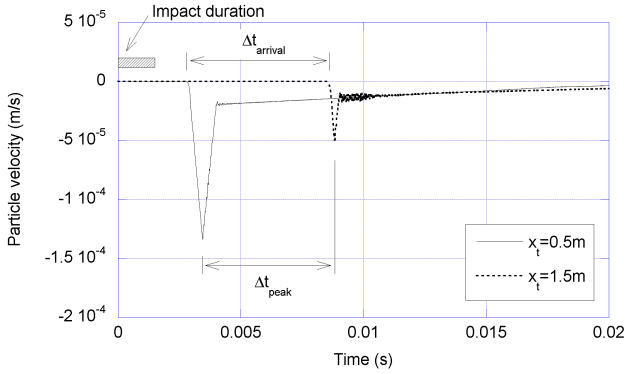

(b) Wave history with $T_d = 1.5 \times 10^{-3}$ s and $P_{I0} = 31.56$ N

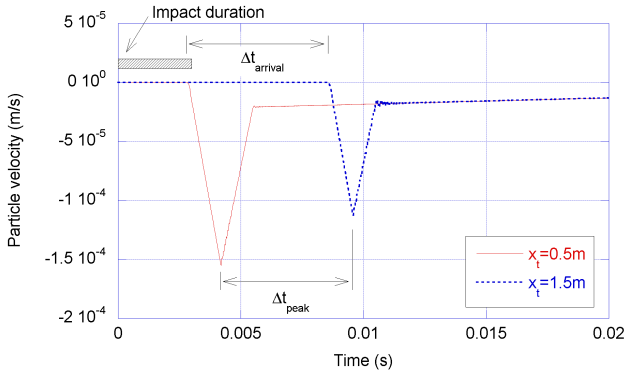

(c) Wave history with $T_d = 3.0 \times 10^{-3}$ s and $P_{I0} = 31.56$ N

Figure 2.21 Particle velocity history for $P_{st} = 1000$ N with different linear momentum of impacts

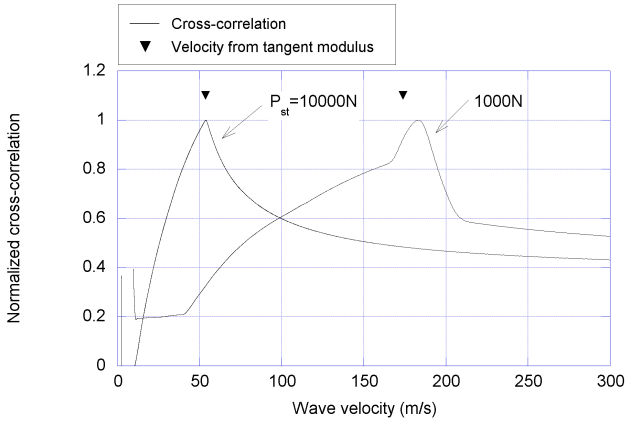

(a) Wave velocity with $T_d = 1.5 \times 10^{-3}$ s and $P_{I0} = 3.156$ N

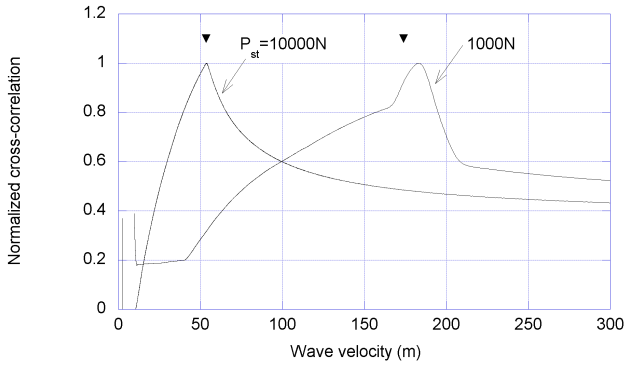

(b) Wave velocity for $T_d = 1.5 \times 10^{-3}$ s and $P_{I0} = 31.56$ N

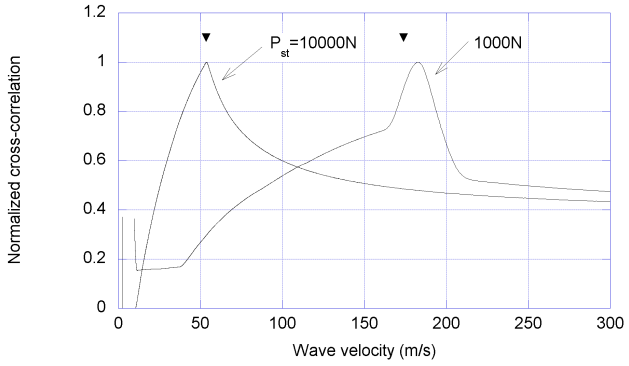

(c) Wave velocity with $T_d = 1.5 \times 10^{-3}$ s and $P_{I0} = 315.6$ N

Figure 2.22 Wave velocity from cross-correlation and tangent modulus with different linear momentum of impacts

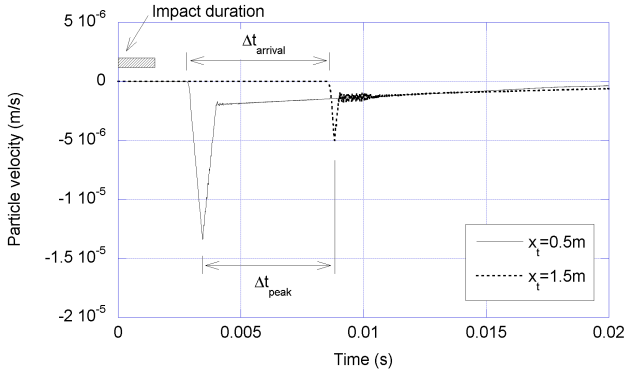

(a) Wave history with $T_d = 1.5 \times 10^{-3}$ s and $P_{I0} = 3.156$ N

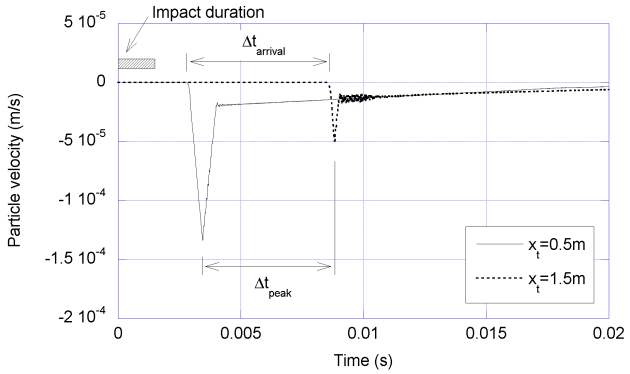

(b) Wave history with $T_d = 1.5 \times 10^{-3}$ s and $P_{I0} = 31.56$ N

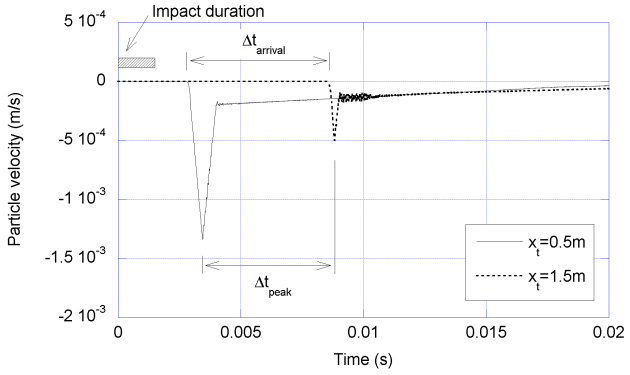

(c) Wave history with $T_d = 1.5 \times 10^{-3}$ s and $P_{I0} = 315.6$ N

Figure 2.23 Particle velocity history for $P_{st} = 1000$ N with different linear momentum of impacts

and the beam length L were increased to 9600 and 24 m, respectively, to prevent arrival of the reflected waves to the measurement point closer to the bottom within the time range considered. An impact duration $T_d = 1.5\times10^{-3}$ s, an impact amplitude $P_{I0} = 31.56$ N, and two different values of the initial shear load $P_{st} = 1000$ N and 10000 N were used.

The cross-correlation results and the particle velocity histories for each set of measurement points are shown in Figures 2.24 to 2.29. As presented in Figures 2.27 to 2.29, for $P_{st} = 10000$ N, the results of cross-correlation are quite close to the tangent wave velocity for all cases. For $P_{st} = 1000$ N, this is no longer the case as shown in Figures 2.24 through 2.26. For $P_{st} = 1000$ N, if the two measurement points used to compute the cross-correlation are close to the excitation source, the predicted wave velocity by cross-correlation is higher than the wave velocity from the tangent modulus because of the shape of the particle velocity history. The width of the peak gets narrower as the wave goes through the beam and the peak-to-peak time difference becomes smaller than the initial arrival time difference. Because the cross-correlation tends to estimate the peak-to-peak time difference, the wave velocity c_{cc} from the cross-correlation estimates a higher propagation velocity than the wave velocity c_{tan} corresponding to the tangent modulus when peaks exist for both signals. Nevertheless, for all the combinations of measurement points used in this study, the cross-correlation estimates were very close to the wave velocity corresponding to the tangent modulus.

2.7. Analysis Results: Harmonic Excitation

The wave velocities obtained from the response of the soil beam to a harmonic load under various conditions was computed to study the effect of variables such as the

Table 2.1 Cross-correlation pairs for impact excitations

(a) First set of pairs

Cross-correlation pairs (m-m)	Distance (m)
0.5 - 1.0	0.5
0.5 - 1.5	1.0
0.5 - 2.0	1.5
0.5 - 2.5	2.0
0.5 - 3.0	2.5

(b) Second set of pairs

Cross-correlation pairs (m-m)	Distance (m)
0.5 - 0.6	0.1
0.5 - 0.7	0.2
0.5 - 0.8	0.3
0.5 - 0.9	0.4
0.5 - 1.0	0.5

(c) Third set of pairs

Cross-correlation pairs (m-m)	Distance (m)
2.5 - 2.6	0.1
2.5 - 2.7	0.2
2.5 - 2.8	0.3
2.5 - 2.9	0.4
2.5 - 2.0	0.5

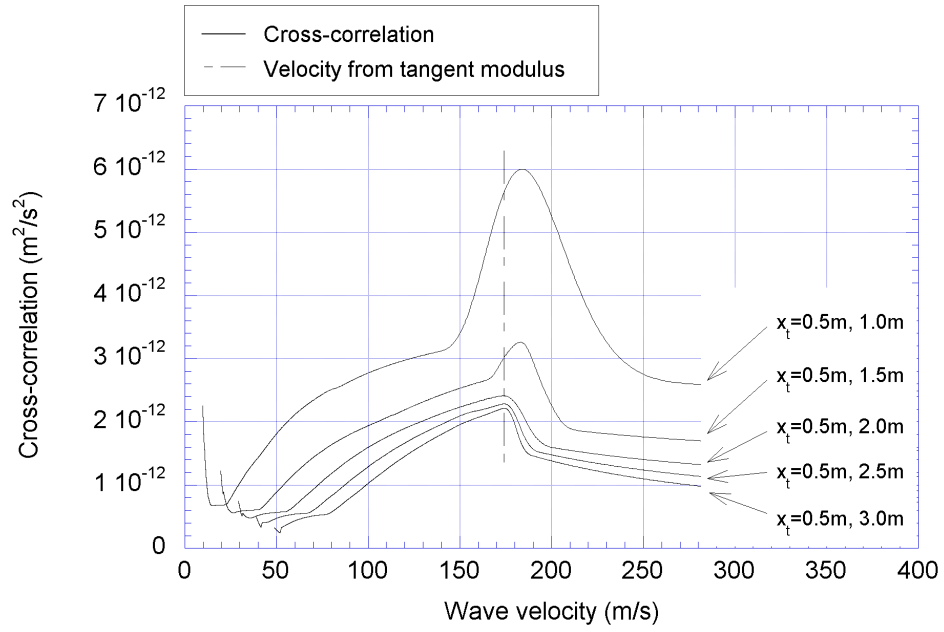

(a) Wave velocities

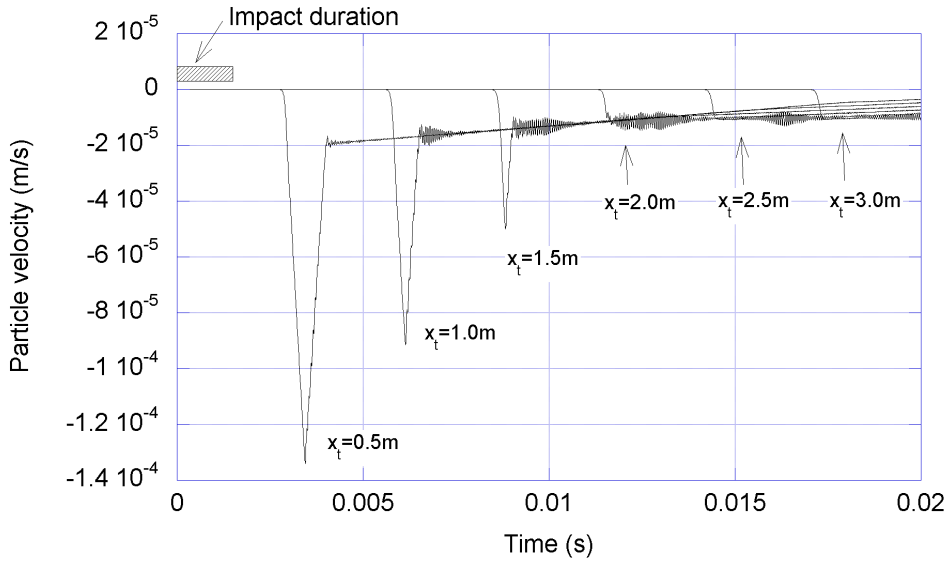

(b) Velocity time histories

Figure 2.24 Wave velocity and velocity history for the first set of measure points with $Pst = 1000$ N, $T_d = 1.5 \times 10^{-3}$ s, and $P_{I0} = 31.56$ N

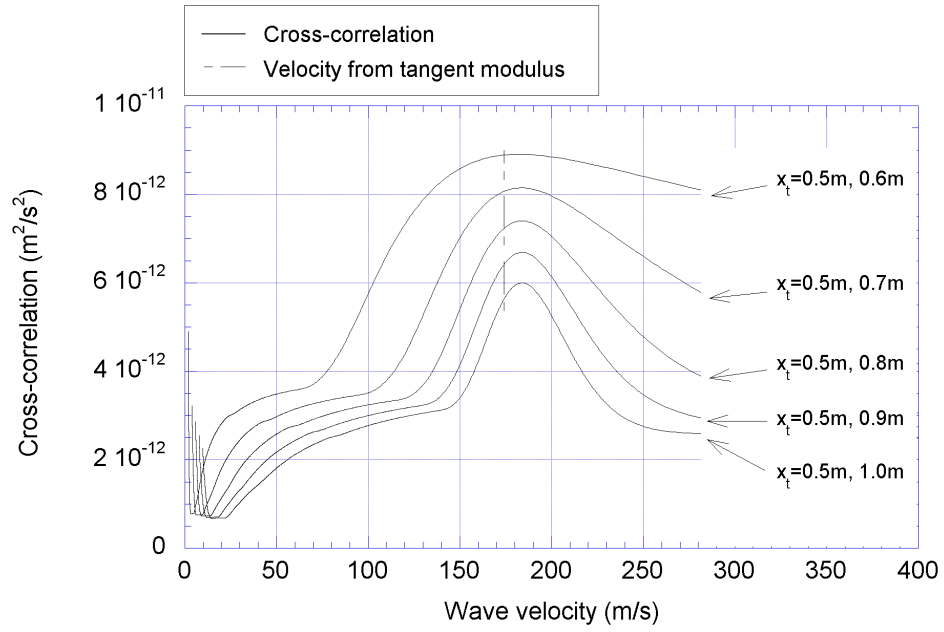

(a) Wave velocities

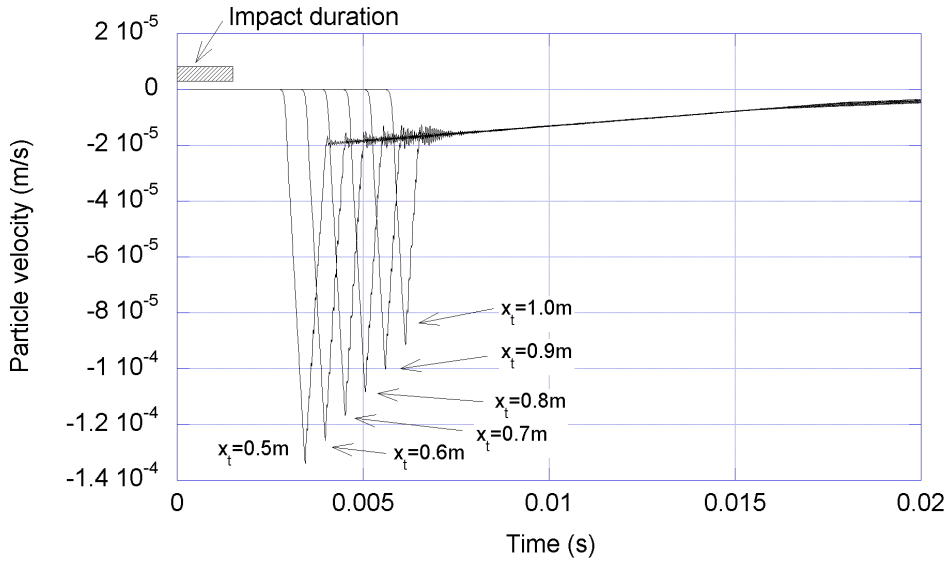

(b) Velocity time histories

Figure 2.25 Wave velocity and velocity history for the second set of measure points with $Pst = 1000$ N, $T_d = 1.5 \times 10^{-3}$ s, and $P_{I0} = 31.56$ N

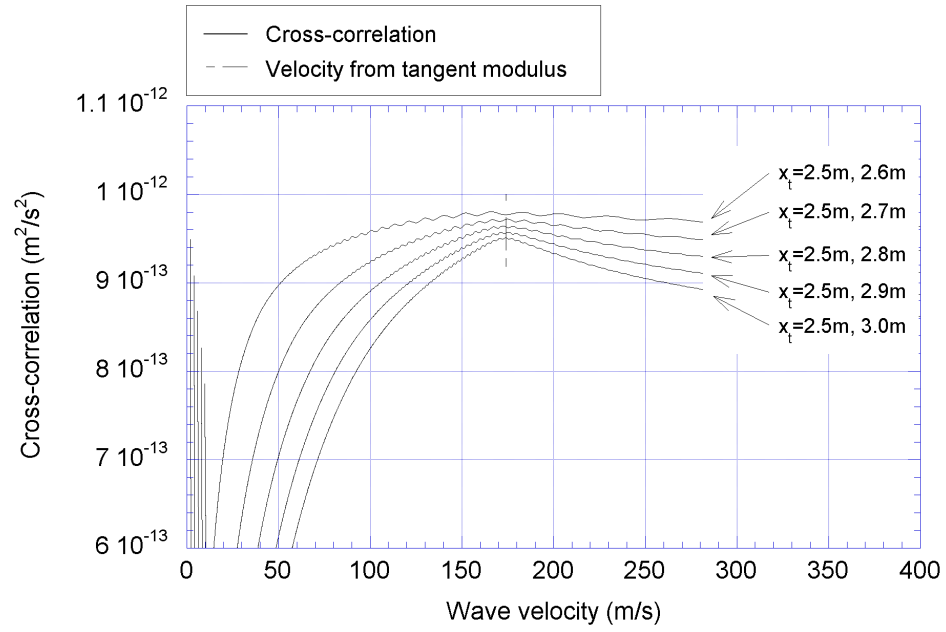

(a) Wave velocities

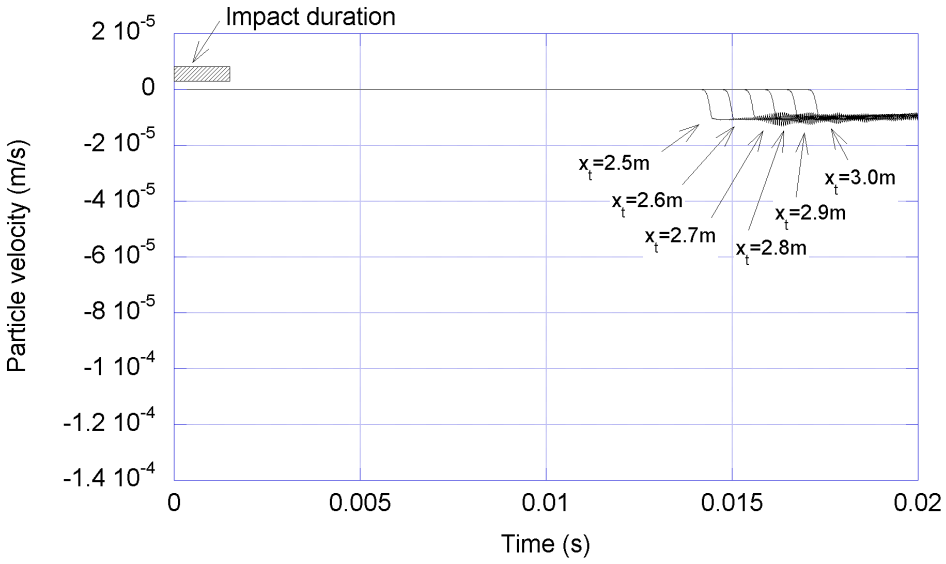

(b) Velocity time histories

Figure 2.26 Wave velocity and velocity history for the third set of measure points with $Pst = 1000$ N, $T_d = 1.5 \times 10^{-3}$ s, and $P_{I0} = 31.56$ N

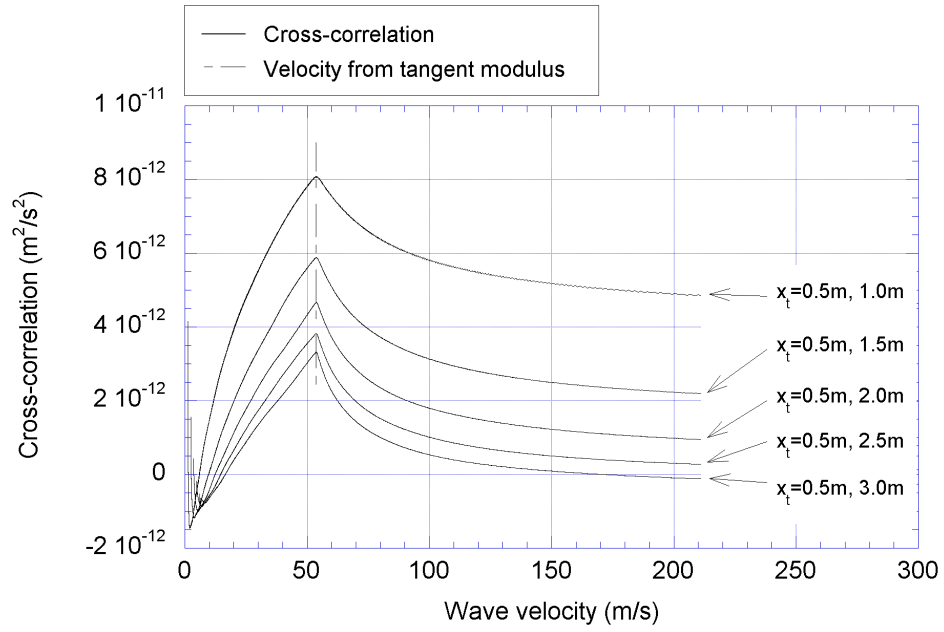

(a) Wave velocities

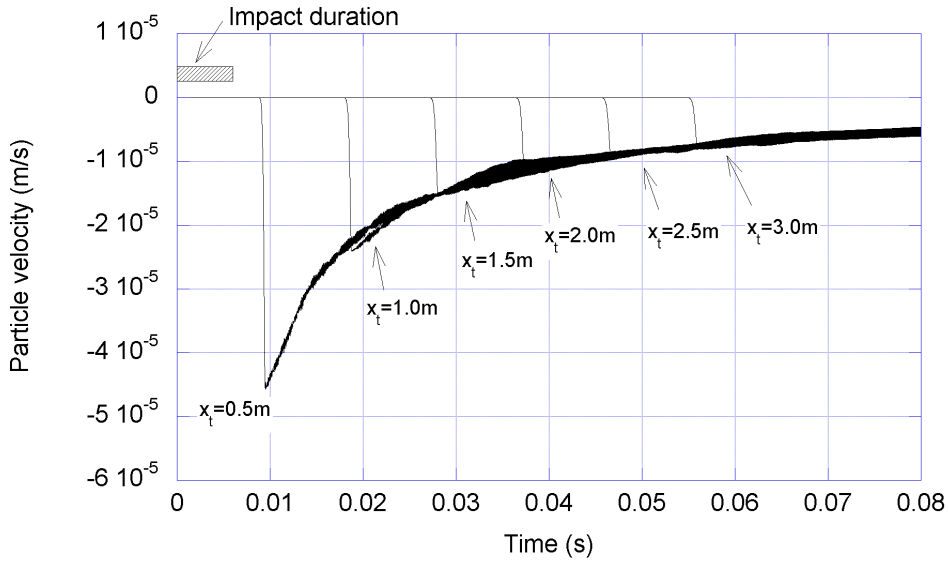

(b) Velocity time histories

Figure 2.27 Wave velocity and velocity time histories for the first set of measure points with $Pst = 10000$ N, $T_d = 1.5 \times 10^{-3}$ s, and $P_{I0} = 31.56$ N

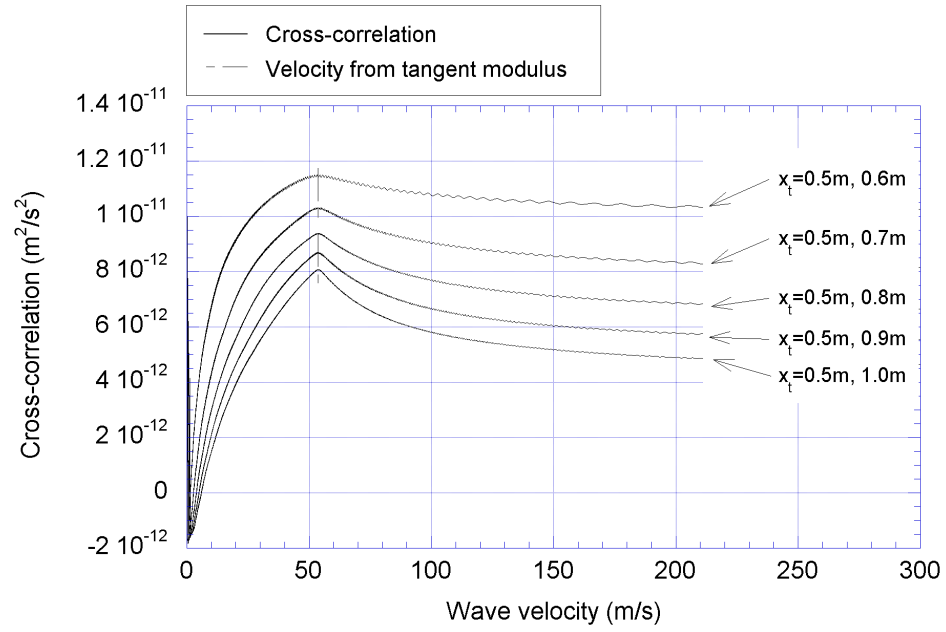

(a) Wave velocities

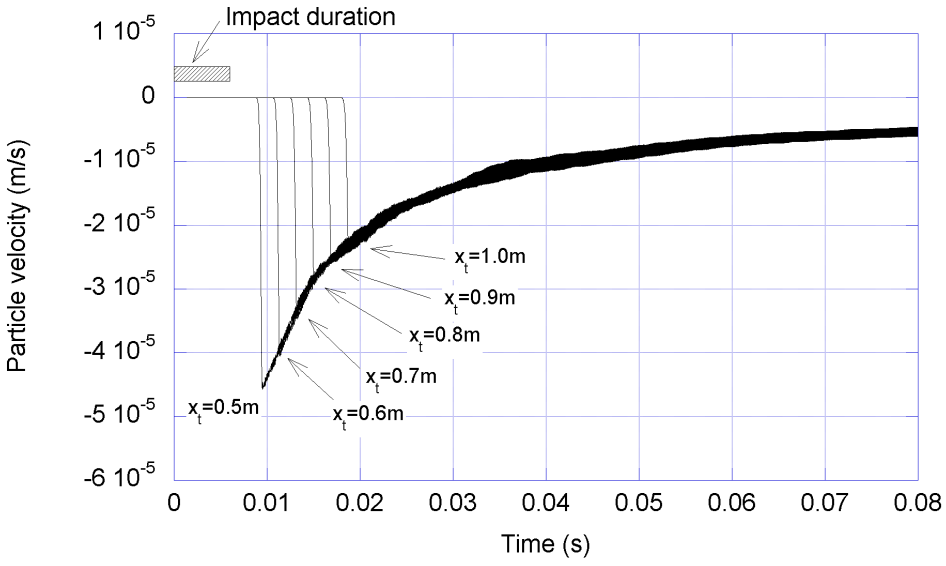

(b) Velocity time histories

Figure 2.28 Wave velocity and velocity time histories for the second set of measure points with $Pst = 10000$ N, $T_d = 1.5 \times 10^{-3}$ s, and $P_{I0} = 31.56$ N

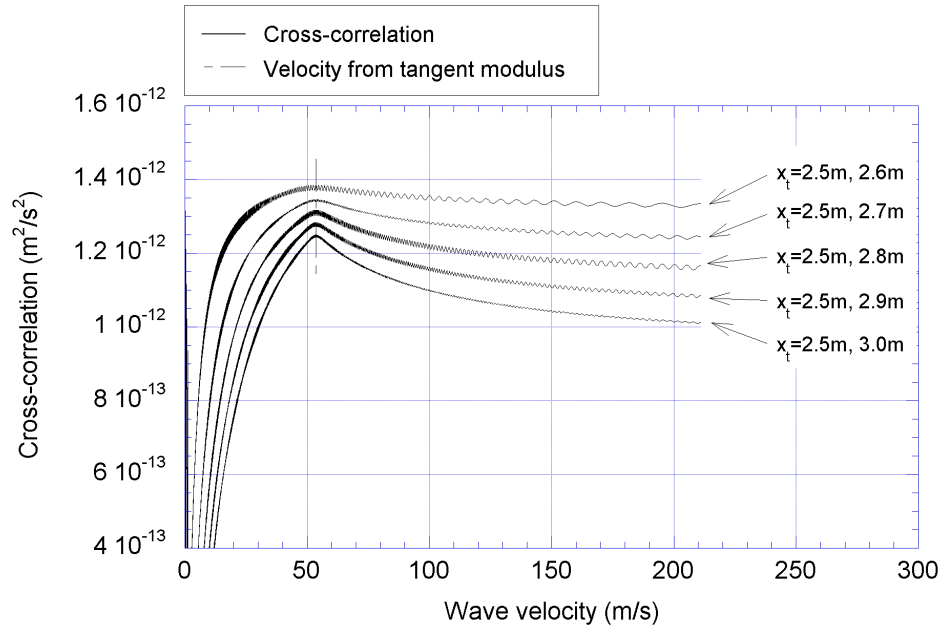

(a) Wave velocities

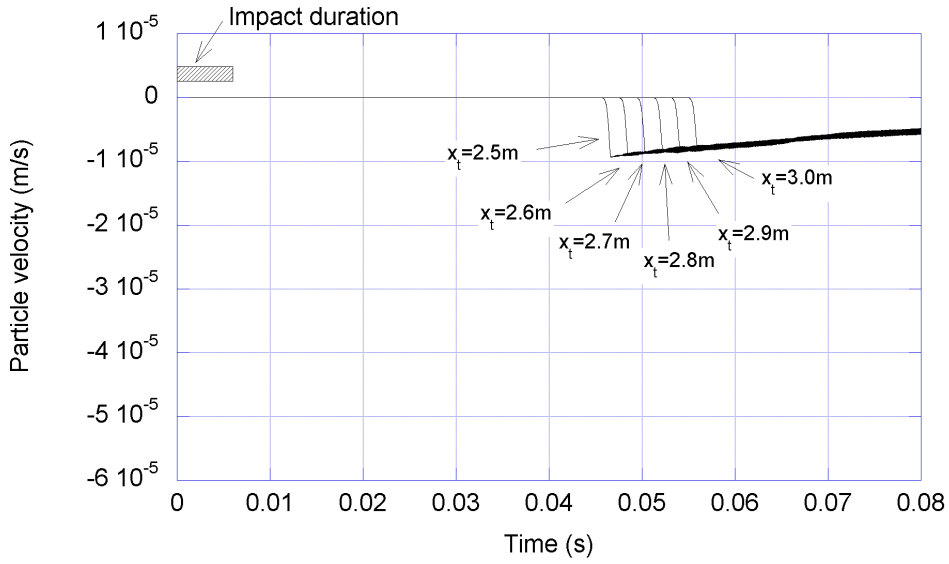

(b) Velocity time histories

Figure 2.29 Wave velocity and velocity time histories for the third set of measure points with $Pst = 10000$ N, $T_d = 1.5 \times 10^{-3}$ s, and $P_{I0} = 31.56$ N

initial state of stress, the amplitude and frequency of the excitation, and the location of the selected cross-correlation points.

2.7.1. Wave Propagation in Elastic Medium

The dynamic response of an elastic soil shear beam under a sinusoidal excitation was investigated first to verify the discrete model by previously obtained closed solution. A number of segments $N = 4800$, for a beam length $L = 480$ m, and a time step $\Delta t = 3.125 \times 10^{-5}$ s were used. The responses were calculated at $x_t = 0.5$ m and 1.5 m, with a loading amplitude $P_{S0} = 5000$ N, and a loading frequency $f = 100$ Hz. The resulting displacement and velocity histories are compared with the results of the closed-form solution, Equation 2.8, and presented in Figures 2.30 and 2.31, respectively.

The velocity time histories at $x_t = 0.5$ m and 1.5 m for $1.0\,\text{s} \leq t \leq 1.512\,\text{s}$ were used for the calculation of the cross-correlation. A Hanning window was introduced to avoid energy leakage before taking the Fourier transforms (Roberts, 2004). An example of Hanning-windowed velocity history is shown in Figure 2.32. The estimated cross-correlation is plotted with respect to time delay in Figure 2.33(a). Several maxima are present because the original velocity signal has multiple peaks. However, from the observation of the signals in Figure 2.31(b), it can be seen that the first maximum of the cross-correlation in 2.33(a) is the time delay of interest, corresponding to the arrival of the first front. Also, since the first peak of the cross-correlation with respect to time represents the last peak of the cross-correlation with respect to wave velocity, Figure 2.33(b) shows that the calculated wave velocity c_s is 200 m/s, which is identical to the theoretical value.

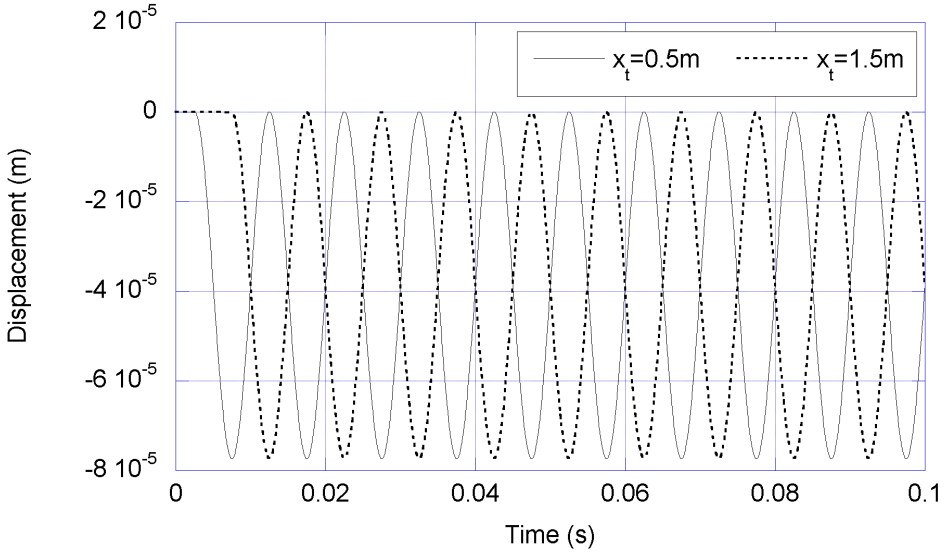

(a) Results from closed-form solution with 5000 modes superposed

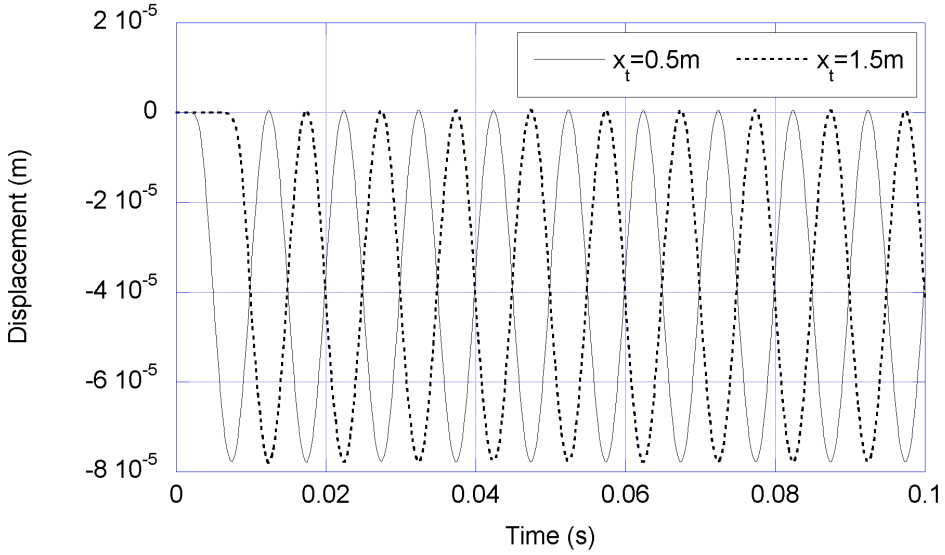

(b) Results from discrete analysis with $f = 100$ Hz and $P_{S0} = 5000$ N

Figure 2.30 Displacement history at $x_t = 0.5$ m and 1.5 m

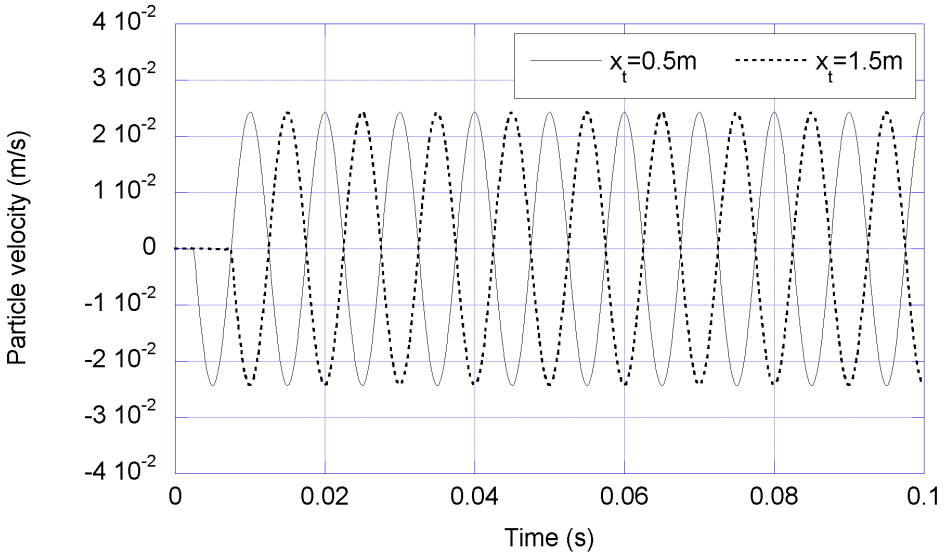

(a) Results from closed-form solution with 5000 modes superposed

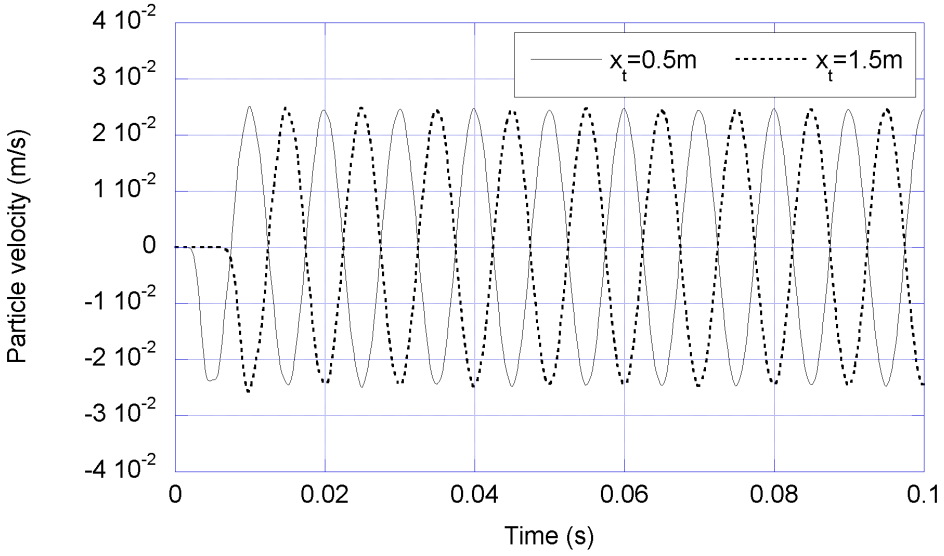

(b) Results from discrete analysis with $f = 100$ Hz and $P_{S0} = 5000$ N

Figure 2.31 Particle velocity history at $x_t = 0.5$ m and 1.5 m

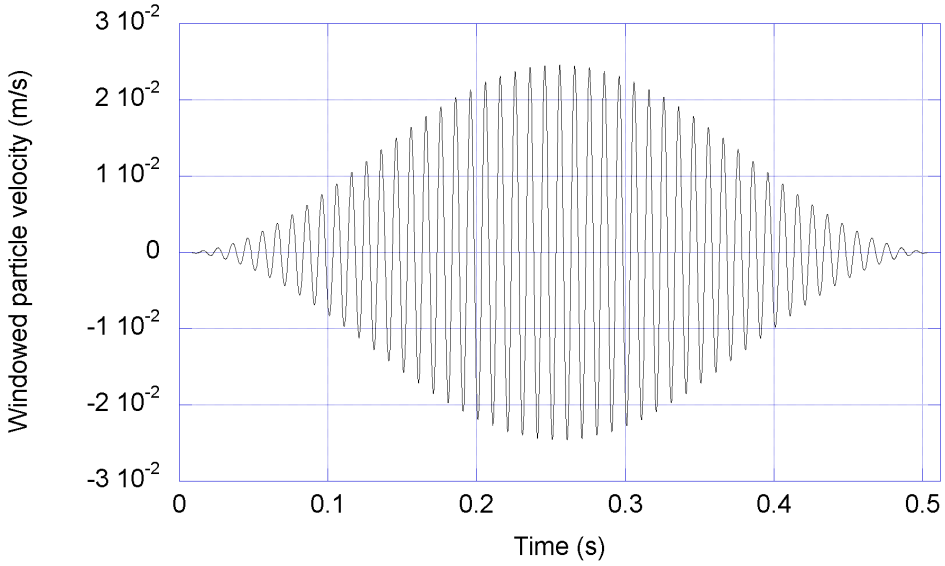

Figure 2.32 Windowed particle velocity at $x_t = 0.5$ m

2.7.2. Steady-State Condition

Preliminary analyses were performed to estimate the time needed to reach steady-state in order to limit the computation time for the problem. The number of segments N was increased to 19,200 for an overall beam length $L = 1,920$ m, while the time step was increased to $\Delta t = 2.5 \times 10^{-4}$ s. The displacement history, the particle velocity history, and the stress-strain curve were inspected in several time ranges such as 2.0 s $\leq t \leq$ 2.512 s, 4.0 s $\leq t \leq$ 4.512 s, 8.0 s $\leq t \leq$ 8.512 s, and 16.0 s $\leq t \leq$ 16.512 s. An initial static load $P_{st} = 10000$ N and a dynamic load amplitude $P_{S0} = 5000$ N were used because trial runs indicated these cases tended to take more time to reach the steady-state than other combinations of loading conditions. The displacement and velocity histories at $x_t = 0.5$ m and the stress-strain trace in the nonlinear spring between $x_t = 0.4$ m and 0.5 m are presented in Figures 2.34 through 2.36. Whereas the displacement keeps increasing in absolute value even after $t = 16$ s, the particle velocity seems to have a uniform behavior and the stress-strain behavior converges

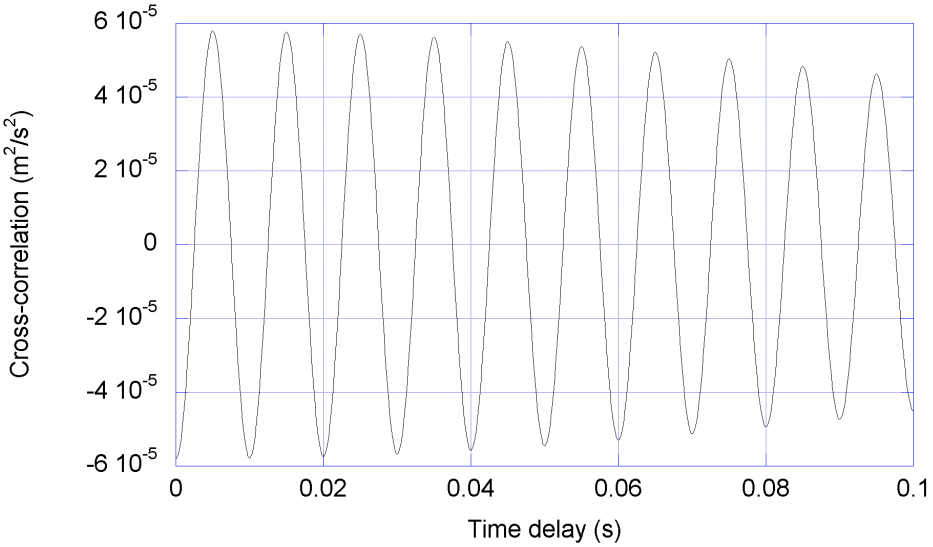

(a) Cross-correlation in terms of time delay

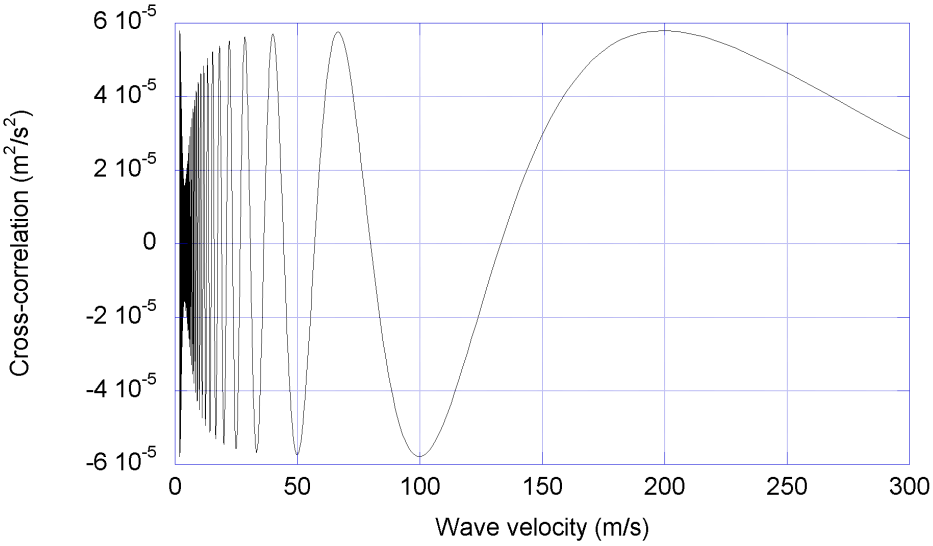

(b) Cross-correlation in terms of wave velocity

Figure 2.33 Cross-correlation from velocity histories in elastic medium with $f = 100$ Hz and $P_{S0} = 5000$ N

for all the cases. Next, the velocity histories in each time range were cross-correlated between following pairs of points x_t = 0.5 m and 0.7 m, x_t = 0.7 m and 0.9 m, x_t = 0.9 m and 1.1 m, x_t = 1.1 m and 1.3 m, and x_t = 1.3 m and 1.5 m. The cross-correlation results in terms of the time delay are shown in Figure 2.37 and the results in terms of wave velocity in Figure 2.38. Because the difference in the cross-correlation results were almost negligible for all four cases, it can be considered that the steady-state had been reached for all the velocity histories considered. After observing the results, a time of 4 s was judged to be sufficient for steady-state to be established and the time range 4.0 s $\leq t \leq$ 4.512 s was then chosen for all subsequent analyses.

2.7.3. Effect of Initial State of Stresses

The wave propagation velocity in the nonlinear soil beam was studied for different combinations of initial static shear load and a sinusoidal load to estimate the effect of the initial state of stresses and the amplitude of the dynamic load. A series of analyses were performed for an initial load P_{st} = 0, 1000 N, 5000 N, and 10000 N with dynamic load amplitudes P_{S0} = 500 N and 5000 N and a loading frequency f = 100. The analyses were performed with 4800 segments, a beam length L = 480 m, and a time step $\Delta t = 3.125 \times 10^{-5}$ s. The cross-correlations were carried out between the the same locations used in the previous section, that is, x_t = 0.5 m 0.7 m, x_t = 0.7 m and 0.9 m, x_t = 0.9 m and 1.1 m, x_t = 1.1 m and 1.3 m, x_t = 1.3 m and 1.5 m. The secant moduli from the nonlinear springs between each set of cross-correlation locations after the steady-state had been reached were averaged to obtain a value representative of the secant modulus over the selected region. The wave velocity c_{sec} corresponding to the averaged secant modulus was then compared with the cross-correlation results c_{cc}. Examples of these stress-strain curves are presented in Figure

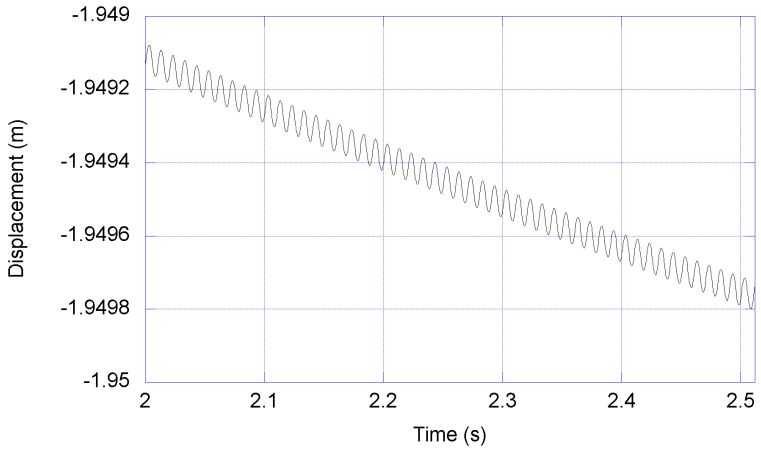

(a) 2.0 s $\leq t \leq$ 2.512 s

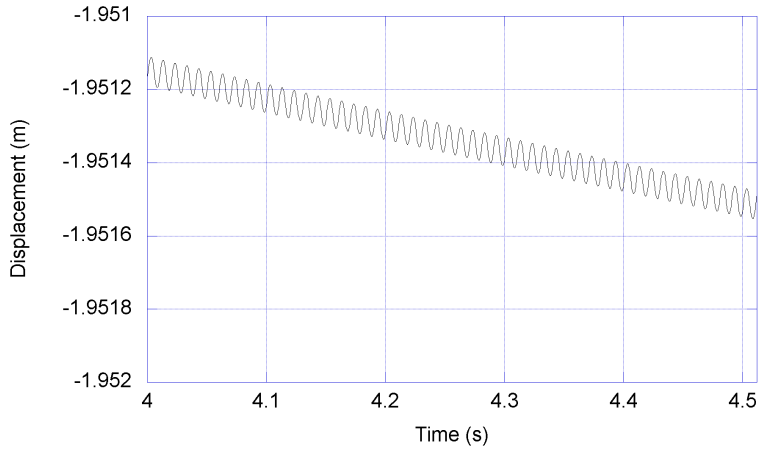

(b) 4.0 s $\leq t \leq$ 4.512 s

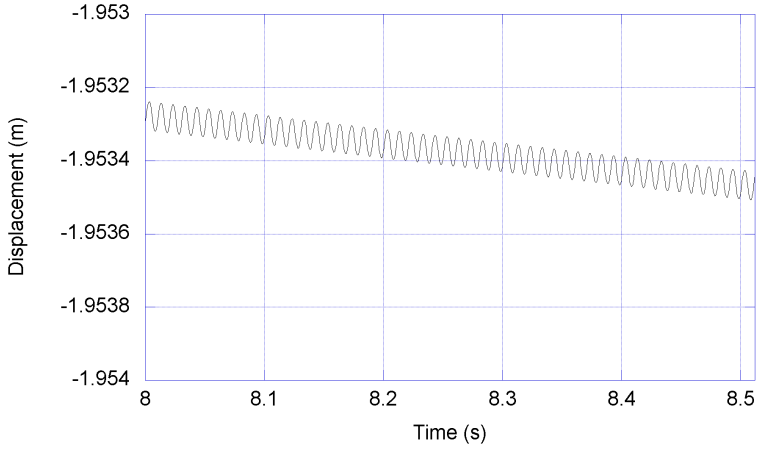

(c) 8.0 s $\leq t \leq$ 8.512 s

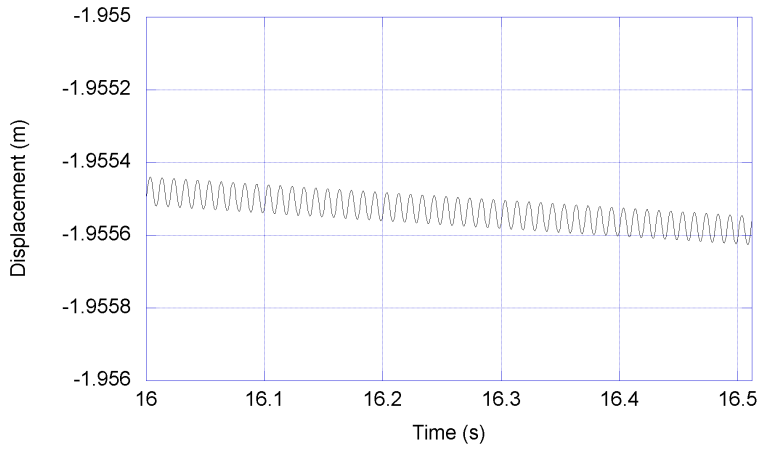

(d) 16.0 s $\leq t \leq$ 16.512 s

Figure 2.34 Displacement history at $x_t = 0.5$ m with $f = 100$ Hz, $P_{st} = 10000$ N, and $P_{S0} = 5000$ N

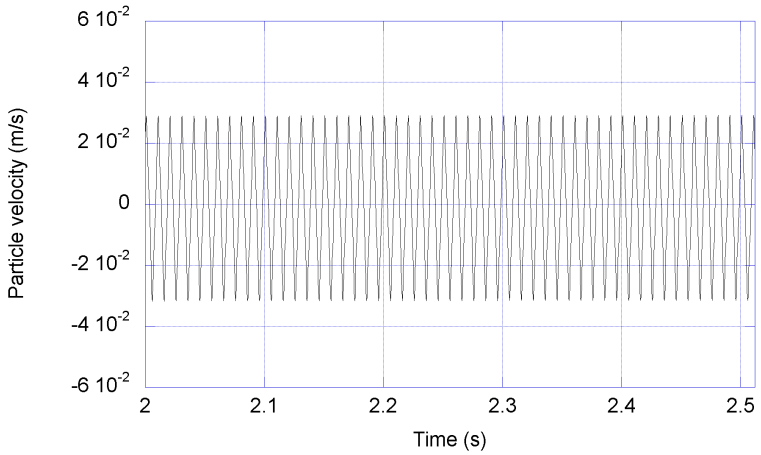

(a) 2.0 s $\leq t \leq$ 2.512 s

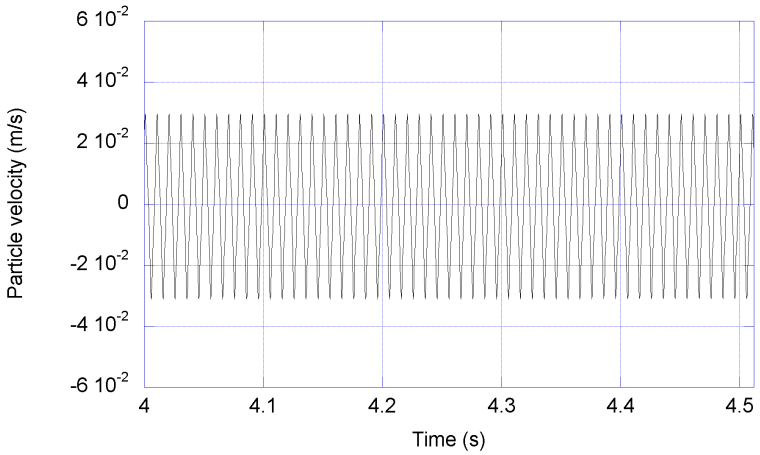

(b) 4.0 s $\leq t \leq$ 4.512 s

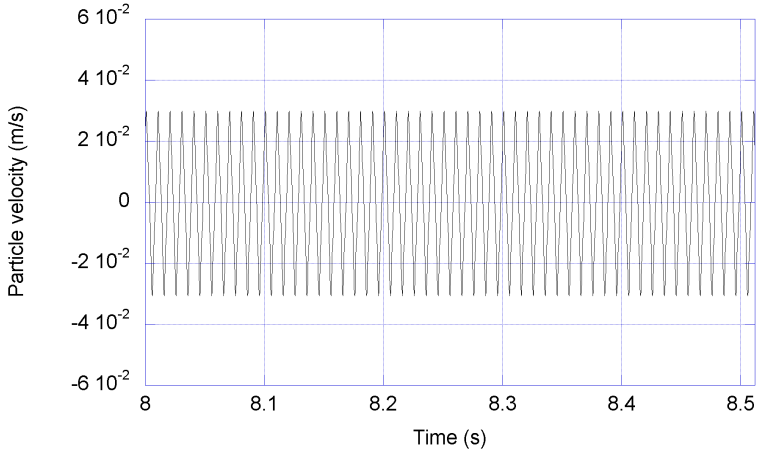

(c) 8.0 s $\leq t \leq$ 8.512 s

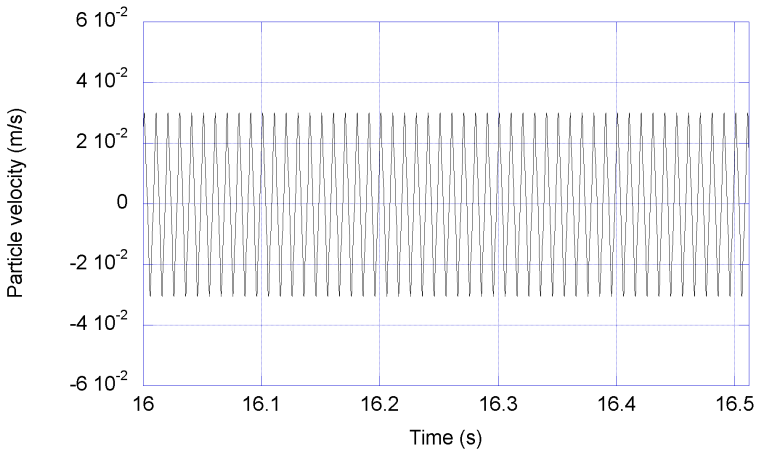

(d) 16.0 s $\leq t \leq$ 16.512 s

Figure 2.35 Particle velocity history at $x_t = 0.5$ m with $f = 100$ Hz, $P_{st} = 10000$ N, and $P_{S0} = 5000$ N

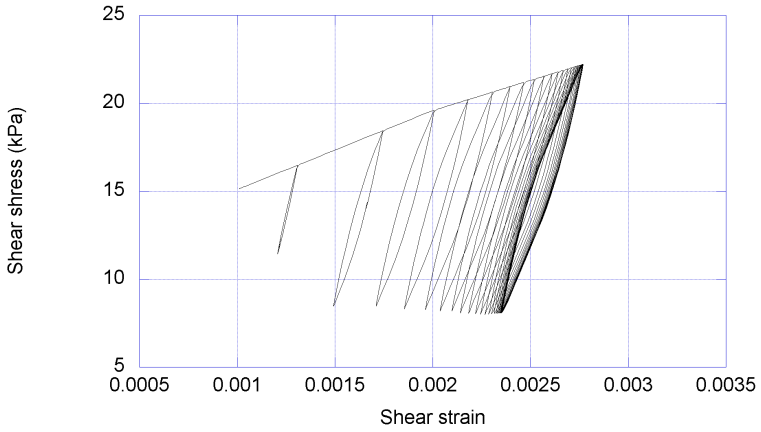

(a) 2.0 s $\leq t \leq$ 2.512 s

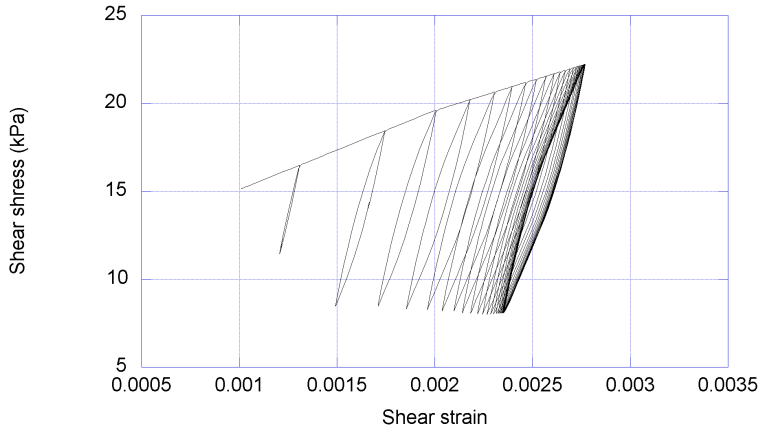

(b) 4.0 s $\leq t \leq$ 4.512 s

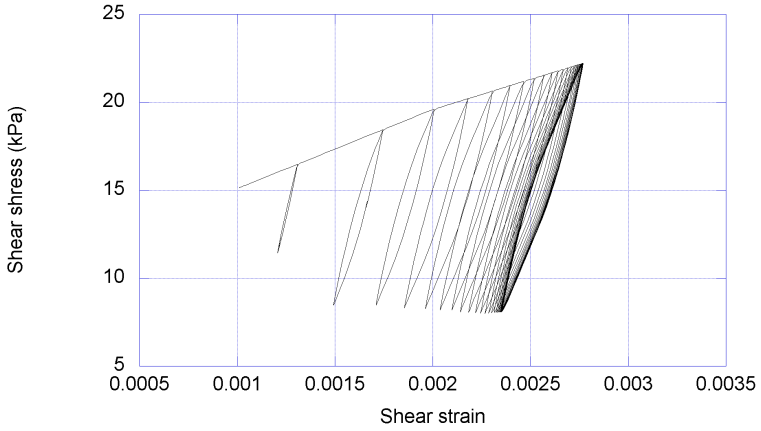

(c) 8.0 s $\leq t \leq$ 8.512 s

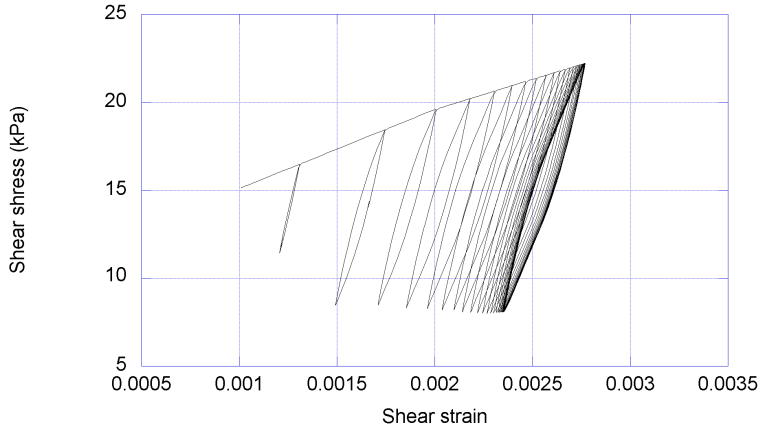

(d) 16.0 s $\leq t \leq$ 16.512 s

Figure 2.36 Stress-strain behavior in nonlinear spring between $x_t = 0.4$ m and 0.5 m with $f = 100$ Hz, $P_{st} = 10000$ N, and $P_{S0} = 5000$ N

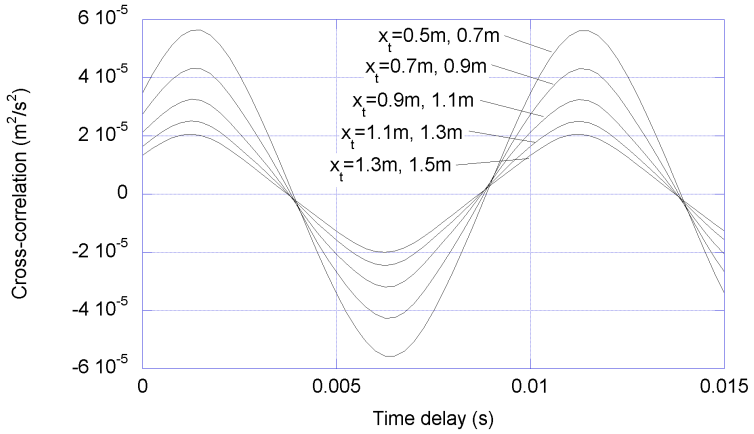

(a) 2.0 s $\leq t \leq$ 2.512 s

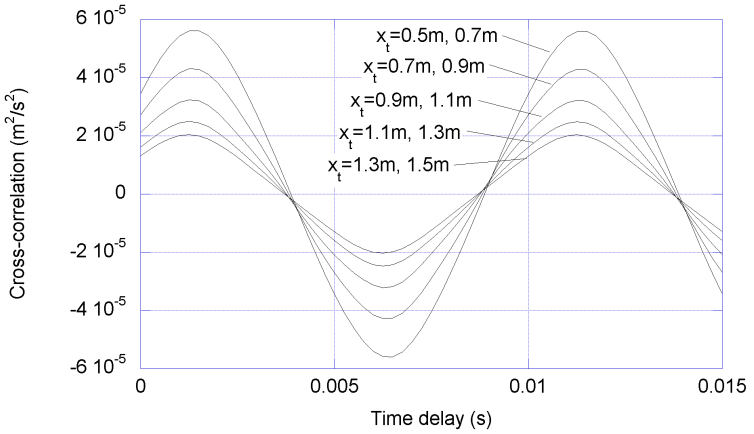

(b) 4.0 s $\leq t \leq$ 4.512 s

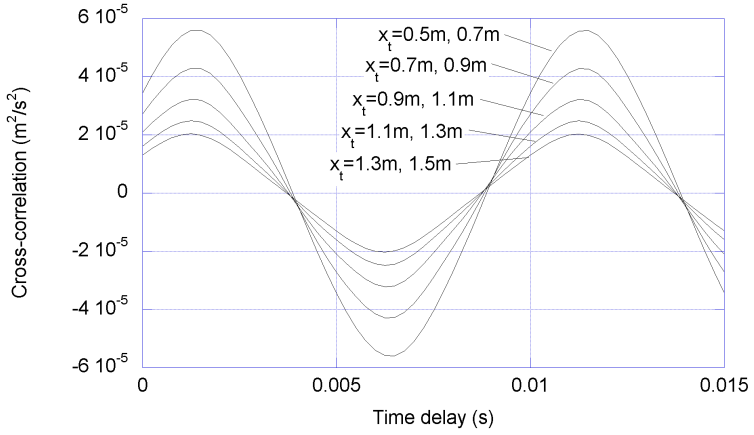

(c) 8.0 s $\leq t \leq$ 8.512 s

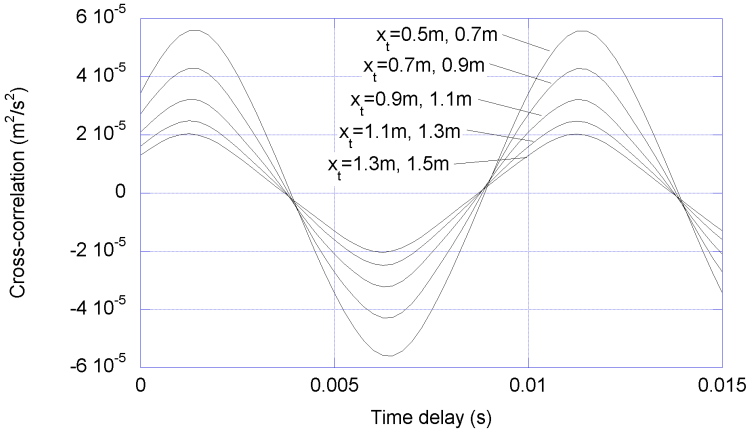

(d) 16.0 s $\leq t \leq$ 16.512 s

Figure 2.37 Cross-correlation in terms of time delay with $f = 100$ Hz, $P_{st} = 10000$ N, and $P_{S0} = 5000$ N

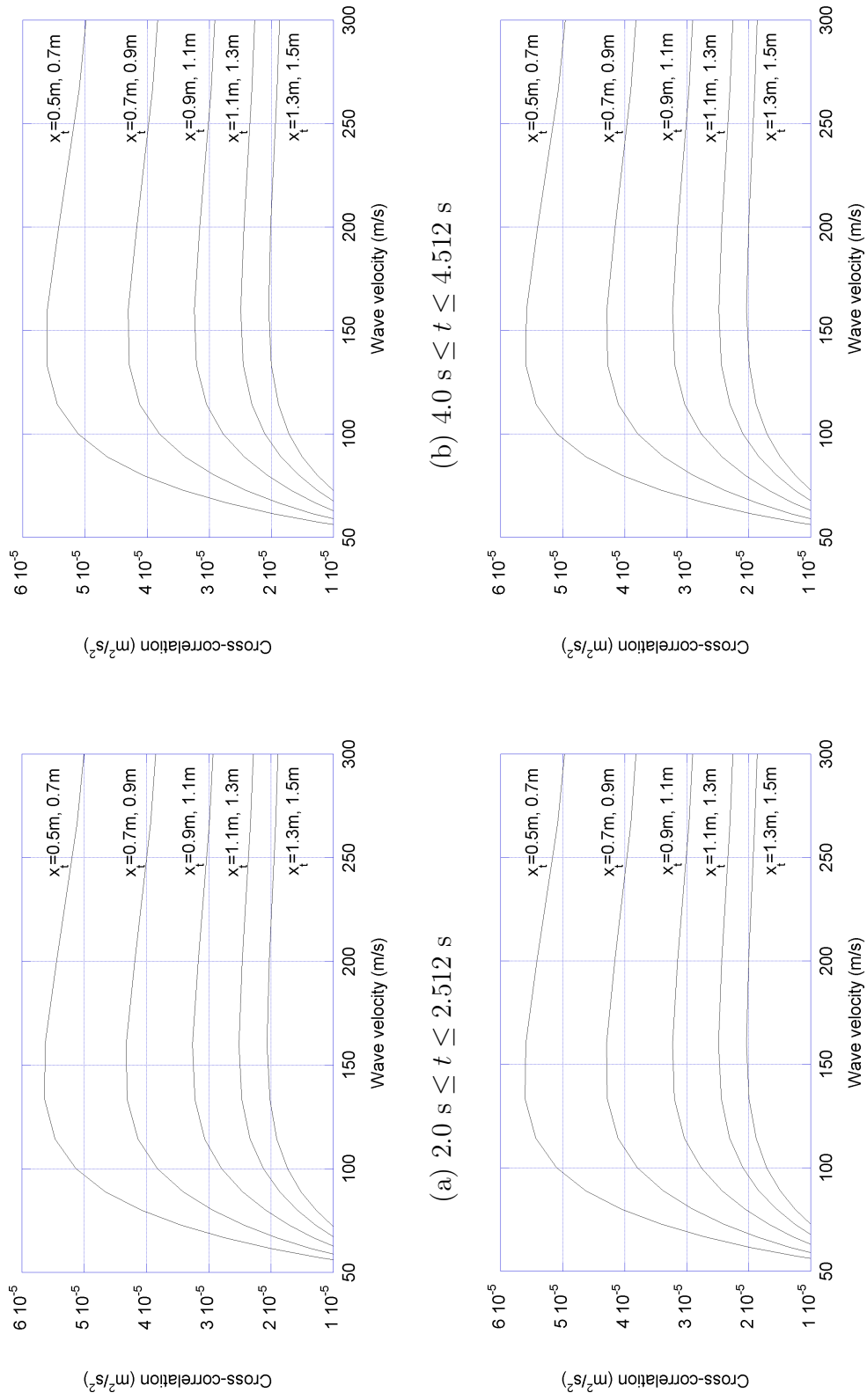

(a) $2.0 \text{ s} \leq t \leq 2.512 \text{ s}$

(b) $4.0 \text{ s} \leq t \leq 4.512 \text{ s}$

(c) $8.0 \text{ s} \leq t \leq 8.512 \text{ s}$

(d) $16.0 \text{ s} \leq t \leq 16.512 \text{ s}$

Figure 2.38 Cross-correlation in terms of wave velocity with $f = 100$ Hz, $P_{st} = 10000$ N, and $P_{S0} = 5000$ N

Table 2.2 Wave velocity c_{sec} calculated from secant modulus with $f = 100$ Hz

Initial shear load P_{st} (N)	Sinusoidal load amplitude P_{S0} (N)	Wave velocity c_{sec} (m/s) from secant modulus at various location				
		0.5 m− 0.7 m	0.7 m− 0.9 m	0.9 m− 1.1 m	1.1 m− 1.3 m	1.3 m− 1.5 m
0	500	192.3	192.3	192.4	192.5	192.7
1000		192.3	192.3	192.4	192.5	192.7
10000		192.3	192.3	192.4	192.5	192.7
0	5000	149.7	152.3	156.1	160.3	163.8
1000		149.7	152.3	156.1	160.3	163.8
10000		149.7	152.3	156.1	160.3	163.8

2.39 for the static loads $P_{st} = 0$ and 10000 N (in the same scale for comparison purpose) followed by a dynamic load of amplitude $P_{S0} = 5000$ N. As the wave moves along the soil beam, energy is dissipated and the intensity of the loading decreases, which induces an increase in the secant modulus. The secant wave velocities c_{sec} for all the cases are summarized in Table 2.2. The wave velocities c_{cc} calculated from the cross-correlations are plotted in Figures 2.40 and 2.41, and summarized in Table 2.3. The wave velocities c_{sec} from the secant moduli in Table 2.2 indicate that the initial static load does not have an influence on the stress-strain behavior in the steady-state region of the nonlinear spring. This is also apparent in the cross-correlation results in Figure 2.40 or 2.41 and Table 2.3. It is also observed that the wave velocity c_{cc} from the cross-correlation is slightly smaller than that from the secant modulus with the difference being less than 5%. Regardless of the initial static load, the cross-correlation estimates a wave velocity c_{cc} very close to the velocity c_{sec} from the secant modulus in the stress-strain loop of the vibration under steady-state.

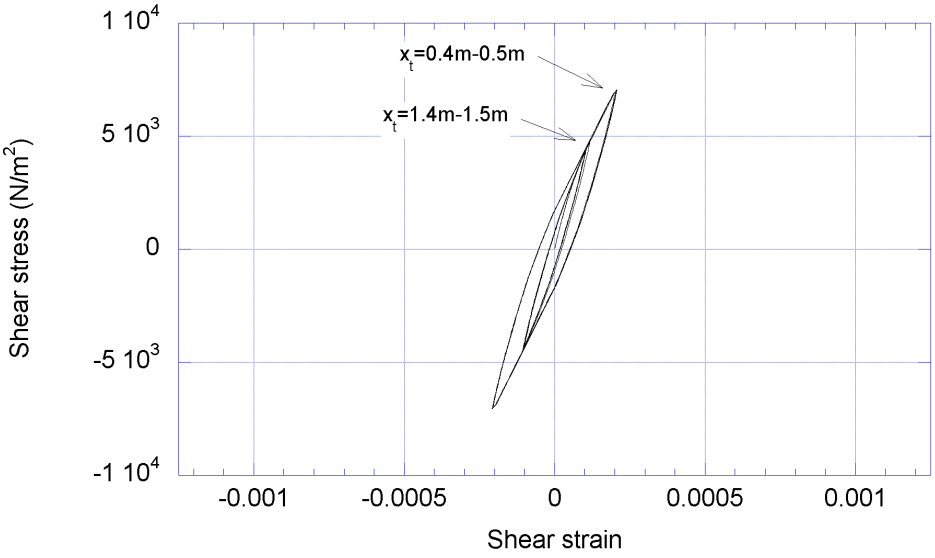

(a) $P_{st} = 0$ and $P_{S0} = 5000$ N

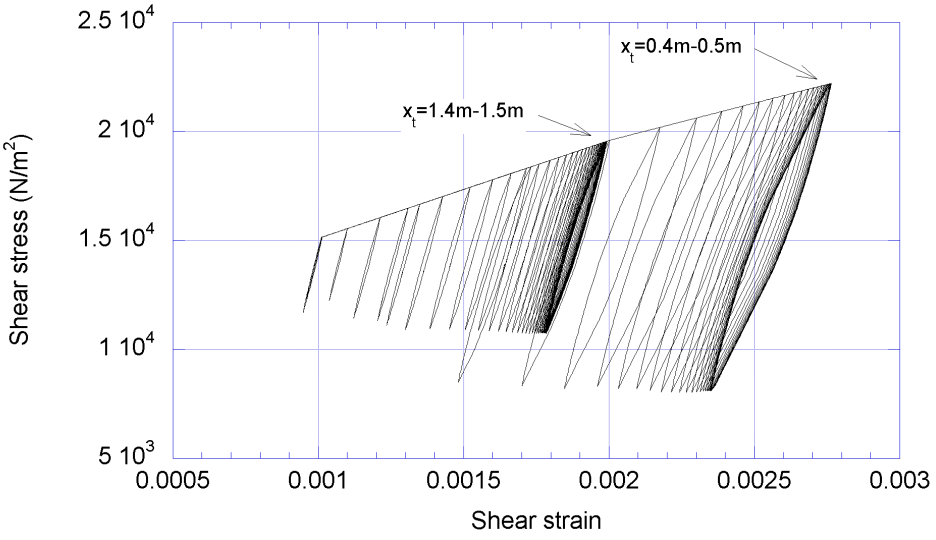

(b) $P_{st} = 10000$ N and $P_{S0} = 5000$ N

Figure 2.39 Stress-strain behavior for different initial static loads with $f = 100$ Hz

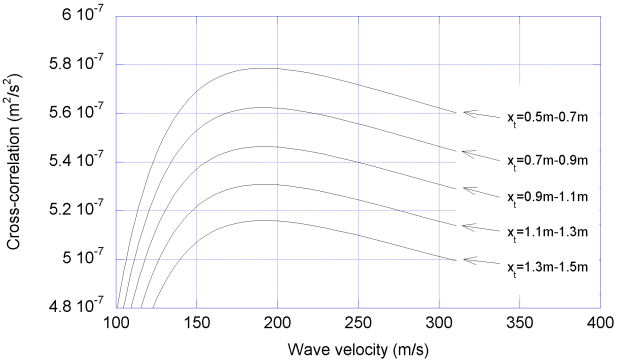

(a) for $P_{st} = 0$ and $P_{S0} = 500$ N

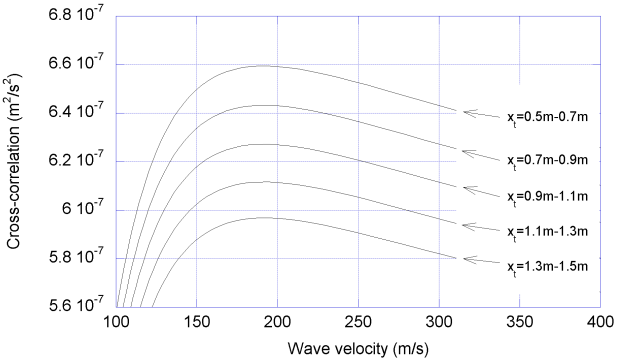

(b) for $P_{st} = 1000$ N and $P_{S0} = 500$ N

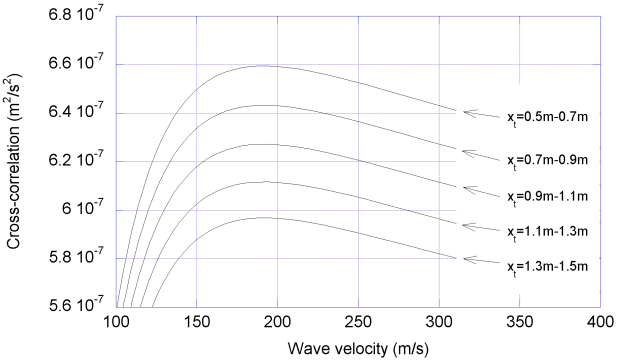

(c) for $P_{st} = 10000$ N and $P_{S0} = 500$ N

Figure 2.40 Cross-correlation results for different initial static load with $f = 100$ Hz

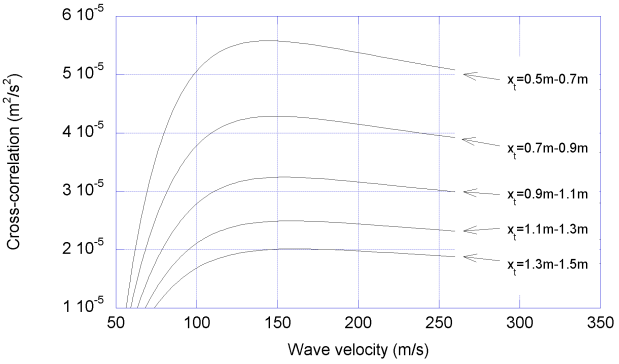

(a) for $P_{st} = 0$and $P_{S0} = 5000$ N

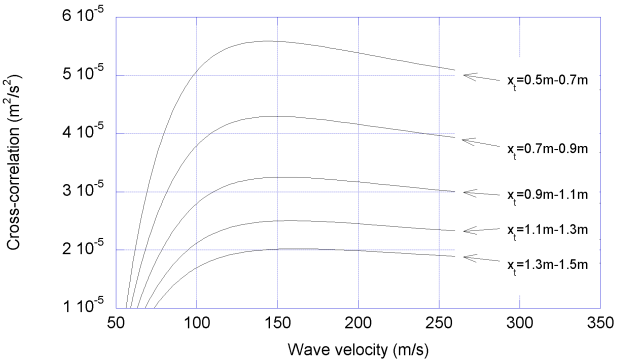

(b) for $P_{st} = 1000$ N and $P_{S0} = 5000$ N

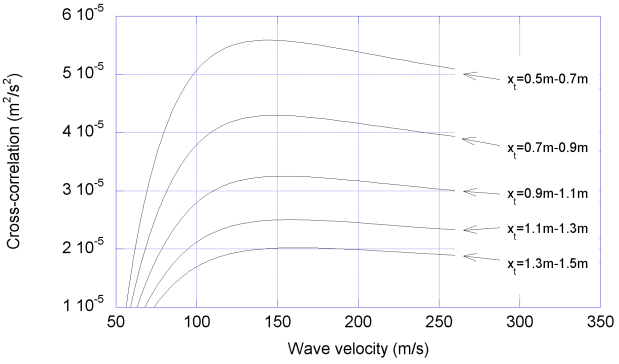

(c) for $P_{st} = 10000$ N and $P_{S0} = 5000$ N

Figure 2.41 Cross-correlation results for different initial static load with $f = 100$ Hz

Table 2.3 Wave velocity c_{cc} calculated using cross-correlation with $f = 100$ Hz

Initial shear load P_{st} (N)	Sinusoidal load amplitude P_{S0} (N)	Wave velocity c_{cc} (m/s) from cross-correlation at various location				
		0.5 m− 0.7 m	0.7 m− 0.9 m	0.9 m− 1.1 m	1.1 m− 1.3 m	1.3 m− 1.5 m
0	500	192	192	192	192	192
1000		192	192	192	192	192
10000		192	192	192	192	192
0	5000	144	149	154	158	162
1000		144	149	154	158	162
10000		144	149	154	158	162

2.7.4. Effect of Loading Amplitude

Tables 2.2 and 2.3 and Figures 2.40 and 2.41, can also provide insight on the effect of the dynamic loading amplitude on the wave propagation velocity in the nonlinear range. In all cases, it was the amplitude of the excitation and not the initial static load that affected the wave propagation velocity under the steady-state response. The cross-correlation estimated value of the velocity c_{cc} matched the wave velocity c_{sec} calculated from the secant modulus in the steady-state stress-strain loop regardless of the excitation amplitude.

2.7.5. Effect of Loading Frequency

A loading frequency $f = 100$ Hz was used for all the analyses previously discussed. A frequency of $f = 50$ Hz was used to observe the effect of the loading frequency on the wave propagation velocity. When the frequency decreases, it takes longer to reach the steady-state condition because the number of cycles in a given time interval is smaller.

The velocity histories in the time ranges 2.0 s $\leq t \leq$ 2.512 s, 4.0 s $\leq t \leq$ 4.512 s, 8.0 s $\leq t \leq$ 8.512 s, and 16.0 s $\leq t \leq$ 16.512 s, are compared in Figure 2.42. These results indicate that the steady-state condition has been reached for 4.0 s $\leq t \leq$ 4.512 s in terms of velocity. The particle velocity history for 4 s $\leq t \leq$ 4.512 s was used also for $f = 50$ Hz to obtain the cross-correlations.

The stress-strain cycles in the springs between $x_t = 0.4$ m 0.5 m, $x_t = 1.4$ m and 1.5 m are plotted in Figure 2.43. When compared with the stress-strain cycles for $f = 100$ Hz in Figure 2.39, the behavior for $f = 50$ Hz exhibits higher amplitudes of strain-strain loops at the same locations, which looks reasonable since a smaller rate of the vibration cycle causes a smaller energy dissipation rate. Since the amplitude of stress-strain loops are higher for $f = 50$ Hz, it can be also inferred that the secant modulus and the wave velocity estimates with $f = 50$ Hz will be lower than those with $f = 100$ Hz. The secant wave velocity c_{sec} and the cross-correlation result c_{cc}, calculated $f = 50$ Hz in the same fashion as before, are tabulated in Tables 2.4 and 2.5, respectively and displayed in Figures 2.44 and 2.45. The results support the above mentioned hypotheses, when compared with the results with $f = 100$ Hz in Tables 2.2 and 2.3, and in Figures 2.40 and 2.41. If the loading frequency decreases, the amplitude of the stress-strain loops in steady-state increases, resulting in a reduction of the secant modulus. However, even for the smaller frequency, the cross-correlation predicts a wave velocity c_{cc} quite close to the wave velocity c_{sec} corresponding to the secant modulus.

2.7.6. Effect of Location of Cross-Correlation Points

As observed the previous section, the wave propagation velocities for a nonlinear soil beam under a sinusoidal shear load depend on the amplitude of the vibration, and thus on the energy dissipation. In that sense, if the measurement locations get farther

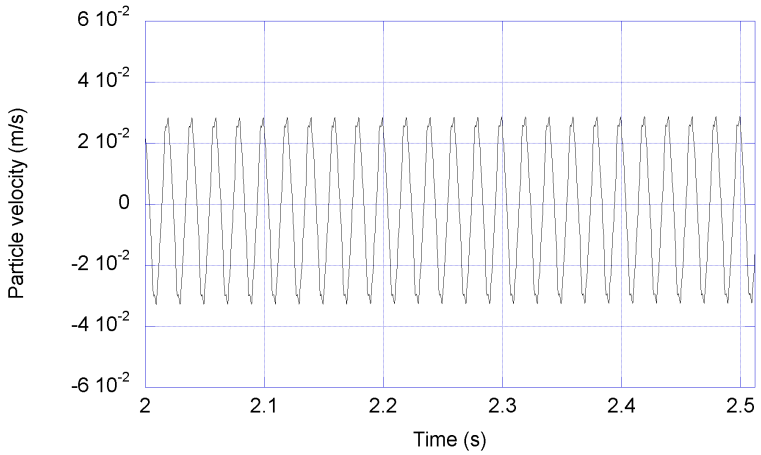

(a) 2.0 s $\leq t \leq$ 2.512 s

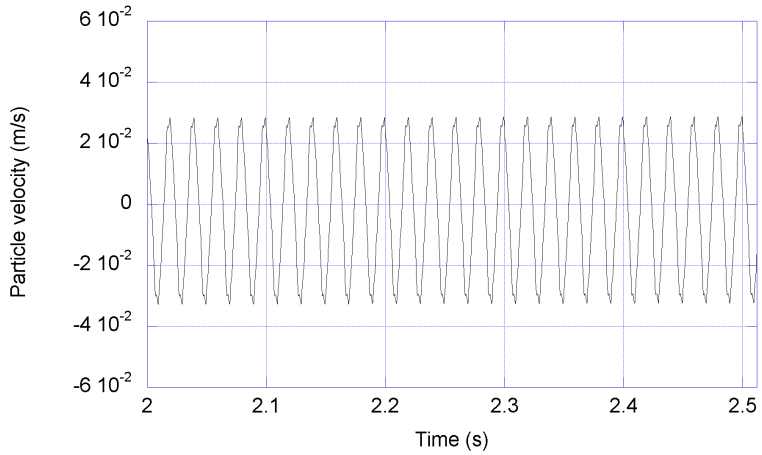

(b) 4.0 s $\leq t \leq$ 4.512 s

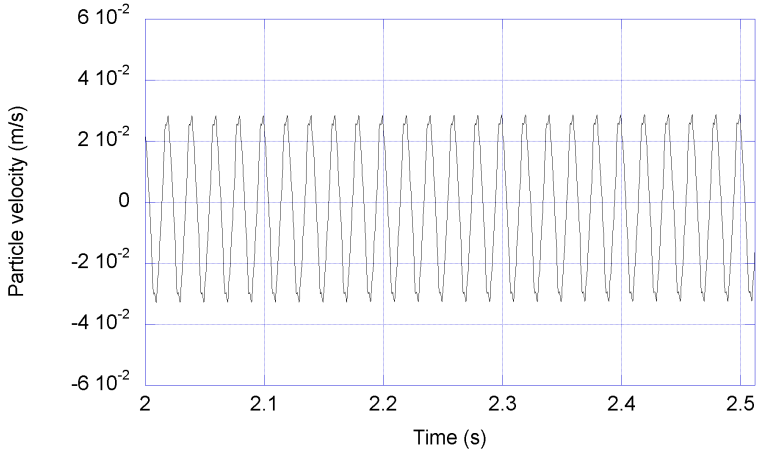

(c) 8.0 s $\leq t \leq$ 8.512 s

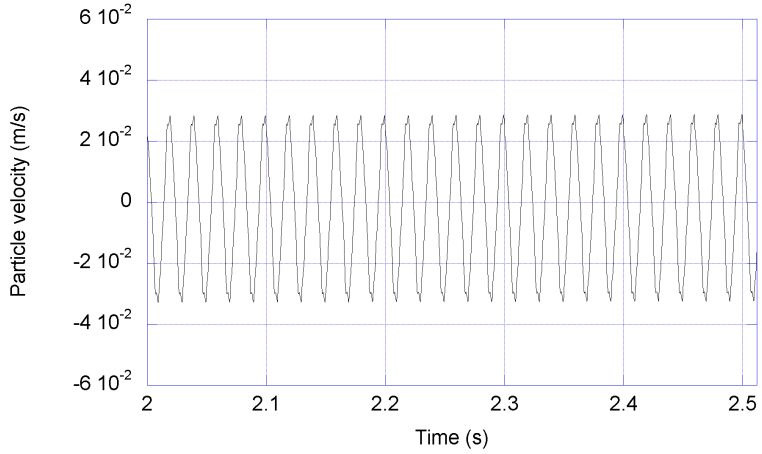

(d) 16.0 s $\leq t \leq$ 16.512 s

Figure 2.42 Particle velocity history at $x_t = 0.5$ m with $f = 50$ Hz, $P_{st} = 10000$ N, and $P_{S0} = 5000$ N

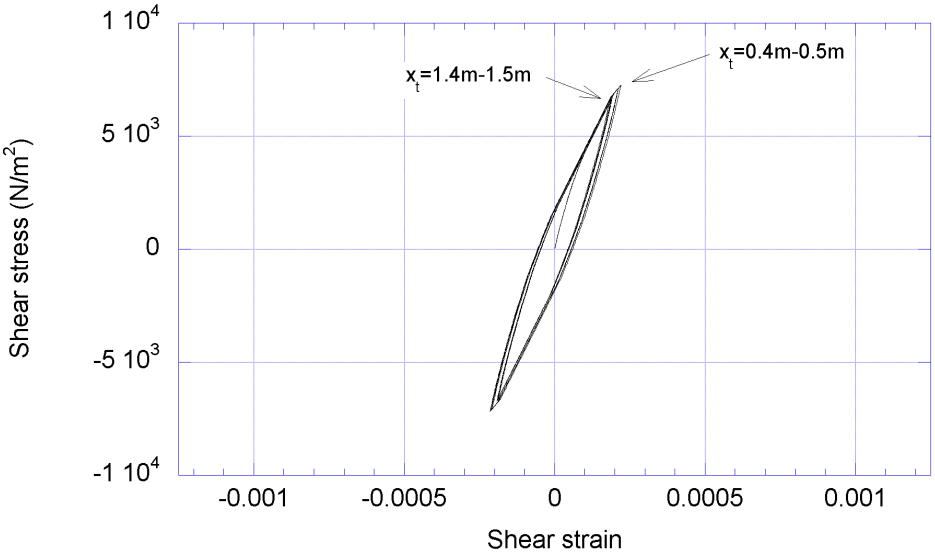

(a) for $P_{st} = 0$ and $P_{S0} = 5000$ N

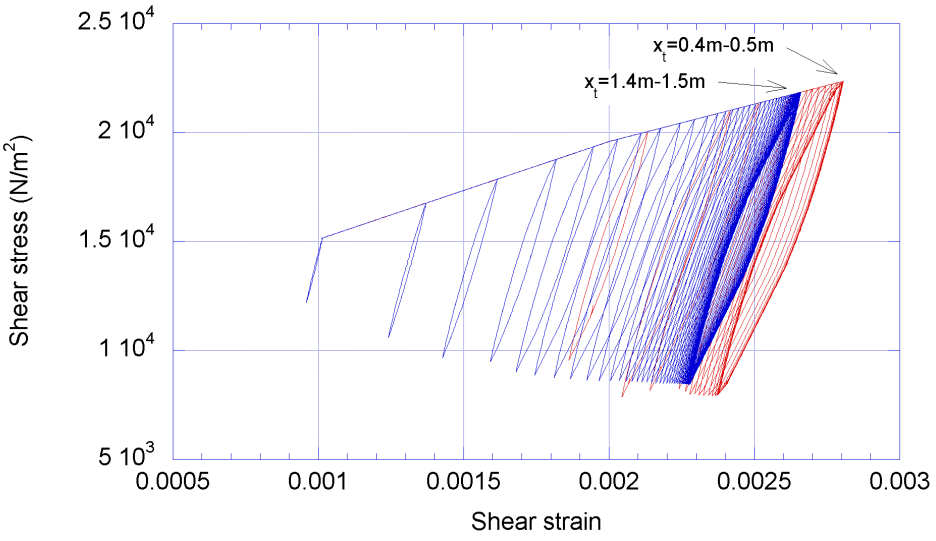

(b) for $P_{st} = 10000$ N and $P_{S0} = 5000$ N

Figure 2.43 Stress-strain behavior for different initial static load with $f = 50$ Hz

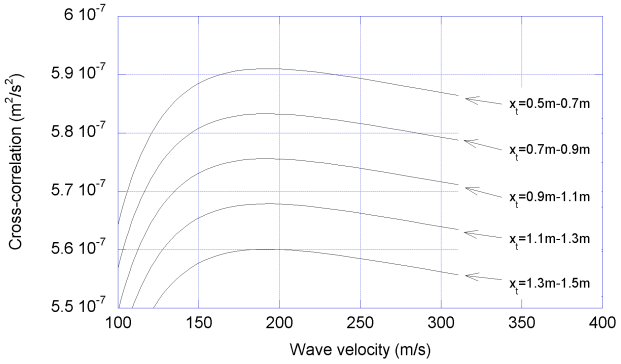

(a) for $P_{st} = 0$ and $P_{S0} = 500$ N

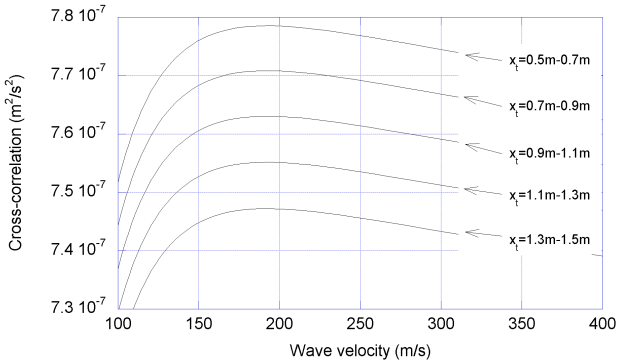

(b) for $P_{st} = 1000$ N and $P_{S0} = 500$ N

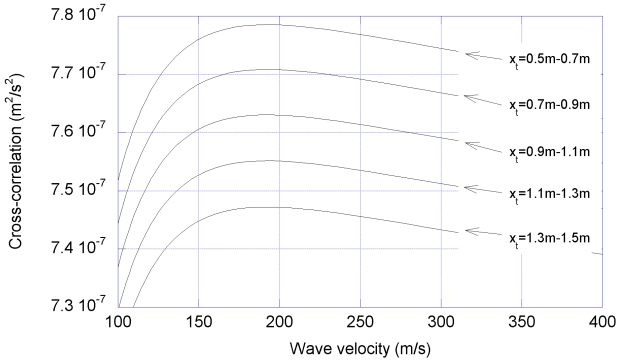

(c) for $P_{st} = 10000$ N and $P_{S0} = 500$ N

Figure 2.44 Cross-correlation results for different initial static load with $f = 50$ Hz and $P_{S0} = 500$ N

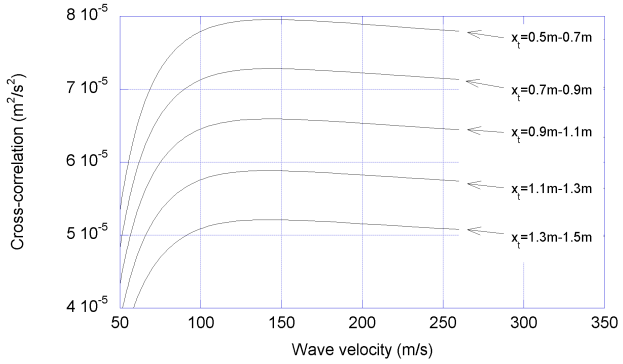

(a) for $P_{st} = 0$ and $P_{S0} = 5000$ N

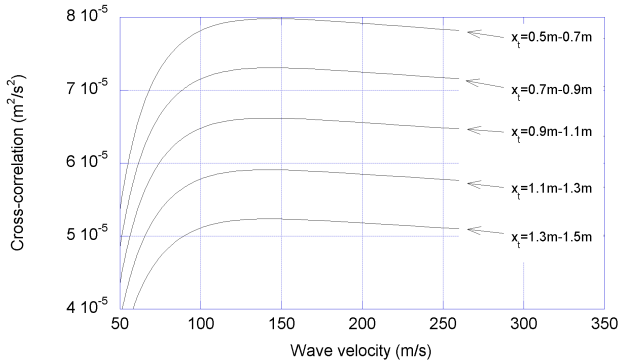

(b) for $P_{st} = 1000$ N and $P_{S0} = 5000$ N

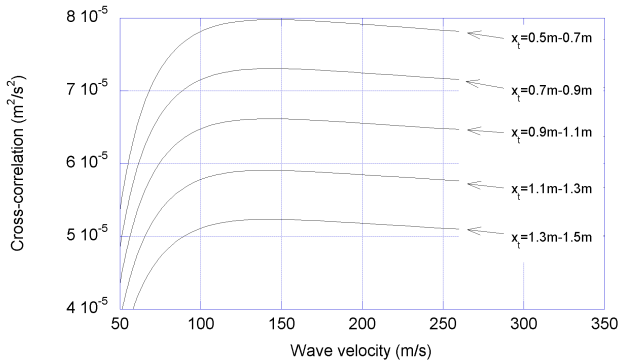

(c) for $P_{st} = 10000$ N and $P_{S0} = 5000$ N

Figure 2.45 Cross-correlation results for different initial static load with $f = 50$ Hz and $P_{S0} = 5000$ N

Table 2.4 Wave velocity c_{sec} calculated from secant modulus with $f = 50$ Hz

Initial shear load P_{st} (N)	Sinusoidal load amplitude P_{S0} (N)	Wave velocity c_{sec} (m/s) from secant modulus at various location				
		0.5 m− 0.7 m	0.7 m− 0.9 m	0.9 m− 1.1 m	1.1 m− 1.3 m	1.3 m− 1.5 m
0	500	192.4	192.4	192.4	192.4	192.4
1000		192.4	192.4	192.4	192.4	192.4
10000		192.4	192.4	192.4	192.4	192.4
0	5000	149.1	149.5	149.3	149.3	149.8
1000		149.1	149.5	149.3	149.3	149.8
10000		149.1	149.5	149.3	149.3	149.8

Table 2.5 Wave velocity c_{cc} calculated using cross-correlation with $f = 50$ Hz

Initial shear load P_{st} (N)	Sinusoidal load amplitude P_{S0} (N)	Wave velocity c_{cc} (m/s) from cross-correlation at various location				
		0.5 m− 0.7 m	0.7 m− 0.9 m	0.9 m− 1.1 m	1.1 m− 1.3 m	1.3 m− 1.5 m
0	500	192	192	192	192	192
1000		192	192	192	192	192
10000		192	192	192	192	192
0	5000	144	144	143	142	143
1000		144	144	143	142	143
10000		144	144	143	142	143

away from the loading source, there will be a further decrease in the amplitude of the stress-strain loops and the wave velocities will become higher. Using the loading frequency $f = 100$ Hz, two sets of additional analyses were performed with different sets of measurement locations. Two dynamic load amplitudes $P_{S0} = 500$ N and 5000 N were used with only one initial static load $P_{st} = 0$ since it has already been shown that the effect of the initial static load on the steady-state behavior is negligible. As before, the number of segments was 4800, the beam length $L = 480$ m, and the time step $\Delta t = 3.125 \times 10^{-5}$ s. In the first analyses, the cross-correlations were calculated at $x_t = 0.5$ m and 1.0 m, $x_t = 1.0$ m and 1.5 m, $x_t = 1.5$ m and 2.0 m, $x_t = 2.0$ m and 2.5 m, and $x_t = 2.5$ m and 3.0 m. The second set was analyzed at $x_t = 2.0$ m and 2.2 m, $x_t = 2.2$ m and 2.4 m, $x_t = 2.4$ m and 2.6 m, $x_t = 2.6$ m and 2.8 m, and $x_t = 2.8$ m and 3.0 m.

The results of the analyses of the first set are presented in Figure 2.46 and summarized in Tables 2.6 and 2.7. To calculate the average secant wave velocity c_{sec}, the values of modulus in the ten springs between the two measurement points were averaged. The results show again that the cross-correlation results c_{cc} compare well with the secant wave velocity c_{sec}. The results for the second set of points are presented in Figure 2.47 and Tables 2.8 and 2.9. The secant wave velocity c_{sec} was calculated again from the averaged secant modulus between the measurement locations. The cross-correlation results c_{cc} show still good agreement with the secant wave velocity c_{sec}. Consequently, though the location of the measurement points will affect the computed wave propagation velocity due to the different amplitudes of the steady-state stress-strain loops, the cross-correlation wave velocity c_{cc} and the secant wave velocity c_{sec} remain always very close to each other.

Table 2.6 Wave velocity c_{sec} calculated from secant modulus with the first set of measurement locations

Initial shear load P_{st} (N)	Sinusoidal load amplitude P_{S0} (N)	Wave velocity c_{sec} (m/s) from secant modulus at various location				
		0.5 m− 1.0 m	1.0 m− 1.5 m	1.5 m− 2.0 m	2.0 m− 2.5 m	2.5 m− 3.0 m
0	500	192.3	192.6	192.9	193.3	193.5
	5000	151.8	161.1	167.4	172.8	175.7

Table 2.7 Wave velocity c_{cc} calculated using cross-correlation with the first set of measurement locations

Initial shear load P_{st} (N)	Sinusoidal load amplitude P_{S0} (N)	Wave velocity c_{cc} (m/s) from cross-correlation at various location				
		0.5 m− 1.0 m	1.0 m− 1.5 m	1.5 m− 2.0 m	2.0 m− 2.5 m	2.5 m− 3.0 m
0	500	192	192	193	192	193
	5000	149	160	166	171	173

Table 2.8 Wave velocity c_{sec} calculated from secant modulus with the second set of measurement locations

Initial shear load P_{st} (N)	Sinusoidal load amplitude P_{S0} (N)	Wave velocity c_{sec} (m/s) from secant modulus at various location				
		2.0 m− 2.2 m	2.2 m− 2.4 m	2.4 m− 2.6 m	2.6 m− 2.8 m	2.8 m− 3.0 m
0	500	193.2	193.3	193.4	193.4	193.5
	5000	171.4	173.5	174.7	175.4	176.3

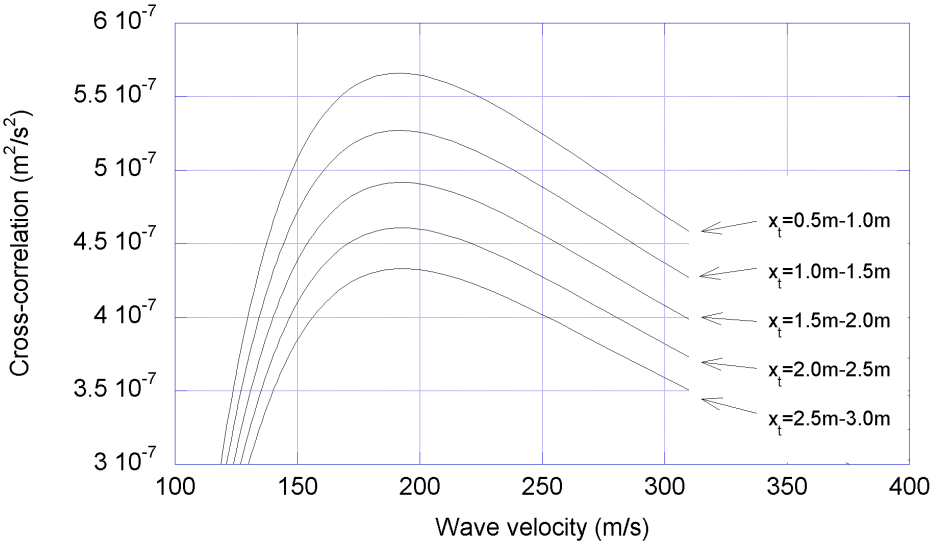

(a) for $P_{st} = 0$ and $P_{S0} = 500$ N

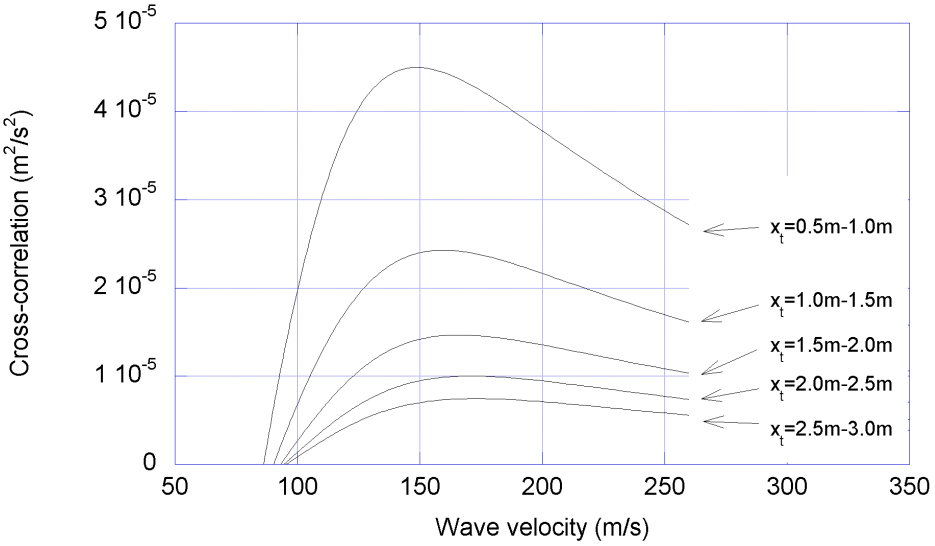

(b) for $P_{st} = 0$ and $P_{S0} = 5000$ N

Figure 2.46 Wave velocity estimate from cross-correlation and secant modulus with the first set of measurement locations

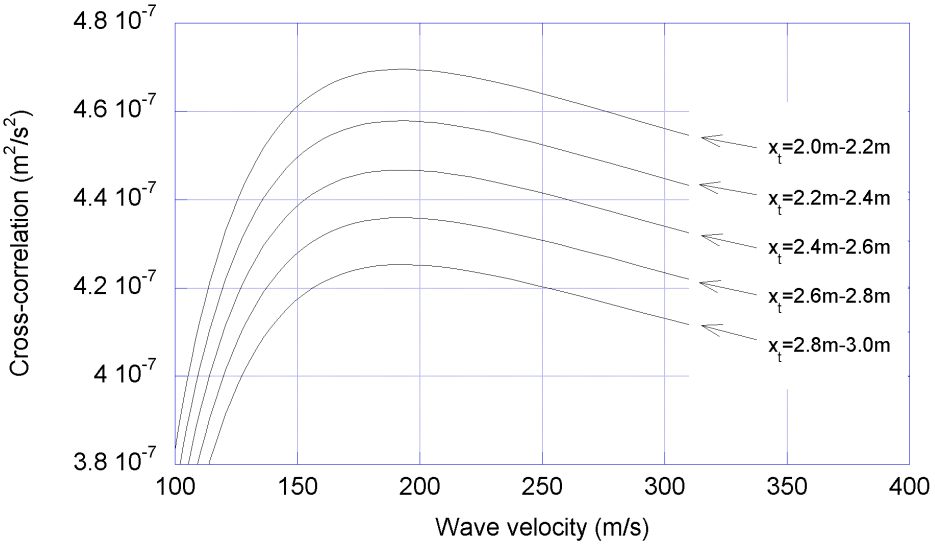

(a) for $P_{st} = 0$ and $P_{S0} = 500$ N

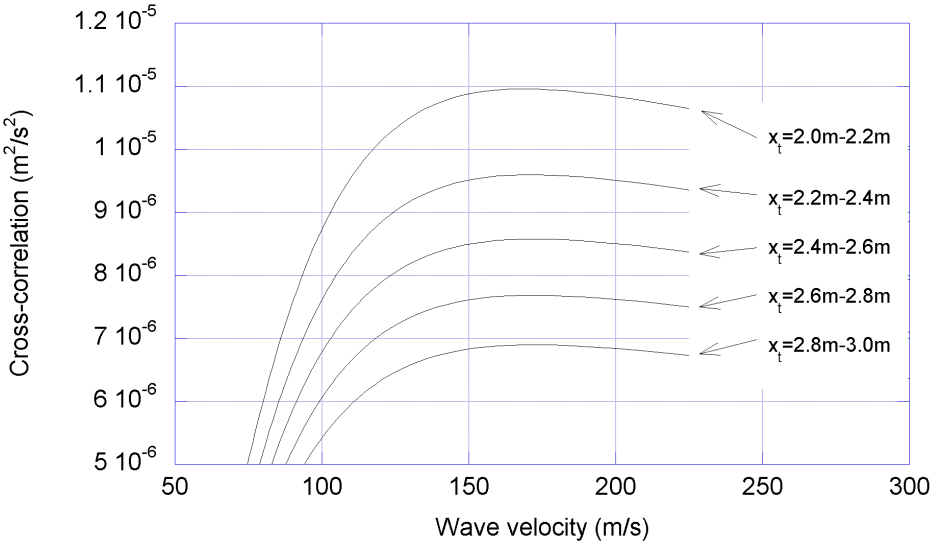

(b) for $P_{st} = 0$ and $P_{S0} = 5000$ N

Figure 2.47 Wave velocity estimate from cross-correlation and secant modulus with the second set of measurement locations

Table 2.9 Wave velocity c_{cc} calculated using cross-correlation with the second set of measurement locations

Initial shear load P_{st} (N)	Sinusoidal load amplitude P_{S0} (N)	Wave velocity c_{cc} (m/s) from cross-correlation at various location				
		2.0 m-2.2 m	2.2 m−2.4 m	2.4 m−2.6 m	2.6 m−2.8 m	2.8 m−3.0 m
0	500	192	192	192	192	192
	5000	169	171	172	172	172

2.8. Summary and Conclusions

The wave propagation in a one dimensional nonlinear soil medium under a triangular impact and a harmonic excitation was investigated using a discrete model with lumped masses and interconnected springs.

When an impact excitation was applied at the free end of the soil shear beam, the measured wave velocity using the cross-correlation between the signals measured at two points was very close to the wave velocity calculated from the tangent modulus corresponding to the state of stress caused by an applied static load. For all the initial stress states considered, the result from cross-correlation was very close to the wave velocity calculated from the tangent modulus corresponding to that particular initial stress. The duration of the impact and the location of the measurement points for the cross-correlation affected the agreement between the cross-correlation result and the tangent wave velocity because the two variables had an influence on the shape of the particle velocity history. The wave velocity calculated from the initial arrival time difference of the signals was quite close to the tangent wave velocity without deviation, whereas the wave velocity resulting from the time difference between the peaks corresponded to the velocity estimated from the cross-correlation. In all cases

considered, the difference was about 5% of the cross-correlation estimate (for the range of the variables used in the study). Therefore, cross-correlation provides a convenient tool to calculate wave velocity, which, in turn, also provides an estimate of the tangent modulus corresponding to the static load before the dynamic excitation is applied. The amplitude of the impact affected the magnitude of the displacement and the particle velocity, but had negligible effect on the estimate of the wave velocity for the magnitudes considered.

When a sinusoidal load was applied, the cross-correlation estimated a wave velocity close to the one calculated from the secant modulus in the stress-strain loops under steady-state vibration. The variables that contributed to change the shear modulus also influence the estimate of wave velocity from cross-correlation. The variables examined here were: the amplitude of the sinusoidal excitation, the frequency of loading, and the cross-correlation locations. However, the effect of the initial stress state of the nonlinear material on the computed wave velocity was negligible. In all cases, the computed wave propagation velocities are very good approximations to the average secant velocity over the region between the cross-correlation points.

CHAPTER III

WAVE PROPAGATION UNDER VERTICALLY EXCITED SURFACE FOUNDATION

3.1. Introduction

A new test method using large scale shakers has been employed to measure nonlinear soil properties in situ. The method involves applying static and dynamic loads at the surface of the soil deposit and measuring the dynamic response of the soil mass beneath the loaded area with embedded instrumentation. The soil response is measured using the velocity transducers. The strains corresponding to each loading case is estimated from pseudo-nonlinear (equivalent-linear) finite element analyses. The corresponding wave propagation velocities are obtained from interpretation of the recorded data. If one considers vertical dynamic loads applied on a disk and the records of displacements, velocities or accelerations that would be recorded by sensors placed at different depths, the first times of arrival (or the inter-arrival times between sensors) for vertical motions will coincide with the arrival times of P waves and would provide therefore the P wave velocity for the material, corresponding to its constrained modulus. When considering on the other hand the phase differences between the motions recorded at the sensors, the resulting propagation velocities will be functions of frequency and depth, and will not correspond exactly to either the constrained modulus or Young's modulus (rod wave velocity). It is necessary then to conduct more rigorous and also more complicated analyses in order to interpret the data. The objective of this chapter is to illustrate this point.

3.2. Formulation

Consider a horizontally layered soil deposit as shown schematically in Figure 3.1. Following Kausel and Roesset (1981) it is possible to derive for each layer, and for an underlying halfspace, a dynamic stiffness matrix, function of the wave number k and the circular frequency ω, relating tractions applied at the two horizontal faces of a layer and the corresponding displacements. Assembling these matrices, following the standard procedures of matrix structural analysis, one can obtain a dynamic stiffness matrix for the complete soil deposit leading to a system of equations

$$\mathbf{KU} = \mathbf{P} \tag{3.1}$$

where $\mathbf{K}$ is the stiffness matrix, $\mathbf{U}$ is the vector of horizontal and vertical displacements at the free surface of the deposit and the layer interfaces, and $\mathbf{P}$ is a vector of applied horizontal and vertical forces at the same levels. Under a steady state harmonic load q uniformly distributed over a circular area of radius R on the surface of the soil, the vertical displacement w_i at a level i and a radial distance r from the center axis of loading area is then given by

$$w_i = qR \int_0^\infty J_1(kR) J_0(kr) U_{2i} dk. \tag{3.2}$$

J_0 and J_1 are the Bessel functions of order 0 and 1; U_{2i} is the $2i$ component of the vector $\mathbf{U}$ obtained solving Equation 3.1 with the right hand side vector components all 0 except the second one (vertical load at the surface), which would equal 1; and the integral extends from 0 to ∞. At points under the axis $r = 0$ and $J_0(0) = 1$. The solution can then be obtained in the general case evaluating the integral numerically.

An alternative to this solution is to use the explicit Green's functions for this problem obtained by Kausel (1981). This approach uses the same analytical solution,

but does not require the numerical evaluation of the integral (the corresponding integrals have explicit solutions) but it is based on some approximations, notably the assumption of a piecewise linear variation of the displacements with depth (Waas, 1972; Kausel, 1974). As a result it is necessary to subdivide each physical layer into a number of sub-layers, each thinner than a fraction of the wavelength of interest. This approach is often referred to as thin layer theory. The solution is quite accurate for a soil deposit resting on much stiffer, nearly rigid rock but it involves another approximation when attempting to simulate an underlying halfspace. These two approaches are not expected to yield exactly the same results (except in the limit) due to the different sources of errors, but they should differ only minimally.

A third approach is to consider a model as shown in Figure 3.2, in which the horizontally stratified soil deposit of Figure 3.1 is represented by a core region under the loaded area. The core region is modeled with toroidal finite elements in cylindrical coordinates, expanding the solution in a Fourier series in the circumferential direction, while the outside region is modeled using the consistent boundary of Kausel (1974) for the same number of the Fourier expansion. For the case of a vertical load the problem is axisymmetric and only the n = 0 term of the expansion is needed. This model requires again the discretization of the soil into thin layers, assuming a linear variation of the displacements in the vertical direction within each layer. In addition the core region is also discretized in the radial direction. This introduces an additional approximation but allows variation of the soil properties in both directions, a feature that will be needed to simulate the tests accounting for the variation in properties with the level of strains. The model assumes the existence of much stiffer, essentially rigid, rock at a certain depth, but it also allows to consider either a distributed load or a circular mat on which the load may be applied. This is again a better model to simulate the experiments and therefore this is the approach that will be used in the

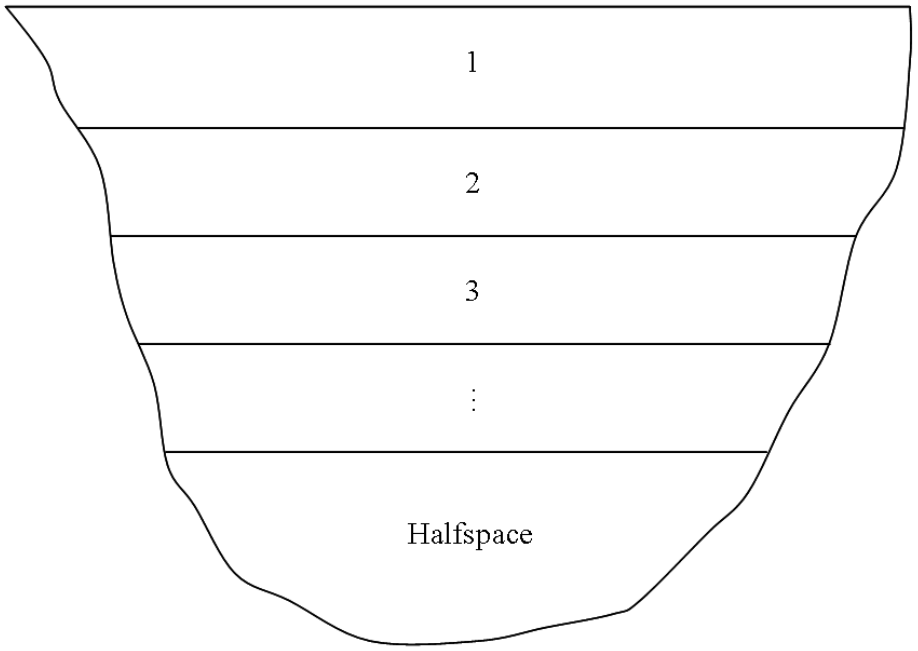

Figure 3.1 Layered halfspace

project to interpret the measurements.

3.3. Time Histories

Consider first a one dimensional model of a column subjected to a vertical load in the form of a triangular pulse with duration of 0.01 s. The column has a Young's modulus of 58 MPa, a mass density of 2000 kg/m^3, a rod wave velocity of 170.29 m/s, and a length of 6 m. Receivers are placed at depths of 1, 2 and 3 m from the top. The displacement time histories that would be recorded at the receivers are illustrated in Figure 3.3. The motion starts at each one of the receivers at times of 0.00587, 0.01174 and 0.01762 s coinciding with the arrival of the wave. The displacement increases over the 0.01 s of duration of the pulse, remains constant and then decreases as the reflected pulse from the bottom of the column reaches the receivers. After this, not

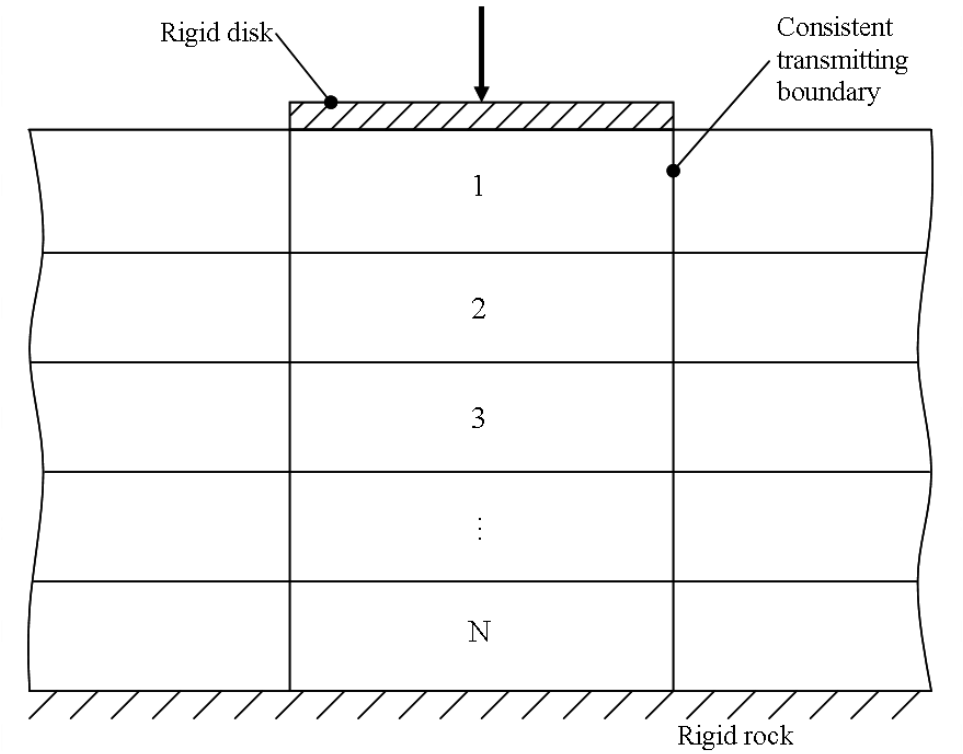

Figure 3.2 Layered system with surface foundation

shown in the figure, there would be pulses reflected from the top (free surface) and the displacements would reproduce themselves with a negative sign. The arrival of the first pulse and of its reflection from the bottom are clearly seen in the velocity records in Figure 3.4. If the column were constrained laterally, the constrained modulus $(\lambda + 2G)$ rather than the Young's modulus E, would be the appropriate material property, resulting in a wave propagation velocity of 331.66 m/s (P wave velocity). The corresponding displacements and velocities for a one dimensional model would be as shown in Figures 3.5 and 3.6, with the same shapes as in the previous case, but different arrival times for the pulses (0.003015, 0.00603 and 0.009045 s at the three receivers). The arrivals of the different waves are very easy to identify when the duration of the pulse is very small, as in this case (duration of 0.01 s, corresponding to a predominant frequency of 100 Hz). For longer durations this is not the case. Figure 3.7 shows for instance the displacement histories of the same column under a pulse of duration 0.04 s. The motion starts at the same arrival times but it is no longer possible to visualize the arrivals of the reflected waves: the column is vibrating at its own natural period (0.074 s, in this case).

Consider now the soil deposit underlying a rigid circular disk of Figure 3.2. It has a shear wave velocity of 100 m/s, a Poisson's ratio of 0.45, a Young's modulus of 58 MPa, a constrained modulus of 220 MPa, an internal, hysteretic, damping of 1%, and a depth of 6 m. The corresponding P wave velocity is again 331.66 m/s. The disk has a radius of $R = 0.5$ m, and receivers are placed below the center of the disk at depths of 1, 2 and 3 m. Figure 3.8 shows the displacement time histories at the three receivers when the disk is subjected again to a triangular pulse with duration of 0.01 s. The displacements start at the times of arrival of the P wave (0.003015, 0.00603 and 0.009045 s), but the shape of the displacements is however very different from those obtained earlier with the one dimensional model. Figure 3.9 shows the

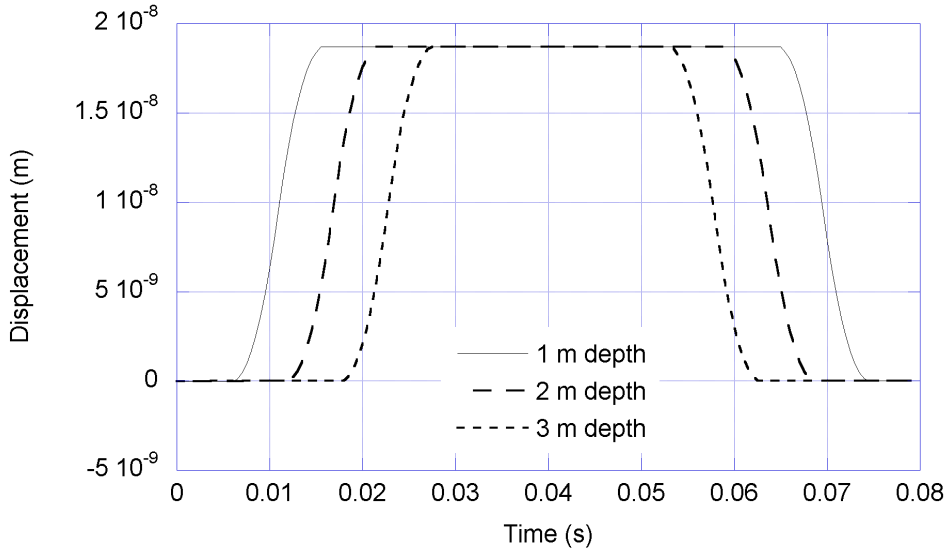

Figure 3.3 Displacement time histories in 1D unconstrained column after impact ($\Delta T_d = 0.01$ s)

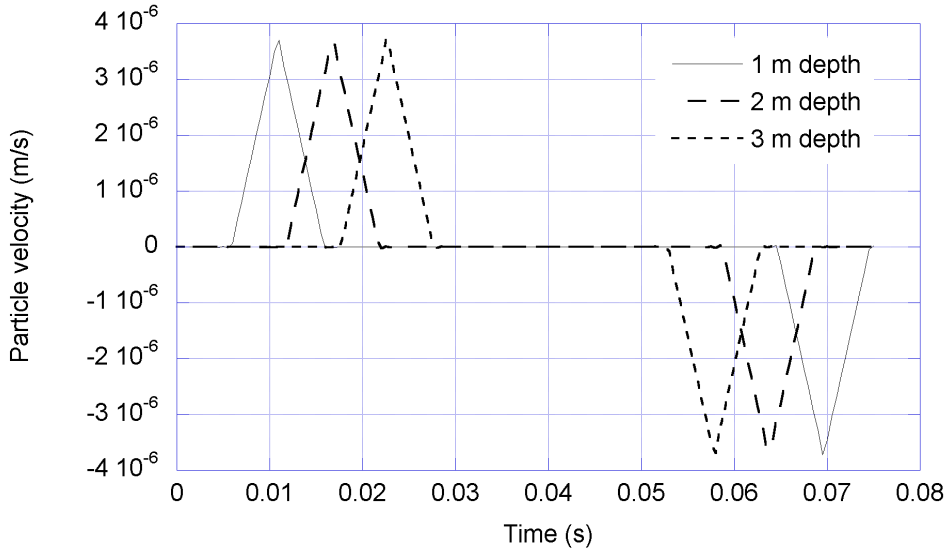

Figure 3.4 Particle velocity time histories in 1D unconstrained column after impact ($\Delta T_d = 0.01$ s)

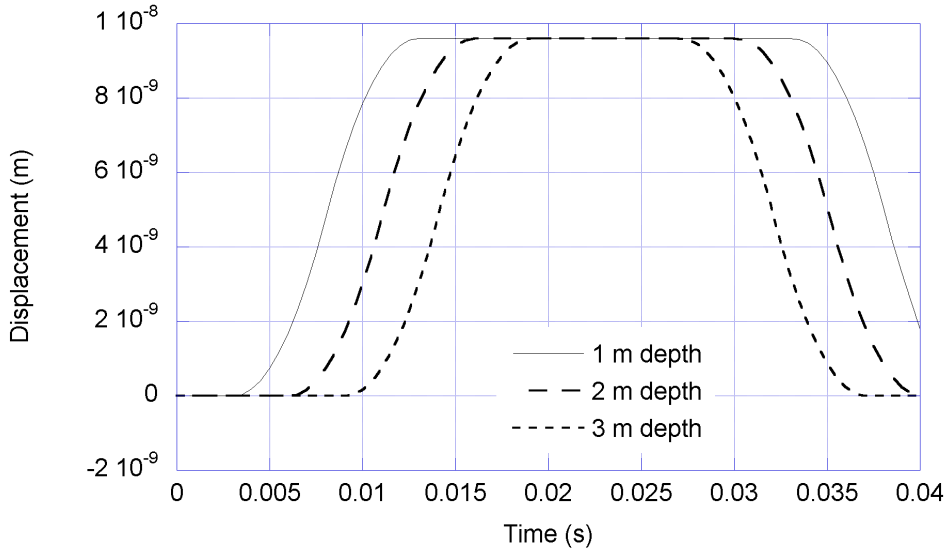

Figure 3.5 Displacement time histories in 1D constrained column after impact ($\Delta T_d = 0.01$ s)

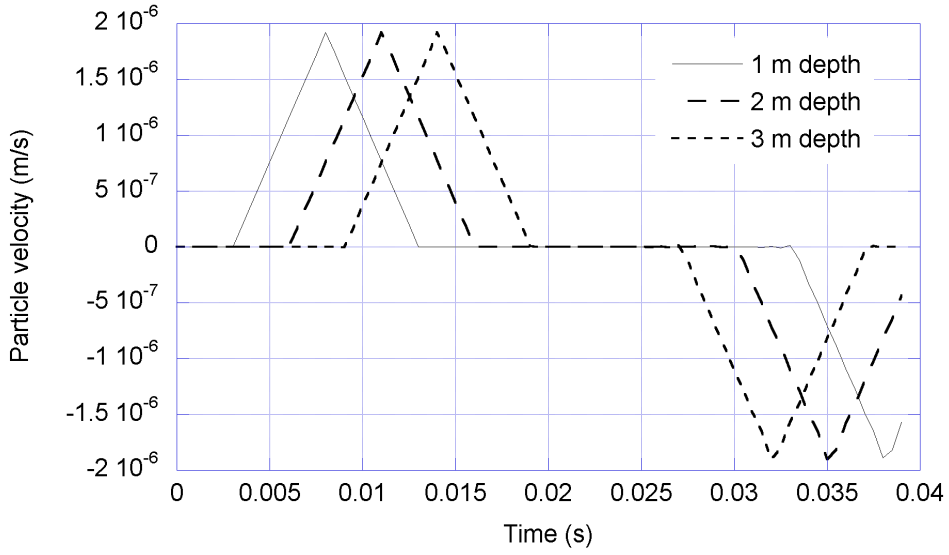

Figure 3.6 Particle velocity time histories in 1D constrained column after impact ($\Delta T_d = 0.01$ s)

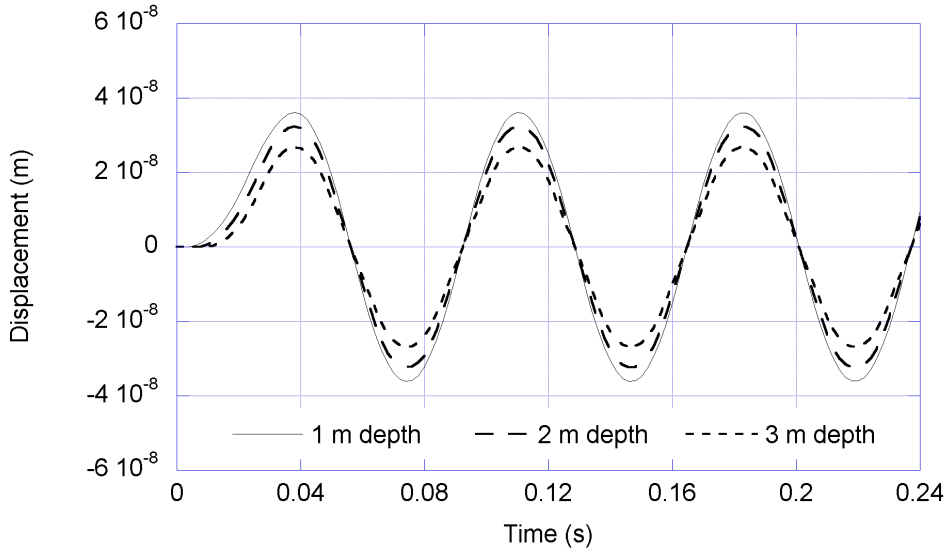

Figure 3.7 Displacement time histories in 1D constrained column after longer impact ($\Delta T_d = 0.04$ s)

corresponding results if the soil around the core region (the far field) were removed, keeping only a three dimensional finite element model of a soil cylinder with a rigid disk on top (two dimensional in cylindrical coordinates because of axisymmetry) and a free lateral boundary. The displacement histories in Figure 3.10 would be recorded for the same cylinder if the lateral boundary were to be constrained (no radial displacements permitted). Comparing these three figures, we see that the times at which the motions start are the same for all three cases, corresponding to the arrival of the P wave, irrespective of the lateral boundary conditions. The shape of the displacements is the same as in the one dimensional solution when the lateral boundary is constrained but it is quite different in the other two cases. The differences in the shape of the displacement histories will affect the phase differences between the motions at the receivers.

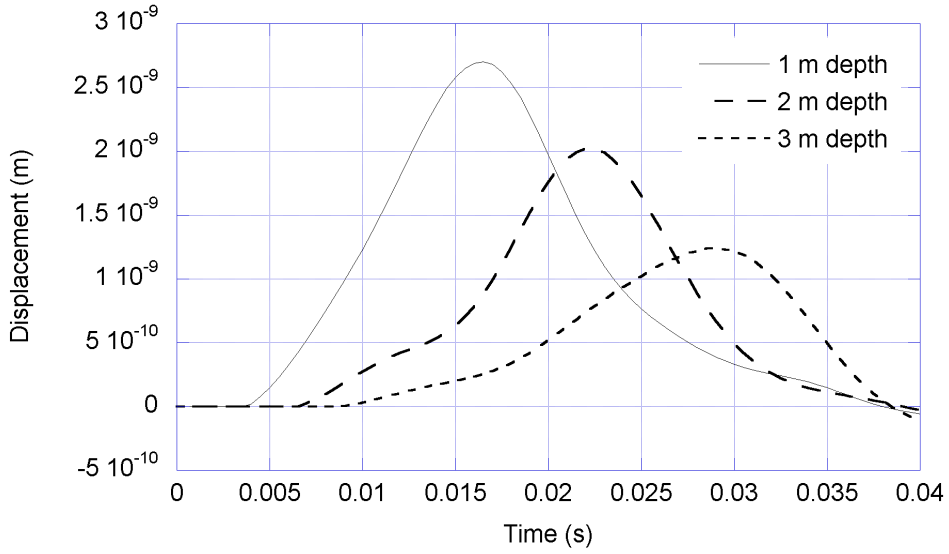

Figure 3.8 Displacement time histories in 3D column with transmitting boundary

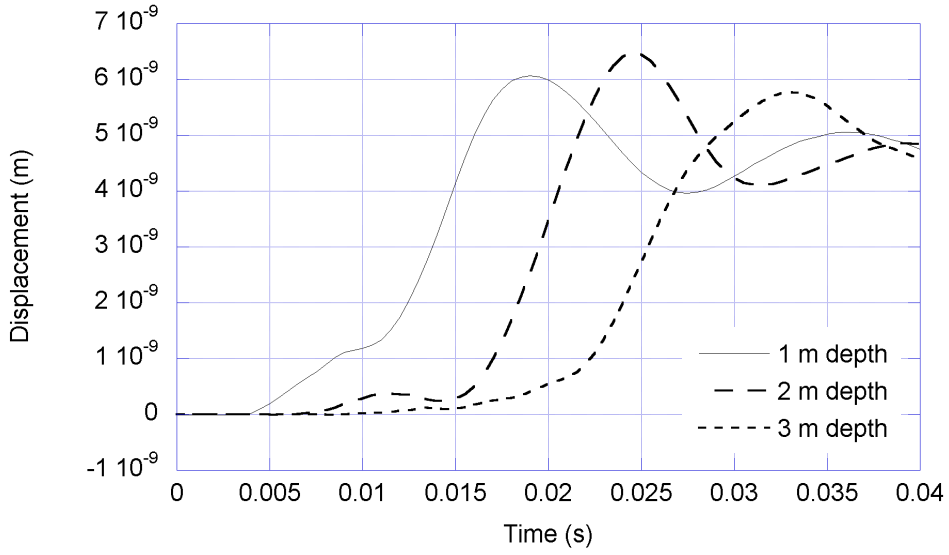

Figure 3.9 Displacement time histories in 3D unconstrained column

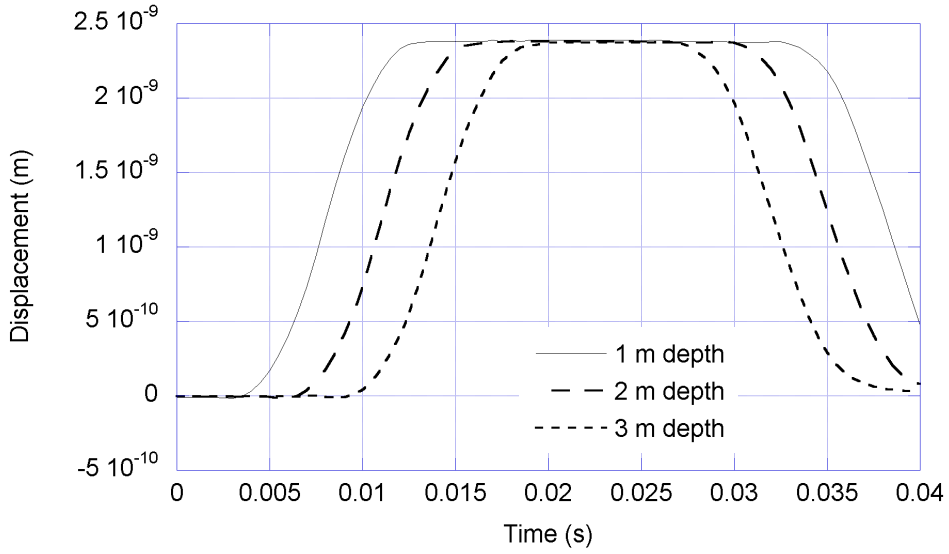

Figure 3.10 Displacement time histories in 3D constrained column

3.4. Dispersion Curves

As shown above, accurately measuring the first time of arrival of the waves would provide in all cases the velocity of propagation of P waves, and therefore the value of the constrained modulus of the material (if its density is known). In the field, identifying the arrival time may not be simple and it is preferred sometimes to use the dispersion curve, the variation of the phases between motions as a function of frequency, instead. The phases can be obtained from the ratio of the Fourier transforms of the motions (displacements, velocities or accelerations) recorded at two receivers. Alternatively one can obtain analytically or numerically the transfer functions between the motions at the two receivers under a steady state harmonic vibration. It should be noted, however, that in the case of a cylinder without any internal damping the transfer functions would be real and all points would be vibrating in phase under steady state conditions, implying that the computed phase differences would be zero for all frequencies. In practice the recorded motions are modified by application of a

window before finding their Fourier transforms. An exponential window was found to be particularly efficient in many situations (Bowen, 1992). Analytically, or numerically, this is equivalent to obtaining the transfer functions using the exponential window method as done for the study of the dynamic response of undamped systems through a solution in the frequency domain (Kausel and Roesset, 1992). The dispersion curve was used in all the cases of analyses presented here due to the benefit when using a limited range of frequency. To use cross-correlation, it is required to calculate the transfer function for a wide range of frequency.

3.4.1. Linear Media

Figure 3.11 shows the variation of the phases between the motions at the three receivers and the top of the column for the one dimensional model with free lateral boundaries while the results foe the column with a constrained boundaries are in Figure 3.12. The phases oscillate vary linearly with frequency. For the receiver at a depth of 1 m, the distance between two consecutive zero up-crossings corresponds to a wavelength. The difference in the frequencies between these two points corresponds then to the wave propagation velocity. For the receiver at 2 m the propagation velocity is equal to the frequency difference between three consecutive up-crossings, and for the receiver at 3 m it is the distance between four up-crossings. The first up-crossing for the first receiver, the second up-crossing for the second receiver and the third up-crossing for the third receiver happen all at the same frequency, resulting in a value of the propagation velocity of roughly 170 m/s for the free column and 331.7 m/s for the constrained one. If the phases were unfolded one would get straight lines with an equation of the form

$$\varphi = 360 \cdot d \cdot f / c_s \tag{3.3}$$

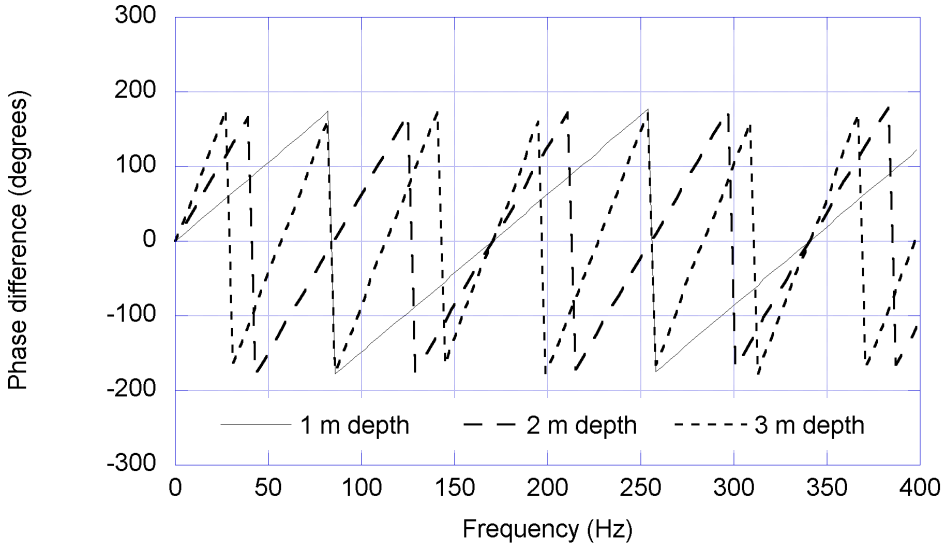

Figure 3.11 Phase differences of signals in 1D unconstrained column

where φ is the phase in degrees, d is the depth of the receiver, f is the cyclic frequency (in Hz), and c is the wave propagation velocity. Alternatively,

$$c = 360 \cdot d \cdot f/\varphi. \tag{3.4}$$

The computed phase differences between each of the three receivers and the surface are obtained with the third model (the core region modeled with finite elements and the far field reproduced through the consistent boundary matrix). The finite elements model used to computation is described in Figure 3.13. The rigid bottom boundary is placed 12 m below the surface to decrease its effect at this time. The results were calculated using different sizes of square mesh $\Delta L = 0.125, 0.0833, 0.0625\,\text{m}$ ($\Delta L = 1/8, 1/12, 1/16\,\text{m}$). The phase differences between the surface foundation and three different depths of 1 m, 2 m, and 3 m are presented in Figure 3.14 for the mesh size of 0.125 m over the range of frequencies of 10 Hz to 25 Hz. For this range of frequencies the plots are nearly, although not exactly, straight lines. The corresponding

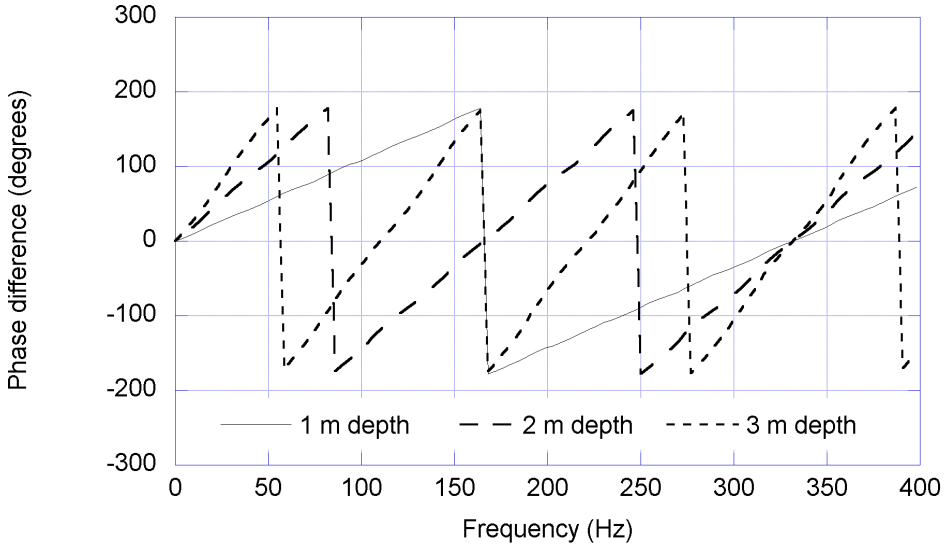

Figure 3.12 Phase differences of signals in 1D constrained column

wave propagation velocities are shown in Figure 3.15. They are nearly constant with frequency but have a small variation. The wave velocity tends to be higher under the center of the disk and at shallow depth. In addition, as could be expected, the wave propagation velocities are higher when the mesh size is coarser since the model is too stiff. Since the relation between wave velocity and mesh size appeared to be almost linear, wave velocities corresponding to mesh size were linearly extrapolated as shown in Figure 3.16, in an effort to minimize the effect of the mesh size. Under the center of the disk ($r = 0$), the average estimated wave velocities are about 225 m/s, 178 m/s, and 164 m/s corresponding to the first, second and third receiver, respectively. They are 211 m/s, 175 m/s, and 163 m/s under the mid point of the disk ($r = 0.5R$), and 177 m/s, 166 m/s, and 159 m/s under the edge ($r = R$), as shown in Table 3.1(a).

The results under the center of a uniformly distributed load, rather than a rigid disk, are presented in Figures 3.17 and 3.18 for the solution by numerical integration of Equation 3.2, and Figures 3.19 and 3.20 for using discrete Green's functions. While

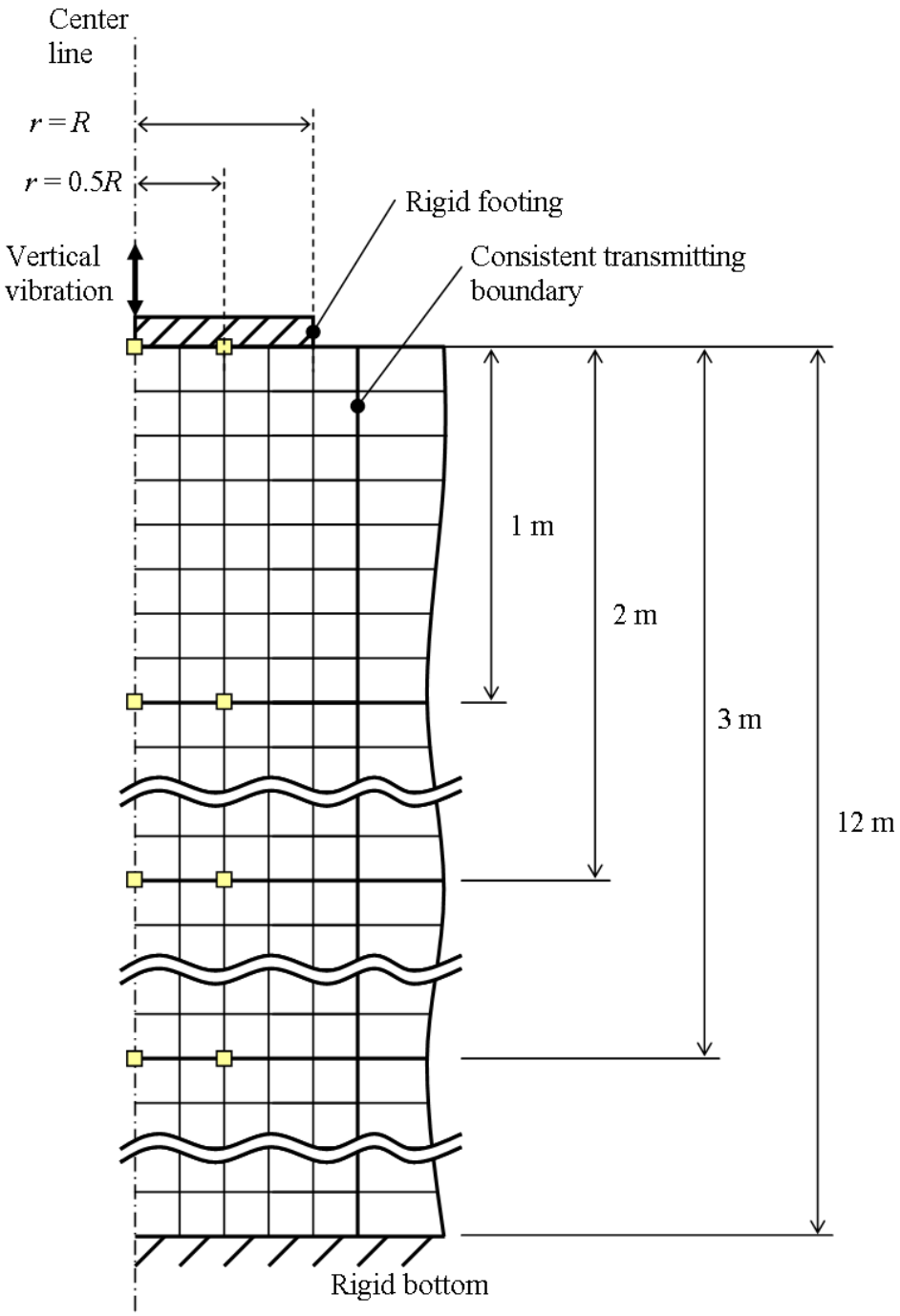

Figure 3.13 Description of finite elements model

the results of these two approaches are not identical, the estimates are very close. The first one yields average velocities over the range of frequencies considered of 204 m/s, 169 m/s and 159 m/s for the three receivers. The second gives values of 201 m/s, 169 m/s and 158 m/s. In both cases the velocity decrease with depth, being largest at the top (when considering the phase difference between the records at 1 m depth and the surface). The velocity estimates are slightly smaller than those resulting from the finite element model, although the trend is the same in all cases. The difference between the results from the first two formulations (analytical solutions) and the third (finite elements) one are due in part to the fact that the former consider a halfspace and a uniformly distributed load while the latter considers a layer of finite depth (12 m) on a rigid base and a load distributed by a rigid disk.

3.4.2. Nonlinear Media

In order to introduce a dependency of the modulus on the confining pressure and the shear strain in three dimensional medium, the shear modulus is assumed to increase due to an increase in mean stress and decrease due to an increase in the octahedral shear strain in this section. Initially the soil deposit has a shear wave velocity of 100 m/s and a Poisson's ratio of 0.45, corresponding to a P wave velocity of 331.66 m/s and a rod wave velocity of 170.29 m/s. The finite element analyses were conducted with sizes of square mesh $\Delta L = 0.125, 0.0833, 0.0625$ m ($\Delta L = 1/8, 1/12, 1/16$ m). In Figure 3.21, distributions of modified wave velocities due to the external force were calculated using finite element analysis, with mesh size ΔL of 0.125 m and the radius of disk of R =0.5 m. In this case, there are five elements in a layer in finite element model, whose distances r from the centerline to the center of elements of mesh are 0.125, 0.375, 0.625, 0.875, and 1.125 times of the radius R as shown in Figure 3.21(a). After the static load of 40 kN was imposed on the disk, the distribution of

Table 3.1 Wave velocities under rigid disk

(a) Linear medium

Depth	Center ($r = 0$)	Mid point ($r = 0.5R$)	Edge ($r = R$)
1 m	225	211	177
2 m	178	175	166
3 m	164	163	159

(unit: m/s)

(b) Nonlinear medium

Depth	Center ($r = 0$)	Mid point ($r = 0.5R$)	Edge ($r = R$)
1 m	237	221	181
2 m	176	173	164
3 m	161	159	156

(unit: m/s)

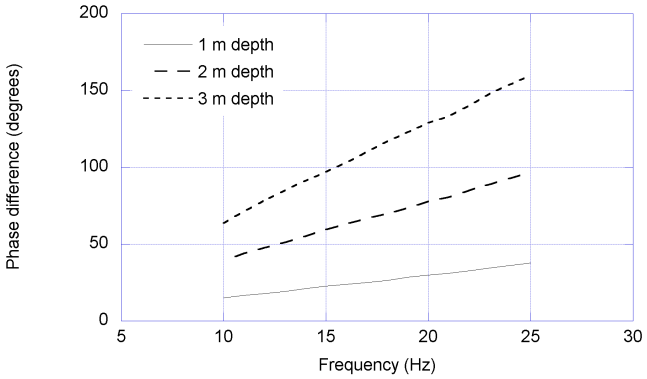

(a) Under center ($r = 0$)

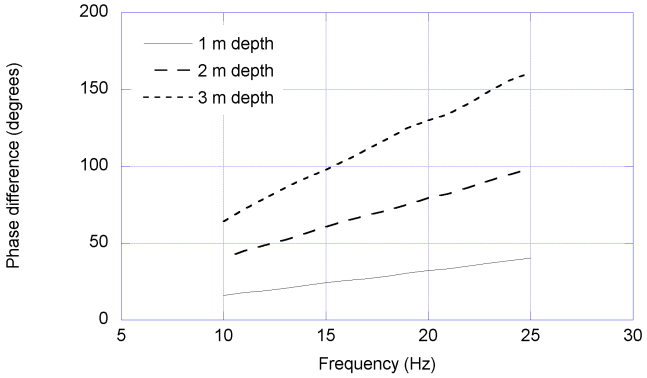

(b) Under mid point ($r = 0.5R$)

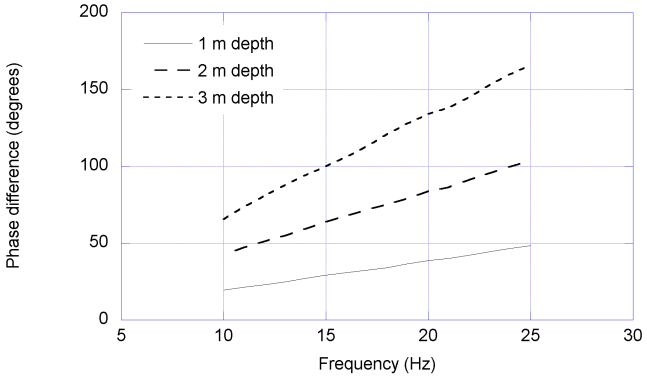

(c) Under edge ($r = R$)

Figure 3.14 Phase differences of signals under rigid disk using FE analysis ($\Delta L = 0.125$ m)

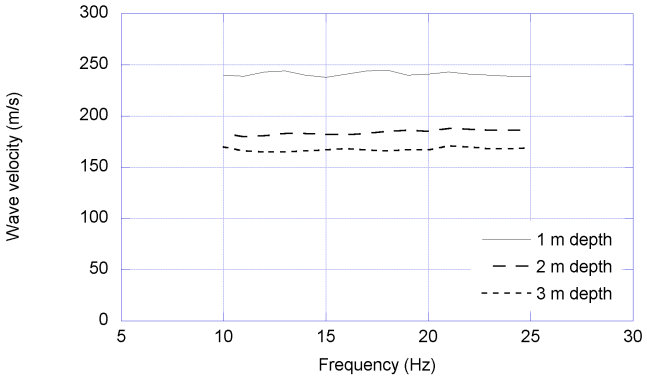

(a) Under center ($r = 0$)

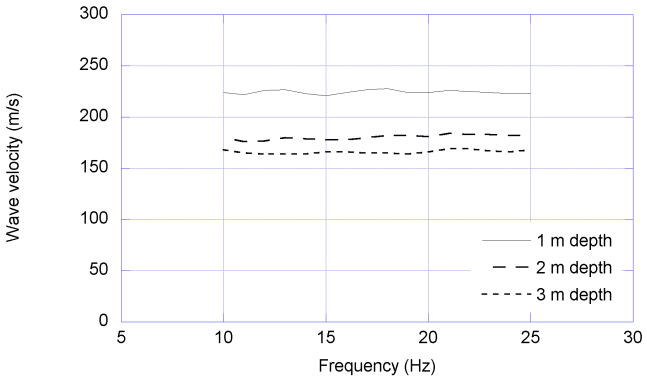

(b) Under mid point ($r = 0.5R$)

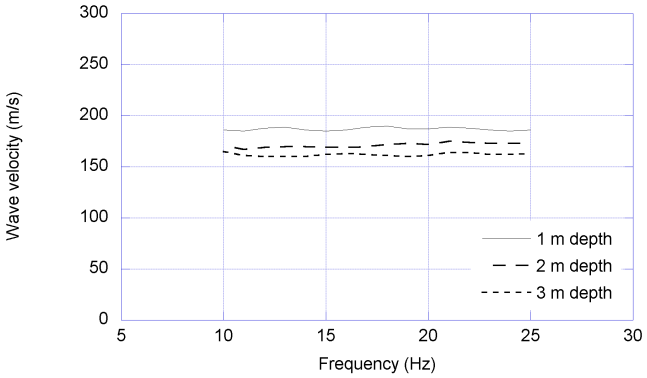

(c) Under edge ($r = R$)

Figure 3.15 Wave velocities under rigid disk using FE analysis ($\Delta L = 0.125$ m)

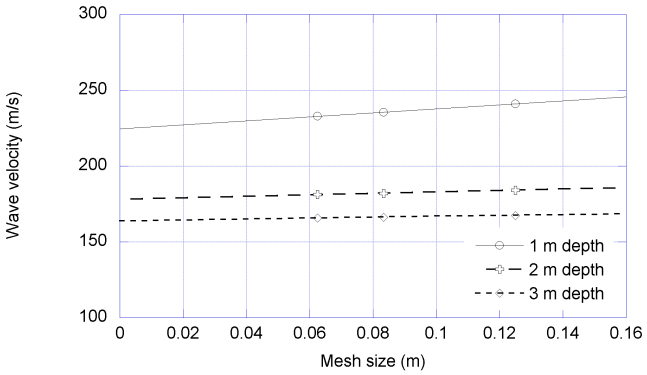

(a) Under center ($r = 0$)

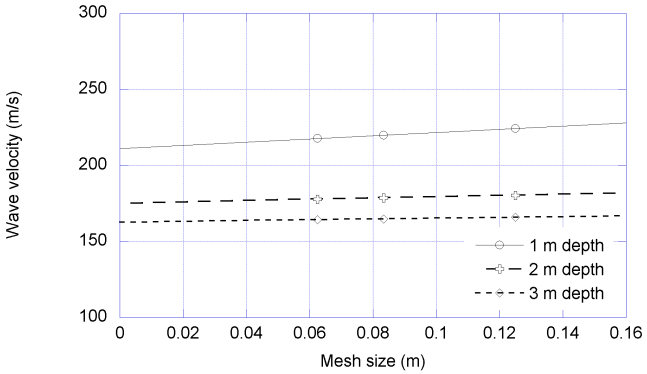

(b) Under mid point ($r = 0.5R$)

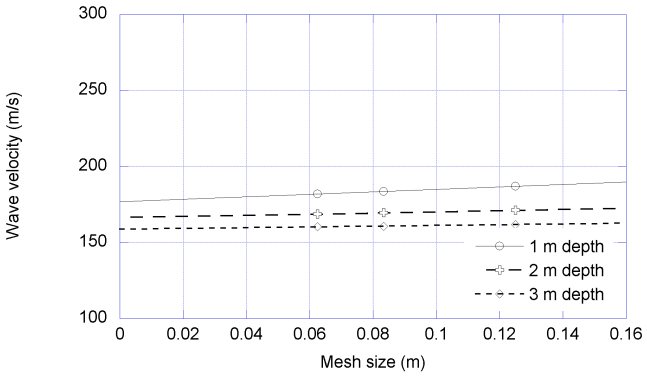

(c) Under edge ($r = R$)

Figure 3.16 Variation of wave velocities with mesh size

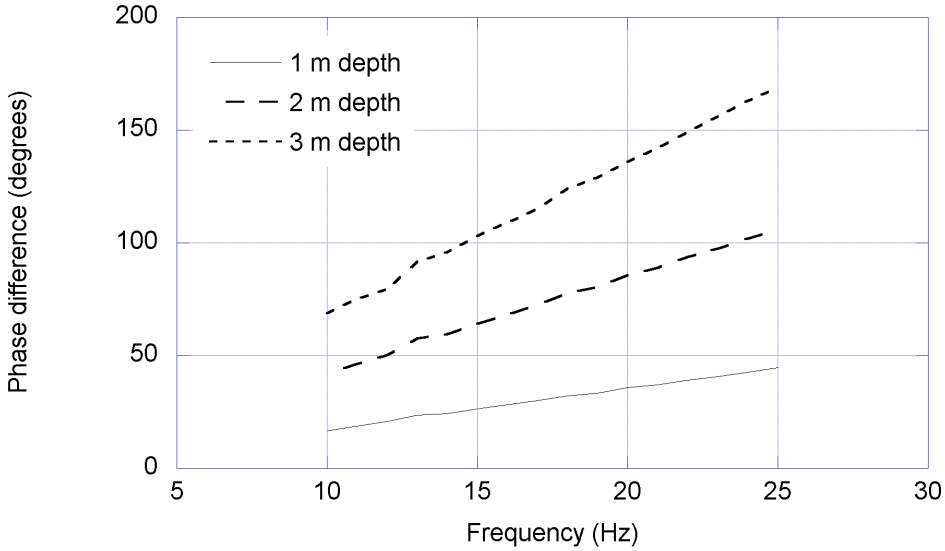

Figure 3.17 Phase differences of signals under loaded area using numerical integration of Equation 3.2

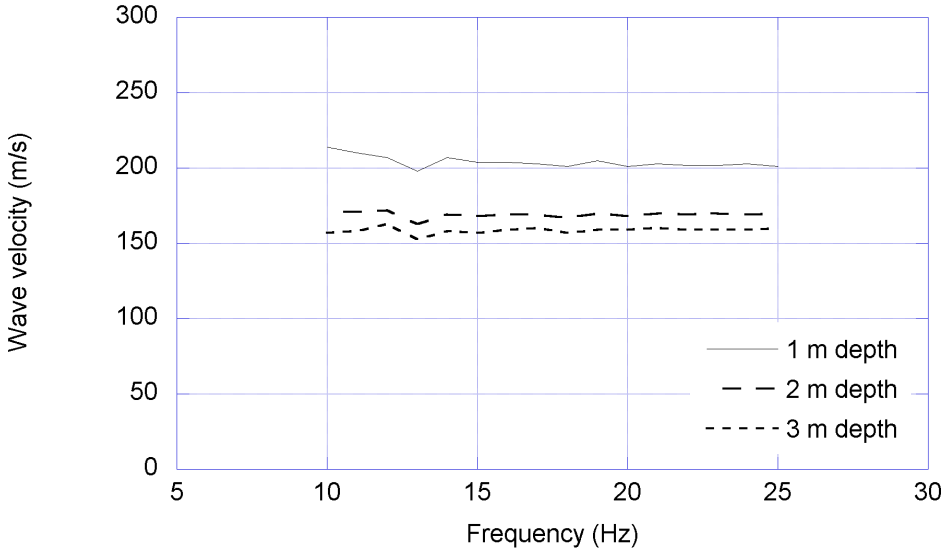

Figure 3.18 Wave velocities under loaded area using numerical integration of Equation 3.2

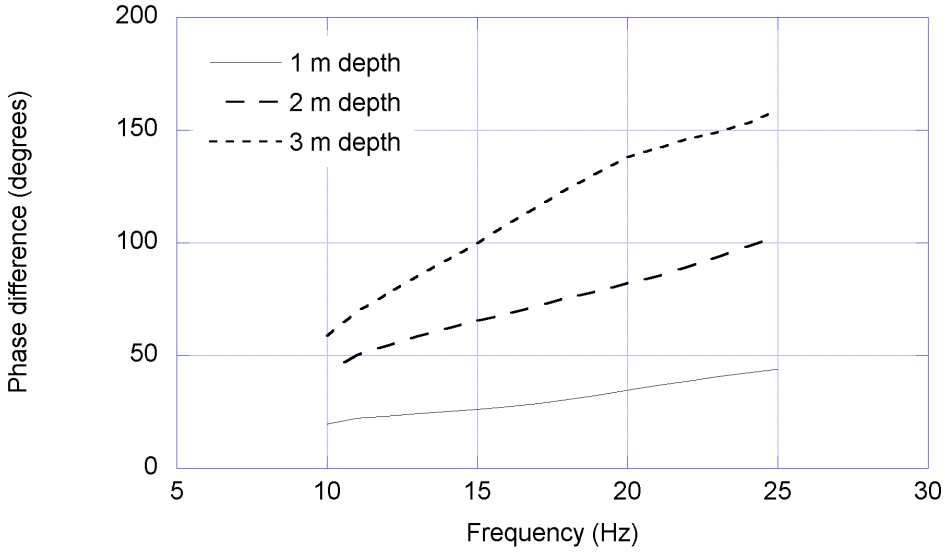

Figure 3.19 Phase differences of signals under loaded area using explicit Green's functions

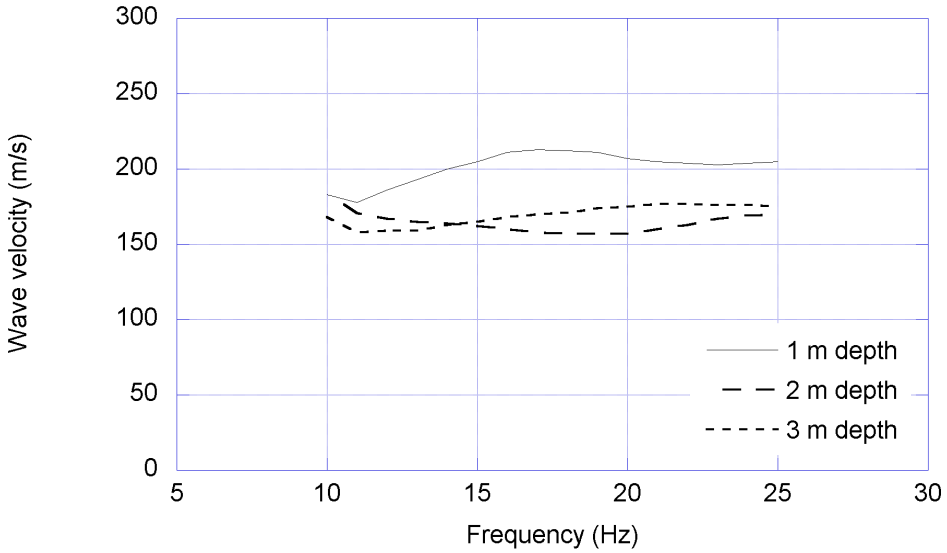

Figure 3.20 Wave velocities under loaded area using explicit Green's functions

the P and rod wave velocities in the finite element model changed as shown in Figure 3.21(b). The distribution of wave velocities after imposing a vertical dynamic load of amplitude 10 kN and frequency 25 Hz is presented in Figure 3.21(c). Less than five iterations were required to make outputs converge in this case, whereas more iterations may be necessary to simulate larger force amplitudes. The distribution of wave velocities for different loading frequencies are all similar to those shown, but only a small range of frequency, 10 Hz to 25 Hz, was analyzed. In the equivalent linear model, a linear analysis is repeated with updated inputs until outputs converge, and the results only depend on the final iteration. Since the equivalent linear model was used in the analyses, the results only depended on the wave velocities after the final iteration shown in Figure 3.21(c). For the assumed soil material and loading level, the wave velocities are higher than the initial values at very shallow depths and smaller below.

The phases differences and wave velocities using the finite element model with mesh size ΔL of 0.125 m are presented in Figures 3.22 and 3.23, respectively. The wave velocities at 1 m, 2 m, and 3 m depth were estimated at the three location, the center ($r = 0$), the mid point ($r = 0.5R$), and the edge ($r = R$) of the foundation. The estimates were 237 m/s, 176 m/s, and 161 m/s at $r = 0$, 221 m/s, 173 m/s, and 159 m/s at $r = 0.5R$, and 181 m/s, 164 m/s, and 156 m/s at $r = R$, using the extrapolation illustrated in Figure 3.24. The estimated results are presented in Table 3.1 with those of linear case. The trend is repeated here, that is, the wave velocity tends to decrease as the recording position gets far from the center of the disk. In the nonlinear case, the results also depend on the stiffness of the soil through which the waves propagate. For example, under the center of the disk ($r = 0$), the wave velocity at 1 m depth in the nonlinear medium is larger than that of the linear medium due to the higher modulus at shallow depth (see Figure 3.21(c)). However, at 2 m and 3 m

depths, the wave velocities are smaller than those of the linear case on the same basis. Similar tendency is observed at $r = 0.5R$ and $r = R$ for the assumed soil material and loading level.

3.5. Summary and Conclusions

Two analytical solutions, solutions using numerical integrations and explicit Green's functions, and a finite element model, with consistent transmitting boundary, were used to investigate the speed of traveling waves under a vertically excited surface foundation. The uniformly distributed load on a elastic halfspace was simulated using first two methods, and the rigid disk on a soil deposit with rigid bottom was simulated using the latter. The estimated wave velocities using different methods had consistent trends.

In a linear material, the results indicate that when the wave propagation velocities in the vertical direction are calculated from the phase differences between the vertical motions recorded at receivers placed at different depths the values obtained may change with location and also with frequency. These values will not correspond exactly to either the P wave velocity, associated with the constrained modulus of the material, nor to the rod velocity associated with Young's modulus. They tend to be between these two values but much closer to the latter.

In a nonlinear material, even though the wave velocities of material may change due to the characteristics of external loading, the estimated wave velocities also corresponded to the modified material properties.

It is thus necessary to exert some care when interpreting the data from field tests based on steady state vibrations.

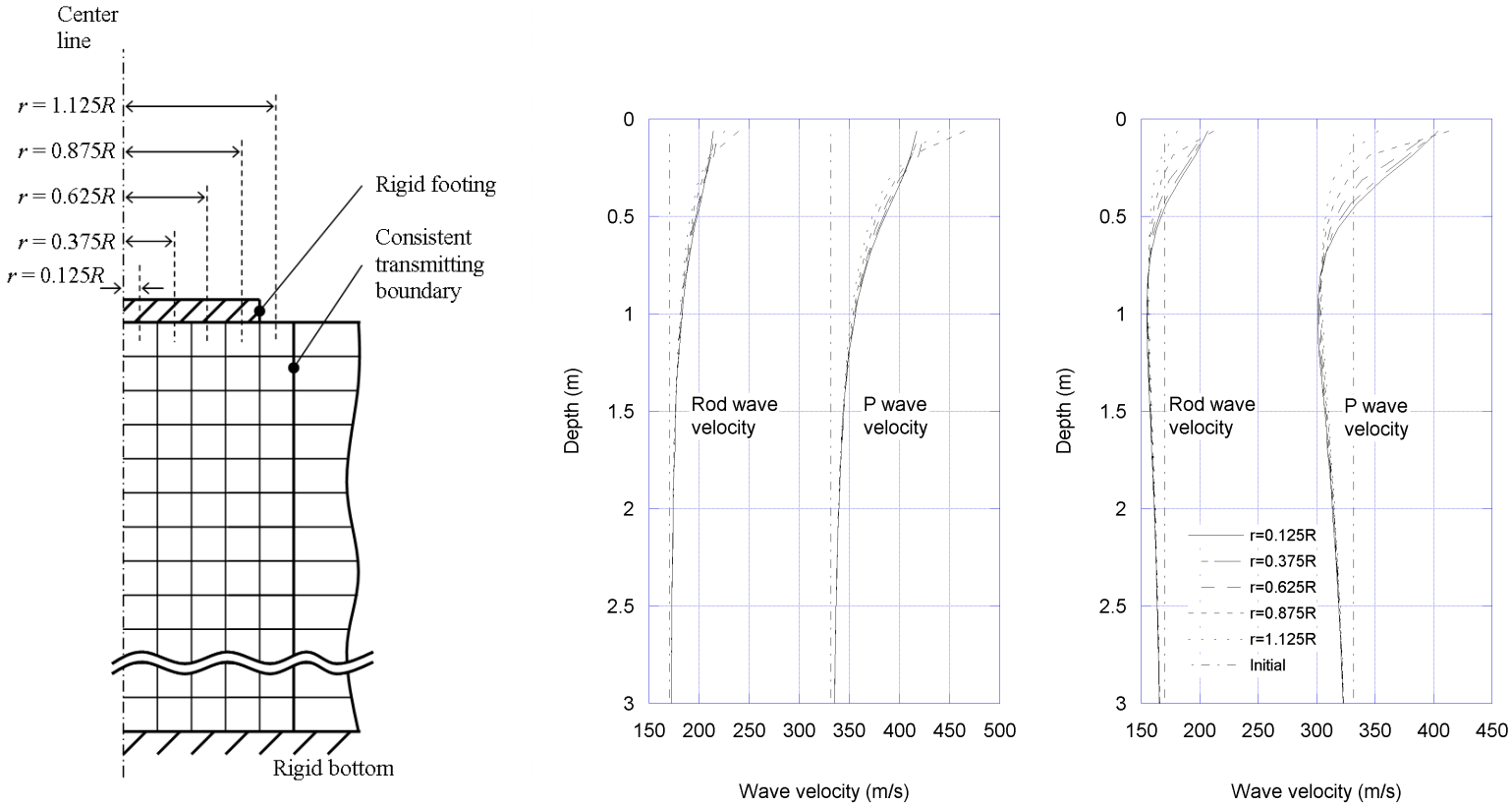

(a) Description of finite elements mesh (b) After imposing static load (c) After imposing dynamic load of 25 Hz

Figure 3.21 Distribution of wave velocities at each location ($\Delta L = 0.125$ m)

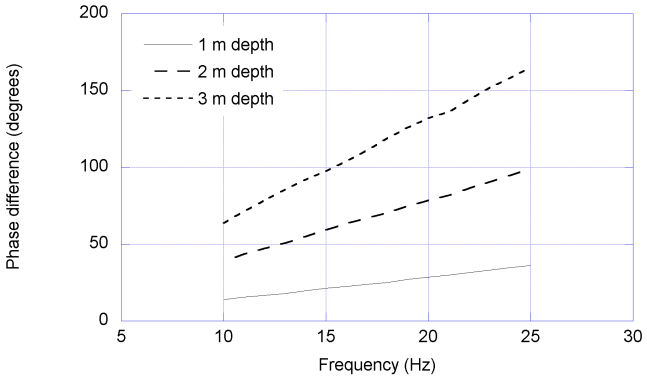

(a) Under center ($r = 0$)

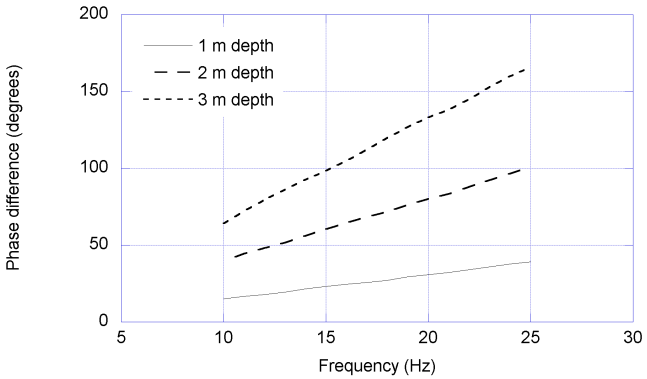

(b) Under mid point ($r = 0.5R$)

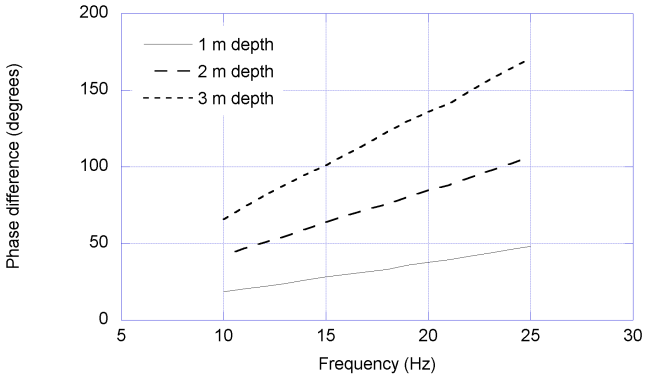

(c) Under edge ($r = R$)

Figure 3.22 Phase difference of signals under rigid disk ($\Delta L = 0.125$ m)

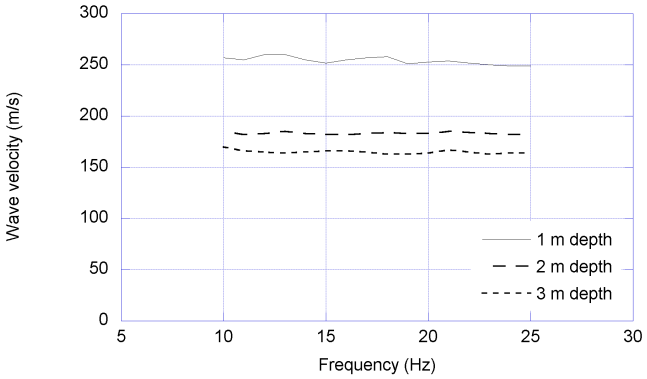

(a) Under center ($r = 0$)

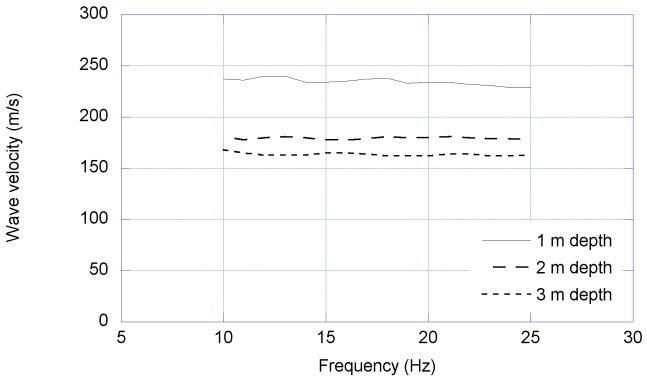

(b) Under mid point ($r = 0.5R$)

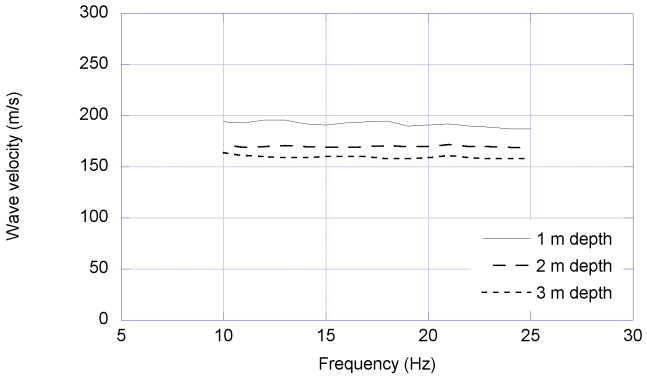

(c) Under edge ($r = R$)

Figure 3.23 Wave velocities under rigid disk ($\Delta L = 0.125$ m)

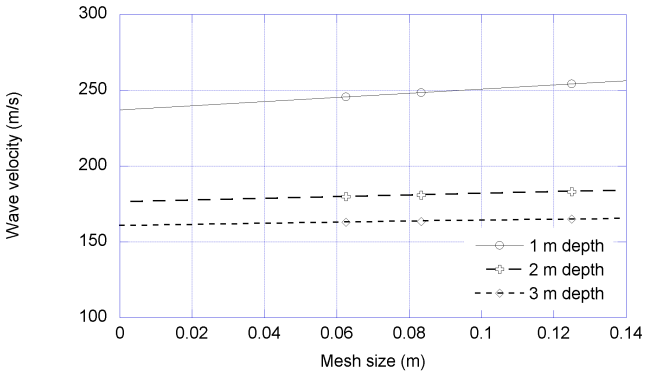

(a) Under center ($r = 0$)

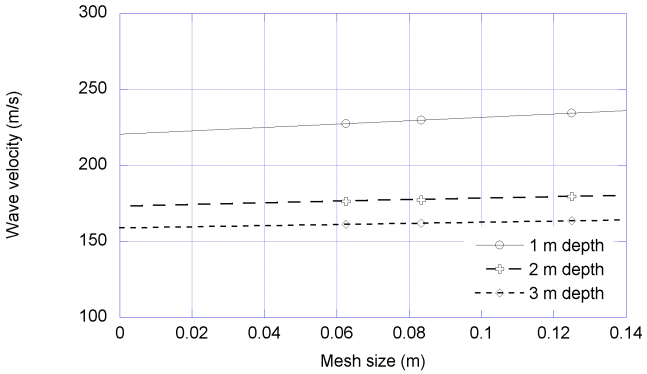

(b) Under mid point ($r = 0.5R$)

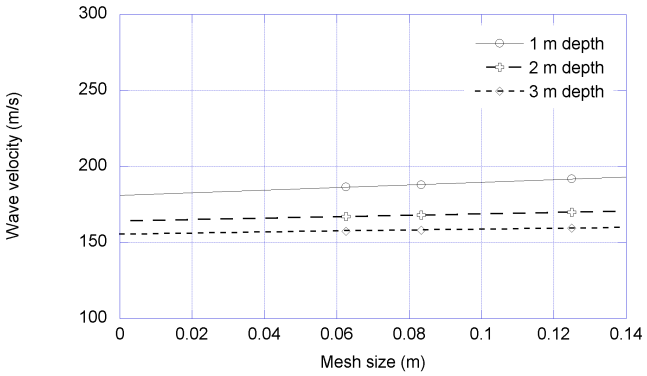

(c) Under edge ($r = R$)

Figure 3.24 Wave velocities corresponding to mesh size

CHAPTER IV

ESTIMATION OF NONLINEAR DYNAMIC SOIL PROPERTIES IN SITU

4.1. Introduction

In the field tests, a short impact or a harmonic excitation are applied on a surface foundation using a handheld hammer or a large scale shaker, after imposing a selected level of vertical static load. The responses of the soil and foundation are measured using geophones embedded in the foundation and in the soil deposit at several depths. If the travel time and length of a shear wave between two sensors in a soil deposit are known, the shear wave velocity can be evaluated. While, in principe, this is a simple way of interpreting the field test data, it requires very accurate reading of the travel time between closely placed geophones. The shear modulus estimated in this way is very sensitive to the reading of the travel time, since the modulus is inversely proportional to the square of this quantity. If the shape of the waves becomes irregular, it becomes more complicated to estimate the travel time consistently. On the other hand, we can use inverse analysis. If the amplitude of the force applied on the surface foundation and the amplitudes of the responses of the geophones are known, the soil modulus can also be estimated using a numerical model by matching the responses of the numerical simulation to the field measurements in the field. This method requires iterations to capture a set of soil moduli matching the response of the numerical simulation to the geophone measurements. One of the most appealing features of this method is the systematic and objective characteristic of the procedure. Amplitudes of responses can also be measured rather in straightforward manner than the phase lags. Moreover, estimated moduli are directly applicable to numerical simulations they are back-calculated using a numerical model.

The vertical or the horizontal harmonic excitation is applied on the surface foundation in the experiments. In the vertical tests, the input force is measured by a load cell placed on top of the foundation. Inverse analysis, which needs the input force, can be used to estimate shear moduli of the soil in this case. In the horizontal tests, however, shear waves are generated under the footing, and phase differences capture the shear wave velocity of the soil. The inverse analysis is not utilized in this case, because the horizontal force input could not be measured during horizontal tests.

The feasibility of estimating the internal damping ratios with the levels of strain using the inversion procedure is also discussed briefly.

4.2. Phase Difference Analysis

Shear wave velocities of propagating waves can be simply calculated from travel times and distances. In our experiments, the horizontal excitation at the footing generates shear waves traveling down to the geophones. Travel times of the waves under steady state can be estimated from either the peak-to-peak time difference Δt_p, or the time intervals between the zero-crossing points Δt_c as shown in Figure 4.1. Appropriate and consistent selection of travel times is required based on the condition and shape of the waveforms measured. The travel distance ΔL is directly measured from the field instrumentation as shown in Figure 4.2(a).

The horizontal excitation induces distortions in the soil deposit at the locations of the geophones, as illustrated in Figure 4.2(b), where u_1 and u_2 indicate the displacements of two geophones from the original location. By definition, the shear strain is the change in the angle formed by the relative positions of two sequential geophones. When the angle is small, the shear strain can be expressed as $\gamma = (u_1 - u_2)/\Delta L$. This definition is appropriate for the tests examined in this work and was used to

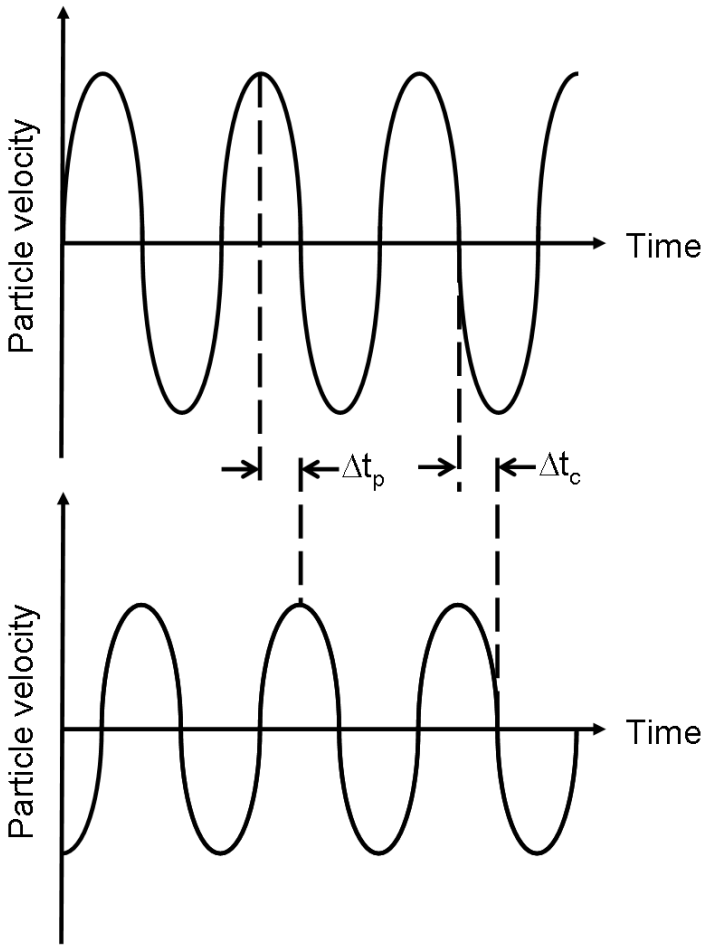

Figure 4.1 Measure of phase difference

estimate the strains during harmonic excitation..

4.3. Inverse Analysis

Inverse analysis aims at establishing a mathematical or numerical model of the system to be estimated based on the measured inputs and outputs. Once a model has been developed for the unknown system, the parameters of the model can be estimated by iteration until the calculated and measured outputs match for the selected inputs. In

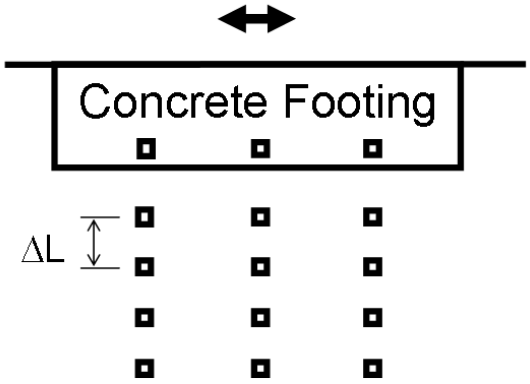

(a) Travel length of waves

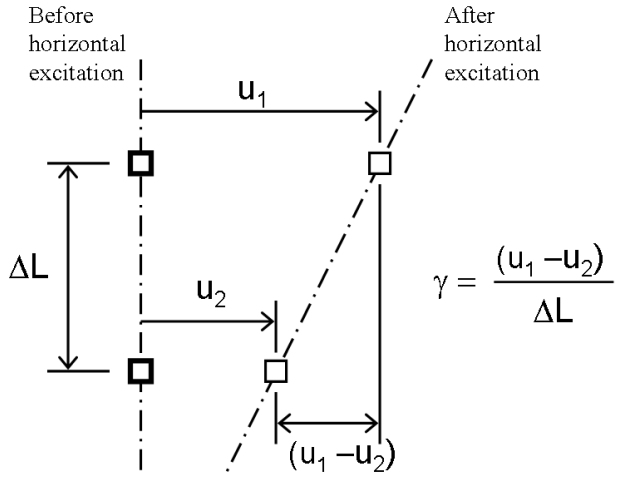

(b) Measure of shear strain

Figure 4.2 Calculation of shear strain

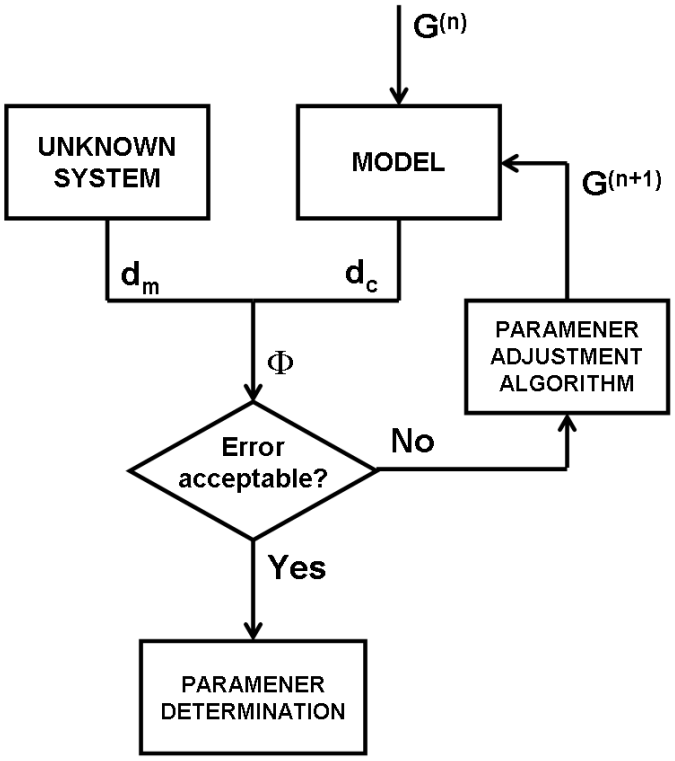

Figure 4.3 Procedure for inverse analysis

general, the forward problem involves calculating outputs of the system based on the established mathematical or numerical model with assigned model parameters. The inverse problem addresses the reverse procedure that estimates the model parameters based on measured data from the unknown system using a parameter adjustment algorithm. The general procedure for the inverse analysis is illustrated in Figure 4.3. In this study, $G^{(n)}$ denotes a set of shear moduli at the n^{th} iteration, d_m and d_c the displacement set measured from the field and calculated from the numerical model, respectively, and Φ the squared differences of d_m and d_c. The finite element model with the consistent transmitting boundary of Kausel (1974) is used for the forward problem, and a nonlinear least squares Levenberg-Marquardt method (Levenberg, 1944; Marquardt, 1963) for the parameter adjustment algorithm.

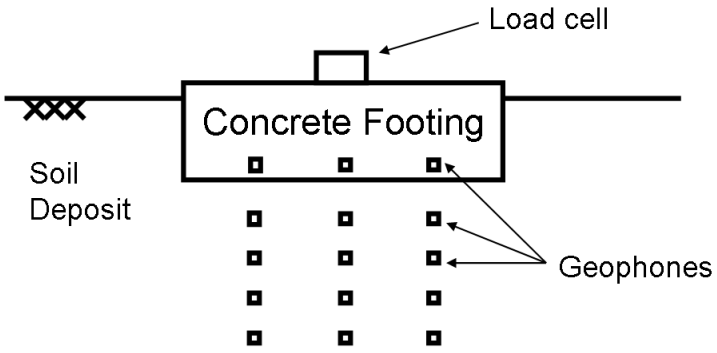

Figure 4.4 Unknown system

4.3.1. Unknown System

In this study, the unknown system corresponds to the surface foundation and soil deposit in Figure 4.4. The geophones are installed in and under the footing to investigate the response of the system. The amplitude of a vertical force imposed on the foundation is captured through a load cell placed on top of the footing. Details of the test setup are described in section 4.5.2.

4.3.2. Numerical Model

An axisymmetric finite element model with the consistent transmitting boundary (Kausel, 1974) was used to simulate the responses of the unknown system. The axisymmetric geometry saves calculational cost, but all the elements at a given radial distance should have the same material properties, which is a condition satisfied for the case of vertical excitations. If vertical excitation is imposed on the system, reduced soil moduli due to increases in shear strains will also be axisymmetric. The geometrical model is illustrated in Figure 4.5. A rigid surface foundation with radius R and mass m is placed on the soil, and the consistent transmitting boundary is used as the lateral boundary.

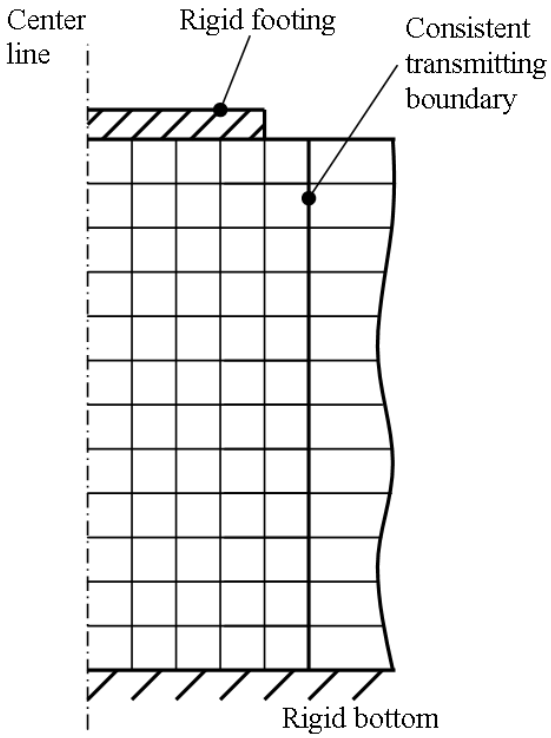

Figure 4.5 Numerical model for inverse analysis

4.3.3. Nonlinear Least Squares Formulation

As a parameter adjusting algorithm, a nonlinear least squares Levenberg-Marquardt method (Levenberg, 1944; Marquardt, 1963) was implemented for the inverse analysis. The principle of linear least squares and the modification for application to nonlinear systems are described in this section.

4.3.3.1. Linear Least Squares

Once a numerical model to represent the unknown system is selected, a backward procedure should be considered as an optimization problem to find a set of model parameters which best reproduces the measured quantities in the numerical simulation. The process starts with initial parameter estimates that are updated iteratively until the error is minimized. It is important to have a reasonable estimate for the initial model parameters. Appropriate initial estimates could be obtained from site investigation results such as the Spectral Analysis of Surface Waves (SASW) (Stokoe et al., 1994).

The amplitudes of displacements at the locations of the geophones are estimated using the numerical model and compared to the experimental values. If the error between the displacement amplitudes from the numerical simulations and the experiments becomes smaller than a selected threshold, the model parameters used at that iteration are considered the model parameters of the system. If the error does not meet the requirement, the model parameters are updated and new values are used to find another set of displacement amplitudes. In some cases, if the initial model parameters are not appropriate, the algorithm may not converge to an acceptable match. It is then necessary to use another set of initial model parameters. The linear least squares procedure for the estimation of shear moduli is presented following the

approach used by Foinquinos et al. (1993).

Define $\mathbf{G}^{(n+1)}$ and $\mathbf{G}^{(n)}$ as the vectors of shear moduli at the $(n+1)^{th}$ and n^{th} iterations. Changing shear moduli of the layers by a small amount $\Delta\mathbf{G}^{(n)}$ gives an updated set of moduli as

$$\mathbf{G}^{(n+1)} = \mathbf{G}^{(n)} + \Delta\mathbf{G}^{(n)}. \tag{4.1}$$

The objective of least squares is to estimate $\Delta\mathbf{G}^{(n)}$ and update $\mathbf{G}^{(n+1)}$ to minimize the error between the calculated and measured outputs. Let the measured amplitude of a displacement at location i be d_i^m, and the calculated amplitude for shear modulus values $\mathbf{G}^{(n+1)}$ as $d_i^c(\mathbf{G}^{(n+1)})$. The amplitude of the displacement at location i with the updated model parameters can be expressed by a Taylor series expansion as

$$\begin{aligned} d_i^c(\mathbf{G}^{(n+1)}) =& d_i^c(\mathbf{G}^{(n)}) + \sum_{j=1}^{N} \frac{\partial d_i^c(\mathbf{G}^{(n)})}{\partial G_j}\Delta G_j \\ &+ \sum_{j=1}^{N}\sum_{m=1}^{N} \frac{\partial^2 d_i^c(\mathbf{G}^{(n)})}{\partial G_j \partial G_m}\Delta G_j \Delta G_m + \cdots . \end{aligned} \tag{4.2}$$

Neglecting the terms of second and higher order results in a relative error between calculated and measured data

$$e_i^{(n+1)} = \frac{d_i^m - d_i^c(\mathbf{G}^{(n+1)})}{d_i^m} = e_i^{(n)} - \sum_{j=1}^{N} p_{ij}\Delta G_j \tag{4.3}$$

where p_{ij} represents $\{\partial d_i^c(\mathbf{G}^{(n)})/\partial G_j\}/d_i^m$. Defining the overall prediction error Φ as the sum of the squared differences (L_2 norm) gives

$$\Phi^{(n+1)} = \sum_{i=1}^{M}(e_i^{(n+1)})^2 = \sum_{i=1}^{M}[e_i^{(n)} - \sum_{j=1}^{N} p_{ij}\Delta G_j]^2. \tag{4.4}$$

To minimize the overall error with respect to one of the model parameters, for example

G_k, the partial derivative $\partial\Phi/\partial G_k$ gives

$$\begin{aligned}\frac{1}{2}\frac{\partial\Phi^{(n+1)}}{\partial G_k} &= \sum_{i=1}^{M}[e_i^{(n)} - \sum_{j=1}^{N} p_{ij}\Delta G_j]p_{ik} \\ &= \sum_{i=1}^{M} e_i^{(n)} p_{ik} - \sum_{j=1}^{N}[\sum_{i=1}^{M} p_{ij}p_{ik}]\Delta G_j = 0.\end{aligned} \tag{4.5}$$

The equation to obtain $\Delta\mathbf{G}$ can be represent in matrix form as

$$\mathbf{A}^{(n)}\Delta\mathbf{G}^{(n)} = \mathbf{g}^{(n)} \tag{4.6}$$

where

$$\mathbf{A}^{(n)} = \mathbf{P}^{(n)T}\mathbf{P}^{(n)} \tag{4.7}$$

$$\mathbf{P}^{(n)} = [p_{ij}] = [\frac{\partial d_i^c(\mathbf{G}^{(n)})}{\partial G_j}\frac{1}{d_i^m}] \tag{4.8}$$

$$\mathbf{g}^{(n)} = \mathbf{P}^{(n)T}\mathbf{R}^{(n)} \tag{4.9}$$

$$\mathbf{R}^{(n)} = [r_i] = [e_i^{(n)}] = [\frac{d_i^m - d_i^c(\mathbf{G}^{(n)})}{d_i^m}]. \tag{4.10}$$

$\mathbf{P}^{(n)}$ is the matrix of partial derivatives at the n^{th} iteration with component p_{ij} for $i = 1$ to M and $j = 1$ to N, and $\mathbf{R}^{(n)}$ is the relative error vector at the n^{th} iteration with component r_i for $i = 1$ to M.

The solution to Equation 4.6, $\Delta\mathbf{G}^{(n)}$, can be introduced in Equation 4.1 to obtain the updated modulus $\mathbf{G}^{(n+1)}$ for the next iteration. The process is repeated until the sum of squares $\Phi^{(n+1)}$ is minimized or drops below a certain level of tolerance.

If the system shows high nonlinearity, it is helpful to correct $\mathbf{G}^{(n+1)}$ by only a fraction of $\Delta\mathbf{G}^{(n)}$. Otherwise, the extrapolation may be beyond the point where the system can be adequately represented by Equation 4.2. Various methods have been used to determine an appropriate step size, $K\Delta\mathbf{G}$, to avoid divergence, where $0 < K \leq 1$. Even so, failure to converge is not uncommon (Marquardt, 1963).

4.3.3.2. Levenberg-Marquardt Method

Since the properties of gradient methods are not scale invariant, it is necessary to scale variables in some convenient manner. In this study, following Marquardt (1963), a scaled matrix $\mathbf{A}^*$ and a scaled vector g^* are defined as

$$\mathbf{A}^* = [a_{ij}^*] = [\frac{a_{ij}}{\sqrt{a_{ii}}\sqrt{a_{jj}}}] \tag{4.11}$$

$$\mathbf{g}^* = [g_i^*] = [\frac{g_i}{\sqrt{a_{ii}}}]. \tag{4.12}$$

Equation 4.6 becomes then

$$\mathbf{A}^* \Delta \mathbf{G}^* = \mathbf{g}^*. \tag{4.13}$$

Then, $\Delta \mathbf{G}$ is calculated as

$$\Delta \mathbf{G} = [\Delta G_i] = [\frac{\Delta G_i^*}{\sqrt{a_{ii}}}]. \tag{4.14}$$

In the Levenberg-Marquardt method, the search direction is defined by

$$(\mathbf{A}^{*(n)} + \lambda \mathbf{I}) \Delta \mathbf{G}^{*(n)} = \mathbf{g}^{*(n)}. \tag{4.15}$$

When $\Delta \mathbf{G}^{*(n)}$ is solved, Equation 4.14 is used to obtain $\Delta \mathbf{G}^{(n)}$. The new trial vector estimated from Equation 4.1 will lead to a new sum of squares $\Phi^{(n+1)}$. It is essential to select $\lambda^{(n)}$ such that

$$\Phi^{(n+1)} < \Phi^{(n)}. \tag{4.16}$$

The optimized $\Delta \mathbf{G}^{(n)}$ is calculated following a systematic algorithm $\Phi^{(n)}$ being the sum of squares from linear least squares ($\lambda = 0$), and $\Phi(\lambda^{(n-1)})$ and $\Phi(\lambda^{(n-1)}/\nu)$ the sum of squares with $\lambda = \lambda^{(n-1)}$ and $\lambda = \lambda^{(n-1)}/\nu$, respectively. The algorithm is illustrated below step-by-step:

- Let $\nu > 1$. Say $\nu = 10$.

- Let $\lambda^{(n-1)}$ denote the value of λ from the previous iteration. Initially let $\lambda^{(0)} = 10^{-2}$.

- Compute $\Phi(\lambda^{(n-1)})$ and $\Phi(\lambda^{(n-1)}/\nu)$.

- If $\Phi(\lambda^{(n-1)}/\nu) \leq \Phi^{(n)}$, let $\lambda^{(n)} = \lambda^{(n-1)}/\nu$.

- If $\Phi(\lambda^{(n-1)}/\nu) > \Phi^{(n)}$, and $\Phi(\lambda^{(n-1)}) \leq \Phi^{(n)}$, let $\lambda^{(n)} = \lambda^{(n-1)}$.

- If $\Phi(\lambda^{(n-1)}/\nu) > \Phi^{(n)}$, and $\Phi(\lambda^{(n-1)}) > \Phi^{(n)}$, increase λ by successive multiplication by ν until for some smallest w, $\Phi(\lambda^{(n-1)}\nu^w) \leq \Phi^{(n)}$. Let $\lambda^{(n)} = \lambda^{(n-1)}\nu^w$.

4.3.4. Proposed Inversion Method

Several sets of preliminary analyses were performed to determine an inversion scheme which would work well for the selected problem. A setup of the numerical model used for the proposed inverse analysis method is illustrated in Figure 4.6. In the procedure, the soil deposit was divided into six layers - Layers 1, 2, 3, and 4, a Transition Layer, and a Bottom Layer. In field tests, data are only obtained in the vicinity of the foundation, where geophones are installed, but the soil properties of the deepers layer will affect the responses at shallow depth. Therefore, it is necessary to have at least some information, even if approximate, for the soil moduli at deeper levels in order to estimate the moduli of Layers 1, 2, 3, and 4. The profile of the small strain shear modulus for the Bottom Layer can be estimated from geophysical methods such as the SASW. It is also necessary to assign a normalized shear modulus (G/G_{max}) variation with strain at the Bottom Layer. A G/G_{max} experimental curve for the specific soil type is selected. The shear moduli of Layers 1, 2, 3, and 4 are estimated using the Levenberg-Marquardt method. To minimize the effect of the G/G_{max} curve approximation for the Bottom Layer on the estimated shear moduli

for Layers 1, 2, 3, and 4, the Transition Layer was set up for a selected height. In section 4.4.1, various sets of parametric studies were carried out to investigate the performance of the proposed inversion method under several assumption. For a given response, there can be more than one valid combination of shear moduli and damping. In other words, the values of shear moduli and damping are not necessarily unique. Only one of these sets, shear moduli or damping, can be estimated and the other one must be assumed. The damping curve was assumed for the entire region of the numerical model in order to estimate the shear moduli. On the other hand, the damping curve could be estimated if the shear modulus reduction curve was known, which will be discussed later in section 4.4.2.

The strategy to estimate nonlinear shear moduli in the vicinity of the surface foundation overcoming the shortage of information at deep layers, where geophones do not exist, consist of a number of steps, illustrated below:

1. Assign the damping curve for the entire region of the numerical model.

2. Assign G_{max} from the SASW tests of the Bottom Layer. Assume G/G_{max} for the Bottom Layer using appropriate curves from literature.

3. Iterate updating shear moduli at Layers 1, 2, 3, and 4, and the Transition Layer until calculated displacements match the measured response. Five measurements either at center or mid point are used.

4. Update damping ratios at all elements and shear moduli of the Bottom Layer based on the octahedral shear strain generated in the current iteration.

5. Repeat steps 3 and 4, until the material properties converge.

6. Determine the shear wave velocities at Layers 1, 2, 3, and 4. Convert estimates to shear moduli.

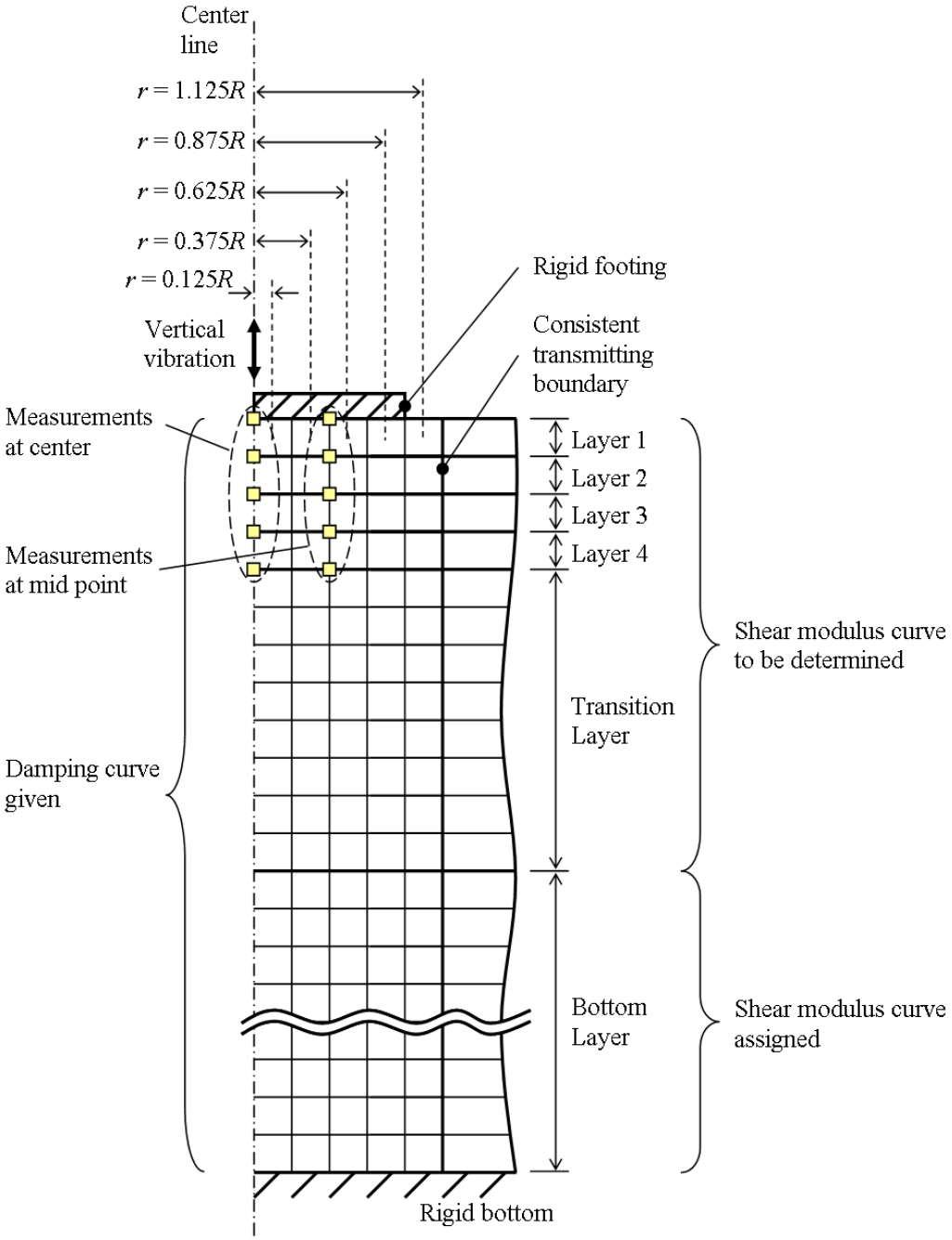

Figure 4.6 Configuration of proposed inversion method

4.4. Validation of Inversion Method

Several sets of parametric studies were performed to investigate the validity of the proposed inversion procedure and to refine the method for the estimation of the shear moduli and damping ratios with levels of shear strain.

4.4.1. Estimation of Nonlinear Shear Moduli

The proposed inversion procedure to estimate the nonlinear shear moduli was validated first. The dynamic responses of the locations where geophones were embedded were simulated using the finite element code with an equivalent-linear model. In the equivalent-linear model, the secant shear moduli are updated based on the reference strains until the response converges (Kramer, 1996). The octahedral shear strain was used as a reference strain. The consistent transmitting boundary was placed, at a distance of 2.5 times the radius of the footing from the edge of the footing to simulate the changes in material properties at the sides of the footing. Then, the shear moduli of the soil layers were back-calculated using the proposed inversion method to check if they matched the baseline. Different sets of shear wave velocity profiles, locations of the particle velocities measurements, normalized modulus reduction curves assumed for the Bottom Layer, and internal damping values were used for the inverse analysis. The effects of various properties on the estimated shear moduli were investigated. In the numerical model, shear wave velocity, damping, density, and Poisson's ratio are material property inputs. In all cases, values of density and Poisson's ratio of 1900 kg/m^3 and 0.2 were used, respectively. A footing radius of 0.457 m and a loading frequency of 50 Hz was used for all analyses. The size of mesh of 0.114 m$\times$0.128 m, fine enough considering wave lengths of propagating waves through finite elements, was used. In the model, there are five finite elements in a layer whose distances r

from the centerline to the centers of element are 0.125, 0.375, 0.625, 0.875, and 1.125 times of the radius R as shown in Figure 4.6. Using the inverse analysis, shear wave velocities were estimated and converted to shear moduli. In this chapter, the terms shear wave velocity and shear modulus are used interchangeably.

4.4.1.1. Effect of Shear Wave Velocity Profile

The distribution of the shear wave velocity in a soil deposit varies due to the soil type or the history of deposition. The confining stresses in the soil deposit also contribute to a nonuniform distribution of the modulus (Janbu, 1963). To investigate the effect of initial distribution of shear wave velocity, and therefore shear modulus, on the back-calculation of soil shear moduli using the proposed inverse analysis procedure, soil deposits with four different shear wave velocity distributions were considered. The initial distributions of the shear wave velocity for four cases - S1, S2, S31 and S32 - are presented in Figure 4.7 with division of layers. For the case S1, the shear wave velocity was assumed to be uniform throughout depth. A value of the shear wave velocity of 200 m/s was used for the whole soil deposit. For the case S2, the shear wave velocity was increased at shallow depth to simulate the effect of an initial static force on the footing, and decreased to a constant value of 200 m/s at greater depth. Changes in the shear wave velocities due to the static load occur horizontally as well as vertically. In Figure 4.7(b), shear wave velocities were averaged at the same depth under the footing to represent a single value for each depth. For the cases S31 and S32, to simulate the variation of shear wave velocity in the field, the shear wave velocities increased step-wise with depth, only at the Bottom Layer, with the variation more prominent for case S32. The vertical displacement amplitudes from geophones at and under the center of the footing were used to estimate the material properties.

When the modulus is estimated using the proposed inversion method, only a

single value of modulus is obtained for a layer but the shear strain varies along that layer. It is necessary to determine the reference strain which the shear modulus is plotted against. To find out what location of shear strain in a layer corresponds to the estimated modulus for the layer, estimated and baseline shear wave velocities were compared. (In the inversion method, shear wave velocities are is estimated and they need to be converted to shear moduli.) In the finite element model used for the inverse analysis, each layer has five finite element elements as shown in Figure 4.6, where the distance r from the centerline to the center of each element is presented in terms of the radius of footing R. The octahedral shear strain calculated at one of five finite elements in each layer whose baseline wave velocity is closest to the estimated wave velocity was selected as the reference strain. In Table 4.1, sample results of estimated and baseline wave velocities for case S31, using a dynamic amplitude of 10000 kN and outputs at the footing center, are presented. For the Layers 1, 2, and 3, estimated wave velocities are most close to baselines for elements at $r = 0.875R$. For the Layer 4, the baseline for the column at $r = 0.625R$ is most close one to the estimated wave velocity. But, the baseline value at the column at $r = 0.875R$ is only 0.3 % larger than the baseline for the the column at $r = 0.625R$ that the baseline at $r = 0.875R$ is also well represented by the estimate. The discrepancy between estimated and baseline wave velocities become larger at farther layer from the surface. The trends observed here were also observed for all the cases S1, S2, S31, and S32 for different levels of dynamic force amplitude. Overall, estimated wave velocities were most close to baselines for the column at $r = 0.875R$, and shear strains calculated at finite elements for the column at $r = 0.875R$ were selected as reference strains.

In Figure 4.8, back-calculated nonlinear shear moduli are plotted against octahedral shear strains for the Column 4. The plots are compared to the baseline curve,

Table 4.1 Estimated and baseline shear wave velocities for case S31 with force amplitude 10000 kN

		Layer 1	Layer 2	Layer 3	Layer 4
Estimated shear wave velocity (m/s)		174.74	175.26	173.70	172.17
Baseline shear wave velocity (m/s)	$r = 0.125R$	184.43	182.02	179.27	178.03
	$r = 0.375R$	183.29	180.76	178.31	177.77
	$r = 0.625R$	180.54	177.97	176.91	177.63
	$r = 0.875R$	172.64	174.54	176.21	178.10
	$r = 1.125R$	167.19	173.82	177.44	179.44

which the estimated properties are supposed to match. For the case of S1, the estimated shear moduli at Layers 1 and 2 match closely the baseline as shown in Figure 4.8(a). However, the moduli estimated at Layers 3 and 4 show some discrepancy from the baseline as the shear strain increases, which was also observed in Table 4.1. For Layers 3 and 4, the deviation of the estimated moduli from the baseline is up to about 5 % and 9 %, respectively, of the maximum modulus 76 MPa for the range of shear strain tried. The reason for this discrepancy is probably only a single value of modulus is assigned to the whole Transition Layer in the proposed inversion method, whereas each element has a different modulus due to the different level of shear strain in the numerical simulation. Case S2 is the only case which has varying modulus for Layers 1, 2, 3, and 4. For this case, in Figure 4.8(b), the baseline shear modulus is larger close to the surface due to the confining stress (see Figure 4.7(b)). The estimated shear moduli for Layers 1 and 2 still show a remarkable match to the baselines, while those of Layers 3 and 4 show again some variation which was up to about 3 % and 6 %, respectively, of the maximum modulus of each layer. The same trend is

present for the S31 case as observed in Figure 4.8(c). Better matchs are observed at Layers 1 and 2 than at Layers 3 and 4. The deviation of Layers 3 and 4, in this case, was up to about 4 % and 9 %, respectively, of the maximum shear modulus 76 MPa. For the S32 case, the estimated moduli match well the baseline at low strain levels, but begin to underestimate the modulus when the strain gets larger than 5×10^{-3} % at all the layers. The largest deviation observed was 15 % of the maximum shear modulus 76 MPa at the Layer 4 for the strain of 6.8×10^{-3} %. The discrepancy is considered, again, due to the approximation in the Transition Layer in Figure 4.6. The suggested procedure worked best for the back-calculation of shear moduli in the vicinity of the surface foundation with the soil deposit which has low to moderate variation of soil modulus.

4.4.1.2. Effect of Measurement Location

In this section, the validity of proposed inversion method using data measurements at different locations was studied. The displacement amplitudes were calculated at and under the mid point, between the center and the edge of the footing and used for the inverse analysis instead of the measurements at the center. The analyses were conducted as in the previous section. The results in Figure 4.9 show the exactly same trends, with the same deviations, of the previous case using measurements at the center. For the cases S1, S2, and S31, the estimations at Layers 1 and 2 were very accurate, whereas discrepancies were observed at Layers 3 and 4. For the case S32, the moduli were underestimated at strain levels higher than 5×10^{-3} %. Using the measured displacement amplitudes at mid points resulted in the same accuracy observed with the measurements at the center.

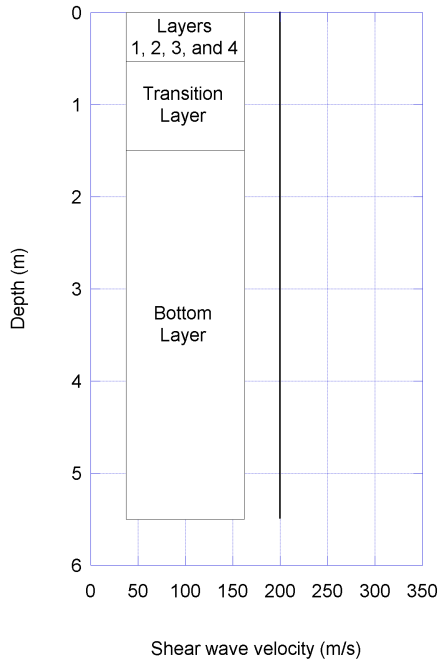

(a) Case S1

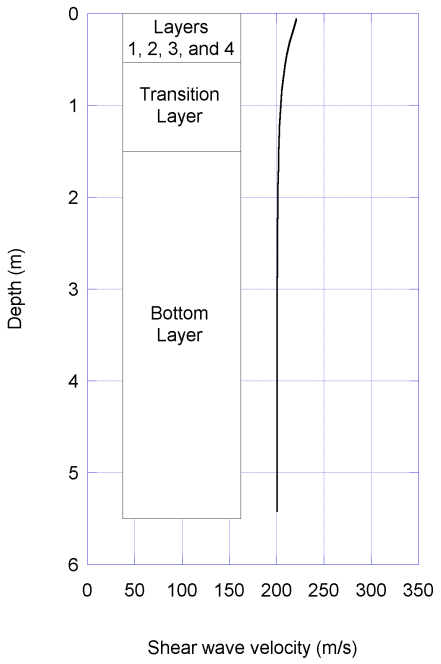

(b) Case S2

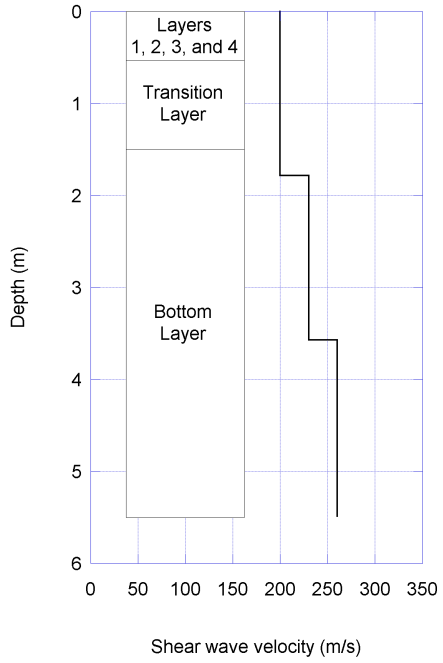

(c) Case S31

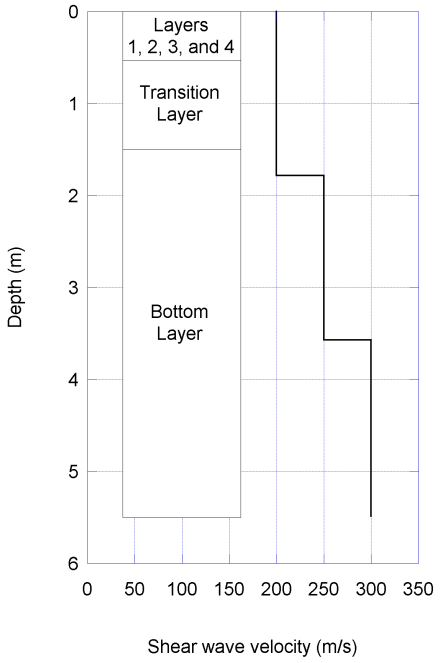

(d) Case S32

Figure 4.7 Shear wave velocity profiles used for inverse analysis

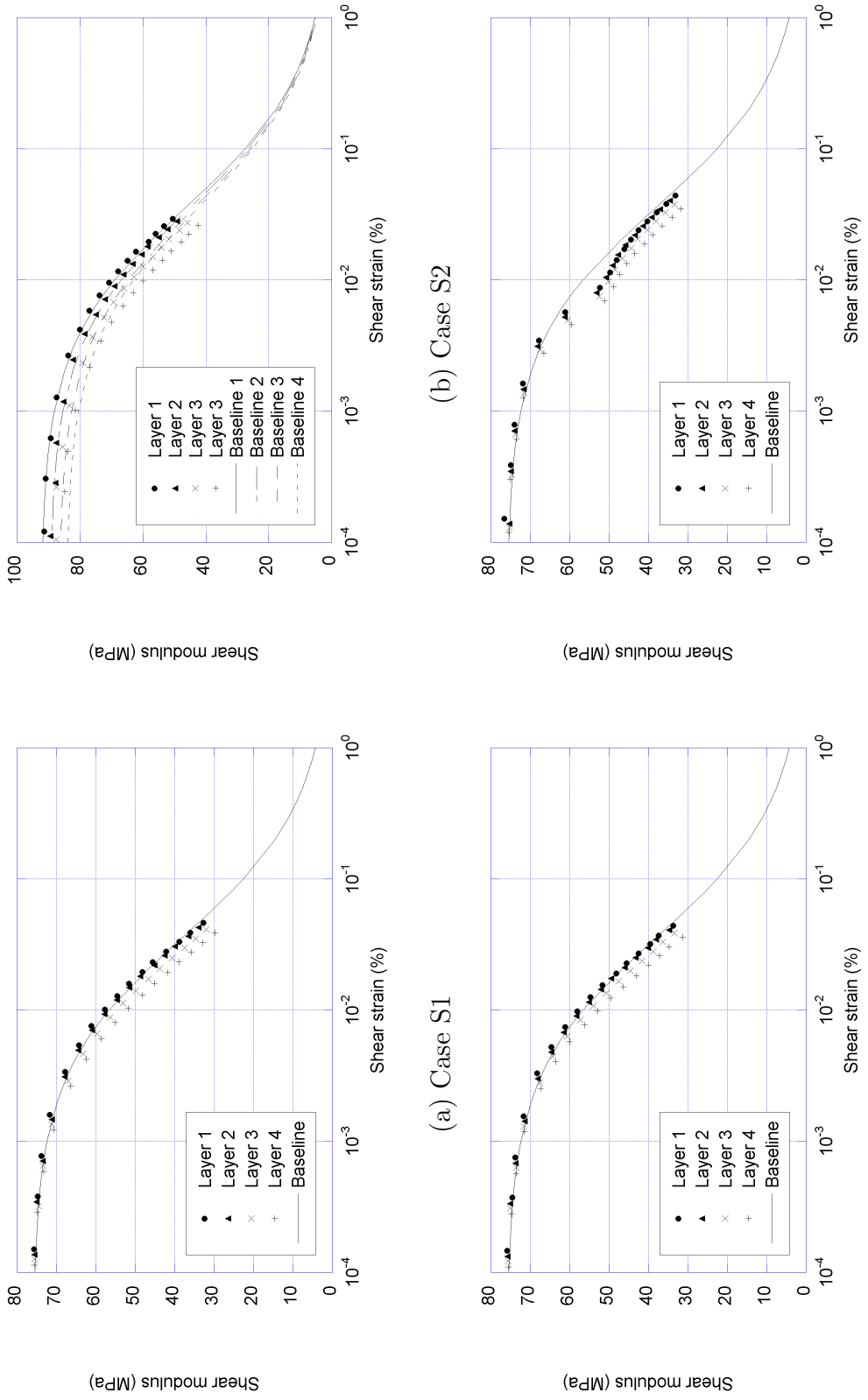

(a) Case S1 (b) Case S2

(c) Case S31 (d) Case S32

Figure 4.8 Estimated shear modulus reduction curves from measurements at center

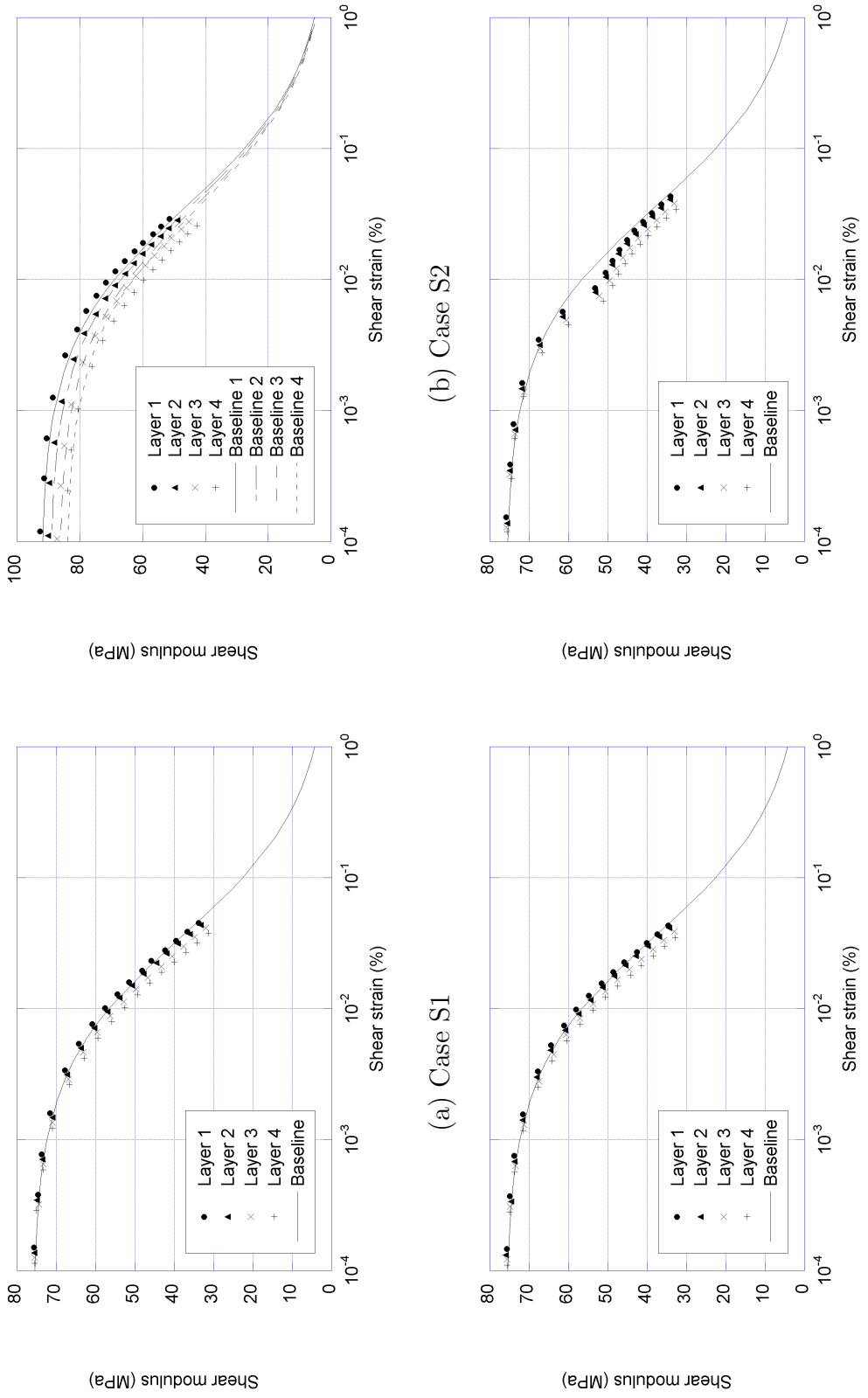

(a) Case S1 (b) Case S2

(c) Case S31 (d) Case S32

Figure 4.9 Estimated shear modulus reduction curves from measurements at mid point

4.4.1.3. Effect of Modulus Reduction Curve

The shear wave velocity profile of the Bottom Layer can be estimated conducting a SASW test ahead of the main experimental program. The normalized shear modulus G/G_{max} reduction curve still would have to be assumed at the Bottom Layer in the proposed inverse analysis. The effect of the G/G_{max} curve assigned to the Bottom Layer on the estimated shear moduli was investigated in this section. Four G/G_{max} curves - lower, mid-lower, mid-upper, and upper - were tried for the Bottom Layer with the mid one being the correct one. The G/G_{max} curves used in the inverse analyses are presented in Figure 4.10. The profile of the shear wave velocity in the case S31 was used for all analyses.

The back-calculated shear moduli, assigning four different G/G_{max} curves to the Bottom Layer, are plotted in Figure 4.11, where a solid line indicates the baseline and a dotted line the assigned curve to the Bottom Layer. In all cases, the difference in the assigned G/G_{max} curve for the Bottom Layer did not affect the estimated shear moduli significantly. As previously observed through sets of parametric studies, the estimated moduli of Layers 1 and 2 show an excellent match with the baseline whereas those of Layers 3 and 4 still present close agreement at small strain level but small discrepancies at larger strain levels. Regardless of the level of approximation of G/G_{max} curve for the Bottom Layer, the back-calculated moduli of Layers 1, 2, 3, and 4 remained essentially the same.

4.4.1.4. Effect of Internal Damping

For a given set of responses, there is more than a single set of shear moduli and damping combinations that could be estimated in the inverse analysis. Since both the shear modulus and the damping can not be estimated simultaneously using the

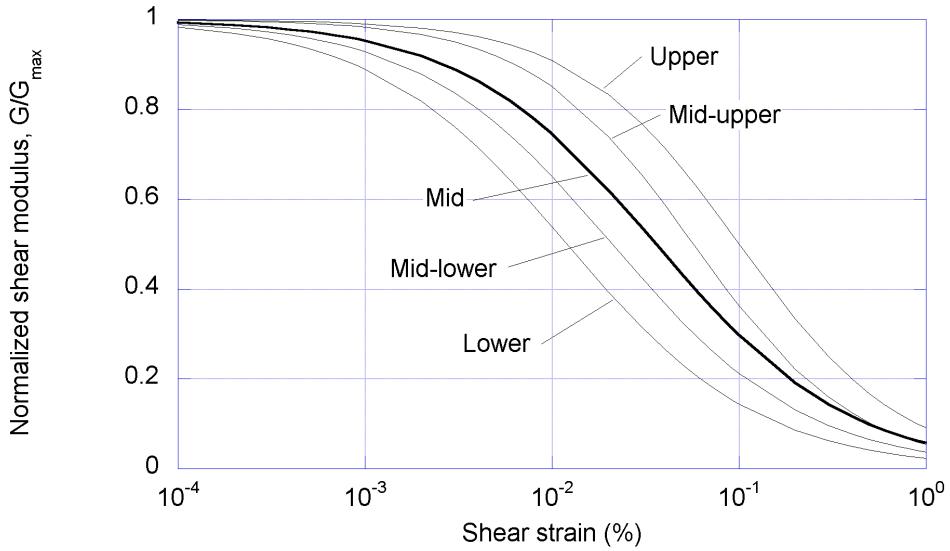

Figure 4.10 Normalized shear modulus reduction curves assigned at Bottom Layer

suggested method, it is necessary to assume a damping curve for each region of the model to estimate shear moduli. The damping curve assigned to the top layers will affect the modulus estimates for these layers. In this section, damping curves, different from the one used in the simulation, were assigned intentionally to see how they affect the shear modulus estimates. Two damping curves shown in Figure 4.12, lower and upper bound curves of cohesionless soils proposed by Seed and Idriss (1970) plotted using hyperbolic equations, were assumed while the mid one is the correct one.

The estimated nonlinear shear moduli obtained using the two different damping curves are presented in Figure 4.13. As shown in Figure 4.13(a), if the lower bound of damping was used (the damping was underestimated), the values of the shear modulus were overestimated, which is expected since the decrease in damping results in larger response and the increase in the shear modulus causes smaller response. The underestimation of shear moduli in Figure 4.13(b), due to overestimation of damping can be explained in the same way.

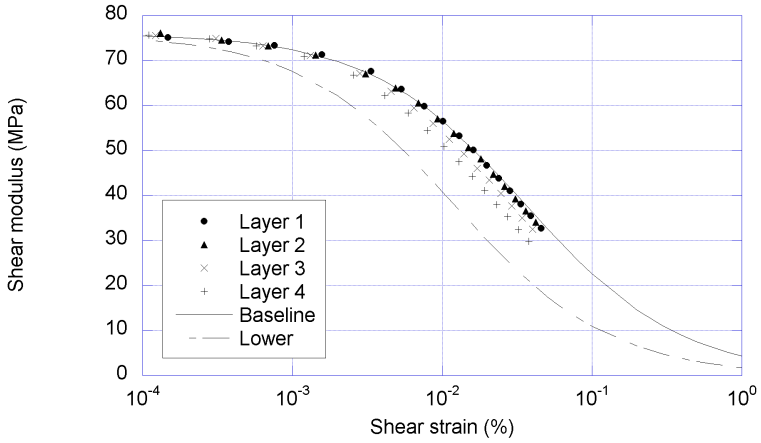

(a) Lower G/G_{max} curve assigned

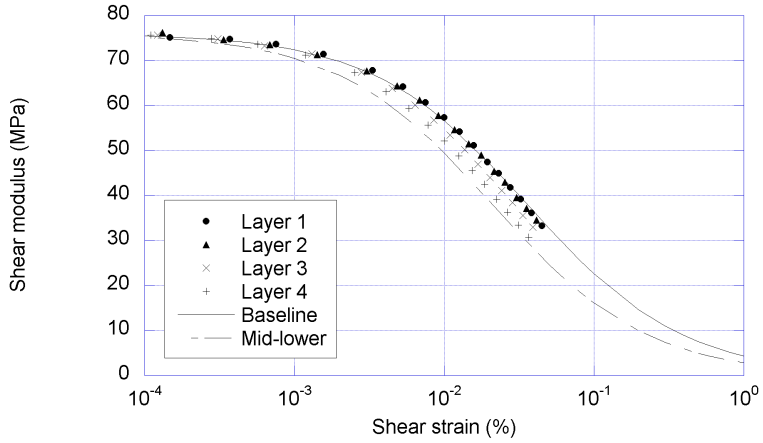

(b) Mid-lower G/G_{max} curve assigned

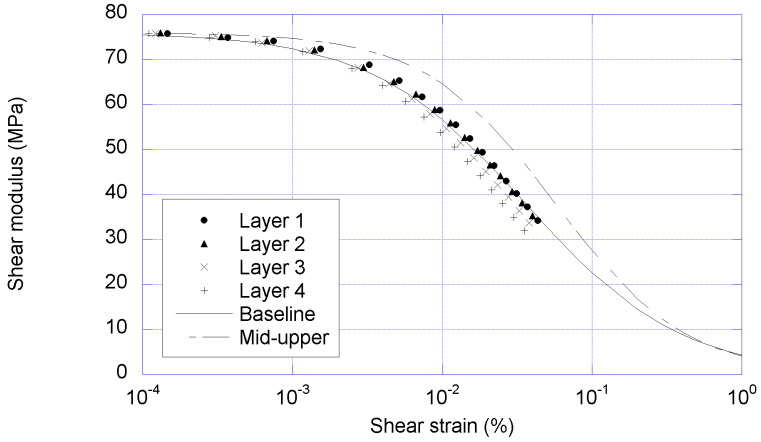

(c) Mid-upper G/G_{max} curve assigned

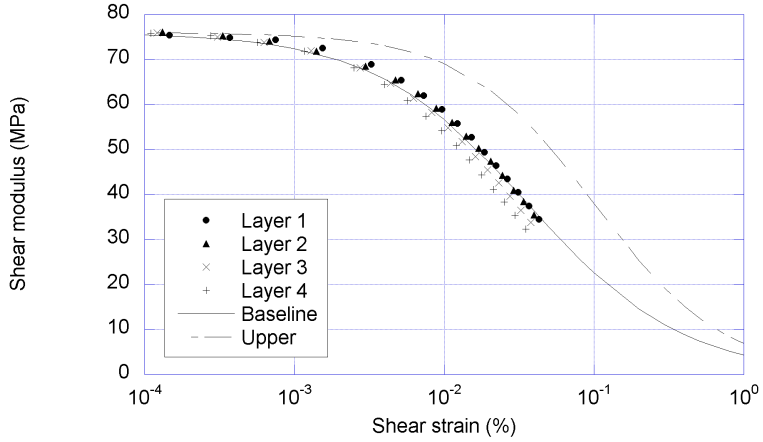

(d) Upper G/G_{max} curve assigned

Figure 4.11 Estimated nonlinear shear moduli with approximately assigned G/G_{max} curve at Bottom Layer

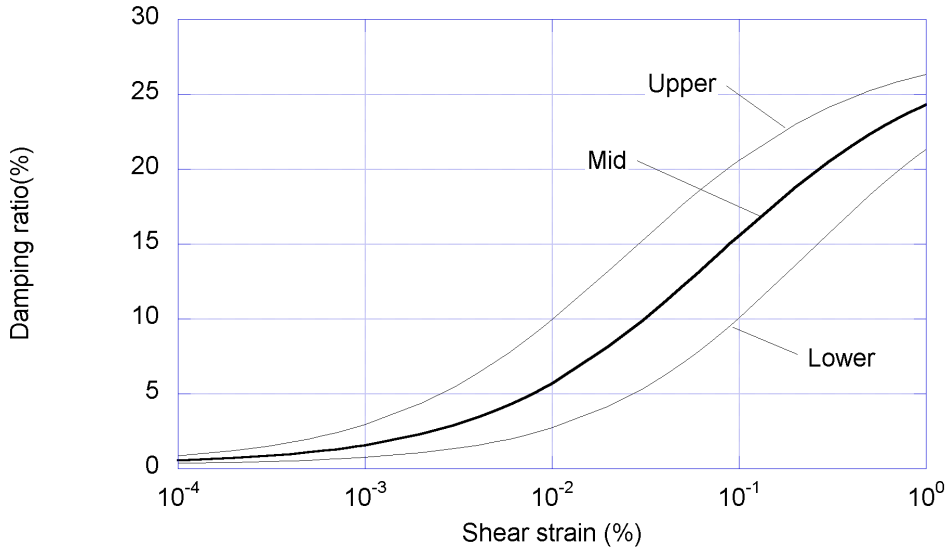

Figure 4.12 Damping curves assigned for entire mesh

As the assigned damping curve in the numerical model affects estimated shear modulus, it is only possible to present a shear modulus reduction curve as a pair with a damping curve. On the other hand, if the shear modulus reduction curve were known from the phase difference analyses, damping curves could be estimated using the inverse analysis.

4.4.2. Estimation of Nonlinear Damping Ratios

A parametric study was performed to validate the proposed inversion procedure for estimating the internal damping ratios. The back-calculation of the internal damping ratios was conducted following the procedure developed for the nonlinear shear moduli, except that the shear moduli were assumed and the damping ratios were to be estimated in this case. The Case S31 with the shear wave velocity profile in Figure 4.7(c) was selected, and the responses of the soil below the footing center were used for the validation. The back-calculated internal damping ratios are presented in

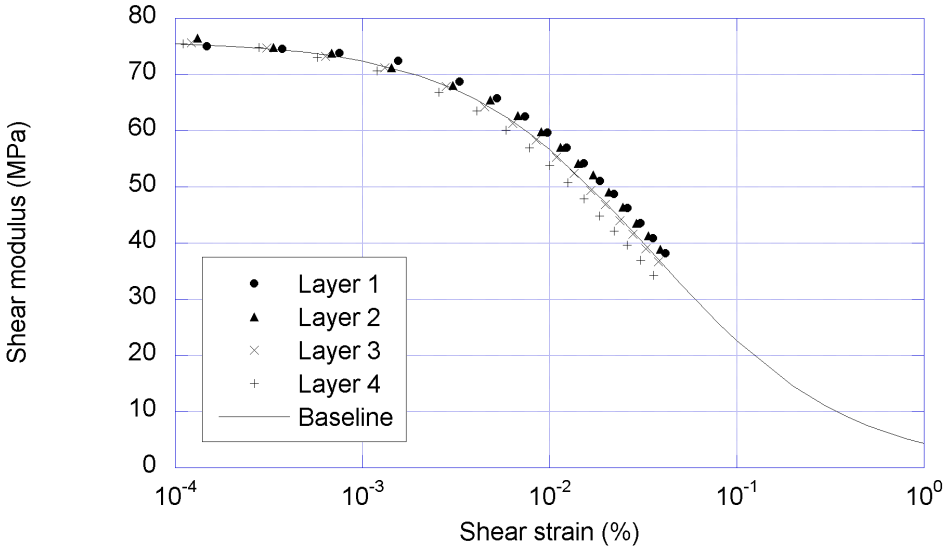

(a) Lower damping curve assigned

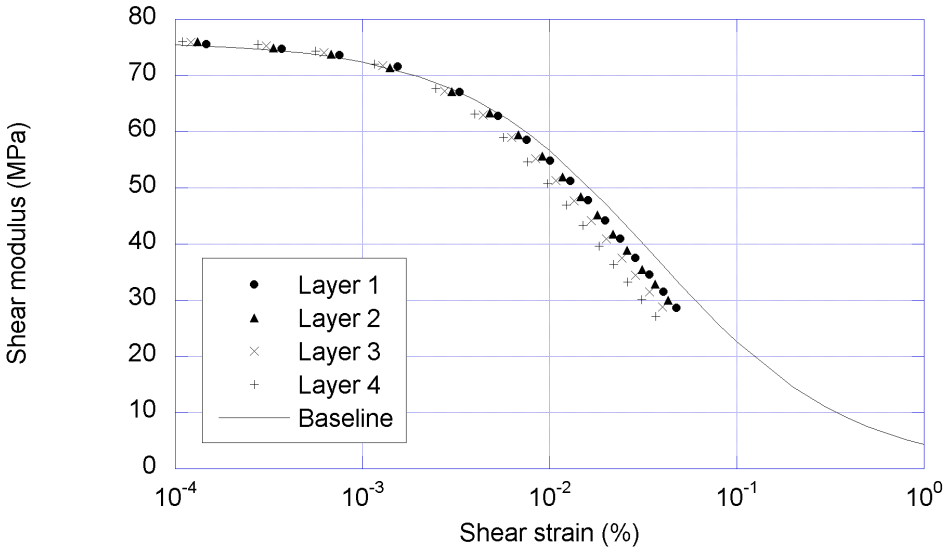

(b) Upper damping curve assigned

Figure 4.13 Estimated nonlinear shear moduli with approximately assigned damping curve for entire mesh

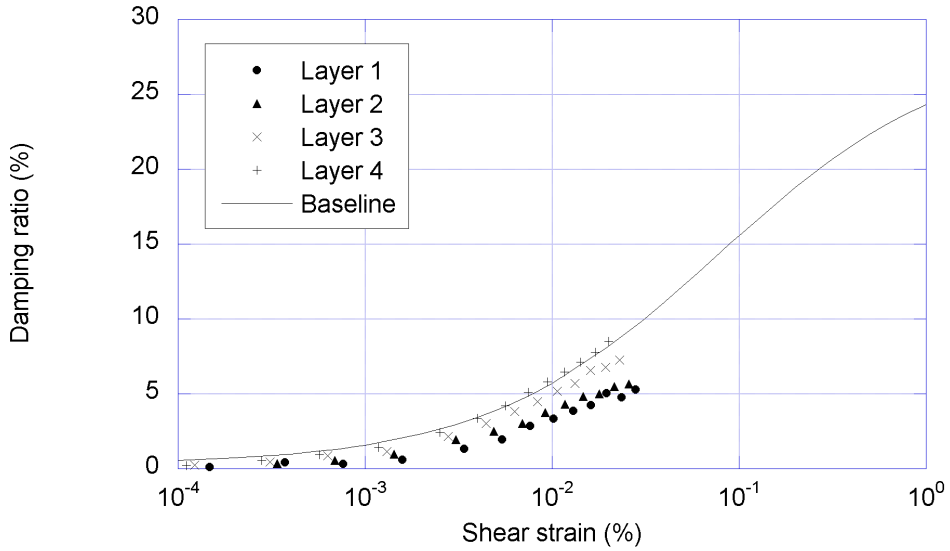

Figure 4.14 Estimated internal damping ratios with wave velocity profile of Case 31

Figure 4.14 with the baseline, which the back-calculated values should match. The estimated damping values were underestimated for all Layers 1, 2, 3, and 4 up to a damping ratio of 2 %. For the low value of damping, because the response of the system is not sensitive to the change in the damping value, the estimation is not accurate. However, if the damping ratio is larger than 2 %, the back-calculated damping matches the baseline value very well in Layer 4, matches fairly well in the Layer 3, and underestimates in Layers 2 and 1.

The internal damping ratios could also be estimated with an alternative procedure using the identification of the shear moduli with the assumed internal damping ratios. As shown in Figure 4.13, the shear moduli are overestimated when the assumed damping ratios are smaller than the correct properties, and the shear moduli are underestimated when the assumed damping ratios are larger. In the alternative procedure the nonlinear shear moduli produced using phase difference analyses are used as the baseline. After assuming a damping ratio curve, the inversion is per-

formed to estimate the nonlinear shear moduli. If the estimated shear moduli are larger than the baseline (moduli using phase difference) for certain strains, increase the assumed damping ratios at those strains. If the estimated moduli are smaller than the baseline, then decrease the assumed damping values. By repeating these steps until the estimated and baseline shear moduli match, the internal damping ratios of the soil can be obtained. In this chapter, however, the experimental data from the horizontal and vertical excitation tests were not available at the same locations at the time of writing thesis, the nonlinear damping ratios were not estimated using the field data.

4.5. Field Experiments

A series of in situ dynamic tests were performed at Texas A&M University Riverside Campus, College Station and at Capitol Aggregate Quarry, Austin using impact and harmonic excitation sources including vibroseis trucks developed by the University of Texas at Austin. Descriptions of the sites and the experiments are presented in this section.

4.5.1. Experimental Sites

A sand site located at Texas A&M University Riverside Campus was selected as a National Geotechnical Experimentation Site (NGES) for geotechnical engineering research together with a clay site in the late 1970's. Since then, this site has been frequently used to perform geotechnical experiments by many researchers in the United States. Material properties at this site are available from a summary report by Briaud (1997) who arranged a series of reports based on the experiments conducted at the site. In situ dynamic tests were performed at the sand site in this study. The

stratigraphy of the sand site is illustrated in Figure 4.15(a). There are four distinct layers. The surface unit is a mottled red and tan silty sand whose thickness averages 4 m. The second unit, the clean sand, generally goes to a depth of about 8 m below the surface. The third one is a heterogeneous of thin interbedded sand, clay and clayey gravel layers, that goes to a depth of about 12.5 m beneath the ground level. The bedrock, shale, beneath the site starts from about 12.5 m below the surface. The groundwater surface was located at about 7.3 m depth. The density profile of the site is also presented in Figure 4.15(b) (Briaud, 1997). The mass density at the surface layer varies from 1500 kg/m^3 to 2100 kg/m^3. An average value of density, 1800 kg/m^3, was used to represent the first silty sand layer. To determine the shear wave velocity profile near the test area, a SASW test was performed at the vicinity of the test region before the measurement devices were installed. The shear wave profile from SASW is presented in Figure 4.15(c) (Park, 2007).

The other testing site is located inside the Capitol Aggregate Quarry, Austin, Texas. The top of soil is comprised of silty sand up to 0.46 m. The second layer is non-plastic silt and continues to 3.84 m and is followed by the third layer to 4.3 m. The groundwater level was found at 4.27 m. Two sets of Spectral Analysis of Surface Waves (SASW) test were performed in the site following two lines perpendicular to each other as shown in Figure 4.16. A density of 1900 kg/m^3 was used for the estimation of the shear moduli based on the density profile in Figure 4.17(a). The lower and upper bounds, and best fit of the evaluated shear wave velocity profiles are plotted in Figure 4.17(b) and 4.17(c). Poisson's ratio was assumed as 0.33 for the soil above the groundwater level, and 0.49 below.

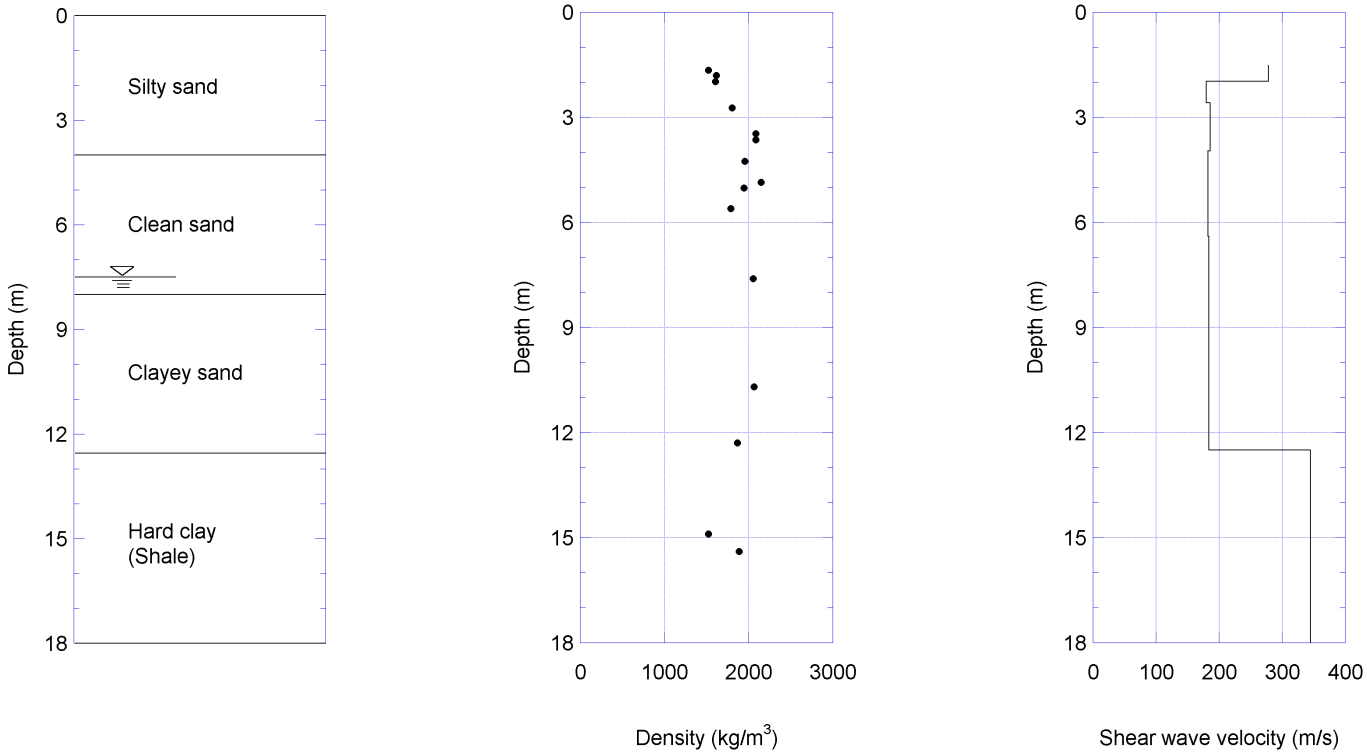

(a) Stratigraphy (Briaud, 1997) (b) Density (Briaud, 1997) (c) Shear wave velocity (Park, 2007)

Figure 4.15 Stratigraphy, density, and shear wave velocity at Texas A&M University Riverside Campus site

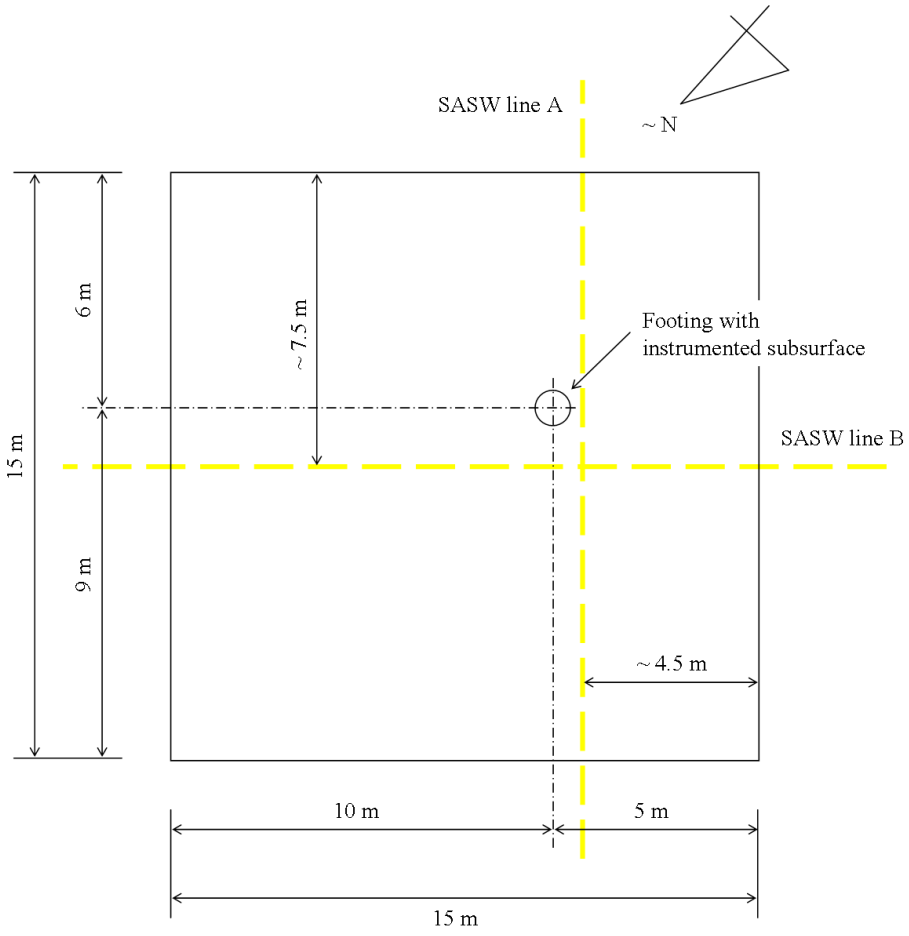

Figure 4.16 Plan view of the Capital Aggregate Quarry site (Kurtulus, 2006)

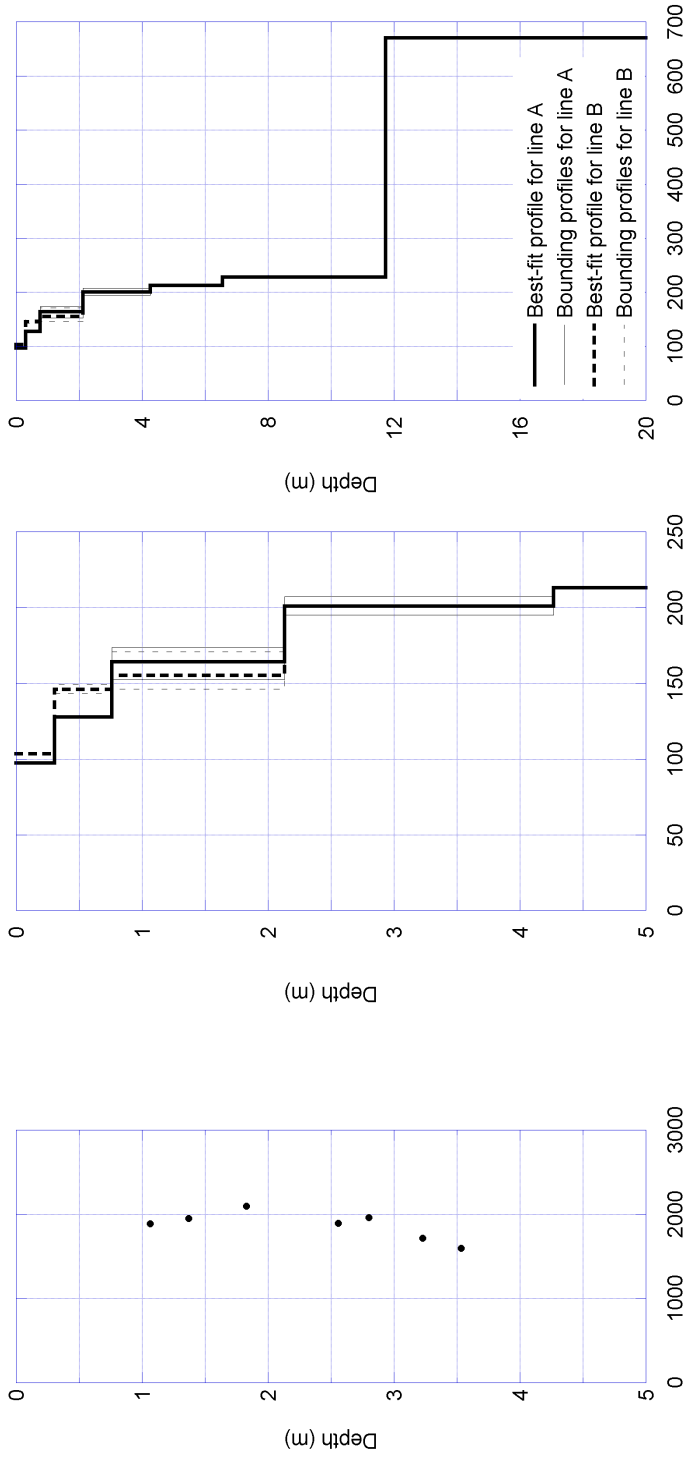

(a) Density profile (b) Wave velocity up to 5 m (c) Wave velocity up to 20 m

Figure 4.17 Density and shear wave velocity profiles at the Capital Aggregate Quarry site (Kurtulus, 2006)

4.5.2. Test Setup

Three dimensional (3D) heophones and one dimensional (1D) geophones and three dimensional (3D) geophones were used at the Texas A&M University Riverside Campus and the Capital Aggregate Quarry sites, respectively. As of 3D geophones, they were manufactured by assembling three 1D geophones together in an acrylic case glued using epoxy to ensure that they would behave as a rigid body. The unit weight of each 3D or 1D geophone was aimed to be approximately equal to that of the soil. The geophones were also embedded with different arrays at different sites as shown in Figure 4.18.

Before the instrumentation, the two sand sites were prepared by excavating the soil and vegetation at the top to expose the ground for the experiments. First, the geophones were embedded in the soil deposit at several depths making an array up to the depth of half the footing radius, as presented in Figure 4.18. A hand auger was used to drill the boreholes of 6 cm diameter for the installation of the geophones. The geophones were carefully installed at the desired depths in an array. A set of geophones was also attached to the rebar close to the bottom of the footing before pouring the concrete. The reinforced circular concrete footing with a diameter of 0.91 m (3 ft) and a height 0.30 m of (1 ft) was cast in the field leaving about one third of the foundation embedded. Since a small part of the footing is embedded, the stiffness and the damping ratio of the system will be affected. However, the tests were performed letting the bond between the foundation and overburden soil loose. If the embedment is backfilled with soil which is less dense than the original soil deposit, the effect of embedment on both the resonant amplitude and frequency decreases. In our case, as the embedment is shallow and backfilled, the effect of embedment becomes negligible (Novak and Beredugo, 1972). Thus, the embedment was not considered in

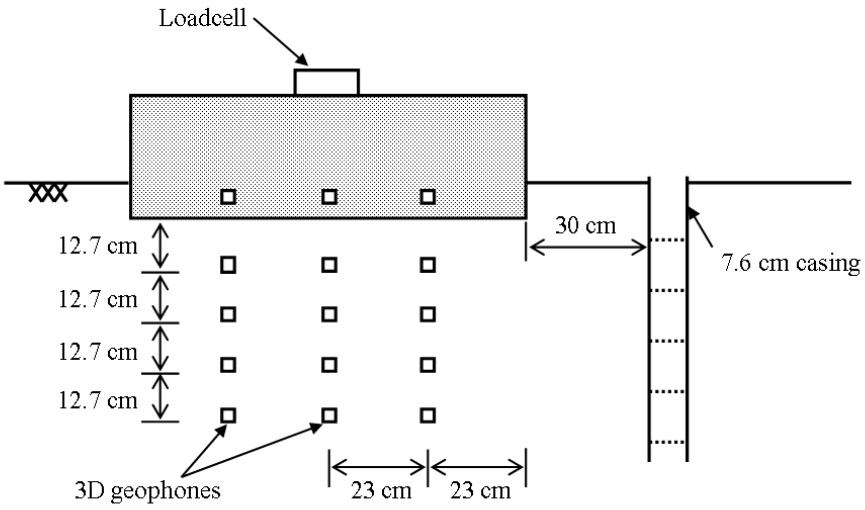

(a) Texas A&M University Riverside Campus site

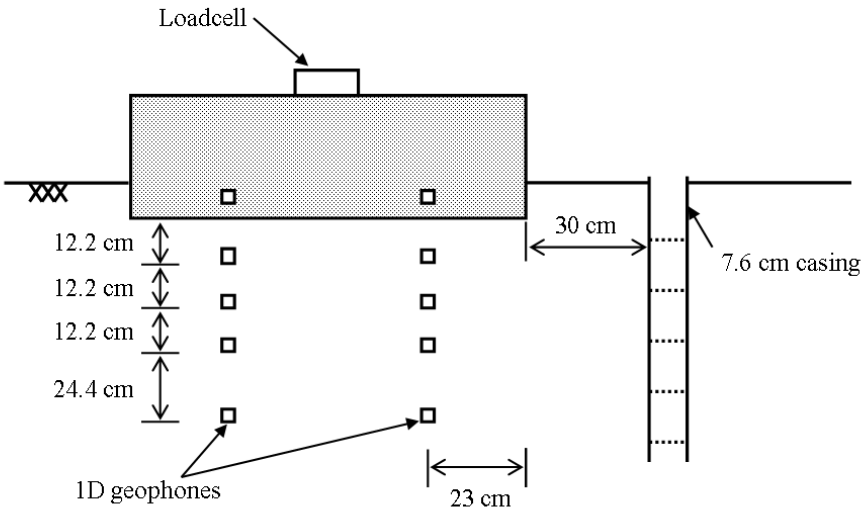

(b) Capital Aggregate Quarry site

Figure 4.18 Instrumentations at two sites

the inverse analysis.

For the small-strain crosshole tests, a borehole casing was installed at about 0.3 m from the edge of the footing with a diameter of 7.6 cm. The casing is made with a PVC pipe segmented into several parts connected by a flexible membrane to act as an isolated source for the wave. In addition to the crosshole tests, small-strain downhole tests were performed using an impact on the footing as the seismic source.

4.5.3. Measurement Devices

During the experiments, the particle velocities of the soil mass and the footing were measured with geophones. The phase lags and the response amplitudes were estimated from the waveforms recorded to determine the soil properties using the phase difference and the inverse analyses. A geophone is comprised of a coil suspended by a spring in the case and a permanent magnet fixed to the case. When the geophone case is vibrated with the permanent magnet, the coil stays still or lags behind the case generating a voltage proportional to the velocity at which the magnet moves relative to the coil. If a geophone is excited at a frequency sufficiently higher than the natural frequency, the ratio of voltage to velocity is a constant. However, at a frequency in the vicinity of the natural frequency, the ratio is a function of frequency. Geospace Corporation GS-14-L9 geophones, with a natural frequency of 28 Hz, were used in this study. All geophones were calibrated using an accelerometer and a proximeter. An example of calibration data is plotted in Figure 4.19. The calibration factor showed some discrepancy depending on the geophones but the values were overall in the range of 0.135 V/cm/s to 0.145 V/cm/s at a frequency of 50 Hz.

Two types of load cells, 55.5 kN (12.5 kips) and 111 kN (25 kips), manufactured by Interface Inc., were used to measure the vertical force applied on top of the footing. A strain gauge based load cell converts the load applied on it into electrical signals.

Strain gauges are bonded onto a piece of precisely machined metal in the load cell. In most cases, four strain gauges are used, completing a full Wheatstone bridge, to obtain maximum sensitivity and temperature compensation. The strain measured from the gauges is proportional to the force acting on the load cell. The calibration results of two load cells are presented in Figure 4.20. A constant excitation voltage should be supplied into the load cell to power the circuit. When an input voltage of 10 V is used, the calibration factors are -262.2 kN/mV for the 55.5 kN load cell and -538.8 kN/mV for the 111 kN load cell, where negative sign indicates compression.

4.5.4. Vibroseis Loading System

A vibroseis truck is a truck with a large scale shaker used as an excitation source in reflection surveys for petroleum exploration. A vibroseis loading system, Thumper, developed by the University of Texas at Austin was used to excite the soil deposit. Thumper has a dead weight of approximately 100 kN and can load dynamically in both vertical and horizontal directions. It can apply a force amplitude of up to 26.7 kN (6 kips) over a frequency range of 17 Hz to 225 Hz. The dynamic motion results from the rotating reaction mass and baseplate, which have masses of 141 kg and 168 kg, respectively.

4.5.5. Experimental Procedure

In the experiments with Thumper, the intention was to induce vibrations in the linear and nonlinear ranges in order to estimate the shear modulus reduction curve. A static load was imposed on the footing first. Then, the footing was excited either vertically or horizontally by the vibroseis loading system with a certain force amplitude at a fixed frequency. The force amplitude on the footing increases in a number of steps inducing nonlinearity in the soil deposit. Particle velocity histories from geophones

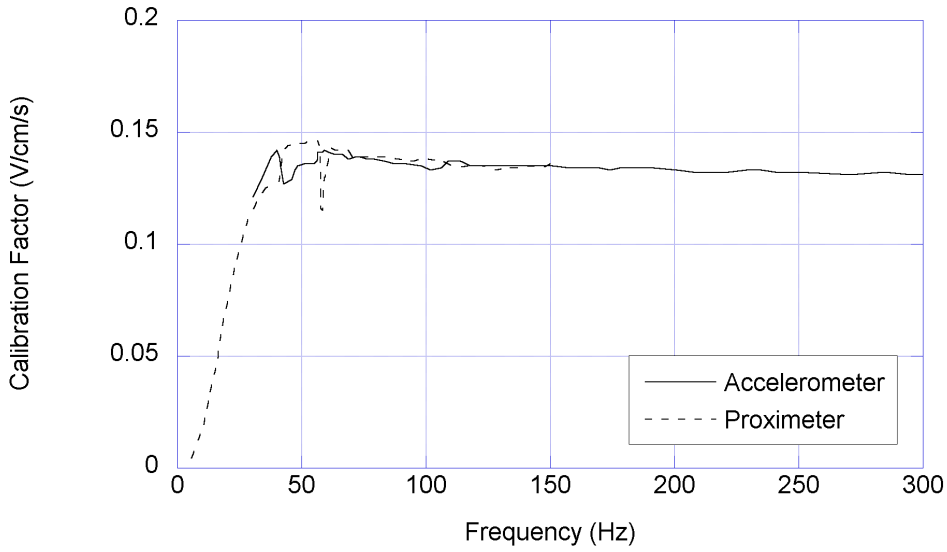

(a) Amplification

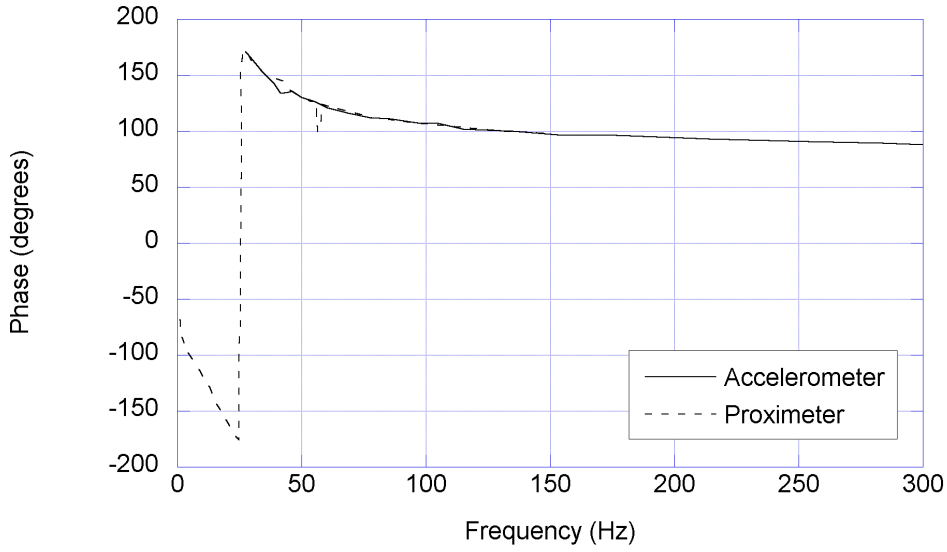

(b) Phase

Figure 4.19 Amplification and phase calibrations of a geophone

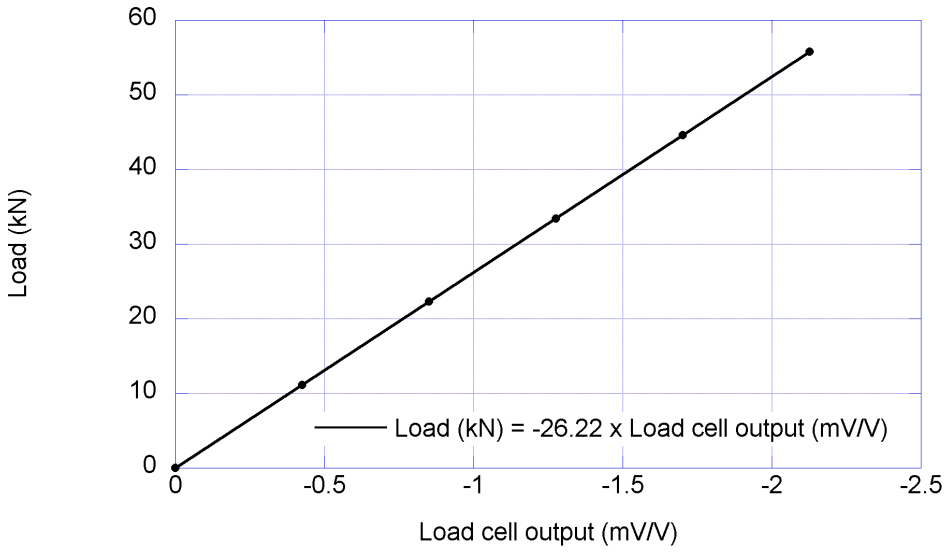

(a) 55.5 kN load cell

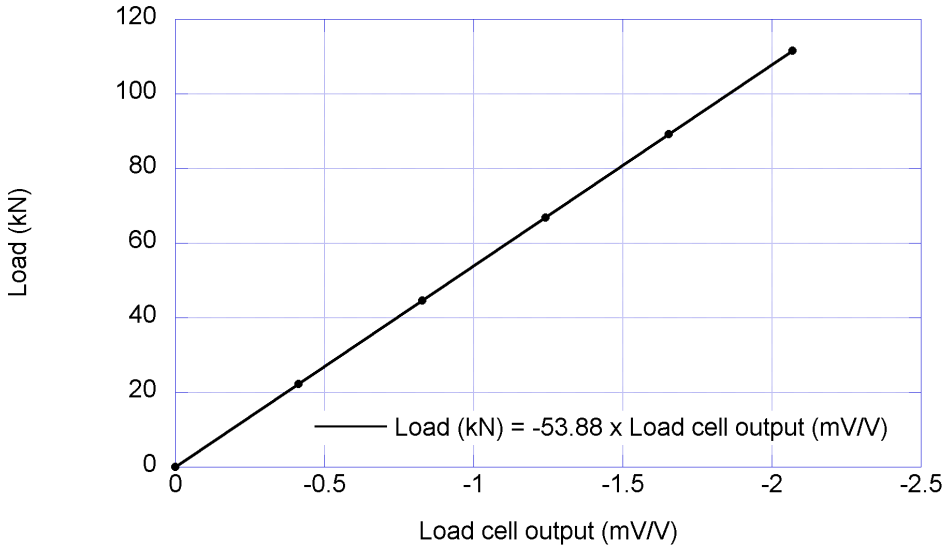

(b) 111 kN load cell

Figure 4.20 Load cell calibrations

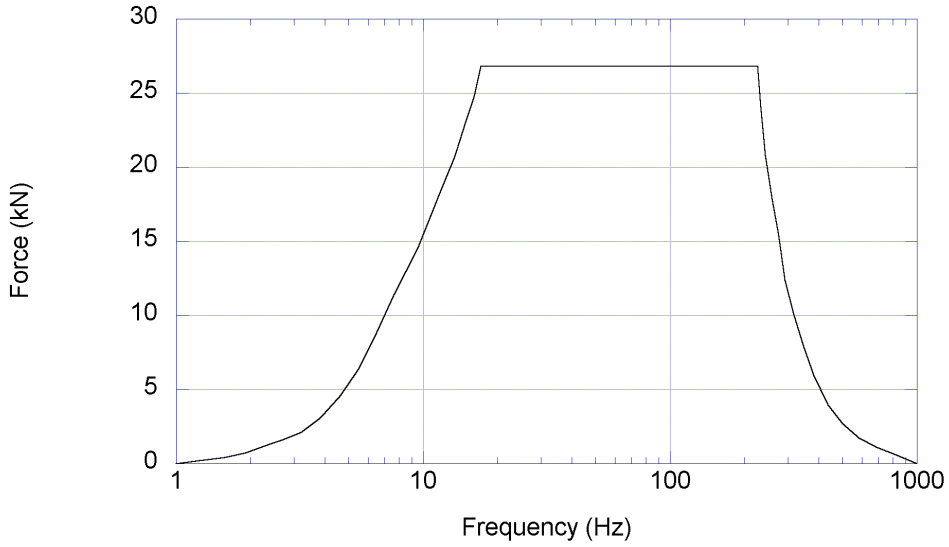

Figure 4.21 Theoretical force output of Thumper

are recorded at every stage. For the vertical excitation tests with an increasing force sequence, measurements were repeated with a small level excitation after a selected number of large amplitude cycles to check the effect of the high level excitation on the soil and the possible presence of damage. For the horizontal excitation tests, small excitations were applied at the end of the tests. The test sequence was repeated with different levels of static load imposed on the footing. Both the horizontal and vertical excitation tests were conducted on the both sites, but only vertical excitation data are available for the Texas A&M University site, and only horizontal data for the Capital Aggregate Quarry site. The data from the first site were used for the inverse analyses, and those from the second site for the phase difference analyses. The static and dynamic force amplitudes used in the experiments are tabulated in Table 4.2 and Table 4.3 for the vertical and horizontal excitation tests, respectively. In all cases, a forcing frequency of 50 Hz was used.

Small-strain crosshole and downhole tests were performed before the static load

Table 4.2 Static and dynamic force sequence for vertical excitation tests performed at the Texas A&M University Riverside Campus site

	Forces used for first set		Forces used for second set	
	(lb)	(kN)	(lb)	(kN)
Static	4000	17.84	8000	35.67
Dynamic	200	0.89	200	0.89
	300	1.34	300	1.34
	400	1.78	400	1.78
	500	2.23	500	2.23
	600	2.68	600	2.68
	800	3.57	800	3.57
	1000	4.46	1000	4.46
	(600)	(2.68)	(600)	(2.68)
	1500	6.69	1500	6.69
	2000	8.92	2000	8.92
	(600)	(2.68)	(600)	(2.68)
	2500	11.15	2500	11.15
	3000	13.38	3000	13.38
	(600)	(2.68)	(600)	(2.68)
			4000	17.84
			(600)	(2.68)

Table 4.3 Static and dynamic force sequence for horizontal excitation tests performed at the Capital Aggregate Quarry site

	Forces used		Forces used	
	(lb)	(kN)	(lb)	(kN)
Static	6000	26.76	6000	26.76
Dynamic	120	0.54	840	3.75
	144	0.64	960	4.28
	192	0.86	1080	4.82
	216	0.96	1200	5.35
	240	1.07	1440	6.42
	264	1.18	1680	7.49
	312	1.96	1920	8.56
	360	1.61	2160	9.63
	420	1.87	2400	10.71
	480	2.14	2640	11.77
	540	2.41	3000	13.38
	600	2.68	(600)	2.68
	660	2.94	(360)	1.61
	720	3.21	(192)	0.86
	780	3.48		

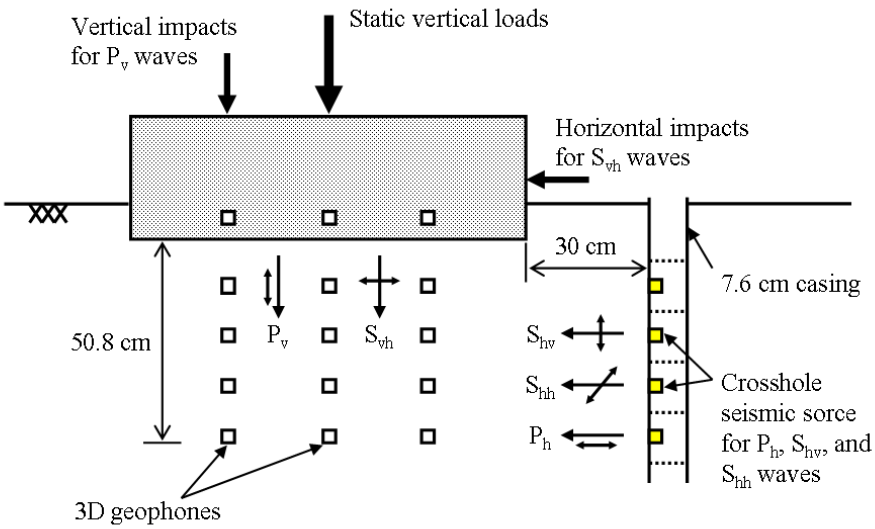

Figure 4.22 Schematic illustration of small-strain seismic tests (not to scale)

was imposed and at every step of the static loading to estimate the shear modulus in the linear range. Vertically propagating compression waves P_v or vertically propagating and horizontally polarized shear waves S_{vh} were generated by applying vertical or horizontal impacts on the footing, respectively. Horizontally propagating compression waves P_h, horizontally propagating and vertically polarized shear waves S_{hv}, or horizontally propagating and horizontally polarized shear waves S_{hh} were generated using a small shaker at the desired depth in the borehole as illustrated in Figure 4.22.

4.6. Shear Modulus Reduction Curve

Nonlinear shear moduli were estimated using phase difference analysis with the horizontal excitation data and using the proposed inversion method with the vertical excitation data. For the inverse analysis, a preliminary study was performed first to check the validity of the method for a shear wave velocity profile at the sand

site. Nonlinear shear moduli were estimated using in situ test data and results were compared to the laboratory data for cohesionless soils proposed by Seed and Idriss (1970).

4.6.1. Phase Difference Analysis Results

A LabVIEW code was produced to extract the amplitudes and phases from the recorded time histories and to estimate the nonlinear shear modului. The data from the horizontal excitation tests at the Capital Aggregate Quarry site were analyzed using this program. For a set of nonlinear dynamic test with horizontal excitations under the static load of 26.76 kN (6 kips), the data recorded from the second and third rows of geophones from the top, on the East and the West of the footing center were used. The nonlinear shear moduli estimated using the horizontal test data are presented in Figure 4.23(a). While the curve for the Eastern array shows a well defined elastic threshold and decreasing trend corresponding to shear strains, the one for the Western location does not follow the expected behavior. The results of the small strain level excitation tests seem consistent with the curve for the East side but not to that for the West. The results of the small strain level excitation tests were not present here. The results derived from the same experimental data by Park (2007) also correspond to the curve for the Eastern array. Many sources of uncertainty contribute to errors in the analyzed results. Some uncertainties are related to the experimental setup such as slight variations in geophones location or imposing an eccentric static and dynamic load, and can not be observed either during or after the tests with the proposed procedure. Errors may also be intrideced in the data interpretation stage. The particle velocity time histories measured at the same time on the East and the West, are plotted in Figure 4.24. As presented in the figure, the recorded time histories in the field do not have a smooth sinusoidal shaped, which

obscures accurate measure of the wave travel times. One should be aware that different ways of interpreting the data could results in different outcomes. Since the curve for the West produced using the LabVIEW code does not seem reasonable, only the one for the East was normalized and compared with the nonlinear moduli for cohesionless soils proposed by Seed and Idriss (1970) in Figure 4.23(b). The measured shear modulus reduction curve remains elastic up to a shear strain of 1.5×10^{-3} %. It then follows the upper bound of the Seed and Idriss (1970) curve, and drops closer to the mean value at strains larger than 6×10^{-3} %. The three solid symbols in the graph represent the result from tests with small levels of force amplitude after having applied greater forces as shown in Table 4.3. These were conducted to check the effect of the high level excitation on the soil and the possible presence of damage. These points are consistent with the overall trend. The level of dynamic forces applied in this set of tests didn't affect the structure of the soil and the shear modulus values significantly.

4.6.2. Preliminary Inverse Analysis

In preparation for the inverse analysis using the data of vertical excitation tests performed at the Texas A&M University Campus Riverside site, a preliminary inverse analysis was performed first to ensure that the proposed method was applicable for the shear wave velocity profile at the testing site. The shear wave velocity profile of the Texas A&M University Riverside Campus site was estimated in the vicinity of the test area using SASW and is presented in Figure 4.15(c). Numerical verification of the proposed inversion procedure was performed with using the shear wave velocity profile for the Bottom Layer. Nonlinear shear moduli were estimated for Layers 1, 2, 3, and 4 using the computed displacements at the centerline of the footing. The results are presented in Figure 4.25. In Figure 4.25(a), the estimated shear moduli for the Layers

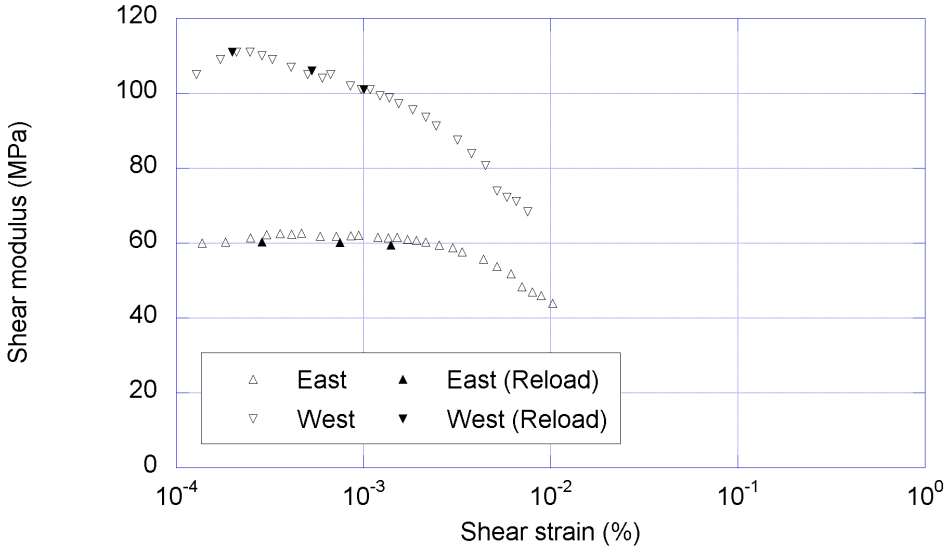

(a) Shear modulus reduction curves from two measurement locations

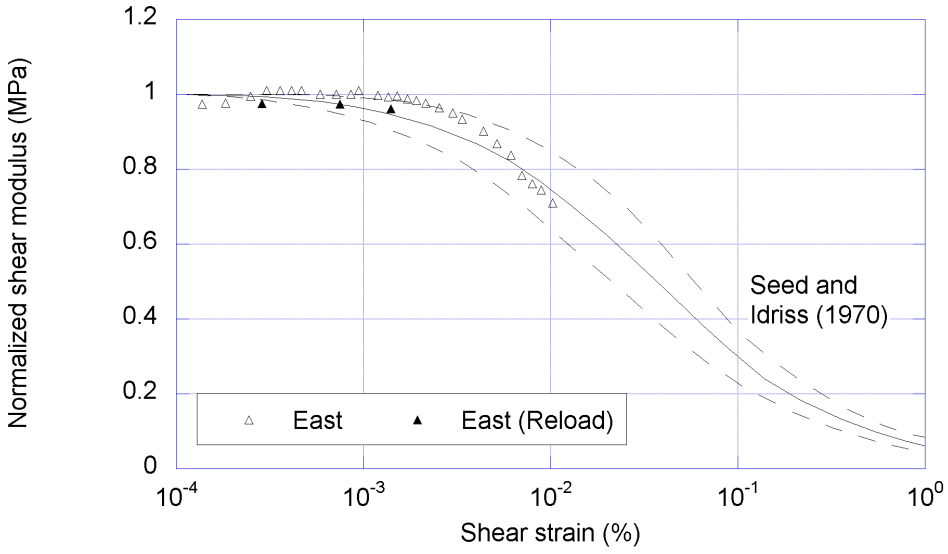

(b) Normalized modulus reduction curves compared to Seed and Idriss (1970)

Figure 4.23 In situ shear modulus reduction curve under 6 kips static load using phase difference analysis

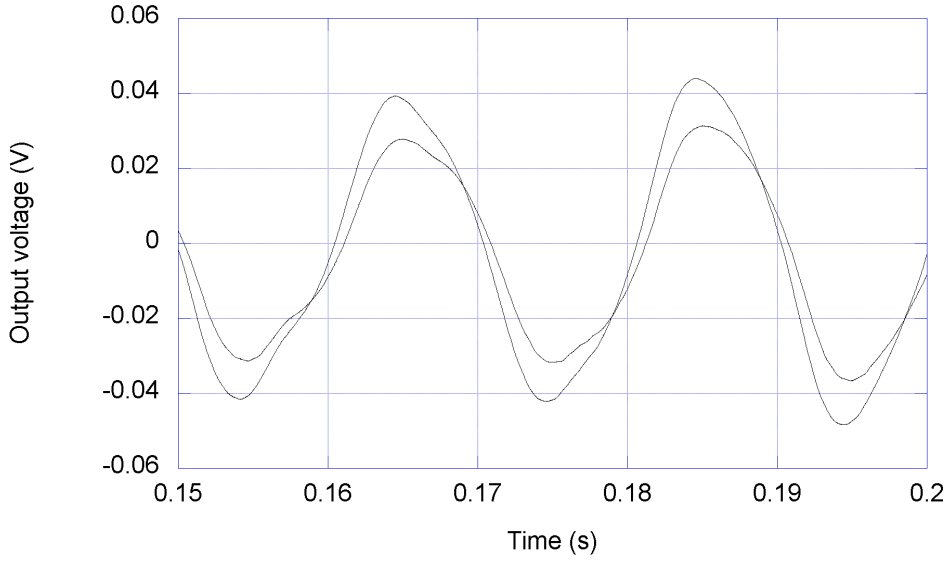

(a) Particle velocity time histories from two geophones on East

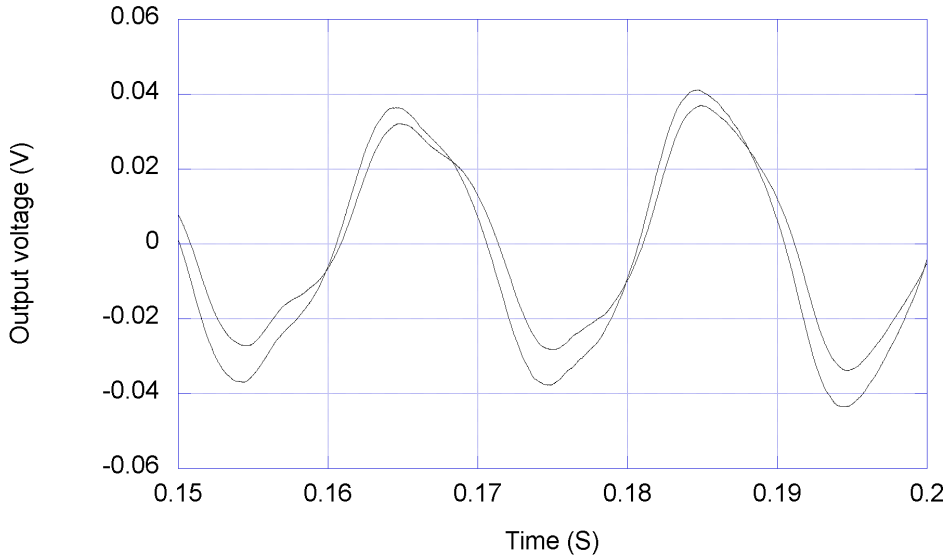

(b) Particle velocity time histories from two geophones on West

Figure 4.24 Particle velocity time histories used for phase difference analysis

1 and 2 match the baseline closely, while those for Layers 3 and 4 diverge from the actual value for large strain levels. In the field the precise measurement of shear wave velocity, therefore soil modulus, for each layer may not be possible because of the uncertainties involved in soil properties and field instrumentation. The shear wave velocities under the footing will likely be defined as an averaged shear wave velocity for Layers 1, 2, 3, and 4. Then, averaged shear wave velocity will be converted to shear modulus. Likewise, shear strains at $r = 0.875R$ of each layer will be averaged. The averaged shear modulus reduction curve is plotted in Figure 4.25(b). The average curve fits the reduction curve well at small strain levels, but deviates from it for strain levels larger than 4×10^{-3} %. The difference between the estimated and the baseline curves increases with the shear strain level. In Figure 4.26, the difference is plotted against G/G_{max}. A correction formula was derived by linearizing the plot. The modified reduction curve using the correction formula is presented in Figure 4.25(c). Same correction formula will be used to compensate approximately the error for the estimation of nonlinear shear moduli in situ using experimental data.

4.6.3. Inverse Analysis Results

To estimate nonlinear shear moduli of the soil at the Texas A&M University Riverside Campus site, inverse analyses were performed with the vertical force amplitude acting on the footing and the vertical response amplitudes of the footing and soil. The shear wave velocity profile obtained in the vicinity of test area using SASW was used for the Bottom Layer. The values of density were simplified as 1800 kg/m^3 at the surface layer and 2000 kg/m^3 below based on the density profile in Figure 4.15(b). Poisson's ratio of 0.3, was assumed based on the ratio of compression and shear wave velocities from small strain level tests. The preliminary analyses indicate that these material properties may affect the estimated modulus values but not the

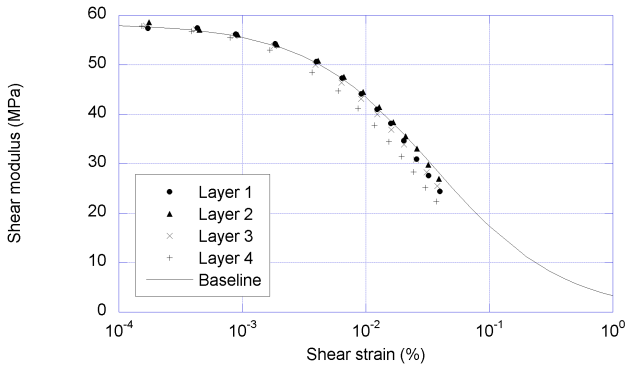

(a) Shear modulus reduction curves in four layers

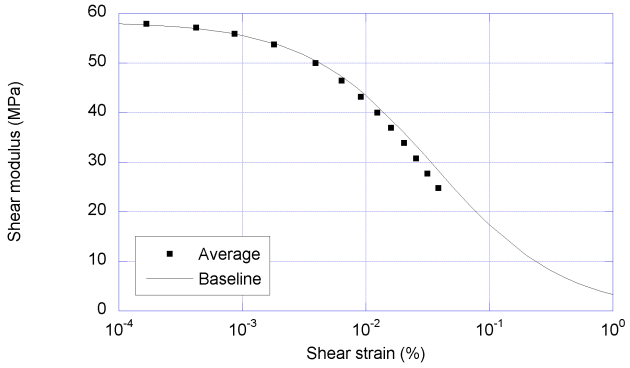

(b) Averaged modulus reduction curve

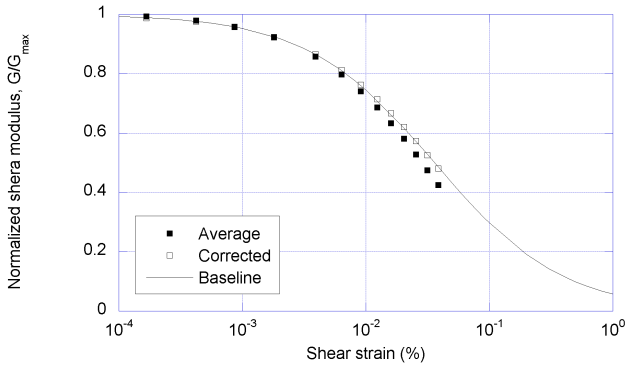

(c) Normalized modulus reduction curve

Figure 4.25 Verification of the inverse analysis scheme for shear wave velocity profile at sand site in Figure 4.15(c)

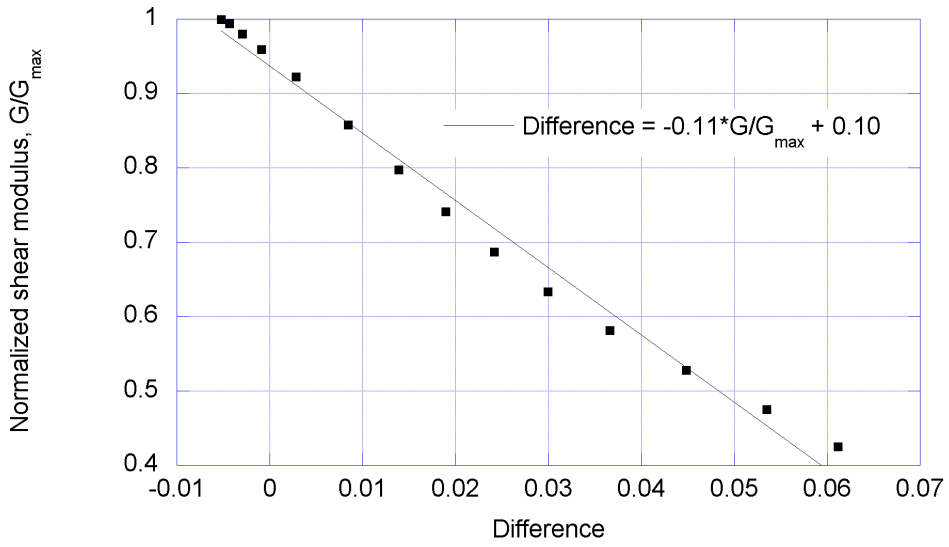

Figure 4.26 Correction formula corresponding to the nonlinear level

modulus reduction trend. The mean damping curve for cohesionless soils proposed by Seed and Idriss (1970), presented in Figure 4.27, was used for the entire model. The response measured from five geophones located North and South of the center of the footing, and at the center itself were used to estimate a set of shear wave velocities for the Layers 1, 2, 3, and 4. An average of the estimated wave velocities from the four layers was converted to shear modulus. The octahedral shear strains at $r = 0.875R$ were also averaged and used as the reference strain for developing the modulus reduction curve. The estimated shear modulus reduction curves were normalized by the modulus at small strain level and modified using the correction formula in Figure 4.26.

For each set of nonlinear dynamic tests, three modulus reduction curves were estimated from the measurements at the North, the South, and the center of the footing. The test results with a static load of 17.84 kN (4 kips) modified using the correction formula in Figure 4.26 are presented in Figure 4.28. In Figure 4.28(a),

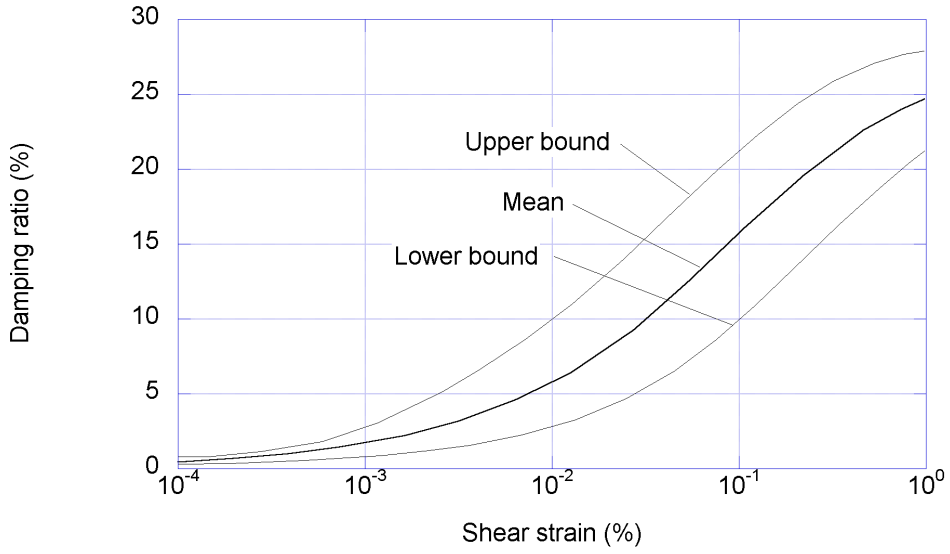

Figure 4.27 Internal damping ratio of cohesionless soils (Seed and Idriss, 1970)

the estimated moduli from measurements at the South are larger than those from the North. Either the material properties at the two different locations are different or the force excitation was applied eccentrically on the footing during the tests (or probably both). However, the normalized curves in Figure 4.28(b) show similar decreasing trends regardless of the measurement locations. Disregarding the three points at a strain of about 6×10^{-4} %, the soil remains linear elastic while the strain level is under 2×10^{-3} %. After crossing the elastic threshold, it follows the upper band of the shear modulus curve for cohesionless soils proposed by Seed and Idriss (1970), then, settles to the mean curve at around 6×10^{-3} % of shear strain. The three solid symbols (for each of three locations) in the graphs represent the results of the tests with a force amplitude of 2.68 kN (600 lb) after having applied greater forces as shown in Table 4.2. These points show some scatter, but they do not contradict the overall trend. It seems that the level of dynamic forces applied in this set of tests did not affect the structure of the soil and the shear modulus values significantly. The results with a

static load of 35.67 kN (8 kips) are presented in Figure 4.29. As in the previous case with a static load of 17.84 kN, the estimated modulus in the South is higher than in the North. The normalized curves also share very similar trends. They show an elastic strain threshold at 2×10^{-3} %, and lay slightly above the mean proposed by Seed and Idriss (1970) at the strain larger than 6×10^{-3} %. More data are required to observe the effect of confining pressure in the trend of the G/G_{max} curve. The four solid symbols (for each of three locations) corresponding to a small level of excitation are again consistent with the overall reduction trend, without any clear evidence of damage in the structure of the soil. Overall, the nonlinear shear moduli using the inverse analysis had similar trends to those using the phase difference analysis with larger elastic strain threshold.

4.7. Summary and Conclusions

The nonlinear shear moduli could be estimated using the phase difference and inverse analyses with the horizontal and vertical excitation tests, respectively.

In the proposed inversion procedure, the input and output amplitude data from large scale in situ dynamic tests are used to estimate the material properties of the soil. The Levengerg-Marquardt method and a finite element model with the consistent transmitting boundary were used as a parameter adjustment algorithm and a numerical model, respectively. The method was validated through numerical verifications for soil deposits with low to medium variation of shear wave velocity. It is recommended to perform preliminary inverse analyses for the given soil condition before using the experimental data in order to check the applicability of the method for specific cases.

Either shear moduli or damping can be estimated in the vicinity of the surface

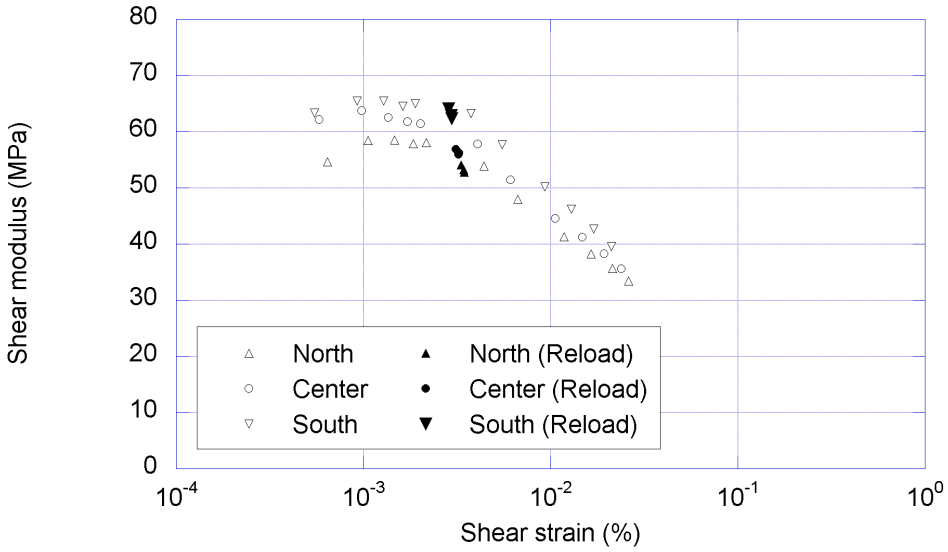

(a) Averaged modulus reduction curves from three measurement locations

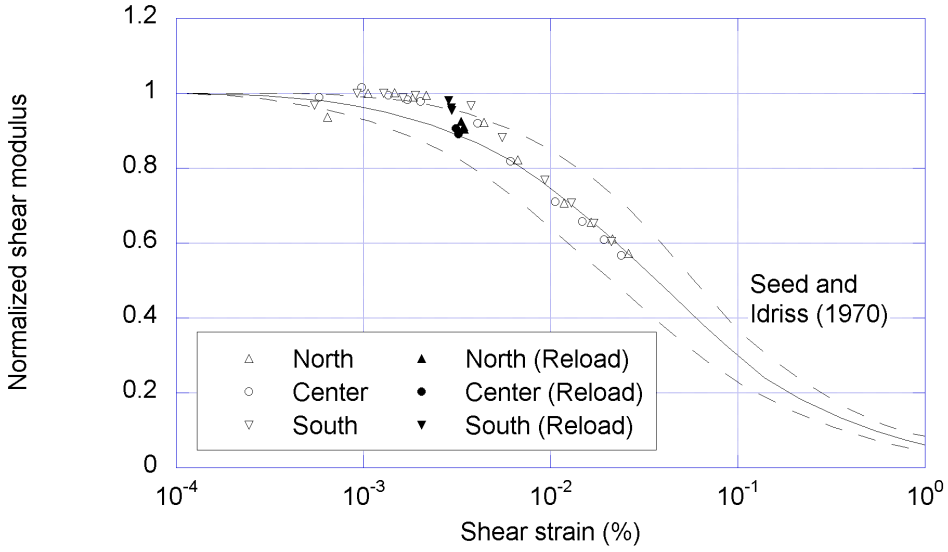

(b) Normalized modulus reduction curves compared to Seed and Idriss (1970)

Figure 4.28 In situ shear modulus reduction curve under 4 kips static load using inverse analysis

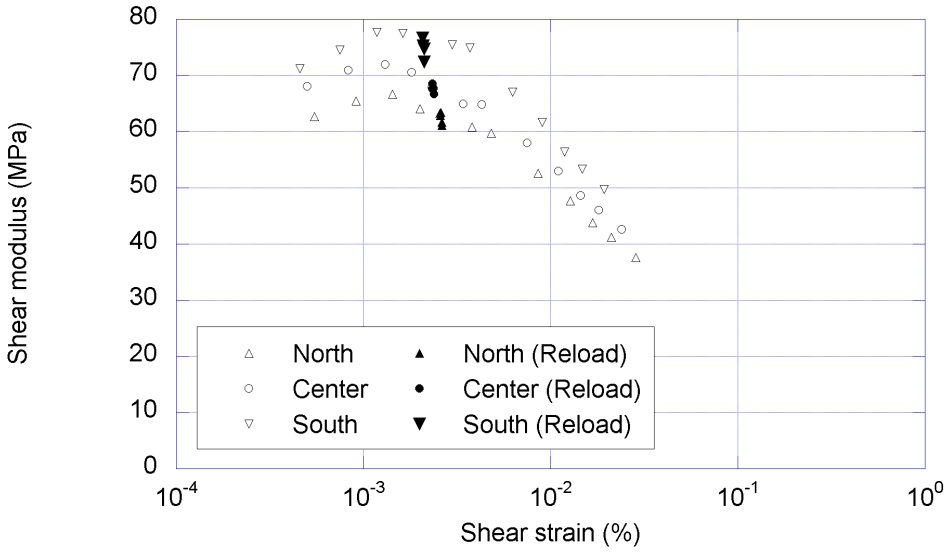

(a) Averaged modulus reduction curves from three measurement locations

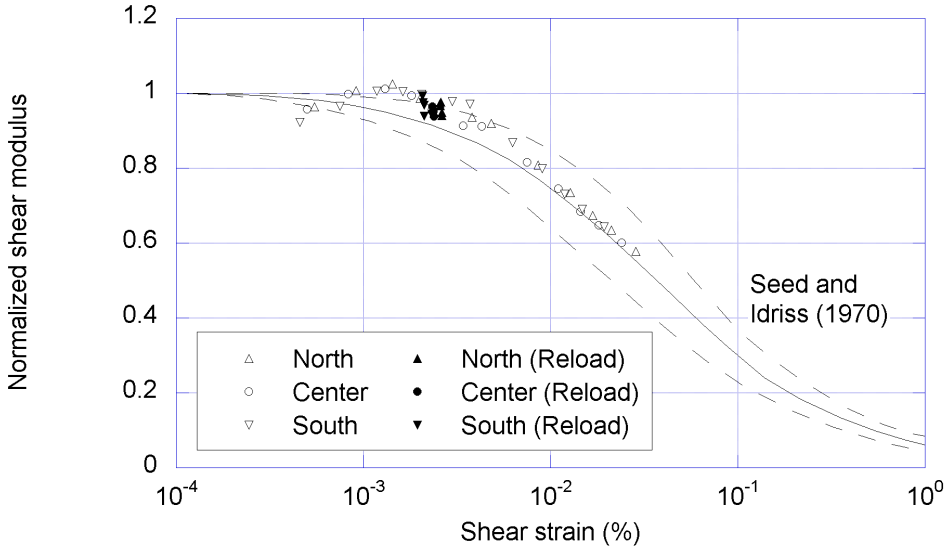

(b) Normalized modulus reduction curves compared to Seed and Idriss (1970)

Figure 4.29 In situ shear modulus reduction curve under 8 kips static load using inverse analysis

foundation using the proposed inversion method. The in situ shear modulus reduction curve can be estimated assuming a damping curve. If the shear modulus reduction curves were estimated from phase differences, the damping curve would be estimated using the proposed inversion procedure.

In situ modulus reduction curves were generated using the phase difference analysis with horizontal excitation data from the Capital Aggregate Quarry site, and using the inverse analysis with vertical excitation data from the Texas A&M University Riverside Campus. The surface layer of both sites was a silty sand. For the inversion procedure, the mean damping curve for cohesionless soils proposed by Seed and Idriss (1970) was assumed in the numerical model. Estimated nonlinear shear moduli presented very consistent trends regardless of analysis method and test site. They showed larger elastic threshold shear strains than those of cohesionless soils proposed by Seed and Idriss (1970) based on laboratory tests. Elastic threshold shear strains were 1.5×10^{-3} % for the Capital Aggregate Quarry site and 2×10^{-3} % for the Texas A&M University site. Then, they closely followed the mean modulus reduction curve of Seed and Idriss (1970) at strains larger than 6×10^{-3} % for both sites..

CHAPTER V

DYNAMIC CHARACTERISTICS OF VERTICALLY EXCITED SURFACE FOUNDATION

5.1. Introduction

In the design stage of the field experiments, it is not an easy task to determine the details of setup and procedure of the field test which produce the levels of response that we want to observe. Therefore, the response of a surface foundation under dynamic loading is an useful information for determination of test setup and procedure. Estimating the behavior of a surface foundation is also an important subject in the field of seismic soil-structure interaction. A number of studies have focused on the dynamic behavior of surface foundations assuming the foundation as a harmonically excited massless disk on an elastic medium (Shah, 1968; Kashio, 1970; Luco and Westmann, 1971; Veletsos and Wei, 1971; Meek, 1972; Veletsos and Verbic, 1974; Kausel, 1974). Once the steady state response of a disk under harmonic excitation is estimated, it can be inserted in the equation of motion for the soil-structure system using an appropriate model for the structure (Parmelee, 1967). The transient response of the soil-structure system under an impact, or any arbitrary loading, can also be evaluated by Fourier analysis assuming the response of the system remains linear.

In this chapter, sets of parametric studies were conducted to investigate the effect of properties of foundation and soil on the response of the foundation under vertical dynamic excitations. To quantify the response of the foundation, the undamped natural, damped natural, and resonant frequencies of a soil-mass system and its damping ratio were calculated assuming the soil-foundation structure as an equivalent SDOF (single degree of freedom) system. The shear wave velocity, density and

Poisson's ratio of the soil, modeled as an elastic material, and the radius and mass of a rigid disk, representing a foundation, were varied in the parametric analysis. The frequency response functions were calculated using the approximated solution formulated by Verbic (1972), and the undamped natural, damped natural and resonant frequencies and the damping ratio were estimated assuming the system as a SDOF. Finite element analyses using the consistent transmitting boundary (Kausel, 1974) were used also to model a uniform case, as well as a simple layered profile with two layers. The effect of different combinations of shear wave velocities or densities in the two layers on the dynamic properties of the system was evaluated. In addition, the frequency dependence of the response of a soil-foundation system was estimated using an experimental study. A set of stepped sine testing was performed with a large scale shaker at the Capital Aggregate Quarry site. The frequencies and damping ratio were also calculated using the experimental results under SDOF assumption. Another set of finite element analyses was conducted with the material properties measured at the Capital Aggregate Quarry site, then the dynamic properties of the foundation obtained from finite element analyses were compared with those from the field experiments as a mean to observe how the results of numerical study are consistent with those of experimental study.

5.2. Rigid Disk on Elastic Halfspace

A set of parametric studies was conducted to investigate the effect of the physical properties of the soil on top on the frequencies and the damping ratio of the soil-mass system. The shear wave velocity, the density and Poisson's ratio of the soil, as well as the radius and the mass of the rigid disk were varied. The frequency response functions were calculated using an approximated solution suggested by Verbic (1972), then

the frequencies and the damping ratio were estimated assuming the soil-foundation structure as a SDOF (single degree of freedom) system.

5.2.1. Background

A vertically excited surface foundation is schematically represented in Figure 5.1. The system includes a rigid, massless disk placed on the surface of a non-dissipative, homogeneous, linear elastic halfspace. The disk is subjected to a harmonic vertical force $P_z e^{i\omega t}$ with an excitation amplitude P_z and a circular frequency ω, resulting in a vertical displacement of amplitude w_0. The amplitudes of excitation and displacement are related as

$$w_0 = H_z(\omega) P_z \tag{5.1a}$$

$$P_z = Q_z(\omega) w_0 \tag{5.1b}$$

where $H_z(\omega)$ and $Q_z(\omega)$ are the frequency response functions of a given system, such that $H_z(\omega) = Q_z(\omega)^{-1}$. The frequency response function Q_z can be represented by real and imaginary terms, K_{real} and K_{imag}, as

$$Q_z = K_{real} + iK_{imag} \tag{5.2}$$

where the imaginary part K_{imag} is the viscous damping c multiplied by the circular loading frequency ω ($K_{imag} = \omega c$). Equation 5.2 is also expressed in dimensionless terms as

$$Q_z = K_z(k_z + ia_0 c_z) \tag{5.3}$$

where k_z and c_z are dimensionless dynamic coefficients, function of the Poisson's ratio ν of the halfspace and the dimensionless frequency parameter $a_0 = \omega R/c_s$. R and c_s represent the radius of the disk, and the shear wave propagation velocity in the

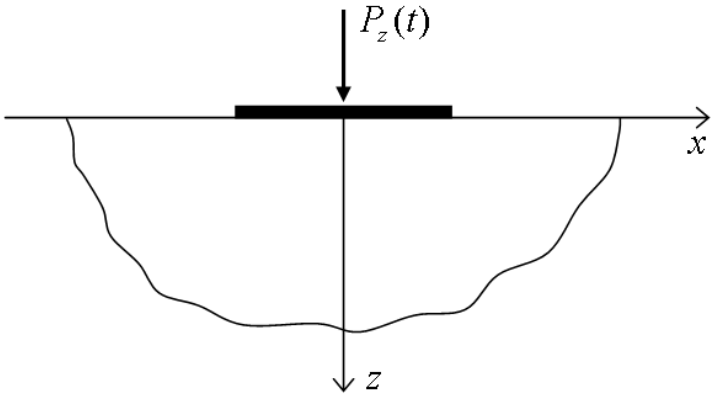

Figure 5.1 Vertically excited rigid disk on elastic halfspace

elastic halfspace, respectively. The quantity K_z is the vertical static stiffness of the system defined as

$$K_z = \frac{4GR}{1-\nu} \tag{5.4}$$

where G is the shear modulus of the elastic halfspace. The shear modulus can be evaluated from the shear wave velocity using the equation, $G = \rho c_s^2$, ρ being the density of the halfspace. The dimensionless dynamic coefficients k_z and c_z are frequency-dependent as presented in solid line in Figure 5.2. Numerical values of these coefficients are available in the work of Shah (1968). The response was estimated assuming that the tangential components of the contact pressure are zero at the interface between the rigid disk and the elastic halfspace (smooth foundation). No load was applied to the surface beyond the disk footprint.

An approximation of the frequency response functions was presented by Verbic

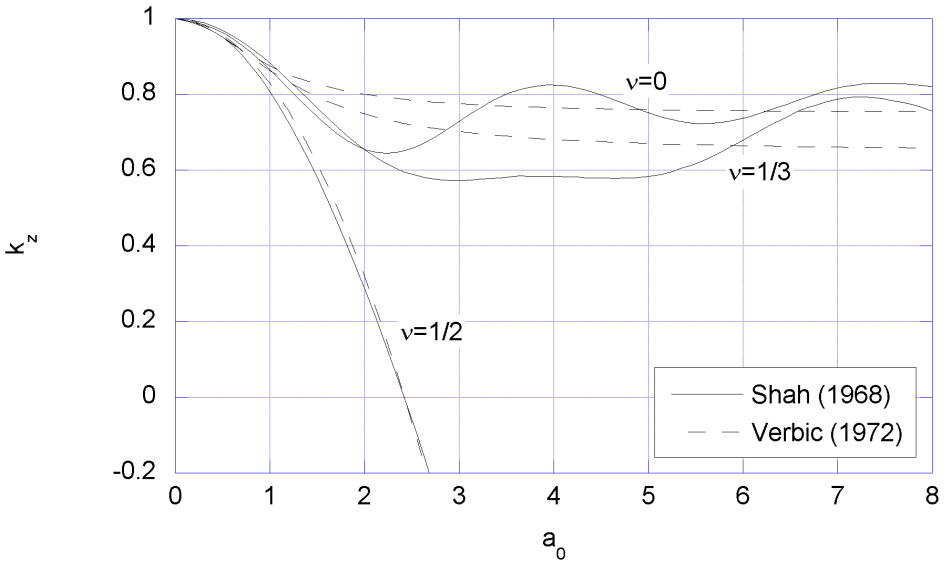

(a) Real part k_z

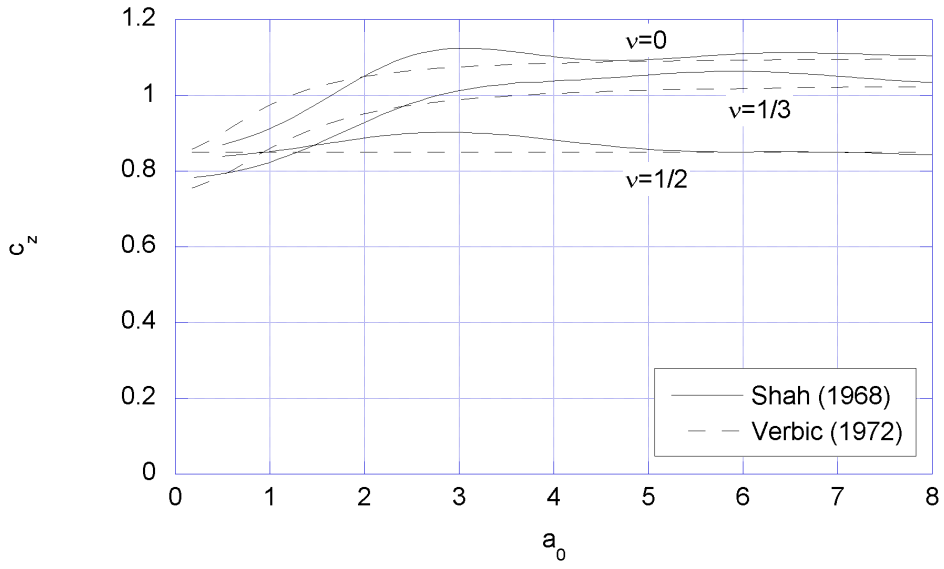

(b) Imaginary part c_z

Figure 5.2 Frequency response functions for vertically excited disk

Table 5.1 Coefficients b_{xi}, $b_{\theta i}$ and b_{zi} for frequency response function (after Verbic, 1972)

ν	0	0.33	0.5
b_{z1}	0.25	0.35	0
b_{z2}	1.0	0.8	0
b_{z3}	0	0	0.17
b_{z4}	0.85	0.75	0.85

(1972):

$$k_z = 1 - b_{z1}\frac{(b_{z2}a_0)^2}{1+(b_{z2}a_0)^2} - b_{z3}a_0^2 \tag{5.5a}$$

$$c_z = b_{z4} + b_{z1}b_{z2}\frac{(b_{z2}a_0)^2}{1+(b_{z2}a_0)^2} \tag{5.5b}$$

$$Q_z = K_z[1 + ib_{z4}a_0 - b_{z1}\frac{(b_{z2}a_0)^2}{1+ib_{z2}a_0} - b_{z3}a_0^2]. \tag{5.6}$$

The coefficients b_{z1}, b_{z2}, b_{z3} and b_{z4} depend on Poisson's ratio as shown in Table 5.1. The coefficients k_z and c_z from the approximate solution are illustrated in Figure 5.2 in dashed lines. The frequency response function of the system including the mass of the rigid disk m can be derived through equilibrium considerations as

$$\frac{P(\omega)}{W(\omega)} = Q_z(a_0) - m\omega^2. \tag{5.7}$$

Equation 5.7 with the approximate frequency response function Q_z, was used to analyze the vertically excited system in this study.

5.2.2. Analytical Approaches

Three different approaches to extract the undamped natural, damped natural and resonant frequencies and the damping ratio from the frequency response functions

are presented in this section. In all the approaches the system consisting of the rigid disk and the elastic halfspace is simplified to a SDOF system considering the disk as a point mass, and the elastic medium as a single, frequency dependent spring and dashpot.

5.2.3. Spring Constant Approach

The undamped natural frequency and the damping ratio of a system can be evaluated based on the real and imaginary dynamic coefficients k_z and c_z of the frequency response function Q_z. The procedure is illustrated schematically in Figure 5.3. The dimensionless undamped natural frequency a_n of the soil-structure system is estimated at the intersection of the curve of k_z and $\omega_n = \sqrt{K_{real}/m}$ as shown in Figure 5.3(a). The dimensionless coefficient c_1 is the value of c_z at the dimensionless undamped natural frequency a_n (Figure 5.3(b)). Then, a_n and c_1 are used to obtain the undamped natural circular frequency ω_n, and the damping ratio ξ. The damped natural circular frequency ω_D and the resonant circular frequency ω_r are estimated from

$$\omega_D = \omega_n \sqrt{1 - \xi^2} \tag{5.8a}$$

$$\omega_r = \omega_n \sqrt{1 - 2\xi^2} \tag{5.8b}$$

which are valid for damping ratio smaller than $1/\sqrt{2}$.

5.2.4. Maximum Response Approach

The resonant frequency and the damping ratio can be evaluated from the dynamic response factor of the SDOF system in Figure 5.4. The resonant frequency is defined as the forcing frequency at which the largest response occurs (Chopra, 2001). Practically, in most common buildings, the difference between the resonant and natural

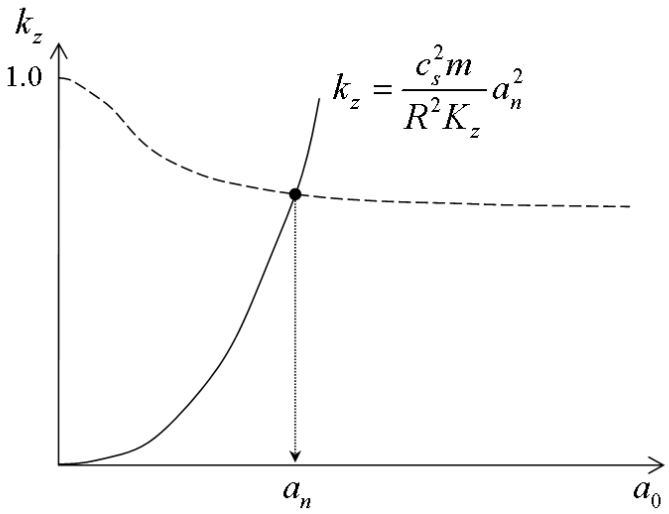

(a) Real part k_z

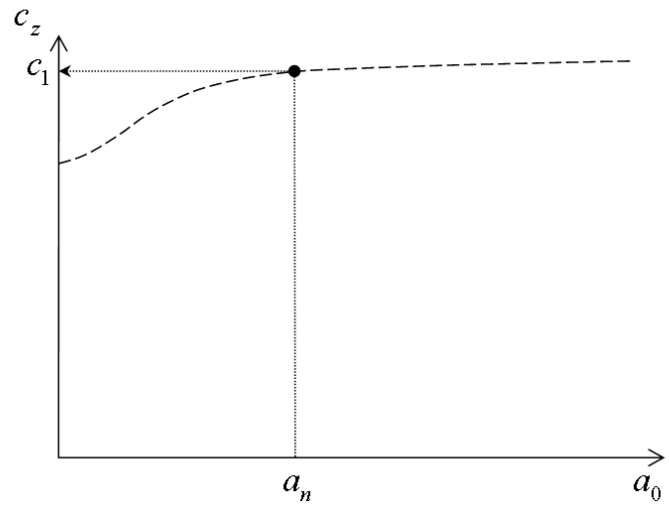

(b) Imaginary part c_z

Figure 5.3 Undamped natural frequency and damping ratio using static spring constant approach

frequencies is not significant. In the system investigated here, the difference is far more than that for a normal building, as the energy dissipation in the halfspace can be very large. For a damping ratio ξ smaller than $1/\sqrt{2}$, the resonant circular frequencies for displacement $\omega_{r,d}$, for velocity $\omega_{r,v}$, and for acceleration $\omega_{r,a}$ are derived as

$$\omega_{r,d} = \omega_n \sqrt{1 - 2\xi^2} \tag{5.9a}$$

$$\omega_{r,v} = \omega_n \tag{5.9b}$$

$$\omega_{r,a} = \omega_n / \sqrt{1 - 2\xi^2}. \tag{5.9c}$$

The maximum dynamic response factors for displacement R_d, velocity R_v, acceleration R_a corresponding to their respective resonant frequencies are

$$R_{d,max} = \frac{1}{2\xi\sqrt{1 - \xi^2}} \tag{5.10a}$$

$$R_{v,max} = \frac{1}{2\xi} \tag{5.10b}$$

$$R_{a,max} = \frac{1}{2\xi\sqrt{1 - \xi^2}}. \tag{5.10c}$$

Since the dynamic response factor for displacement, R_d, is the ratio of the amplitude of the dynamic displacement to the static displacement, it can be evaluated from the frequency response function H_z which is the inverse of Q_z as

$$R_d = K_z |H_z(\omega)|. \tag{5.11}$$

The resonant frequency for displacement $\omega_{r,d}$ and the damping ratio ξ were estimated from the maximum value of the dynamic response factor for displacement in this part of study.

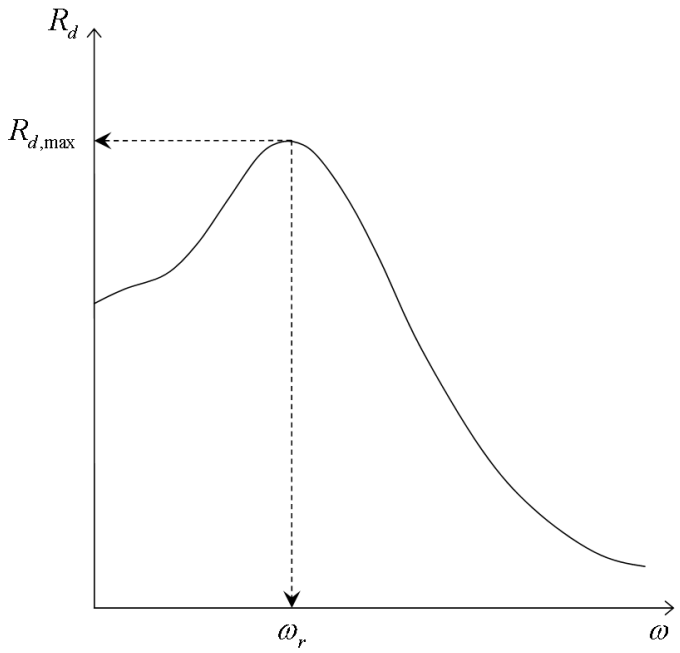

Figure 5.4 Resonant frequency and damping ratio using maximum response approach

5.2.5. Velocity Time History Approach

The damped natural frequency and the damping ratio can be estimated from the free vibration response history of the system. A triangular impulse with the duration T_d, shown in Figure 5.5, is transformed to the frequency domain and multiplied by the frequency response function Q_z. The displacement time history of the system is obtained by transforming the result back to the time domain using the inverse Fourier transform. Although this is not the true free vibration response of the system, the two are quite similar for small impact durations. The damped natural frequency and damping ratio are evaluated from the ratio of two successive maximum and minimum, or minimum and maximum. The displacement $u(t)$ of a viscously damped SDOF system in the free vibration at time t is

$$u(t) = e^{-\xi\omega_n t}[A\cos\omega_D t + B\sin\omega_D t] \tag{5.12}$$

where the coefficients A and B can be obtained from the initial conditions as $A = u(0)$, $B = [\dot{u}(0) + \xi\omega_n u(0)]/\omega_D$. The ratio of the displacement at time t to the displacement at $T_D/2$, a half vibration period later, is

$$\frac{u(t)}{u(t + T_D/2)} = -e^{\xi\omega_n T_D/2}. \tag{5.13}$$

Then, the damping ratio can be evaluated from

$$\xi = \frac{\delta}{\sqrt{\delta^2 + \pi^2}} \tag{5.14}$$

where $\delta = \ln[-u_i/u_{i+1}]$. The quantities u_i and u_{i+1} represent two successive maximum and minimum, or minimum and maximum. The damped natural frequency is estimated from the half of the damped period $T_D/2$. This approach is illustrated in Figure 5.6 and is also valid for the velocity or the acceleration time history. The

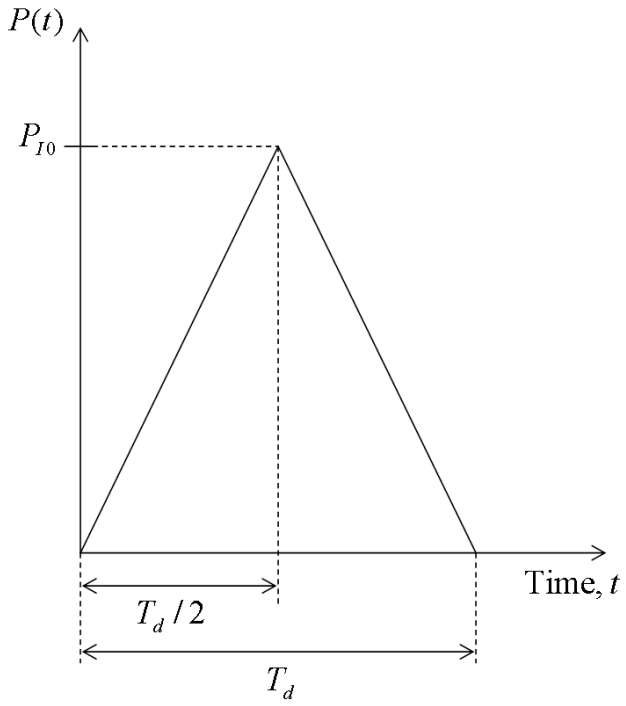

Figure 5.5 Triangular impact used in analysis

velocity time history was used to estimate the dynamic properties in this study.

5.2.6. Parametric Studies

A series of parametric studies were performed to evaluate the effect of the properties of the foundation, represented by a rigid disk, and the soil, as an elastic halfspace, on the frequency response and the damping ratio of the vertically excited system. The effects of the shear wave velocity c_s, the density ρ and Poisson's ratio ν of the halfspace, the radius R and the mass m of the disk, and the duration of an impact T_d are presented in this section. After performing an analysis with a baseline set of properties, each property was modified independently to assess changes in the results. The baseline set of properties used is presented in Table 5.2.

The undamped natural cyclic frequency f_n, the damped natural cyclic frequency

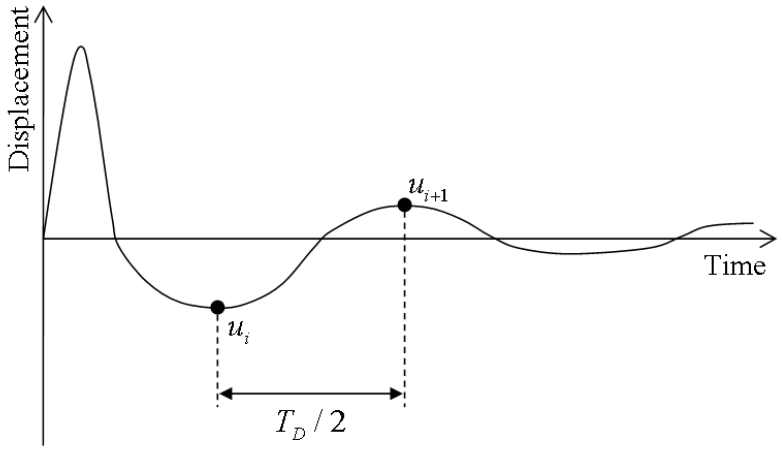

Figure 5.6 Damped natural frequency and damping ratio using velocity time history approach

Table 5.2 Baseline set of properties used for parametric study

Property	Value
c_s	180 m/s
ρ	2000 kg/m^3
ν	0.25
R	0.457 m
m	500 kg
T_d	1.0×10^{-2} s

f_D, the resonant cyclic frequency f_r, and the damping ratio ξ for the different sets of input properties were estimated using the three different approaches described in the previous sections and are tabulated in Tables 5.3 to 5.5. Although the results show some differences due to the interpretations, they display the same trends. The shear wave velocity c_s of an elastic halfspace has the largest effect on the frequencies of the system, as the modulus depends on the wave velocity following a quadratic relationship. Since the wave velocity shows no effect on the damping ratio ξ, it affects all the frequencies in the same way. Thus, all the frequencies - the undamped natural frequency f_n, the damped natural frequency f_D, and the resonant frequency f_r - increased when the shear wave velocity c_s increased. The damping ratio ξ increases when the density of the medium, ρ, increases. The effects of ρ on the frequencies are not straightforward. The undamped natural frequency f_n and the damped natural frequency f_D increase, while the resonant frequency f_r decreases with increasing density. The effect of Poisson's ratio ν is not significant, considering the wide range of values tried herein. The radius R of the disk has a large effect on the damping ratio and a limited one on the frequencies (since the damping in the system is 'geometric' damping). The undamped natural frequency f_n increases with increasing radius; however the changes in the damped natural frequency f_D and the resonant frequency f_r are not straightforward as they are also influenced by the damping ratio ξ, which increases when the radius increases. The mass m of a disk also has significant effect on the damping ratio and a limited one on the frequencies, but in a reversed trend to that of the radius R. The undamped natural frequency f_n and the damping ratio ξ tends to decrease when the mass m increases. The frequencies and the damping ratio estimated with three different durations of impact T_d for the velocity time history approach are presented at the bottom of Table 5.5. The effect of the impact duration T_d is not critical within the range of values used here, which may not be true for larger

value of T_d. Not only the results described here are meaningful by themselves, they also provide useful information for the preparation of the field tests. The response of a foundation under selected amplitude of dynamic excitation can be controlled by changing size, mass of the foundation, or excitation frequency.

5.3. Rigid Disk on Layered Media

A subsurface profile can be generally described by a series of horizontal layers with different material properties. This causes wave reflections and refractions on the interfaces between layers and prevents the system of interest from acting as a uniform ideal system. In this section, the effects of layers on the frequencies and the damping ratio of the system consisting of a vertically excited rigid circular footing on a layered medium were observed using a finite element program with the consistent transmitting boundary of Kausel (1974).

5.3.1. Background

A rigid footing imposed on the stratified soil deposit is considered. The core region under the footing is modeled with toroidal finite elements in cylindrical coordinates, expanding the solution in a Fourier series in the circumferential direction, and the outside region is modeled using the consistent boundary for the same number of the Fourier expansion. For the case of a vertical load, the problem is axisymmetric and only the $n = 0$ term of the expansion is needed. This model requires the discretization of the soil into thin layers, assuming a linear variation of the displacements in the vertical direction within each layer. In addition, the core region is also discretized in the radial direction. The model assumes the existence of much stiffer, essentially rigid, rock at a depth.

Table 5.3 Frequencies and damping ratio of system with elastic halfspace (spring constant approach)

Modified property		f_n (Hz)	f_D (Hz)	f_r (Hz)	ξ
c_s	141	63.5	50.9	33.7	0.60
(m/s)	162	73.0	58.4	38.7	0.60
	180	81.1	64.9	43.0	0.60
	198	89.2	71.4	47.3	0.60
	216	97.3	77.9	51.6	0.60
ρ	1600	73.2	61.9	48.0	0.53
(kg/m^3)	1800	77.3	63.6	46.1	0.57
	2000	81.1	64.9	43.0	0.60
	2200	84.6	65.7	38.3	0.63
	2400	88.1	66.2	31.7	0.66
ν	0.00	71.7	53.0	42.7	0.57
	0.25	81.1	64.9	43.0	0.60
	0.33	85.1	67.2	42.1	0.61
	0.50	88.8	70.8	46.3	0.60
R	0.229	61.7	60.4	59.2	0.20
(m)	0.305	69.6	66.0	62.2	0.32
	0.457	81.1	64.9	43.0	0.60
m	500	81.1	64.9	43.0	0.60
(kg)	750	67.4	58.9	49.0	0.49
	1000	59.1	53.7	47.8	0.42
	1250	53.3	49.5	45.4	0.37

Table 5.4 Frequencies and damping ratio of system with elastic halfspace (maximum response approach)

Modified property		f_n (Hz)	f_D (Hz)	f_r (Hz)	ξ
c_s	141	53.1	45.0	35.2	0.53
(m/s)	162	61.0	51.7	40.4	0.53
	180	67.8	57.5	44.9	0.53
	198	74.5	63.2	49.4	0.53
	216	81.3	69.0	53.9	0.53
ρ	1600	65.0	56.7	47.0	0.49
(kg/m^3)	1800	66.5	57.2	46.0	0.51
	2000	67.8	57.5	44.9	0.53
	2200	68.7	57.6	43.7	0.55
	2400	69.3	57.4	42.3	0.56
ν	0.00	62.1	53.2	42.5	0.52
	0.25	67.8	57.5	44.9	0.53
	0.33	70.3	59.3	45.8	0.54
	0.50	89.4	71.3	46.7	0.60
R	0.229	61.6	60.4	59.1	0.20
(m)	0.305	68.3	64.9	61.3	0.31
	0.457	67.8	57.5	44.9	0.53
m	500	67.8	57.5	44.9	0.53
(kg)	750	61.8	55.1	47.4	0.45
	1000	56.1	51.5	46.3	0.40
	1250	51.6	48.2	44.4	0.36

Table 5.5 Frequencies and damping ratio of system with elastic halfspace (velocity time history approach)

(a) With varying material properties of soil

Modified property		f_n (Hz)	f_D (Hz)	f_r (Hz)	ξ
c_s	141	57.5	46.5	32.0	0.59
(m/s)	162	64.8	52.6	36.6	0.58
	180	73.2	59.5	41.6	0.58
	198	81.8	66.7	46.9	0.58
	216	87.4	71.4	50.6	0.58
ρ	1600	65.5	55.6	43.4	0.53
(kg/m^3)	1800	70.8	58.8	43.7	0.56
	2000	73.2	59.5	41.6	0.58
	2200	73.9	58.8	38.3	0.60
	2400	75.3	58.8	35.4	0.62
ν	0.00	65.4	54.1	39.6	0.56
	0.25	73.2	59.5	41.6	0.58
	0.33	72.8	58.8	40.2	0.59
	0.50	89.6	71.4	46.7	0.60

Table 5.5 Continued

(b) With varying properties of footing and duration of impact

Modified property		f_n (Hz)	f_D (Hz)	f_r (Hz)	ξ
R	0.229	60.1	58.8	57.6	0.20
(m)	0.305	65.9	62.5	58.8	0.32
	0.457	73.2	59.5	41.6	0.58
m	500	73.2	59.5	41.6	0.58
(kg)	750	63.6	55.6	46.1	0.49
	1000	56.5	51.3	45.5	0.42
	1250	51.3	47.6	43.6	0.37
T_d	2.0×10^{-3}	71.6	57.5	38.5	0.60
(s)	4.0×10^{-3}	72.3	58.1	39.1	0.59
	1.0×10^{-2}	73.2	59.5	41.6	0.58

The real and imaginary parts of the frequency response function Q_z of the rigid footing on the layered medium can be evaluated using finite element analysis. The frequencies and the damping ratio of the system will be evaluated by the three approaches presented above considering the system as a SDOF system. The frequency response function Q_z is expressed in terms of dimensionless terms following Equation 5.3 as

$$Q_z = K_z(k_z + ia_0c_z).$$

If $a_0 = 0$, the frequency response function Q_z becomes the static stiffness of the system. In the parametric study, the real part of the frequency response function Q_z from finite element analysis when $a_0 = 0$ is considered as the static stiffness.

5.3.2. Definition of Finite Element Model

The estimated dimensionless coefficients k_z and c_z from finite element analysis were compared with those from the elastic halfspace solution. The finite element analysis was performed with $c_s = 180$ m/s, $\rho = 2000$ kg/m^3, $\nu = 0.25$, $R = 0.457$ m. The rigid bottom boundary was at a depth of $48R$ away from the surface. A mesh with square elements of size $\Delta L = R/4$ was used for the whole finite element region and 5 % internal hysteric damping was applied to prevent excessive fluctuation of the frequency response functions due to the natural frequencies of the soil layer. This damping effect was then subtracted from the results after calculation of the frequency response functions. The real and imaginary parts of the frequency response function without internal damping K'_{real} and K'_{imag} can be calculated from those with internal

damping K^D_{real} and K^D_{imag}as:

$$K'_{real} = K^D_{real} + D \cdot K^D_{imag} \tag{5.15}$$

$$K'_{imag} = K^D_{imag} - 2 \cdot D \cdot K^D_{real}. \tag{5.16}$$

Figures 5.7 and 5.8 show the results of the finite element analysis compared with the elastic halfspace solution by Shah (1968), and Figure 5.9 with the approximated solution of Verbic (1972). For the purpose of comparison, and only in this case, the analytical static stiffness for an elastic halfspace, $K_z = 4GR/(1-\nu)$, was used for the interpretation of the finite element analysis results. The results from the finite element model and the analytical solutions are in good agreement, which indicates that the finite element model can replicate the analytical elastic halfspace solutions.

To ensure that the finite element analysis gives reasonable results with different properties, two sets of finite element analyses were conducted and compared with those from the approximate solution of Verbic (1972). The analyses were performed with finite elements for 0.8, 0.9, 1.0, 1.1, 1.2 times the shear wave velocity $c_s = 180$m/s and the same scales of density $\rho = 2000\ \mathrm{kg/m^3}$. In Tables 5.6 to 5.8, the results of both sets are tabulated. The results from two methods have same trends for varying parameters, showing the finite element analysis gives consistent results with the analytical solution. In next section, the analysis of the rigid footing system on layered medium will be made within the range of c_s and ρ used here using the finite element analysis.

5.3.3. Parametric Studies

A set of parametric studies was performed using the finite element model to estimate the effect of varying shear wave velocity or density in a layered soil deposit on the evaluation of frequencies and damping ratio of the system. The schematic represen-

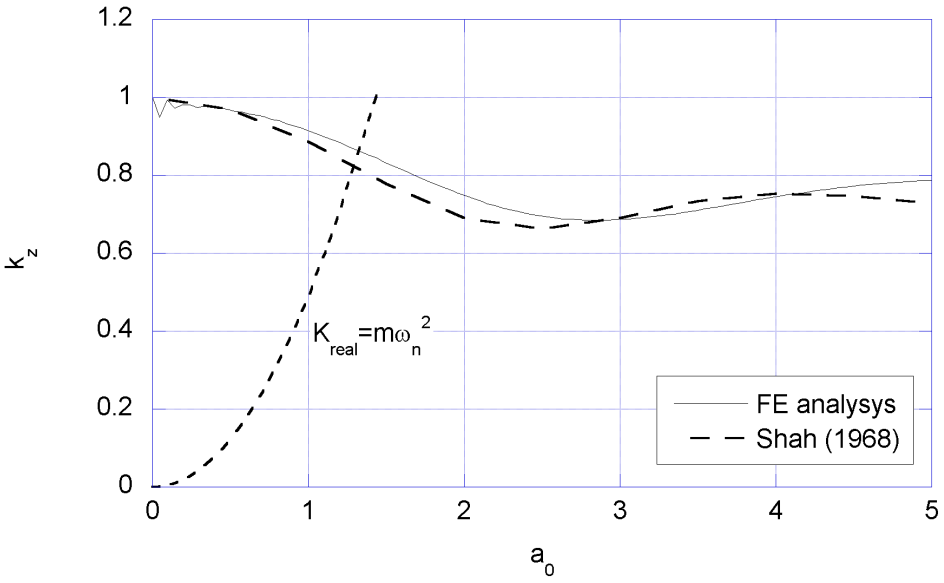

(a) Real part k_z

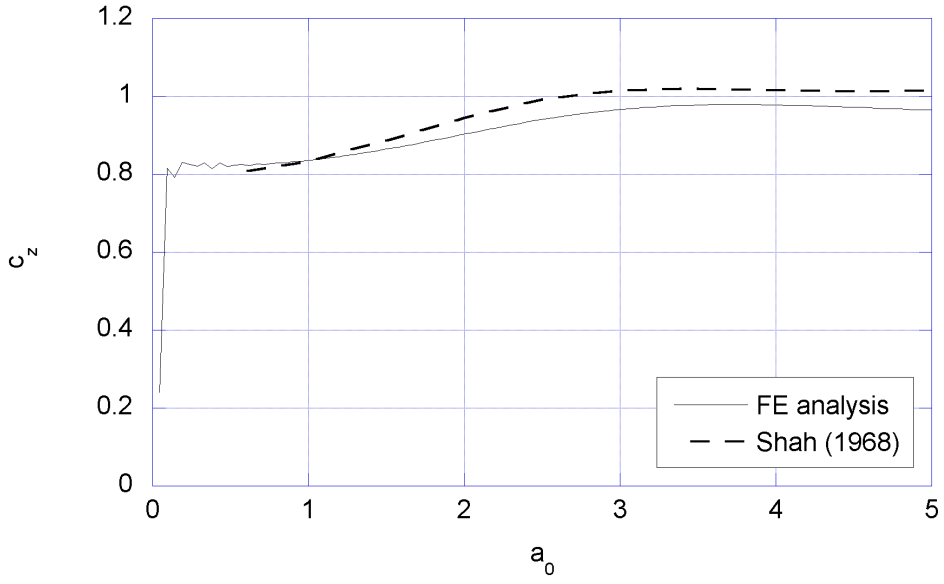

(b) Imaginary part c_z

Figure 5.7 Frequency response functions from FE analysis and exact solution

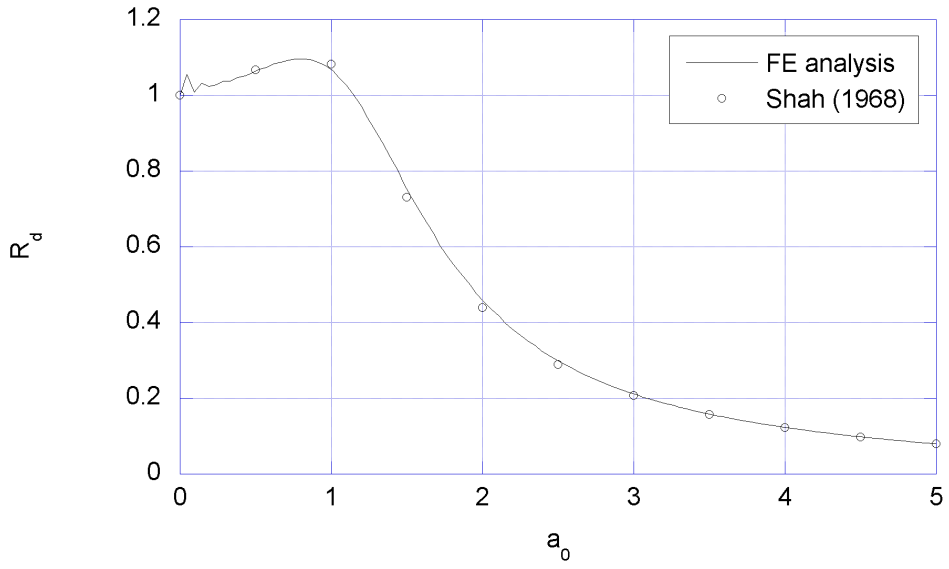

Figure 5.8 Dynamic response factors from FE analysis and exact solution

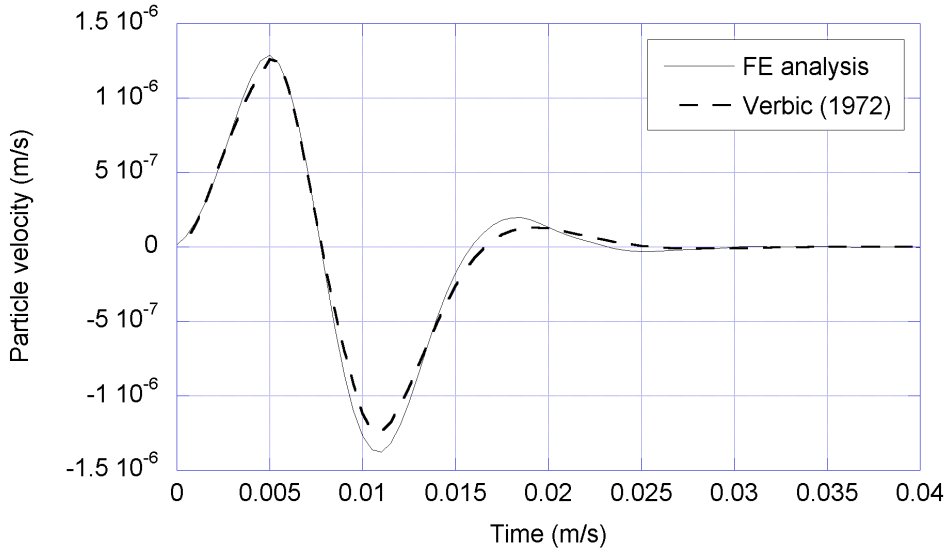

Figure 5.9 Particle velocity time histories from FE analysis and exact solution

Table 5.6 Comparison of results of the approximate solution and FE analysis (spring constant approach)

(a) FE analysis results

Modified parameter		f_n (Hz)	f_D (Hz)	f_r (Hz)	ξ
c_s	141	65.1	53.7	39.1	0.57
(m/s)	162	74.8	61.7	44.9	0.57
	180	83.1	68.5	49.9	0.57
	198	91.4	75.4	54.9	0.57
	216	99.7	82.2	59.9	0.57
ρ	1600	75.2	64.8	52.4	0.51
(kg/m^3)	1800	79.3	66.9	51.5	0.54
	2000	83.1	68.5	49.9	0.57
	2200	86.7	69.8	47.3	0.59
	2400	90.0	70.8	43.8	0.62

(b) Approximated solution results

Modified parameter		f_n (Hz)	f_D (Hz)	f_r (Hz)	ξ
c_s	141	63.5	50.9	33.7	0.60
(m/s)	162	73.0	58.4	38.7	0.60
	180	81.1	64.9	43.0	0.60
	198	89.2	71.4	47.3	0.60
	216	97.3	77.9	51.6	0.60
ρ	1600	73.2	61.9	48.0	0.53
(kg/m^3)	1800	77.3	63.6	46.1	0.57
	2000	81.1	64.9	43.0	0.60
	2200	84.6	65.7	38.3	0.63
	2400	88.1	66.2	31.7	0.66

Table 5.7 Comparison of results of the approximate solution and FE analysis (maximum response approach)

(a) FE analysis results

Modified parameter		f_n (Hz)	f_D (Hz)	f_r (Hz)	ξ
c_s	141	59.5	49.9	38.0	0.54
(m/s)	162	67.2	56.4	43.0	0.54
	180	76.6	64.3	49.0	0.54
	198	81.3	68.2	52.0	0.54
	216	90.6	76.1	58.0	0.54
ρ	1600	74.2	64.4	53.0	0.49
(kg/m^3)	1800	77.5	66.2	52.5	0.52
	2000	76.6	64.3	49.0	0.54
	2200	77.9	64.3	47.0	0.56
	2400	82.2	66.8	46.5	0.58

(b) Approximated solution results

Modified parameter		f_n (Hz)	f_D (Hz)	f_r (Hz)	ξ
c_s	141	53.1	45.0	35.2	0.53
(m/sec)	162	61.0	51.7	40.4	0.53
	180	67.8	57.5	44.9	0.53
	198	74.5	63.2	49.4	0.53
	216	81.3	69.0	53.9	0.53
ρ	1600	65.0	56.7	47.0	0.49
(kg/m^3)	1800	66.5	57.2	46.0	0.51
	2000	67.8	57.5	44.9	0.53
	2200	68.7	57.6	43.7	0.55
	2400	69.3	57.4	42.3	0.56

Table 5.8 Comparison of results of the approximate solution and FE analysis (velocity time history approach)

(a) FE analysis results

Modified parameter		f_n (Hz)	f_D (Hz)	f_r (Hz)	ξ
c_s	141	62.2	52.6	40.9	0.53
(m/s)	162	76.0	64.5	50.5	0.53
	180	78.4	66.7	52.3	0.53
	198	84.4	71.4	55.5	0.53
	216	91.4	76.9	59.0	0.54
ρ	1600	73.4	64.5	54.3	0.48
(kg/m^3)	1800	77.0	66.7	54.4	0.50
	2000	78.4	66.7	52.3	0.53
	2200	79.7	66.7	50.4	0.55
	2400	81.1	66.7	48.0	0.57

(b) Approximated solution results

Modified parameter		f_n (Hz)	f_D (Hz)	f_r (Hz)	ξ
c_s	141	57.5	46.5	32.0	0.59
(m/s)	162	64.8	52.6	36.6	0.58
	180	73.2	59.5	41.6	0.58
	198	81.8	66.7	46.9	0.58
	216	87.4	71.4	50.6	0.58
ρ	1600	65.5	55.6	43.4	0.53
(kg/m^3)	1800	70.8	58.8	43.7	0.56
	2000	73.2	59.5	41.6	0.58
	2200	73.9	58.8	38.3	0.60
	2400	75.3	58.8	35.4	0.62

tation of the uniform and the layered systems used in the analysis is shown in Figure 5.10.

The shear wave velocities and the geometrical characteristics of the various systems used in the analysis are shown in Table 5.9. The first digit in the case number represents the height of the top layer h_t, norimalized by the radius, while zero means the profile is uniform. The second digit indicates the selection of the shear wave velocity for the bottom layer c_{sb}, where the numbers 1, 2, 3, 4, and 5 represent c_{sb} =141 m/s, 162 m/s, 180 m/s, 198 m/s, and 216 m/s, respectively. All the dynamic properties are summarized in Table 5.10. The results of the three different approaches in the case of $h_t = R$ (Figures 5.11, 5.12, and 5.13) are slightly different, but show the same trend with shear wave velocity as the uniform case. The undamped natural frequency f_n of the system - the frequency at the intersection of K_{real} and $K_{real} = m\omega^2$ - increases when the shear wave velocity of the bottom layer c_{sb} increases (Figure 5.11(a)). The damping ratio ξ evaluated from Figure 5.11(b) decreases when c_{sb} increases. The numerical values of the frequencies and the damping ratio are presented in Table 5.10. The numerical results for the layered profile are presented only for the higher shear wave velocity at the bottom (L14, L15, L24, and L25). For the lower shear wave velocity of the bottom layer, the damping ratio is larger than $1/\sqrt{2}$ and Equation 5.8 can no longer be used. The damped natural frequency f_D increases with increasing c_{sb} as shown in Figure 5.13 (the distance between the second and the third peaks gets smaller) and the resonant frequency f_r also increase when c_{sb} increases, as can be seen in Figure 5.12 (the peak of the curve moves to higher frequencies). The damping ratio ξ decreases with increasing c_{sb} in two figures (the particle velocity time history decays slower and the peak of the dynamic response factor R_d increases).

The results for $h_t = 2R$ are presented in Figures 5.14 to 5.16 and Table 5.10. In this case, the change in the shear wave velocity at the bottom c_{sb} has less effect

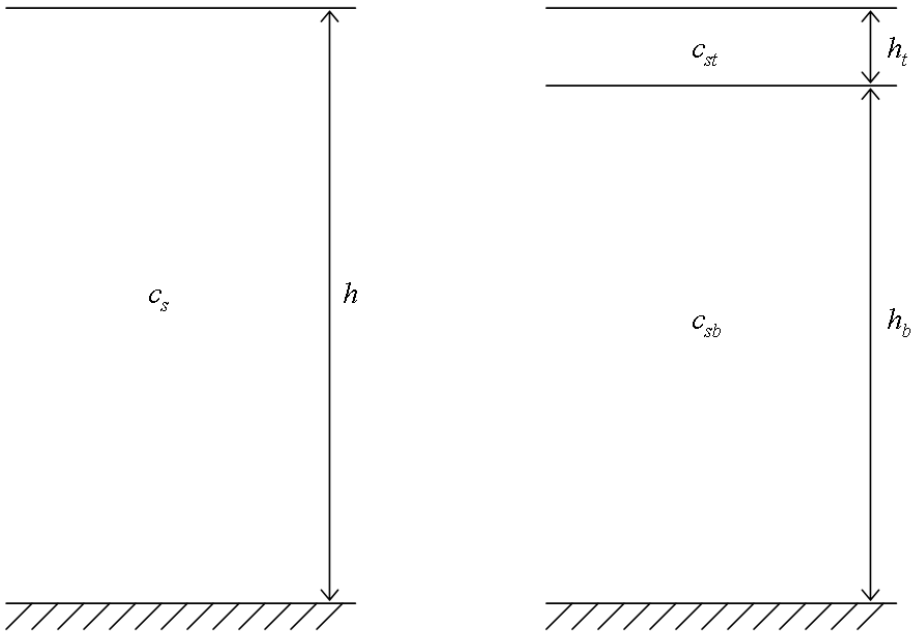

(a) Uniform medium (b) Layered medium

Figure 5.10 Uniform and layered media for varying shear wave velocities

on the dynamic properties of the system since only the deeper part of the profile is affected. In Figure 5.14(a), the undamped natural frequency f_n decreases with increasing shear wave velocity of the bottom layer c_{sb}, because the K_{real} curves for the layered medium intersect at a frequency of approximately 50 Hz and are reversed in order compared to the cases of the uniform medium or $h_t = R$. The damped natural frequency f_D remains approximately the same and the resonant frequency f_r increases with increasing c_{sb} as shown in Figures 5.16 and 5.15, respectively. In both figures, a decreasing damping ratio ξ with increasing c_{sb} is observed. These trends can also be found in the numerical data in Table 5.10.

To estimate the effect of density on the response of a layered system, several finite element analyses with the characteristics given in Table 5.11 were performed. The geometry of the layered system is the same as in the previous section, where

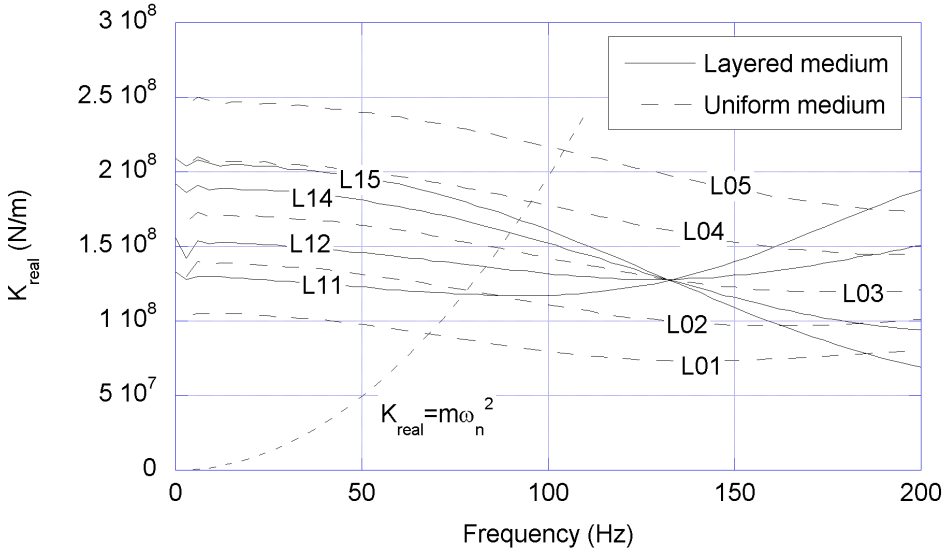

(a) Real part

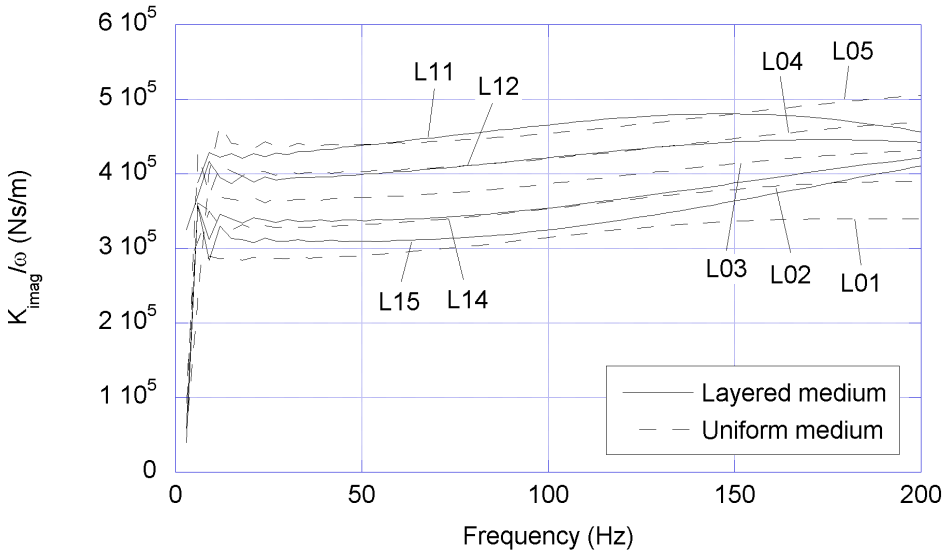

(b) Imaginary part

Figure 5.11 Real and imaginary parts of the frequency response functions for varying shear wave velocities, and $h_t = R$

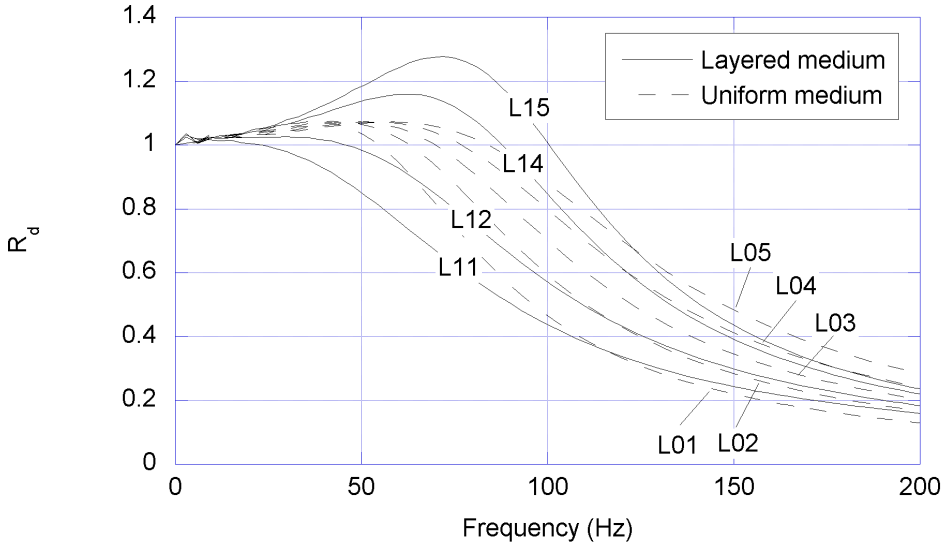

Figure 5.12 Dynamic response curves for varying shear wave velocities, and $h_t = R$

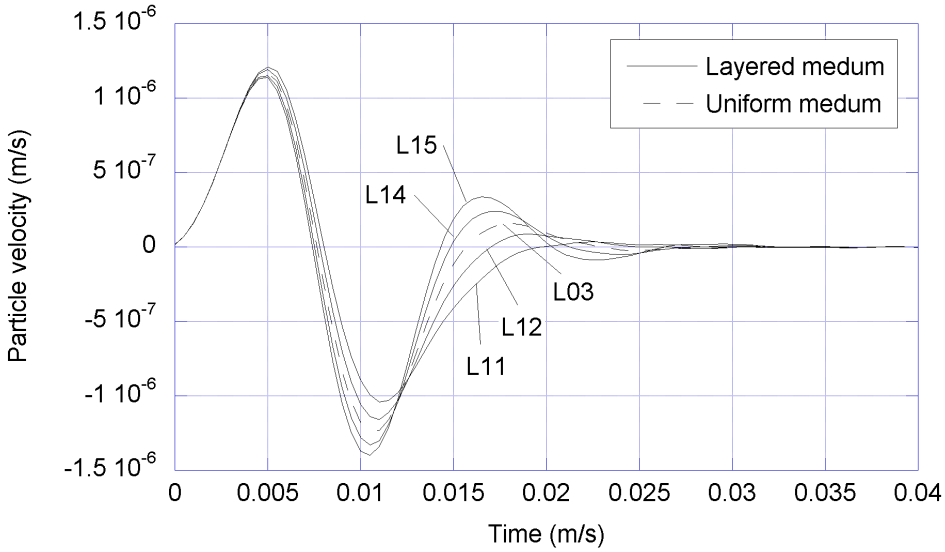

Figure 5.13 Particle velocity time histories for varying shear wave velocities, and $h_t = R$

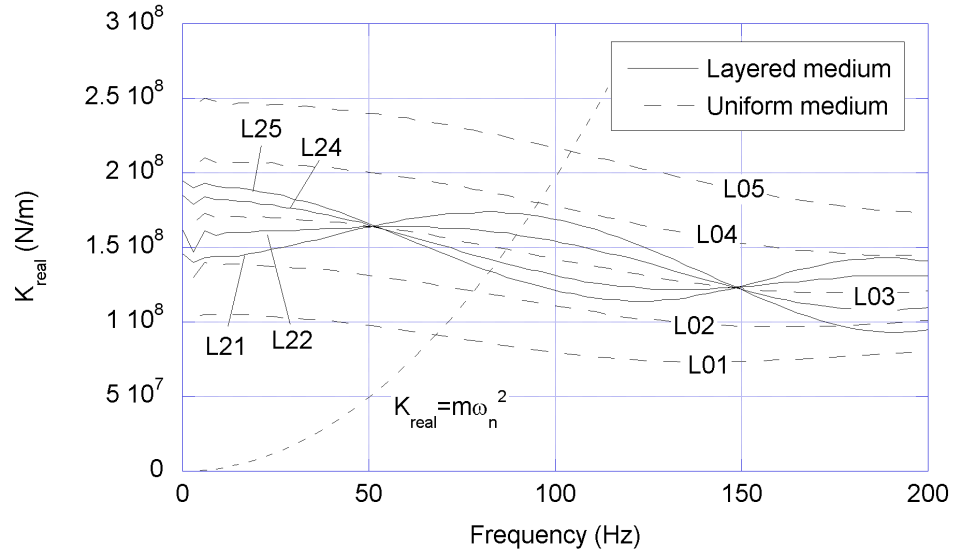

(a) Real part

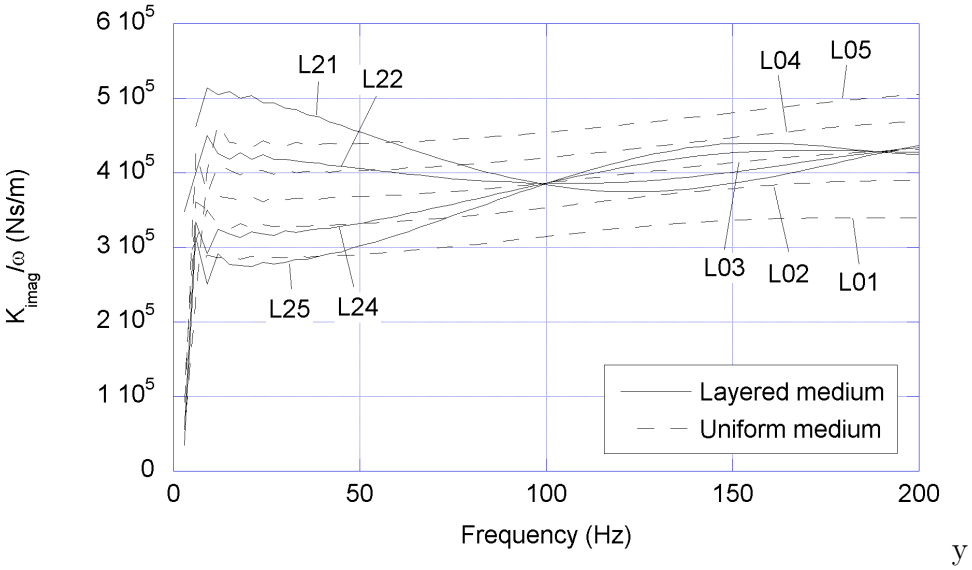

y

(b) Imaginary part

Figure 5.14 Real and imaginary parts of the frequency response functions for varying shear wave velocities, and $h_t = 2R$

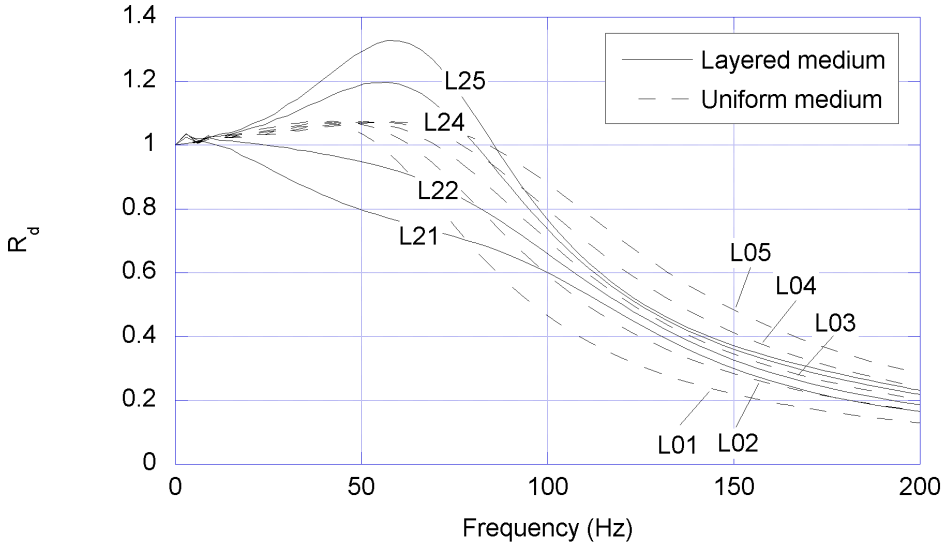

Figure 5.15 Dynamic response curves for varying shear wave velocities, and $h_t = 2R$

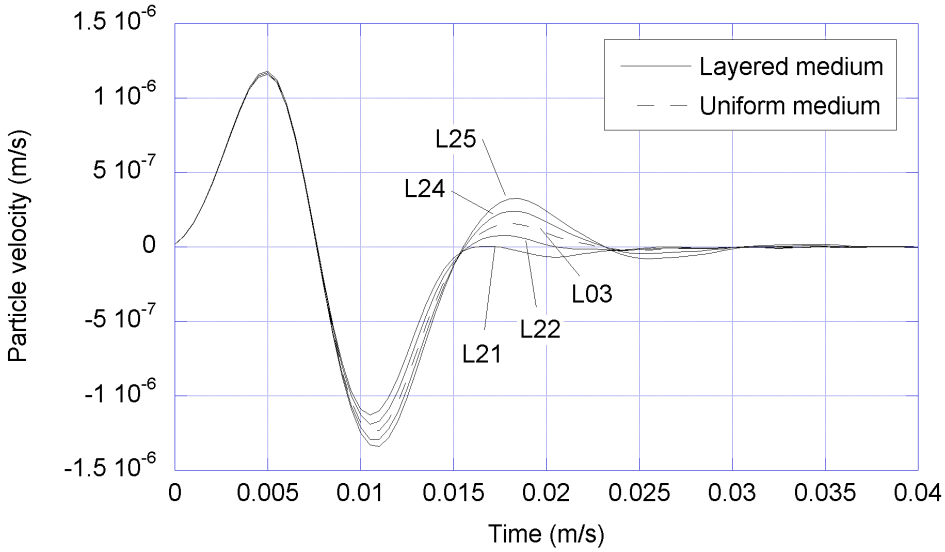

Figure 5.16 Particle velocity time histories for varying shear wave velocities, and $h_t = 2R$

Table 5.9 Properties for the parametric analyses for varying shear wave velocities

(a) Uniform cases

Case number	h	c_s (m/s)
L01	48R	141
L02	48R	162
L03	48R	180
L04	48R	198
L05	48R	216

(b) Layered cases

Case number	h_t	h_b	c_{st} (m/s)	c_{sb} (m/s)
L11	R	$47R$	180	141
L12	R	$47R$	180	162
L14	R	$47R$	180	198
L15	R	$47R$	180	216
L21	$2R$	$46R$	180	141
L22	$2R$	$46R$	180	162
L24	$2R$	$46R$	180	198
L25	$2R$	$46R$	180	216

Table 5.10 Frequencies and damping ratio for uniform and layered media system for varying shear wave velocities

(a) Static spring constant approach

Case number	h	c_s (m/s)	f_n (Hz)	f_D (Hz)	f_r (Hz)	ξ
L01	$48R$	141	68.0	54.7	36.9	0.59
L02	$48R$	162	78.2	62.9	42.4	0.59
L03	$48R$	180	86.9	69.9	47.1	0.59
L04	$48R$	198	95.5	76.9	51.9	0.59
L05	$48R$	216	104.2	83.9	56.6	0.59

Case number	h_t	h_b	c_{st} (m/s)	c_{sb} (m/s)	f_n (Hz)	f_D (Hz)	f_r (Hz)	ξ
L14	R	$47R$	180	198	89.8	77.1	61.9	0.51
L15	R	$47R$	180	216	92.2	82.6	71.6	0.45
L24	$2R$	$46R$	180	198	84.4	71.7	56.2	0.53
L25	$2R$	$46R$	180	216	82.4	72.6	61.3	0.47

Table 5.10 Continued

(b) Maximum response approach

Case number	h	c_s (m/s)	f_n (Hz)	f_D (Hz)	f_r (Hz)	ξ
L01	$48R$	141	61.4	50.7	37.0	0.56
L02	$48R$	162	71.3	58.9	43.0	0.56
L03	$48R$	180	78.1	64.5	47.0	0.56
L04	$48R$	198	86.2	71.2	52.0	0.56
L05	$48R$	216	94.6	78.1	57.0	0.56

Case number	h_t	h_b	c_{st} (m/s)	c_{sb} (m/s)	f_n (Hz)	f_D (Hz)	f_r (Hz)	ξ
L14	R	$47R$	180	198	85.7	74.4	61.0	0.50
L15	R	$47R$	180	216	90.0	81.1	71.0	0.43
L24	$2R$	$46R$	180	198	75.6	66.5	56.0	0.48
L25	$2R$	$46R$	180	216	71.5	65.1	58.0	0.41

Table 5.10 Continued

(c) Velocity time history approach

Case number	h	c_s (m/s)	f_n (Hz)	f_D (Hz)	f_r (Hz)	ξ
L01	$48R$	141	63.4	52.6	39.0	0.56
L02	$48R$	162	74.8	62.5	47.1	0.55
L03	$48R$	180	79.7	66.7	50.4	0.55
L04	$48R$	198	92.8	76.9	56.7	0.56
L05	$48R$	216	101.2	83.3	60.4	0.57

Case number	h_t	h_b	c_{st} (m/s)	c_{sb} (m/s)	f_n (Hz)	f_D (Hz)	f_r (Hz)	ξ
L14	R	$47R$	180	198	87.6	76.9	64.5	0.48
L15	R	$47R$	180	216	91.5	83.3	74.3	0.41
L24	$2R$	$46R$	180	198	78.1	69.0	58.4	0.47
L25	$2R$	$46R$	180	216	73.1	66.7	59.6	0.41

here the density is varied, as opposed to shear wave velocity, as illustrated Figure 5.17. The results of the analysis are shown in Figures 5.18 to 5.23 and summarized in Table 5.12. For $h_t = R$, the undamped natural frequency f_n increases and the damping ratio ξ decreases when the density of bottom layer ρ_b increases (cases M03, M14, and M15). The damped natural frequency f_D and the resonant frequency f_r are affected by the values of f_n and ξ. For $h_t = 2R$, the undamped natural frequency f_n remains about the same and the damping ratio ξ decreases with increasing ρ_b (cases M03, M24, and M25). In this case, the effect on the damping ratio ξ is dominant that it also affects the estimation of the damped natural frequency f_D and the resonant frequency f_r.

It is important to consider, however, that these trends hold only for the cases studied herein. The response may be different if the soil properties or the height of the layer changes.

5.4. Evaluation of Frequencies and Damping Ratio in the Field

The frequencies and damping ratio of a system with a rigid concrete footing on soil is investigated using the field measurements obtained from testing at the Capital Aggregate Quarry site. The description of the site and test setup can be found in Chapter IV. Two different types of excitation, an impact and a stepped sine load, were used to evaluate the frequencies and the damping ratio of the given system. The effect of the footing embedment was also neglected in all analyses following Novak and Beredugo (1972).

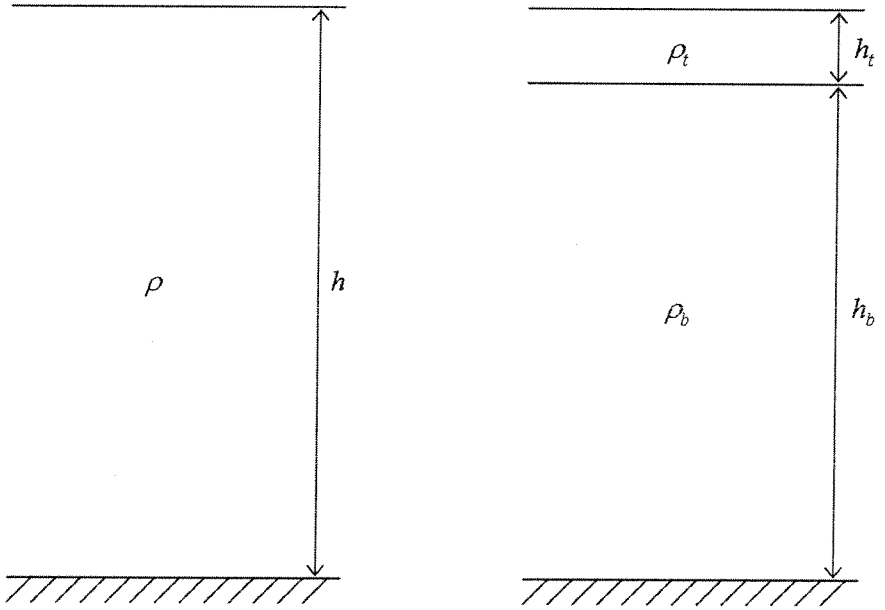

(a) Uniform medium (b) Layered medium

Figure 5.17 Uniform and layered media for varying densities

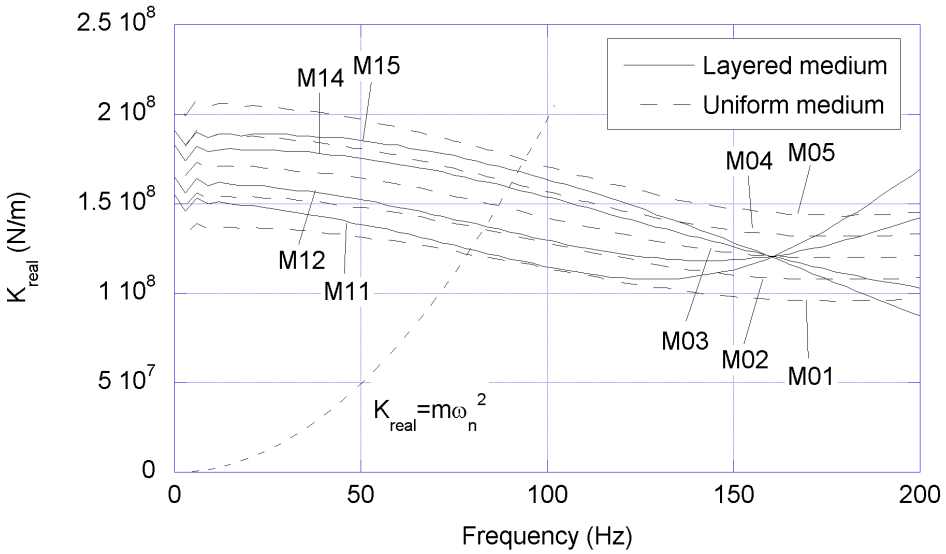

(a) Real part

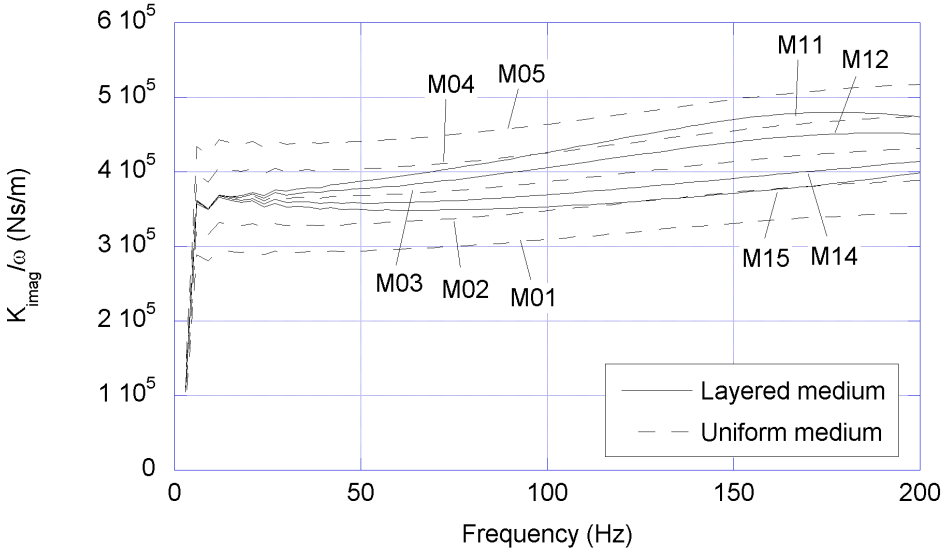

(b) Imaginary part

Figure 5.18 Real and imaginary parts of the frequency response functions for varying densities, $h_t = R$

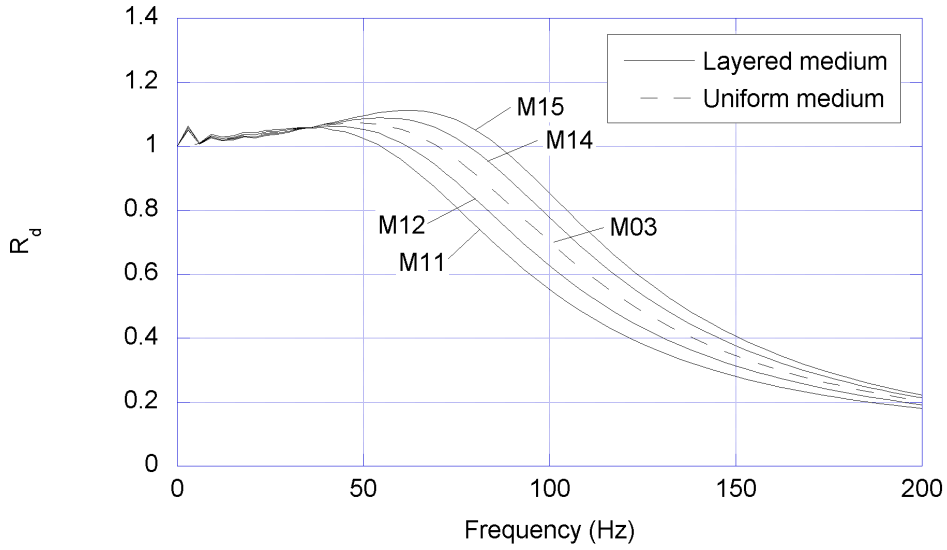

Figure 5.19 Dynamic response curves for varuyng densities, $h_t = R$

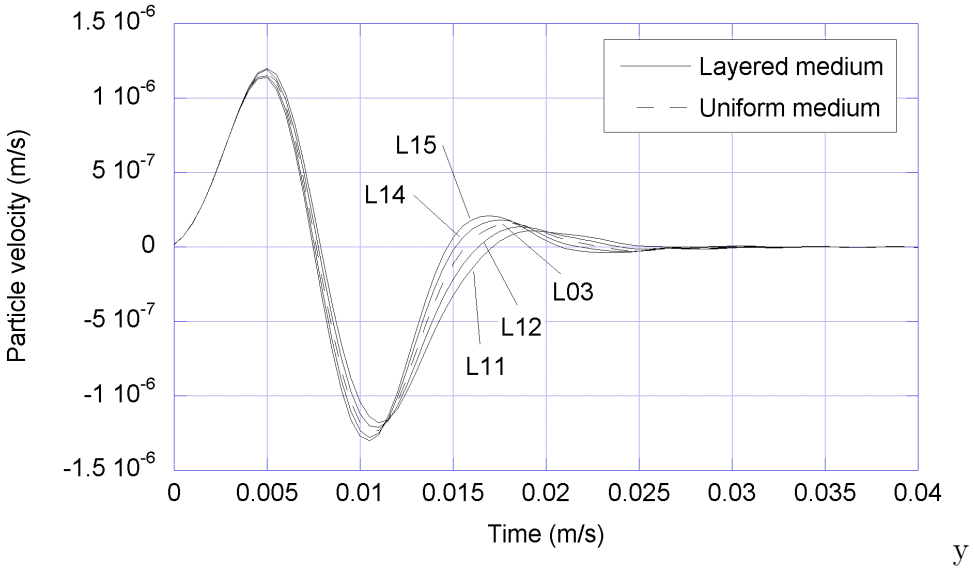

y

Figure 5.20 Particle velocity time histories for varying densities, $h_t = R$

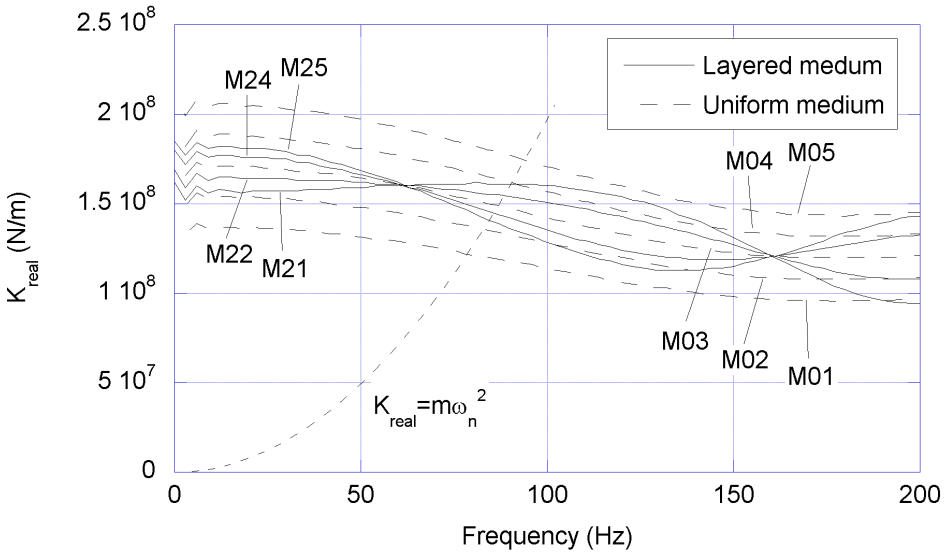

(a) Real part

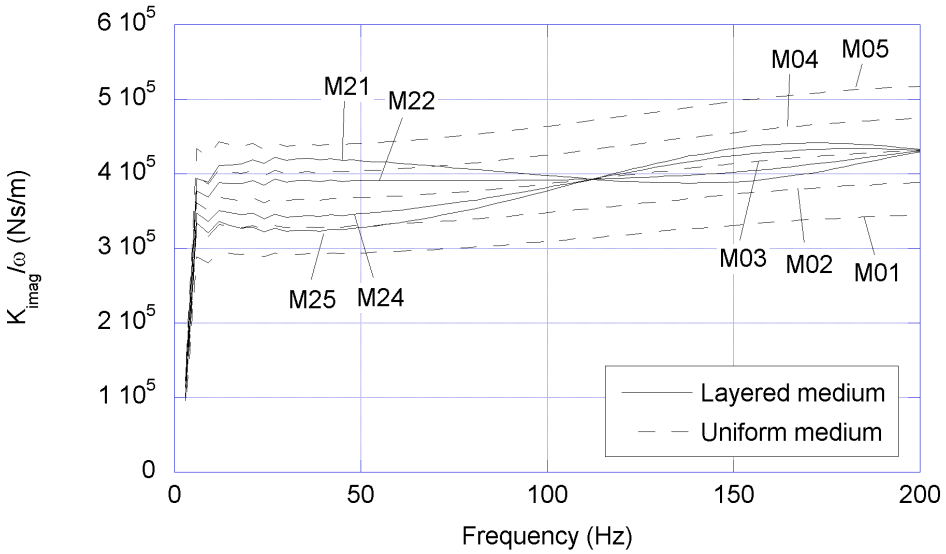

(b) Imaginary part

Figure 5.21 Real and imaginary parts of the frequency response functions for varying densities, $h_t = 2R$

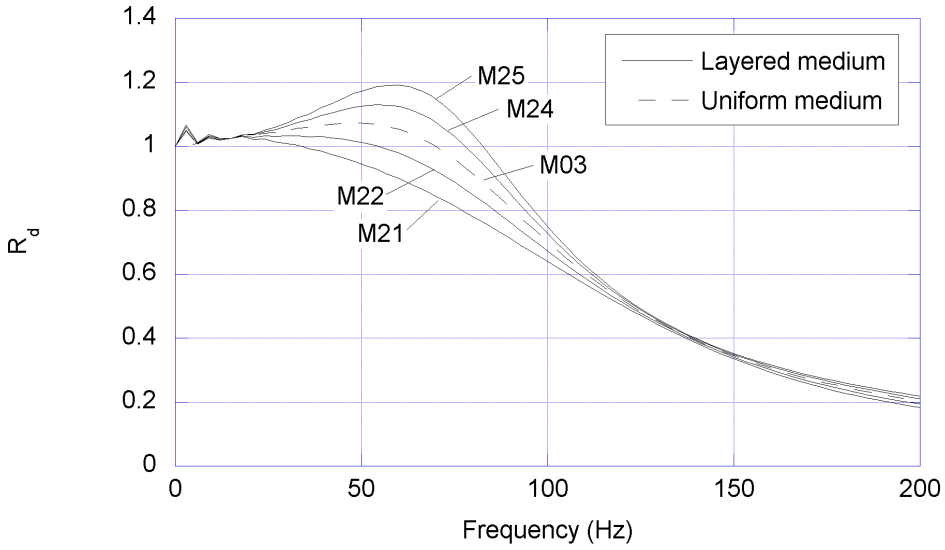

Figure 5.22 Dynamic response curves for varying densities, $h_t = 2R$

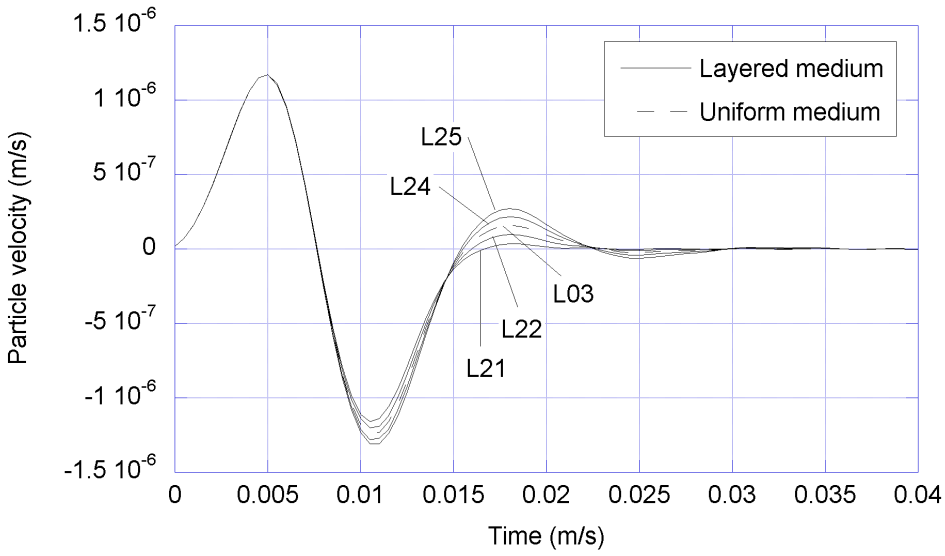

Figure 5.23 Particle velocity time histories for varying densities, $h_t = 2R$

Table 5.11 Properties for the parametric analyses for varying densities

(a) Uniform cases

Case number	h	$\rho\,(\mathrm{kg/m^3})$
M01	48R	1600
M02	48R	1800
M03	48R	2000
M04	48R	2200
M05	48R	2400

(b) Layered cases

Case number	h_t	h_b	$\rho_t\,(\mathrm{kg/m^3})$	$\rho_b\,(\mathrm{kg/m^3})$
M11	R	$47R$	2000	1600
M12	R	$47R$	2000	1800
M14	R	$47R$	2000	2200
M15	R	$47R$	2000	2400
M21	$2R$	$46R$	2000	1600
M22	$2R$	$46R$	2000	1800
M24	$2R$	$46R$	2000	2200
M25	$2R$	$46R$	2000	2400

Table 5.12 Frequencies and damping ratio for uniform and layered media system for varying densities

(a) Spring constant approach

Case number	h		$\rho(\text{kg/m}^3)$		f_n (Hz)	f_D (Hz)	f_r (Hz)	ξ
M01	$48R$		1600		78.7	66.6	51.7	0.53
M02	$48R$		1800		82.9	68.5	50.0	0.56
M03	$48R$		2000		86.9	69.9	47.1	0.59
M04	$48R$		2200		90.5	70.9	43.1	0.62
M05	$48R$		2400		94.0	71.6	37.5	0.65
Case number	h_t	h_b	$\rho_t(\text{kg/m}^3)$	$\rho_b(\text{kg/m}^3)$	f_n (Hz)	f_D (Hz)	f_r (Hz)	ξ
M14	R	$47R$	2000	2200	89.8	74.2	54.5	0.56
M15	R	$47R$	2000	2400	92.3	78.1	60.8	0.53
M24	$2R$	$46R$	2000	2200	85.6	71.4	53.6	0.55
M25	$2R$	$46R$	2000	2400	84.5	72.5	58.0	0.51

Table 5.12 Continued

(b) Maximum response approach

Case number	h		$\rho(\text{kg/m}^3)$		f_n (Hz)	f_D (Hz)	f_r (Hz)	ξ
M01	$48R$		1600		76.9	65.8	52.5	0.52
M02	$48R$		1800		76.3	64.1	49.0	0.54
M03	$48R$		2000		78.1	64.5	47.0	0.56
M04	$48R$		2200		83.0	67.3	46.5	0.59
M05	$48R$		2400		84.8	67.6	44.0	0.60
Case number	h_t	h_b	$\rho_t(\text{kg/m}^3)$	$\rho_b(\text{kg/m}^3)$	f_n (Hz)	f_D (Hz)	f_r (Hz)	ξ
M14	R	$47R$	2000	2200	87.2	72.9	55.0	0.55
M15	R	$47R$	2000	2400	92.9	78.8	61.5	0.53
M24	$2R$	$46R$	2000	2200	80.5	68.9	55.0	0.52
M25	$2R$	$46R$	2000	2400	80.0	70.3	59.0	0.48

Table 5.12 Continued

(c) Velocity time history approach

Case number	h		$\rho(\text{kg/m}^3)$		f_n (Hz)	f_D (Hz)	f_r (Hz)	ξ
M01	$48R$		1600		76.8	66.7	54.7	0.50
M02	$48R$		1800		78.2	66.7	52.6	0.52
M03	$48R$		2000		79.7	66.7	50.4	0.55
M04	$48R$		2200		81.2	66.7	47.9	0.57
M05	$48R$		2400		82.9	66.7	44.9	0.59
Case number	h_t	h_b	$\rho_t(\text{kg/m}^3)$	$\rho_b(\text{kg/m}^3)$	f_n (Hz)	f_D (Hz)	f_r (Hz)	ξ
M14	R	$47R$	2000	2200	84.1	71.4	56.0	0.53
M15	R	$47R$	2000	2400	88.9	76.9	62.6	0.50
M24	$2R$	$46R$	2000	2200	76.6	66.7	55.0	0.49
M25	$2R$	$46R$	2000	2400	77.1	69.0	59.7	0.45

5.4.1. Finite Element Analysis

The material properties for the finite element model were from the SASW test. Since the SASW averages test gives the properties of soil over distance, it does not necessarily yield the cirrect value at a specific location under the footing. Therefore, the results of the finite element analysis may not represent exact characteristics of the system with small sized footing but represent those of the whole area where SASW tests were performed.

The finite element analyses also considered the variability observed in the SASW shear wave velocity profile by using best fit, low and upper bounds of both SASW line A and B. Results for line A are plotted in Figures 5.24, 5.25, and 5.26 for the different approaches‘, and those of SASW line B in Figure 5.27, 5.28, and 5.29. The numerical value of the estimated frequencies and damping ratio using the three approaches are tabulated in Table 5.13. Other combinations of shear wave velocities using for example the upper bound value at certain depth and the lower bound value at a different one, may result in frequencies and damping ratios which do not fall in the range of the results in the table. However, those cases were not considered.

5.4.2. Experimental Results

Two different types of dynamic loads, an impact and a stepped sine excitation, were used in the seismic test of the system with a rigid concrete footing. An impact excitation test is simple to perform, however the signal-to-noise-ratio of the obtained signal may be low. A hand-held hammer was used to excite the concrete footing and attempts were made to produce an impact duration of 4.0×10^{-3} s. In a stepped sine excitation test, the footing is vibrated at low to high frequency level with a fixed force amplitude. This test is different from the harmonic excitation test in Chapter

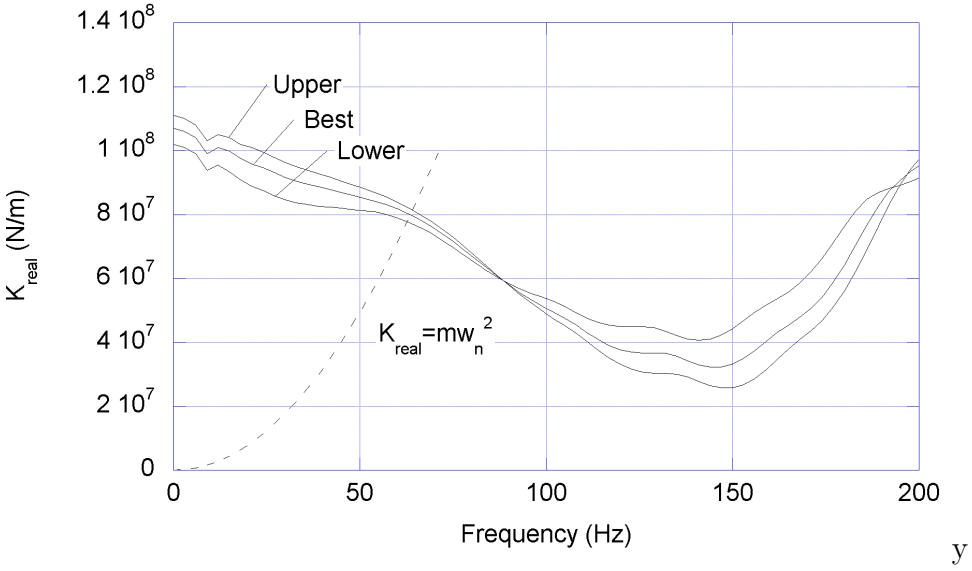

y

(a) Real part

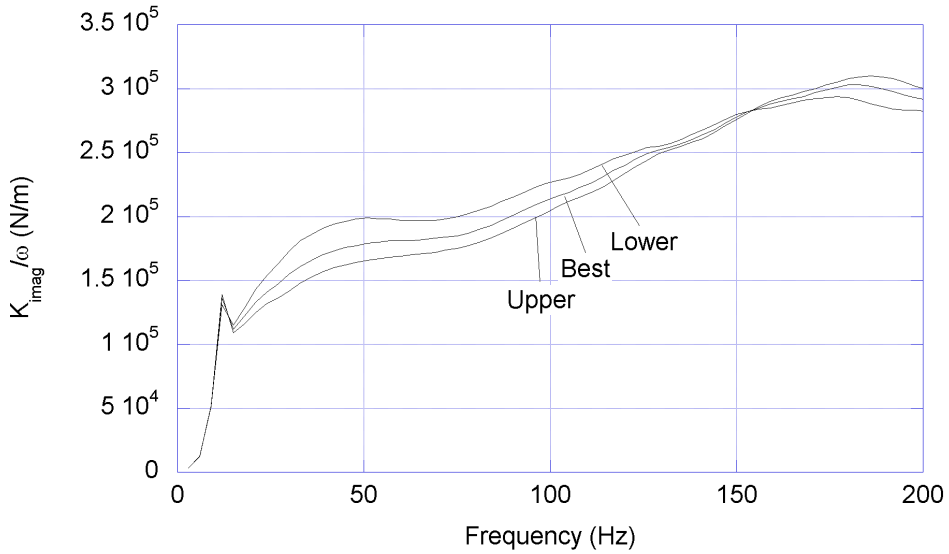

(b) Imaginary part

Figure 5.24 Real and imaginary part of frequency response functions from FE analysis (SASW profile line A)

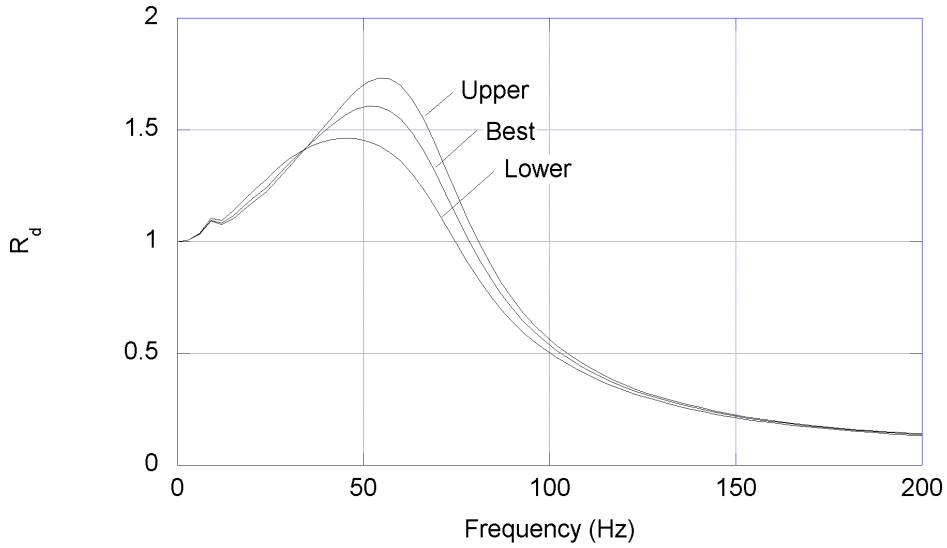

Figure 5.25 Dynamic response curves from FE analysis (SASW profile line A)

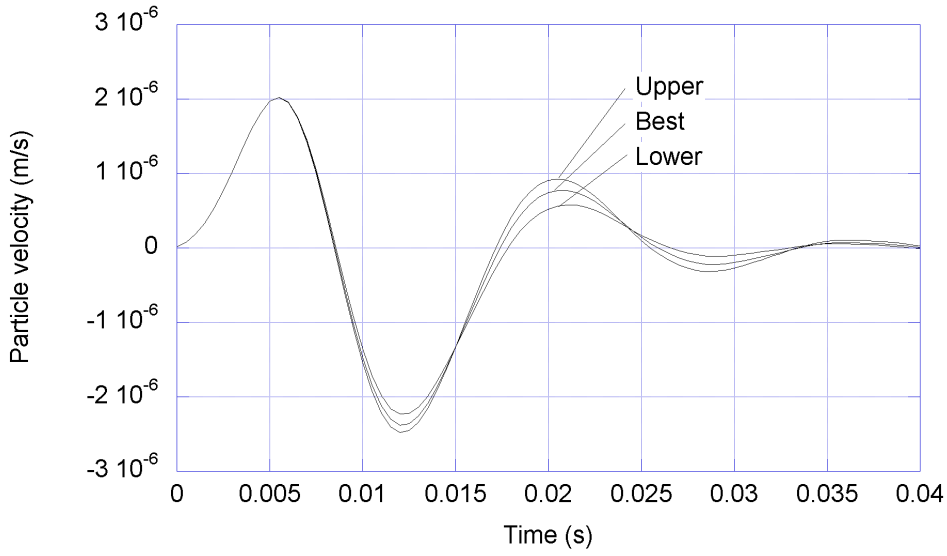

Figure 5.26 Particle velocity time histories from FE analysis (SASW profile line A)

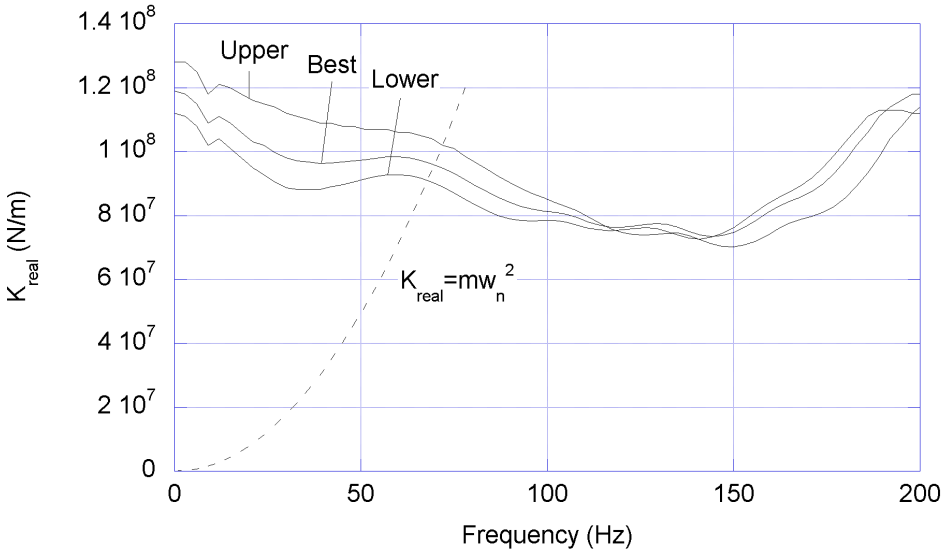

(a) Real part

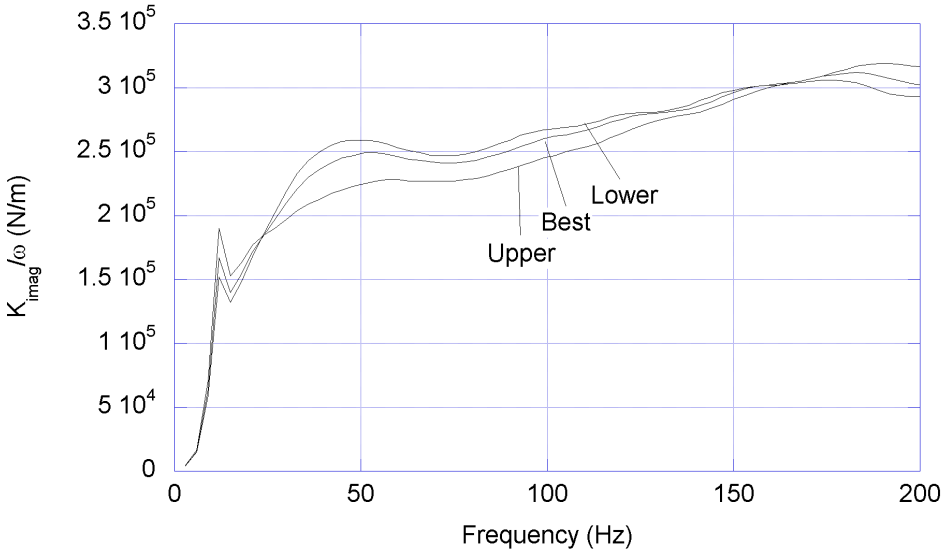

(b) Imaginary part

Figure 5.27 Real and imaginary part of frequency response functions from FE analysis (SASW profile line B)

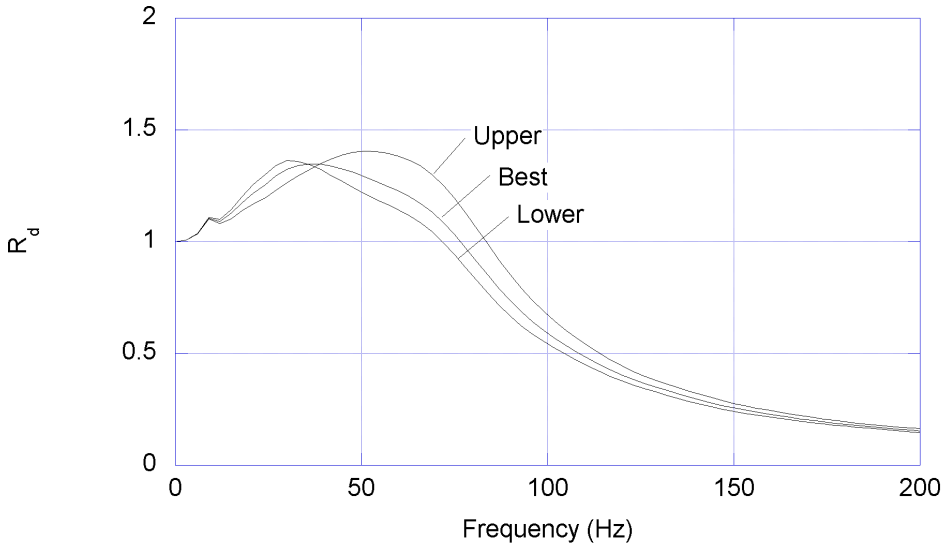

Figure 5.28 Dynamic response curves from FE analysis (SASW profile lone B)

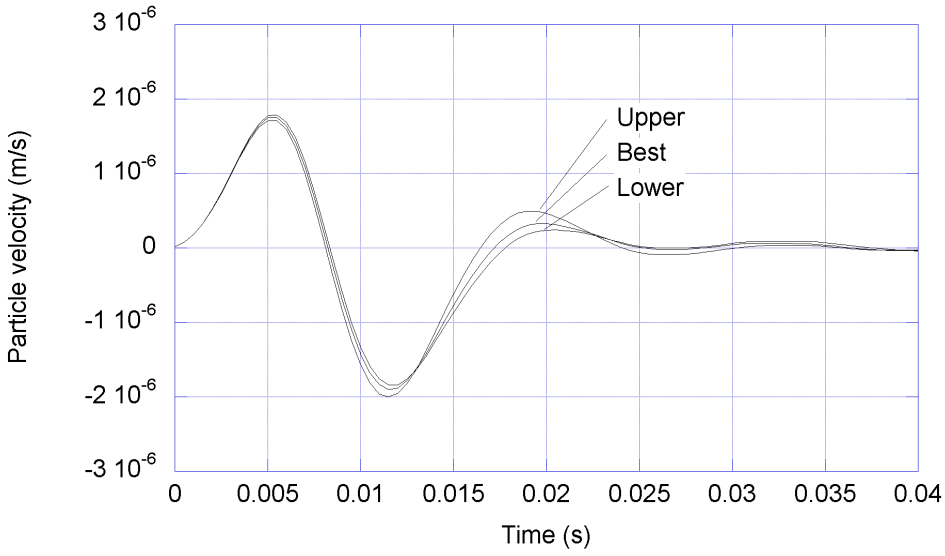

Figure 5.29 Particle velocity time histories by FE analysis (SASW profile line B)

Table 5.13 Frequencies and damping ratio calculated by FE analysis using shear wave velocity profile from SASW tests

(a) Spring constant approach

SASW line used		f_n (Hz)	f_D (Hz)	f_r (Hz)	ξ
Line A	Lower bound	62.8	58.0	52.9	0.38
	Best fit	63.6	59.9	55.8	0.34
	Upper bound	64.2	61.0	57.7	0.31
Line B	Lower bound	67.9	59.8	50.5	0.47
	Best fit	69.7	62.4	54.1	0.45
	Upper bound	72.0	66.0	59.4	0.40

(b) Maximum response approach

SASW line used		f_n (Hz)	f_D (Hz)	f_r (Hz)	ξ
Line A	Lower bound	53.8	50.1	46.0	0.37
	Best fit	58.8	55.5	52.0	0.33
	Upper bound	60.9	58.0	55.0	0.30
Line B	Lower bound	37.6	34.5	31.0	0.40
	Best fit	45.8	41.9	37.5	0.41
	Upper bound	60.8	56.1	51.0	0.39

(c) Velocity time history approach

SASW line used		f_n (Hz)	f_D (Hz)	f_r (Hz)	ξ
Line A	Lower bound	60.5	55.6	50.2	0.39
	Best fit	62.5	58.8	54.9	0.34
	Upper bound	61.7	58.8	55.8	0.30
Line B	Lower bound	68.1	57.1	43.5	0.54
	Best fit	67.5	58.8	48.7	0.49
	Upper bound	73.0	66.7	59.7	0.41

IV which used low to high force amplitude at a fixed frequency. A shaker is required to excite the rigid foundation, however the signal-to-noise-ratio is relatively high in this type of test. A large scale shaker, Thumper, developed at the University of Texas at Austin, was used. The applied static and dynamic load combinations were P_{st} =18.6 kN and P_{dyn} =8.8 kN, P_{st} =27.6 kN and P_{dyn} =13.2 kN, and P_{st} =35.6 kN and P_{dyn} =17.7 kN.

An example of particle velocity time history in terms of output voltage from the impact excitation test is presented in Figure 5.30. The second and third peaks were used to calculate the damped natural frequency and the damping ratio. Four sets of impact test results from two vertically oriented geophones in the concrete footing were analyzed and the data are tabulated in Table 5.14(a). The averages of the undamped natural cyclic frequency f_n, the damped natural cyclic frequency f_D, and the resonant cyclic frequency f_r from the two vertical geophones are 86.1 Hz, 76.6 Hz, and 65.7 Hz, respectively, and the damping ratio ξ is 0.45. The estimated damping ratio is close to the value obtained from finite element analysis using the shear wave velocity profile in the SASW line B, while the frequencies are higher.

The results of the stepped sine test are plotted in Figure 5.31. Because of high noise in the data from geophone B, only the results from geophone A are presented. The absolute value of the frequency response function H_z, which represents the displacement of the system corresponding to a unit load amplitude at a certain frequency, is shown in Figure 5.31(a). The dynamic response factor R_d is also plotted in Figure 5.31(b), after smoothing of excessive fluctuations by moving average. Since the static stiffness K_z was not measured in the field test, it was assumed as 195,000 kN/m based on a modulus of the frequency response function 5.12×10^{-6} m/kN at a loading frequency of about 17 Hz, the lowest frequency possible in the test. In other words, the displacement at the loading frequency of 17 Hz was assumed as the static dis-

placement. As the static stiffness is assumed, the damping ratio from the maximum response approach may be less reliable that that from the half power band width approach.

The frequencies and the damping ratio were estimated using the half power bandwidth and the maximum response approaches. Since the resonant amplitude and frequency do not vary much with excitation amplitudes, the system was assumed to display linear response. The quadratic terms of ramping ratio are often neglected in the half power bandwidth approach; however they must be included in this case because of the large energy dissipation in this problem. The equation of half power bandwidth approach derived without neglecting the quadratic terms of damping ratio is

$$\frac{\omega_a - \omega_b}{\omega_n} = \sqrt{2 - 4\xi^2 - 2\sqrt{1 - \frac{4\xi^2(1-\xi^2)}{A^2}}} \tag{5.17}$$

where ω_a and ω_b denote the circular frequencies when the peak of dynamic response factor R_d is A times the peak value of R_d. In the half power band width approach, the constant A is $1/\sqrt{2}$. The calculated dynamic properties are tabulated in Table 5.14(b). Dynamic response curves from the finite element analyses and the experimental tests are presented in Figure 5.32. The evaluation based on the finite element analyses using the SASW profile from line A shows better agreement with the experimental results than profile B.

It is not possible to decide which type of dynamic tests would estimate the dynamic properties of the given system more accurately, since the material properties under the localized area are not known with certainty. The damping ratios from the impact excitation were close to those from the finite element analyses with SASW profile B, whereas the damping ratio from the stepped sine excitation are closer to those with SASW profile A. In terms of the evaluation of the resonant frequency, the

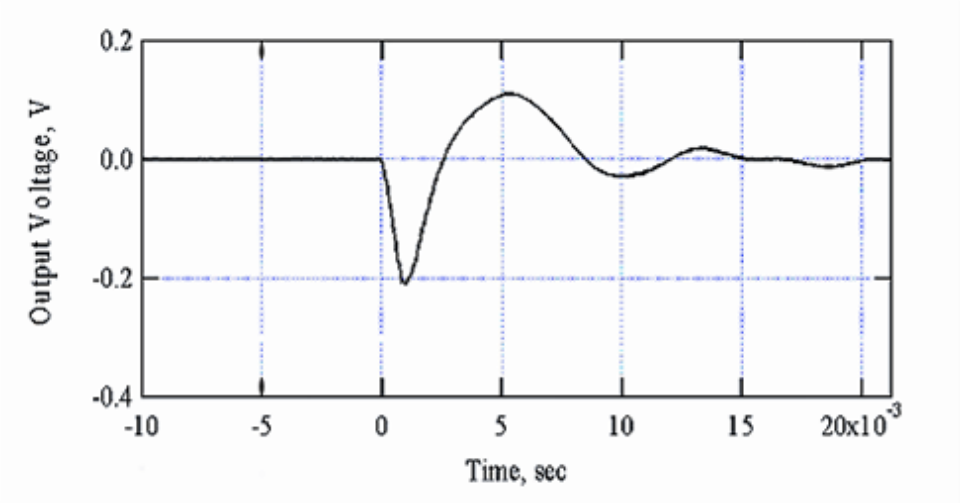

Figure 5.30 Particle velocity time history from impact excitation test

results from the stepped sine texts matched the results of the finite element model better than the impact test, with the agreement being better for soil profile A.

5.5. Summary and Conclusions

The effects of various parameters on the undamped natural, damped natural, and resonant frequencies and the damping ratio of a system consisting of a circular rigid disk on a uniform or layered medium were investigated through numerical studies using approximate solutions or finite element analyses with a consistent transmitting boundary. Experimental results from field tests were analyzed.

In the case of the elastic halfspace, the most significant effect on the frequencies is achieved by the shear wave velocity of the medium. The disk radius seems to have a limited influence on frequencies, but the range of the radii tried was also quite limited. Both the mass of the disk and the density of the medium affect the natural undamped, damped and resonant frequencies in contrasting trends, due to the influence of these properties on damping ratio. The largest changes on the damping

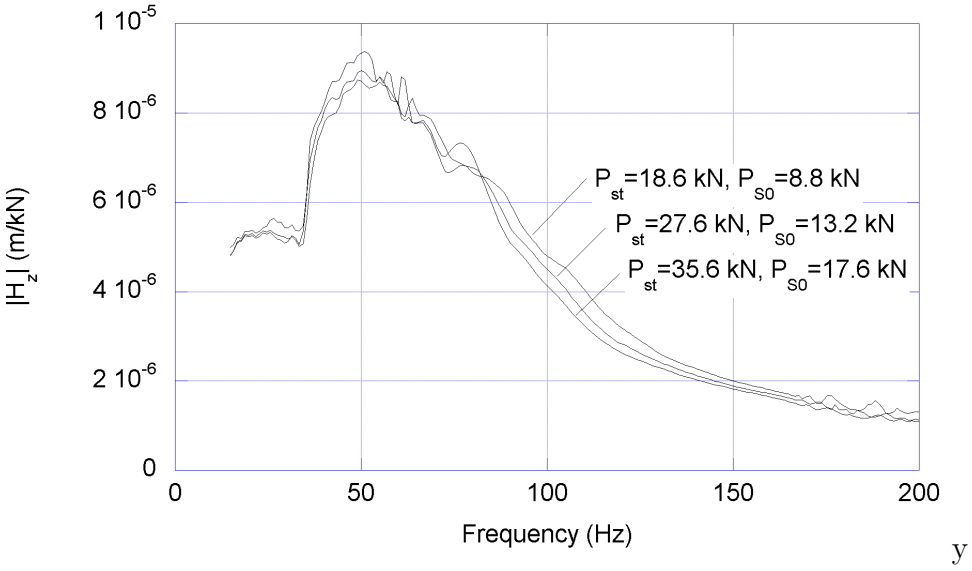

(a) Frequency response function

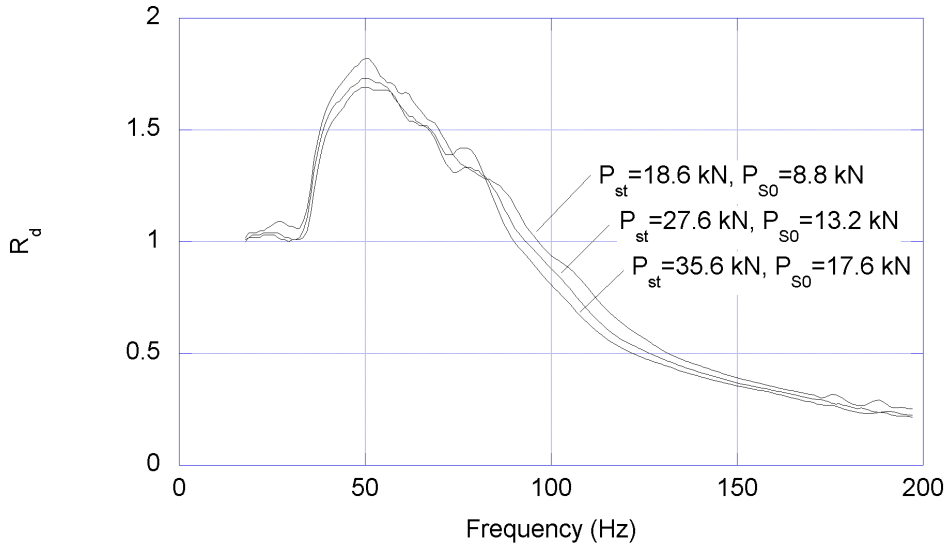

(b) Moving-averaged dynamic response curve

Figure 5.31 Results of the stepped sine tests

Table 5.14 Frequencies and damping ratio from experimental test

(a) Impact test

Test number	Accelerator	f_n (Hz)	f_D (Hz)	f_r (Hz)	ξ
Trial 1	A	89.3	78.9	66.7	0.47
	B	81.0	73.3	64.8	0.42
Trial 2	A	86.7	77.2	66.3	0.46
	B	81.8	74.8	67.2	0.40
Trial 3	A	90.5	78.9	65.2	0.49
	B	89.5	77.2	62.5	0.51
Trial 4	A	88.6	78.2	66.2	0.47
	B	81.4	74.4	66.8	0.40
Average	A	88.8	78.3	66.1	0.47
	B	83.4	74.9	65.3	0.43

(b) stepped sine test

Applied load	Approach	f_n (Hz)	f_D (Hz)	f_r (Hz)	ξ
$P_{st} = 18.6\,\text{kN}$	Half power band width	57.1	53.7	50.1	0.34
$P_{dyn} = 8.8\,\text{kN}$	Maximum response	54.9	52.6	50.1	0.29
$P_{st} = 27.6\,\text{kN}$	Half power band width	57.7	54.0	50.1	0.35
$P_{dyn} = 13.2\,\text{kN}$	Maximum response	55.3	52.8	50.1	0.30
$P_{st} = 35.6\,\text{kN}$	Half power band width	57.1	53.7	50.1	0.34
$P_{dyn} = 17.6\,\text{kN}$	Maximum response	55.7	53.0	50.1	0.31
Average	Half power band width	57.3	53.8	50.1	0.34
	Maximum response	55.3	52.8	50.1	0.30

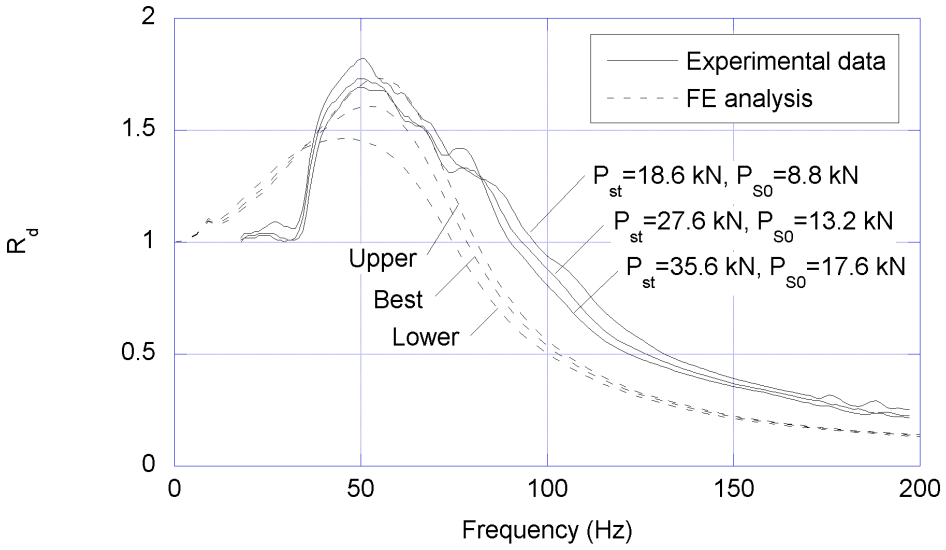

(a) For SASW line A

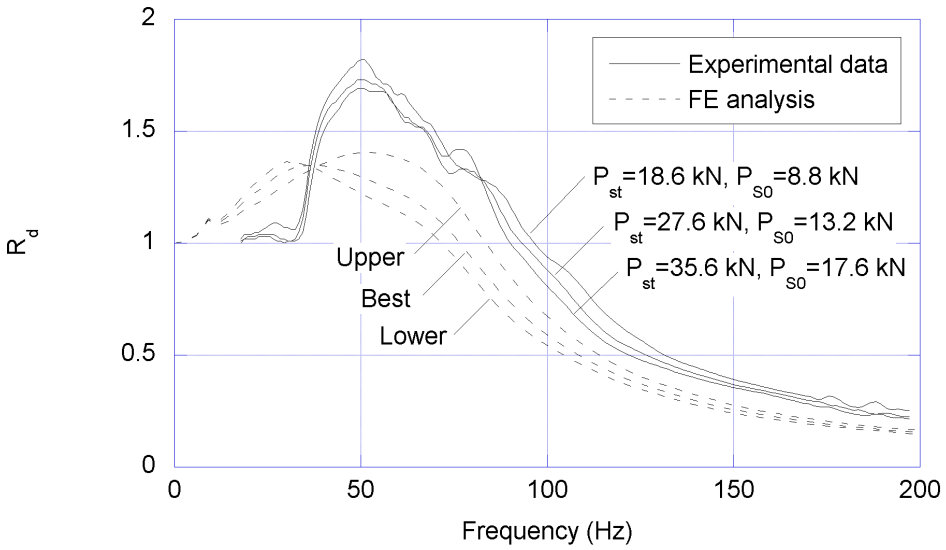

(b) For SASW line B

Figure 5.32 Dynamic response curves from FE analysis and experimental test

ratio are caused by the radius and mass of the disk, with smaller effects due to the density of the medium. The shear wave velocity of the medium does not affect the damping ratio. The Poisson's ratio of the medium has limited effect on the dynamic properties. The duration of the impact had little influence on the results within the range of values considered herein. The three different approaches for estimating dynamic characteristics exhibit the same trends but give different results. If we had a real SDOF system, these results should be identical but the real system is more complex. It is important when conducting these approaches with experimental data that the values obtained are not exact. The parametric study on shear wave velocity for a uniform profile was also carried out with finite element analysis, leading to results that are similar to those observed with the elastic halfspace solutions.

In a layered system the bottom layer was assigned a different shear wave velocity from the top layer, and the thickness of the latter was also changed. In this case, the damping ratio, which was not affected in the uniform case, also changes. The natural frequency of the layered soil profile depends on the thickness of the layers. The response of the layered system becomes quite complex and the interpretation of the results is also more difficult to generalize. Changes in the density of the bottom layer also affected both the frequencies and the damping ratio with less pronounced trends. A simple system consisting of only two layers was examined here. With each additional layer introduced into the system the level of complexity will also rise. It is important to consider that the trends observed hold only for the cases studies herein. The response may be different if the soil properties or the height of the layers change.

Two types of dynamic loading tests, an impact and a stepped sine excitations, were performed on the concrete footing in the field and analyzed. The resonant frequency of the system from the stepped sine tests showed better agreement to the finite element analyses with material properties measured in the field.

CHAPTER VI

CONCLUSIONS

6.1. Summary and Conclusions

6.1.1. Wave Propagation in Nonlinear One-Dimensional Soil Model

The wave propagation in a one-dimensional nonlinear soil medium under a triangular impulse and a harmonic excitation was investigated using a discrete model with lumped masses and interconnected springs. When an impact excitation was applied at the free end of a soil shear beam, the measured wave velocity using the cross-correlation between the signals measured at two points was very close to the wave velocity calculated from the tangent modulus corresponding to the state of stress caused by an applied static load. When a sinusoidal load was applied, the cross-correlation estimated a wave velocity close to the one calculated from the secant modulus in the stress-strain loops under steady-state vibration. The variables that contributed to change the shear modulus also influence the estimate of wave velocity from cross-correlation.

The implication of parametric study with sinusoidal loads in the field testing is straightforward. If a modulus is determined from the wave velocity with a sinusoidal load, the estimate is the secant modulus of the stress-strain loop regardless of initial vertical static load. However, the study with impact loads is applicable to the field testing only in limited case. In the numerical study, the tangent modulus at the stress level increased by a static load was determined when the direction of static and impact loads are exactly same, which occurs during field test only when the vertical impact is imposed on top of a vertical static load.

6.1.2. Wave Propagation under Vertically Excited Surface Foundation

Two analytical solutions, using numerical integrations and explicit Green's functions, and a finite element model, with consistent transmitting boundary, were used to investigate the speed of traveling waves under a vertically excited surface foundation through a linear or nonlinear medium. In a linear material, the results indicate that when the wave propagation velocities in the vertical direction are calculated from the phase differences between the vertical motions recorded at receivers placed at different depths the values obtained may change with location and also with frequency. These values will not correspond exactly to either the P wave velocity, associated with the constrained modulus of the material, nor to the rod wave velocity associated with Young's modulus. They tend to be between these two values but much closer to the latter. In a nonlinear material, even though the wave velocities of the material may change due to the characteristics of the external loading, the estimated wave velocities also did not correspond to either constrained or Young's modulus.

Since the wave velocity measured using the phase difference under vertically excited footing does not correspond to either exactly P wave or rod wave, it is recommended to use the inverse analysis to estimate shear modulus with the data from vertical excitation tests as shown in Chapter IV.

6.1.3. Estimation of Nonlinear Dynamic Soil Properties In Situ

The nonlinear shear moduli could be estimated using the phase difference and inverse analyses in the horizontal and vertical excitation tests, respectively.

In the proposed inversion procedure, the input and output amplitude data from large scale in situ dynamic tests are used to estimate the material properties of the soil. The Levengerg-Marquardt method and a finite element model with the consis-

tent transmitting boundary were used as a parameter adjustment algorithm and a numerical model, respectively. The method was validated through numerical verifications for soil deposits with low to medium variation of shear wave velocity. Either shear moduli or damping can be estimated in the vicinity of the surface foundation using the proposed inversion procedure. In situ shear modulus reduction curves can be estimated assuming an associated damping curve as a pair. If the shear modulus reduction curve can be estimated from phase differences, a damping curve can be estimated using the proposed inverse procedure.

In situ modulus reduction curves were generated using the phase difference analysis with horizontal excitation data from the Capital Aggregate Quarry site, and using the inverse analysis with vertical excitation data from the Texas A&M University Riverside Campus. The surface layer of both sites was a silty sand. For the inversion procedure, the mean damping curve for cohesionless soils proposed by Seed and Idriss (1970) was assumed in the numerical model. Nonlinear moduli were estimated up to a shear stain of 1×10^{-2} % for the Capital Aggregate Quarry site, and 3×10^{-2} % for the Texas A&M University Riverside Campus site. Estimated nonlinear shear moduli presented very consistent trends regardless of the analysis methods and test sites. They showed larger elastic threshold shear strains, 1.5×10^{-3} % for the Capital Aggregate Quarry site and 2×10^{-3} % for the Texas A&M University site, then, they closely followed the mean modulus reduction curve for cohesionless soils of Seed and Idriss (1970) at strains larger than 6×10^{-3} % for both sites.

6.1.4. Dynamic Characteristics of Vertically Excited Surface Foundation

The response of a surface foundation under dynamic loading is useful information for test setup and procedure. To provide guidance for the field test, the effect of varying foundation and soil properties on the response of the foundation under vertical

dynamic excitations was investigated through sets of parametric studyes. To quantify the response of the foundation, the undamped natural, damped natural, and resonant frequencies of a soil-mass system and its damping ratio were calculated assuming the soil-foundation structure as an equivalent SDOF (single degree of freedom) system. The approximated solution formulated by Verbic (1972) and finite element analysis with the consistent transmitting boundary (Kausel, 1974) were used to simulate the response of a surface foundation on uniform or layered medium. Experimental field tests were also performed and analyzed to observe the consistency of the numerical and experimental methods.

The effect of various parameters on the undamped natural, damped natural, and resonant frequencies and the damping ratio of a system consisting of a circular rigid disk on a uniform or layered medium was investigated through numerical studies using approximate solutions and finite element analyses with a consistent transmitting boundary. In the case of the elastic halfspace, the most significant effect on the frequencies is attributed to the shear wave velocity of the medium. The largest changes on the damping ratio are caused by the radius and mass of the disk, with smaller effects due to the density of the medium. The shear wave velocity of the medium does not affect the damping ratio. In the layered system the bottom layer was assigned a different shear wave velocity from the top layer, and the thickness of the latter was also changed. In this case, the damping ratio, which was not affected in the uniform case, also changed. The natural frequency of the layered soil profile depends on the thickness of the layers. The response of the layered system becomes quite complex and the interpretation of the results is also more difficult to generalize. The change of the density at the bottom layer also affected both the frequencies and the damping ratio with less pronounced trends. A simple system consisting of only two layers was examined. With each additional layer introduced into the system the

level of complexity would rise.

Two types of dynamic loading tests, an impact and a stepped sine excitation, were performed on a concrete footing in the field and analyzed. The resonant frequency of the system from the stepped sine tests showed better agreement with the results of the finite element analysis with material properties measured in the field than the resonant frequency obtained from the impact tests. The impact tests produced results for damping that matched relatively well those of the finite element analyses for one set of soil properties while the stepped sine test had a better match with the damping values of the finite element model with the other set of measured soil properties.

If the shear wave velocity profile of the test site is known from geophysical methods such as the SASW test, the response of the footing can be estimated by finite element analysis. The response of footing can also be estimated directly by field tests such as impact and stepped sine tests. The stepped sine test is recommended since it clearly shows the relation between response and frequency. Once the response of a footing on a given soil condition is estimated, the mass and radius of the footing, and the frequency and sequence of dynamic loading of the main test can be determined in such a way that well defined shear modulus curve (or damping curve) would be estimated.

6.2. Further Studies

6.2.1. Extensive Data Analysis

There are still more data to analyze from the vast set of field experiments conducted in this research project.

The effect of confining stress on the magnitude and reduction curve of the shear modulus has been studied using laboratory tests. It can be estimated using measured

data from the field experiments. It would be meaningful to compare estimated trends to the results of laboratory data. The change in modulus magnitude and reduction curve due to a loading rate would also be an interesting topic to study. Harmonic excitations are applied with several different frequencies in the tests.

One of most interesting aspects of this study is the possibility of damping estimation using dynamic field tests and the inverse analysis. If nonlinear shear moduli can be estimated using phase difference analysis, the damping can be determined using the inverse analysis.

6.2.2. Advanced In Situ Test Method

In the proposed dynamic field tests using vibroseis trucks, a large soil mass would be affected in situ. On the other hand, the soil mass at a deep level cannot be tested using the proposed test method, while the dynamic soil properties at depth are still of interest in dynamic soil response problems and needed to make the inversion procedure more reliable. Therefore, it will be necessary to place geophones at bigger depths and to excite the footing with higher force amplitudes. In this way, not only the nonlinear dynamic properties will be estimated over a larger range of strains but also the uncertainties in the inversion will diminish. A numerical study will be required to configure the array of geophones. A reliable device to embed geophones at larger depths is also necessary.

6.2.3. Development in Implementation Methods

The nonlinear shear moduli estimated with the phase differences using the established LabVIEW code worked only for the selected data due to non consistent shapes of the measured waveforms. It is necessary to develop a systematic method which works better with the irregularly shaped sinusoidal waveforms to compute the phase

differences.

The currently proposed inversion procedure is only valid when the soil deposit has low to medium variation of shear wave velocities. The error in estimated modulus seems to increases with strain level. The inversion procedure needs to be improved to reduce these shortcomings. If the test method is modified by considering more unidentified layers in the soil deposit, the computational cost will increase proportionally to the number of layers.

REFERENCES

Anderson, D. G. and Stokoe, K. H. (1978). "Shear Modulus: A Time Dependent Soil Property." *Dynamic Geotechnical Testing, ASTM*, STP654, 66–90.

Anderson, D. G. and Woods, R. D. (1975). "Comparison of Field and Laboratory Shear Modulus." *Proc. ASCE conference on In-Situ Measurements of Soil Properties*, Vol. 1, 69–92.

Anderson, D. G. and Woods, R. D. (1976). "Time-Dependent Increase in Shear Modulus of Clay." *Journal of the Geotechnical Engineering Division, ASCE*, 102(GT5), 525–537.

Axtell, P. J., Stokoe, K. H., Rathje, E. M., and Chang, W. (2002). "Development of Methods to Measure Nonlinear Properties and Liquefaction Characteristics of Near-Surface Soils." *Report No. GR02-4*, The University of Texas at Austin.

Bowen, B. (1992). "Damage Detection in Concrete Elements with Surface Wave Measurements," PhD thesis, The University of Texas at Austin.

Briaud, J.-L. (1997). "The National Geotechnical Experimentation Sites at Texas A&M University: Clay and Sand." *Report No. NGES-TAMU-007*, Texas A&M University.

Chopra, A. K. (2001). *Dynamics of Structures*. Prentice Hall, Upper Saddle River, New Jersey.

Darendeli, M. B. (2001). "Development of a New Family of Normalized Modulus Reduction and Material Damping Curves," PhD thesis, The University of Texas at Austin.

Dominguez, J. (1978). "Dynamic Stiffness of Rectangular Foundations." *Report No. R78-20*, Massachusetts Institute of Technology, Cambridge, MA.

Foinquinos, R., Roesset, J. M., and Stokoe, K. H. (1993). "FWD-DYN: A Computer Program for Forward Analysis and Inversion of Falling Weight Deflection Data." *Report No. 1970-1F*, The University of Texas at Austin.

Henke, R. and Henke, W. (1993). "Laboratory Evaluation of in situ Geotechnical Torsional Cylindrial Impulse Shear Test for Earthquake Resistant Design." *Bulletin of the Seismological Society of America*, 83(1), 245–263.

Iwan, W. D. (1967). "On a Class of Models for the Yielding Behavior of Continuous and Composite Systems." *Journal of Applied Mechanics, ASME*, 34(3), 612–617.

Janbu, N. (1963). "Soil Compressibility as Determined by Oedometer and Triaxial Tests." *European Conference on Soil Mechanics and Foundation Engineering*, Vol. 1, Wissbaden, Germany, 19–25.

Kalinski, M. E. (1998). "Determination of in situ V(s) and G(max) Using Surface Wave Measurements in Cased and Uncased Boreholes," PhD thesis, The University of Texas at Austin.

Kashio, J. (1970). "Steady-state Response of a Circular Disk Resting on a Layered Medium," PhD thesis, Rice University, Houston, TX.

Kausel, E. (1974). "Forced Vibration of Circular Foundations on Layered Media," PhD thesis, Massachusetts Institute of Technology, Cambridge, MA.

Kausel, E. (1981). "An Explicit Solution for the Green Functions for Dynamic Loads in Layered Media." *Report No. R81-13*, Massachusetts Institute of Technology, Cambridge, MA.

Kausel, E. and Roesset, J. M. (1981). "Stiffness Matrices for Layered Soils." *Bulletin of the Seismological Society of America*, 71(6), 1743–1761.

Kausel, E. and Roesset, J. M. (1992). "Frequency Domain Analysis of Undamped Systems." *Journal of the Engineering Mechanics, ASCE*, 118(4), 721–734.

Kim, D.-S. (1991). "Deformational Characteristics of Soils at Small to Intermediate Strains from Cyclic Tests," PhD thesis, The University of Texas at Austin.

Kramer, S. L. (1996). *Geotechnical Earthquake Engineering*. Prentice Hall, Upper Saddle River, New Jersey.

Kurtulus, A. (2006). "Field Measurements of the Linear and Nonlinear Shear Moduli of Soils Using Drilled Shafts as Dynamic Cylindrical Sources," PhD thesis, The University of Texas at Austion.

Levenberg, K. (1944). "A Method for the Solution of Certain Problems in Least Squares." *Quarterly of Applied Mathematics*, 2, 164–168.

Lewis, M. D. (1990). "A Laboratory Study of the Effect of Stress State on the Elastic Moduli of Sand (Wave Propagation)," PhD thesis, The University of Texas at Austin.

Luco, J. E. and Westmann, R. A. (1971). "Dynamic Response of Circular Footings." *Journal of the Engineering Mechanics Division, ASCE*, 97, 1381–1395.

Marquardt, D. W. (1963). "An Algorithm for Lease-Squares Estimation of Nonlinear Parameters." *Journal of the Society for Industrial and Applied Mathematics*, 11(2), 431–441.

Meek, J. W. (1972). "Analysis and Behavior of Soil-Structure Interaction Systems," PhD thesis, Rice University, Houston, TX.

Novak, M. and Beredugo, Y. O. (1972). "Vertical Vibration of Embedded Footings." *Journal of the Soil Mechanics and Foundations Division, ASCE*, 98(SM12), 1291–1310.

Park, K. (2007). "Field Measurement of the Linear and Nonlinear Shear Moduli of Soils Using Dynamically Loaded Surface Footings," PhD thesis, The University of Texas at Austin (in progress).

Parmelee, R. A. (1967). "Building-Foundation Interaction Effects." *Journal of the Engineering Mechanics Division, ASCE*, EM2, 131–152.

Roberts, M. J. (2004). *Signals and Systems.* McGraw-Hill, New York, NY.

Roblee, C. and Riemer, M. (1998). "The Downhole Freestanding Shear Device Concept." *Geotechnical Earthquake Engineering and Soil Dynamics III Conference*, Vol. 1, ASCE, Seattle, Washington, 201–212.

Roesset, J. M. and Whitman, R. V. (1969). "Theoretical Background for Amplification Studies." *Report No. R69-15*, Massachusetts Institute of Technology, Cambridge, MA.

Safaqah, O. A. and Riemer, M. F. (2006). "Minimizing Sampling Disturbance Using a New in situ Device." *Soil Dynamics and Earthquake Engineering*, 26, 153–161.

Seed, H. B. and Idriss, I. M. (1969). "Influence of Soil Conditions on Ground Motions During Earthquakes." *Journal of the Soil Mechanics and Foundations Division, ASCE*, 95(SM1), 99–137.

Seed, H. B. and Idriss, I. M. (1970). "Moduli and Damping Factors for Dynamic Response Analysis." *Report No. EERC 70-10*, University of California, Berkeley.

Shah, P. M. (1968). "On the Dynamic Response of Foundation Systems," PhD thesis, Rice University, Houston, TX.

Stokoe, K. H., Kurtulus, A., and Park, K. (2006). "Development of Field Methods to Evaluate the Nonlinear Shear and Compression Moduli of Soil." *Earthquake Geotechnical Engineering Workshop*, Christchurch, New Zealand.

Stokoe, K. H., Wright, S. G., Bay, J. A., and Roesset, J. M. (1994). "Characterization of Geotechnical Sites by SASW Method." *Geophysical Characterization of Sites*, R. D. Woods, ed., Vol. 10, XIII ICSMFE, New Delhi, India.

Veletsos, A. S. and Verbic, B. (1974). "Basic Response Functions for Elastic Foundations." *Journal of the Engineering Mechanics Division, ASCE*, 100, 189–202.

Veletsos, A. S. and Wei, Y. T. (1971). "Lateral and Rocking Vibrations of Footings." *Journal of the Soil Mechanics and Foundations Division, ASCE*, 97, 1227–1248.

Verbic, B. (1972). "Analysis of Certain Structure-Foundation Interaction Systems," PhD thesis, Rice University, Houston, TX.

Waas, G. (1972). "Linear Two-Dimensional Analysis of Soil Dynamic Problems in Semi-Infinite Layered Media," PhD thesis, University of California, Berkeley.

Wolf, J. P. (1985). *Dynamic Soil-Structure Interaction.* Prentice Hall, Upper Saddle River, New Jersey.

VITA

Jaehun Ahn was born in Seoul, Korea. After graduation from Young-Dong High School in 1995, he entered Korea University, where he received a Bachelor of Science degree in Civil and Environmental Engineering in 1999. He was conferred a Master of Science degree in Civil and Environmental Engineering also at Korea University in 2001 under the supervision of Professor In-Mo Lee. In September 2003, he entered the Graduate School of Texas A&M University. He then received a Graduate Student Award for Excellence in Doctoral-Level Research while he was employed as a graduate research associate. During the last semester of Ph.D., he also worked for Prairie View A&M University as an Adjunct Professor. On 10th August 2007, a Doctor of Philosophy in Civil Engineering was conferred upon Mr. Ahn.

Department of Civil Engineering care of Dr. Giovanna Biscontin, 3136 TAMU, Department of Civil Engineering, Texas A&M University, College Station, Texas 77843

The typist for this thesis was the author.